Development of reconstruction tools and sensitivity of the SuperNEMO demonstrator

Steven Calvez

NNT : 2017SACLS285

Development of reconstruction tools and sensitivity of the SuperNEMO demonstrator

Thèse de doctorat de l'Université Paris-Saclay
préparée à l'Université Paris-Sud

École doctorale n°576 PHENIICS
Spécialité de doctorat : Physique des particules

Thèse présentée et soutenue à Orsay, le 21 septembre 2017, par

Steven Calvez

Composition du Jury :

Achille Stocchi Professeur, Université Paris-Sud – LAL	Président
Dominique Duchesneau Directeur de recherche, LAPP	Rapporteur
Stefan Schönert Professeur, TU München	Rapporteur
Fabrice Piquemal Directeur de recherche, CENBG	Examinateur
Marco Zito Chercheur, CEA Saclay	Examinateur
Laurent Simard Maître de conférences, Université Paris-Sud – LAL	Directeur de thèse
Xavier Garrido Maître de conférences, Université Paris-Sud – LAL	Co-Directeur de thèse

Thèse de doctorat

Laboratoire de l'Accélérateur Linéaire n° LAL 17-056

Remerciements

Je voudrais commencer par remercier profondément mes directeurs de thèse Xavier Garrido et Laurent Simard. Vous avez toujours été disponibles malgré vos emplois du temps chargés d'enseignant et de chercheur. Vous avez su aiguiller et suivre mes travaux tout en me laissant la liberté d'explorer et de mettre en place mes propres solutions, le tout dans la bonne humeur. Je n'aurais sincèrement pas pu demander de meilleurs directeurs. Merci aussi à Xavier pour m'avoir permis d'étoffer mon répertoire de blagues. Plus sérieusement, tu auras joué un rôle déterminant dans mon parcours à Orsay, depuis l'entretien d'entrée au Magistère jusqu'à mon doctorat, en passant par le stage de L3 et les cours de C++ en M1 (avec le recul, j'avoue qu'il y avait sûrement plus intéressant à faire qu'un jeu d'échecs). Merci pour tout.

Je tiens naturellement à remercier Achille Stocchi pour m'avoir permis d'effectuer mon stage de L3 ainsi que ma thèse au Laboratoire de l'Accélérateur Linéaire. Merci beaucoup d'avoir assuré la présidence de mon jury ainsi que pour ton soutien dans ma recherche de post-docs.

Je tiens aussi à exprimer ma gratitude envers mes rapporteurs, Stefan Schönert et Dominique Duchesneau, ainsi que mes examinateurs, Fabrice Piquemal et Marco Zito, pour avoir accepté et pris le temps de faire partie de mon jury.

Je remercie également tous les membres du groupe NEMO au LAL. Merci Mathieu Bongrand pour m'avoir converti à la physique du neutrino lors de la Fête de la Science 2012 et de m'avoir beaucoup appris lors de ma thèse. Nos chambres à brouillard auront quand même pas trop mal fonctionnées. Serge Jullian pour m'avoir fait profité de ton expérience. J'espère pouvoir conserver dans le futur ne serait-ce que la moitié de ton énergie et de ton enthousiasme. Pia Loaiza pour avoir partagé ton expertise dans les mesures basse radioactivité et avoir apprécié la presqu'île de Crozon. Xavier Sarazin pour ses nombreux conseils, bonne chance dans tes futurs travaux. Carla Macolino pour les discussions de statistique et les parties de tennis.

Merci aussi à Mathieu Brière pour avoir partagé le nettoyage des blindages et Christian Bourgeois, Bruno Leluan, Joel Collin (joyeux anniversaire !), Rémy Dorkel et Olivier Vitez pour les intenses semaines passées à Modane, mais toujours dans la joie et la bonne humeur. Vous m'avez aussi beaucoup appris.

Merci au personnel administratif du LAL, et plus particulièrement Geneviève Gilbert pour sa patience et son dévouement.

Je voudrais aussi remercier tous les collaborateurs, français et étrangers, de la collaboration SuperNEMO, pour les échanges fructueux et les réunions de collaboration très

enrichissantes. Je voudrais en particulier remercier François Mauger, pour ses conseils et son impressionnant travail sur le logiciel SuperNEMO, Cédric Cerna, pour avoir permis le succès de l'intégration du démonstrateur et m'avoir également beaucoup appris lors de nos semaines à Modane, et une fois de plus Fabrice Piquemal, pour avoir assuré la cohésion et la coordination de la collaboration pendant de nombreuses années et avoir accepté de me recommander.

Félicitations à mes homologues bordelais, Arnaud Huber, et annécien, Thibaud Le Noblet, pour l'obtention de leurs thèses : on aura réussi à soutenir trois thèses SuperNEMO en l'espace d'une semaine ! Bon courage à Guillaume Oliviero pour la dernière année (et mollo sur RL et CSGO).

Je tiens aussi à remercier les thésards et post-doc avec qui j'ai eu le plaisir de partager le bureau : Guillaume Eurin pour avoir pris le temps de répondre à mes questions pendant ta rédaction ainsi que pour tes leçons de skis (tu me dois un pouce), Delphine Boursette avec qui on a refait le monde plus d'une fois, Luiz Manzanillas pour sa patience (promis je te laisse bientôt mon bureau) et Cloé Girard qui assure maintenant ma succession.

Je remercie et félicite également mes amis de promo, Gabriel Jung pour tous les bons souvenirs du magistère, Pierre Favier et Baptiste Abeloos pour nos parties de tennis, Renato Quagliani pour tout le vocabulaire italien que tu m'as appris, Julia Casanueva pour ta constante bonne humeur et bien-sûr Christophe Goudet, qui me supporte depuis les TP de L3, merci pour les bonnes recettes élaborées lors de notre été au CERN et pour les discussions, parfois sérieuses, résultant de mes incursions impromptues dans ton bureau. Nos parcours se séparent finalement, bonne chance pour la suite.

Merci aussi aux autres promotions de thésards du LAL qui furent bien plus que de simples collègues : Marta Spinelli pour son énergie et sa joie de vivre, Cyril Bécot pour un peu le contraire, Mohamad Ayoub pour m'avoir motivé à aller à la muscu plus régulièrement, David Delgove pour sa malchance au poker, Luca Garolfi pour partager mes goûts cinématographiques, Charles Delporte pour nos soirées Civ, Antinéa Guerguichon pour m'avoir toujours bien assuré à l'escalade et pour tes fous rires communicatifs, Corentin Allaire pour assurer la continuité des soirées films, Antoine Laudrain pour… ah bah non il est au CERN, Sylvain Vanneste pour avoir été un bon cosmolo-guide catas, et bien d'autres.

Je remercie aussi Maxime Esnault, *bro* depuis presque 20 ans, pour m'avoir permis d'oublier le travail pendant les vacances et de décompresser pendant nos nombreuses soirées gaming.

Enfin, cette thèse, je la dois à ma famille, qui m'a toujours soutenu et encouragé. En particulier, je remercie profondément mes parents et ma soeur qui ont tout fait pour rendre mon parcours possible. Cette thèse est autant la vôtre que la mienne.

Contents

Introduction

Neutrinos are the most abundant particles of matter in the Universe. Yet, because they barely interact with matter, the neutrino remains one of the least understood particles. The Standard Model of particle physics fails to describe the properties of this particle. Over the past few decades, experiments have shown that neutrinos not only exist in three flavors (electron, muon and tau) but that they can oscillate between these different flavor eigenstates. The observation of neutrino oscillations proved that neutrinos were massive particles but neither the value of their mass eigenstates nor their ordering are known to this day. In addition, the nature of the neutrino has yet to be determined. Since the neutrino is a neutral particle, it could either be a Dirac or a Majorana particle. If, like the other Standard Model fermions, the neutrino is a Dirac particle, then neutrino and antineutrino are two distinct particles. On the contrary, if the neutrino was found to be a Majorana particle, this would mean that the neutrino is its own antiparticle.

The best way to unveil the nature of the neutrino is to look for the neutrinoless double beta decay $0\nu\beta\beta$. This process has never been observed and is only possible if the neutrino is a Majorana particle. It is similar to two simultaneous beta decay within the same nucleus, but without emission of neutrinos. Observing this process would not only prove the Majorana nature of the neutrino but the measurement of its half-life could also help constrain the neutrino masses.

The search for the neutrino nature is a major topic in particle physics. A wide variety of experimental approaches has been developed to address this issue. SuperNEMO is the successor of the NEMO-3 experiment. The first SuperNEMO module, called the demonstrator, is currently under construction and partial commissioning in the Laboratoire Souterrain de Modane. Its unique experimental design combines tracking and calorimetry techniques in order to study a separated source enriched in $\beta\beta$ emitters. The source is composed of 7 kg of ^{82}Se, in the form of thin foils. It is surrounded by a wire chamber which allows a 3-dimensional reconstruction of the charged particles tracks. SuperNEMO is also able to measure the individual particles' energies thanks to a segmented calorimeter. The latter is made up of photomultipliers coupled to plastic scintillators. In addition, a magnetic field can be applied to the tracking volume in order to curve the tracks of charged particles and thus achieve a charge identification. The particle identification and full kinematics reconstruction are not only very efficient means to reject background events but it also allows SuperNEMO to discriminate between the different hypothesized underlying $0\nu\beta\beta$ mechanisms, should this process be observed.

The first Chapter of this thesis provides an introduction to neutrino physics and the

double beta decay. It also includes an overview of the current experimental effort invested in unveiling the nature of the neutrino via the search for the neutrinoless double beta decay.

The second Chapter focuses on the SuperNEMO experiment. Its design and the principle of the search for the $0\nu\beta\beta$ decay are exposed in details.

The third Chapter is dedicated to the presentation of the simulation and reconstruction software developed by the SuperNEMO collaboration, to which several contributions were made during this thesis. It also presents the analysis strategy as well as the tools employed in the data analysis.

Different works related to the magnetic field in the SuperNEMO demonstrator are presented in the fourth Chapter. The optimization of the magnetic field value using Monte-Carlo simulations is first explained. A characterization of the magnetic shielding and its impact on the detector performances is then provided.

The fifth Chapter summarizes the characterization and performances of new γ-reconstruction algorithms developed during this thesis, in an effort to maximize the γ reconstruction efficiency and improve the γ energy reconstruction.

After having presented the different background origins (Chapter 2) and how they can be measured thanks to dedicated analysis channels (Chapter 3), the sixth Chapter provides a study of the demonstrator sensitivity to its main backgrounds. In particular, this Chapter shows the temporal evolution of the statistical and systematic uncertainties on the background activities, or half-lives, measured by the demonstrator.

The seventh and last Chapter holds the estimation of the SuperNEMO demonstrator sensitivity to the neutrinoless double beta decay, under different background assumptions. It also illustrates how taking advantage of the several topological variables available in a multivariate analysis can help improve the demonstrator sensitivity.

Chapter 1

Neutrino phenomenology and experimental review

Neutrinos have yielded some of the most unexpected discoveries in particle physics over the last few decades and still continue to elude our understanding. The Standard Model of particle physics, shortly described in this Chapter, does not explain the neutrinos flavor mixing, nor how they acquire their non-zero masses. In addition, the nature of the neutrino is still unknown to this day. An overview of the experimental effort addressing this problem concludes this Chapter.

1.1 The Standard Model of particle physics

The Standard Model of particle physics is a theory finalized in the mid-1970s aiming at describing the interactions of elementary particles. It is a quantum field theory relying on quantum mechanics and special relativity which successfully describes the electromagnetic, weak and strong interactions. It especially proved successful at classifying the subatomic particles discovered at the time but also at predicting new ones which would later be discovered like the top quark, the tau neutrino or more recently the Higgs boson. This theory depicts how ordinary matter, or fermions, interact through each of the three forces aforementioned, via the exchange of mediating particles, called bosons. This model does not describe gravity, however.

1.1.1 Fermions

According to the Standard Model, fermions are elementary particles with half-integer spin, obeying the Pauli exclusion principle. There are 12 fermions composing the ordinary matter, each having an associated antiparticle (see Figure 1.1). These fermions can be classified according to how they interact:

- 6 leptons: electron e^-, muon μ^-, tau τ^-, electron neutrino ν_e, muon neutrino ν_μ, tau neutrino ν_τ. They all interact through the weak force and only the first three, having an electric charge, interact through the electromagnetic force as well.

- 6 quarks: up, down, charm, strange, top, bottom. In addition to carrying an electric charge and a weak isospin, they also carry a color charge, which means that they interact through the electromagnetic, the weak and the strong interaction respectively. The latter makes the quarks bound strongly together to form color-neutral particles called hadrons. Hadrons made of a quark-antiquark pairs are called mesons and those made of three quarks are called baryons: protons, composed of two up quarks and a down quark, and neutrons, composed of two down quarks and an up quark, make up atomic nuclei, which, along with electrons orbiting them, are the building blocks which constitute most of the matter surrounding us.

The fermions can be further classified in 3 generations. Each generation contains two leptons and two quarks, sharing the same physical properties between generations except from the flavor quantum number and the increasing masses (see Table 1.1). The second and third generation quarks, as well as the muon and the tau, are unstable and decay to the first generation fermions with the same quantum numbers.

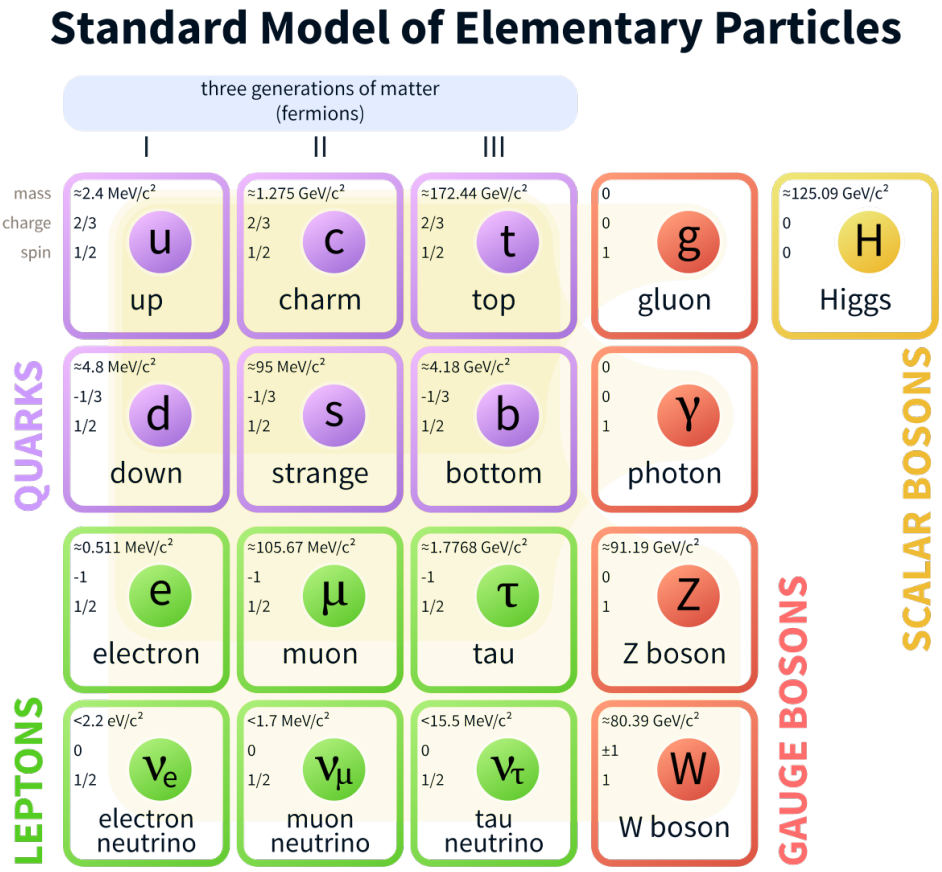

Figure 1.1 – The Standard Model of elementary particles.

	Symbol	Electric charge	Weak isospin	Weak hypercharge	Color charge	Mass
First generation:						
Electron	e	-1	-1/2	-1	1	511 keV
Electron neutrino	ν_e	0	+1/2	-1	1	< 2.05 eV
Quark up	u	+2/3	+1/2	+1/3	3	$2.2^{+0.6}_{-0.4}$ MeV
Quark down	d	-1/3	-1/2	+1/3	3	$4.7^{+0.5}_{-0.4}$ MeV
Second generation:						
Muon	μ	-1	-1/2	-1	1	105.7 MeV
Muon neutrino	ν_μ	0	+1/2	-1	1	< 170 keV
Quark charm	c	+2/3	+1/2	+1/3	3	1.27 ± 0.03 GeV
Quark strange	s	-1/3	-1/2	+1/3	3	96^{+8}_{-4} MeV
Third generation:						
Tau	τ	-1	-1/2	-1	1	1.777 GeV
Tau neutrino	ν_τ	0	+1/2	-1	1	< 18 MeV
Quark top	t	+2/3	+1/2	+1/3	3	173.21 ± 1.22 GeV
Quark bottom	b	-1/3	-1/2	+1/3	3	$4.18^{+0.04}_{-0.03}$ GeV

Table 1.1 – Properties of the elementary fermions. The Standard Model does not explain how neutrinos acquire their very small masses. Only limits on their masses have been obtained.

1.1.2 Bosons and interactions

Bosons are particles with integer spin, following the Bose-Einstein statistics. Most bosons are composite particles, like mesons which are made up of a quark-antiquark pair. However, there are only a few elementary bosons in the Standard Model and these bosons are mediating the interactions. This means that these bosons are exchanged by two particles interacting with each other. The Standard Model's gauge bosons all have spin 1 and mediate the strong, weak and electromagnetic interactions while the recently discovered Higgs boson H^0, with a spin 0, is a scalar boson (see Table 1.2).

The elementary bosons are the following:

- Eight gluons: The gluons are massless particles carrying a combination of color and anti-color charge (among the three possible: red, green and blue). They are responsible for the strong force and their interactions are described by quantum chromodynamics (QCD). Also, since a gluon carries a color charge, it can interact with itself.

- Photon: It is a massless gauge boson mediating the electromagnetic interaction between electrically charged particles, as described by quantum electrodynamics (QED).

- W^-, W^+ and Z^0: They are massive gauge bosons mediating the weak interaction between quarks or leptons of different flavors. The electroweak theory managed to unify the photon and the Z and $W^\pm$ bosons in a single theoretical framework.

- Higgs boson H^0: It is a massive boson with no intrinsic spin. It was first introduced by Peter Higgs in 1964 in an attempt to explain the $W^\pm$ and Z bosons masses while

keeping the gauge invariance of the Lagrangian. Its existence was confirmed by two LHC experiments, ATLAS and CMS, in 2012. It explains why the photon and the gluon have no mass and how the other gauge bosons, and by extent the leptons and the quarks, acquire theirs.

Boson	Interaction	Mass [GeV]	Coupling strength
8 gluons	strong	0	$\alpha_s \equiv 1$
photon	electromagnetic	0	$\alpha = 1/137.04$
$W^{\pm}$	weak	80.385 ± 0.015	$\approx 10^{-5}$
Z^0	weak	91.1876 ± 0.0021	$\approx 10^{-5}$
H^0	–	125.09 ± 0.24	

Table 1.2 – Properties of the elementary bosons

1.1.3 Mathematical formulation

The Standard Model mathematical framework is provided by quantum field theory where the particles are described as fields pervading space-time and which dynamics and kinematics are described in a Lagrangian. The local SU(3)xSU(2)xU(1) gauge symmetry satisfies the postulated symmetries of the system and generates the three fundamental interactions. It was then found that the most general renormalizable Lagrangian depends on 19 parameters which have now all been measured experimentally (see Table 1.3).

1.1.4 Limitations

Although the Standard Model was very successful in predicting the existence and properties of the $W^{\pm}$ and Z bosons, the gluons, and top and charm quarks, before they were even experimentally discovered, it is known to be incomplete because of the following reasons:

- Gravity: The theory does not include gravitation and even the discovery of the graviton, mediating the gravitational interaction, would not be enough to unify quantum field theory and general relativity in order to describe experimental observations (unless further modifications, yet to be formulated, are brought to the model).

- Neutrino masses: The Standard Model describes massless neutrinos. However, the discovery of neutrino oscillations, rewarded by the 2015 Physics Nobel prize, proves that neutrinos are massive particles. Adding mass terms for the neutrinos in the Standard Model without introducing new theoretical problems is nontrivial.

- Dark matter and dark energy: Latest experimental observations showed dark matter comprises about 27 % of the mass and energy of the observable universe and dark energy about 68 %. No good candidates for dark matter can be supplied by the Standard Model while dark energy cannot be explained in terms of vacuum energy. Actually, the Standard Model only explains 5 % of the energy present in the universe.

Parameter	Symbol	Value
Electron mass	m_e	511 keV
Muon mass	m_μ	105.7 MeV
Tau mass	m_τ	1.78 GeV
Up quark mass	m_u	2.2 MeV
Down quark mass	m_d	4.7 MeV
Strange quark mass	m_s	96 MeV
Charm quark mass	m_c	1.27 GeV
Bottom quark mass	m_b	4.18 GeV
Top quark mass	m_t	173 GeV
CKM 12-mixing angle	θ_{12}	13.1°
CKM 23-mixing angle	θ_{23}	2.4°
CKM 13-mixing angle	θ_{13}	0.2°
CKM CP-violating phase	δ	0.995
U(1) gauge coupling	g'	0.357
SU(2) gauge coupling	g	0.652
SU(3) gauge coupling	g_s	1.221
QCD vacuum angle	θ_{QCD}	≈ 0
Higgs vacuum expectation value	v	246 GeV
Higgs mass	m_H	125 GeV

Table 1.3 – Parameters of the Standard Model. The errors are small compared to the quoted values.

- Matter-antimatter asymmetry: The Standard Model predicts equal amounts of matter and anti-matter created at the beginning of the Universe and thus does not explain why our Universe is mostly made out of matter today.
- Other considerations: This model depends on a relatively large number of parameters, as summed up in Table 1.3, which values are measured experimentally, and with no apparent relation between them. It also does not explain why there are 3 generations of quarks and leptons or why the electron and proton electrical charges are exactly opposite.

1.2 Neutrino phenomenology

1.2.1 Discovery of the neutrino

In 1914, J. Chadwick showed that the electrons in the beta decay exhibit a continuous energy spectrum [1]. This was, at the time, a controversial result since it raised concerns about the validity of the energy conservation law. In order to save this principle, Pauli proposed in his famous letter in 1930 [2], the existence of a new particle, emitted along with the electron during a beta decay, that he called "neutron". In 1934, Fermi formulated a theory of the beta decay (see Equation 1.1) involving a new particle [3]: the neutrino (Chadwick having discovered in 1932 the neutron that we know today). Indeed, in this

3-body decay, if the available energy is carried[a] by the electron, which can be detected, and the neutrino, which would escape the detection, and considering that the energy shared between these two particles can vary for each decay, the expected spectrum is a continuous spectrum. The mother and the daughter nuclei having the same spin values, the hypothesized particle was required to have a spin 1/2 *i.e.* to be a fermion. In a β decay, this new lepton is actually required to be an antiparticle in order to satisfy the conservation of the lepton number.

$$n \rightarrow p + e^{-} + \overline{\nu}_e \tag{1.1}$$

The first experimental detection was only reported a couple of decades later, in 1956, by C. L. Cowan and F. Reines [4] through the observation of the inverse beta decay (see Equation 1.2). This process has a very small cross section and consists in the transformation of a proton into a neutron and a positron, induced by an electron antineutrino.

$$\overline{\nu}_e + p \rightarrow n + e^{+} \tag{1.2}$$

They used a water tank with dissolved $CdCl_2$ surrounded by two liquid scintillators in order to detect photons in coincidence: two prompt 511 keV photons from the annihilation of the positron and a few delayed photons from the neutron capture on a Cd nucleus. They placed their detector near different nuclear reactors which were used as neutrino sources and made positive observations at the Savannah River (USA) reactor.

1.2.2 Neutrino flavors and oscillations

The particle observed by Cowan and Reines is the electron antineutrino. In 1962, L. Lederman, M. Schwartz and J. Steinberger proved the existence of a different type of neutrino, the muon neutrino, by observing the creation of muon particles in a spark chamber located on an almost pure ν_μ beam at the Brookhaven accelerator [5] and later confirmed at CERN. The discovery of a third type of lepton, the tau, in SLAC in 1975, motivated the search for the associated tau neutrino. Then in 1989, it was deduced from the Z decay width measurement at LEP [6] that there were three flavors of light left-handed neutrinos (with mass inferior to $M_Z/2$). The tau neutrino existence was only confirmed in 2000 by the DONUT collaboration at Fermilab [7].

Back in the late 1960s, several experiments reported a deficit in the number of electron neutrinos coming from the Sun. They observed less than half the number predicted by the solar Standard Model. This solar neutrino problem can be explained by neutrino oscillations, first suggested by B. Pontecorvo in 1957 [8][9]. This phenomenon was later understood in 1985 due to the Mikheyev-Smirnov-Wolfenstein effect [10][11], which explains how flavors are modified as neutrinos propagate through matter (through the dense solar core concerning electron neutrinos). Experiments looking at solar neutrinos, like the Sudbury Neutrino Observatory [50], and atmospheric neutrinos, like SuperKamiokande [13], confirmed that neutrinos can oscillate between flavors, discovery for which they were

[a] The transfer of momentum to the nucleus is negligible.

awarded the 2015 Physics Nobel prize (Arthur B. McDonald and Takaaki Kajita respectively).

Neutrino oscillations are explained by the fact that neutrino flavor eigenstates $\begin{pmatrix}\nu_e\\ \nu_\mu\\ \nu_\tau\end{pmatrix}$ are different from the mass eigenstates[b] $\begin{pmatrix}\nu_1\\ \nu_2\\ \nu_3\end{pmatrix}$ and, similarly to the quarks, the mixing is described by a unitary matrix called U_{PMNS} (Pontecorvo – Maki – Nakagawa – Sakata)[14]:

$$\begin{bmatrix}\nu_e\\ \nu_\mu\\ \nu_\tau\end{bmatrix} = \begin{pmatrix}U_{e1} & U_{e2} & U_{e3}\\ U_{\mu 1} & U_{\mu 2} & U_{\mu 3}\\ U_{\tau 1} & U_{\tau 2} & U_{\tau 3}\end{pmatrix} \cdot \begin{bmatrix}\nu_1\\ \nu_2\\ \nu_3\end{bmatrix} \tag{1.3}$$

Unlike the CKM matrix in the quark sector, the mixing angles were measured to be large mixing angles, as illustrated by Figure 1.2.

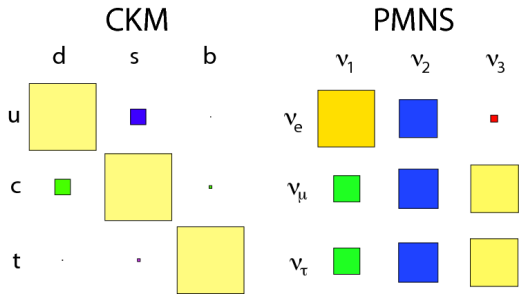

Figure 1.2 – Comparison of the CKM and PMNS matrices: each area of a square represents the square of the corresponding matrix element. The PMNS matrix off-diagonal terms are larger than for quarks mixing, which makes the neutrino oscillations more important.

The PMNS matrix values are measured experimentally and can be decomposed in three matrices according to the source of neutrinos used for the measurement, namely, atmospheric neutrinos, solar neutrinos or reactor neutrinos:

$$U_{\text{PMNS}} = \overbrace{\begin{pmatrix}1 & 0 & 0\\ 0 & c_{23} & s_{23}\\ 0 & -s_{23} & c_{23}\end{pmatrix}}^{\text{Atmospheric}} \cdot \overbrace{\begin{pmatrix}c_{13} & 0 & s_{13}e^{-i\delta_{\text{CP}}}\\ 0 & 1 & 0\\ -s_{13}e^{i\delta_{\text{CP}}} & 0 & c_{13}\end{pmatrix}}^{\text{Solar}} \cdot \overbrace{\begin{pmatrix}c_{12} & s_{12} & 0\\ -s_{12} & c_{12} & 0\\ 0 & 0 & 1\end{pmatrix}}^{\text{Reactor}} \tag{1.4}$$

$$\text{or } U_{\text{PMNS}} = \begin{pmatrix}c_{12}c_{13} & s_{12}c_{13} & s_{13}e^{-i\delta}\\ -s_{12}c_{23} - c_{12}s_{23}s_{13}e^{-i\delta} & c_{12}c_{23} - s_{12}s_{23}s_{13}e^{-i\delta} & s_{23}c_{13}\\ s_{12}s_{23} - c_{12}c_{23}s_{13}e^{i\delta} & -c_{12}s_{23} - s_{12}c_{23}s_{13}e^{i\delta} & c_{23}c_{13}\end{pmatrix}$$

where $c_{ij} = \cos\theta_{ij}$ and $s_{ij} = \sin\theta_{ij}$.

All mixing angles θ_{ij} have been determined experimentally, the last measurement being θ_{13}, whose non-zero value will give access to the neutrino CP-violating phase δ, in reactor and accelerator experiments. The following section provides a quick look at the mathematical formalism explaining neutrino oscillations.

[b] As will be shown later, for oscillations to occur, the mass eigenstates must be different from each other.

Oscillations in vaccum

Neutrinos created from weak charged currents are emitted as flavor eigenstates *e.g.* of flavor α, which is a combination of the mass eigenstates as described by:

$$|\nu_\alpha\rangle = \sum_i U_{\alpha i}|\nu_i\rangle \tag{1.5}$$

The evolution of a mass eigenstate over space and time is obtained from the Schrödinger equation, such that, in natural units ($c = 1$, $\hbar = 1$):

$$|\nu_i(t)\rangle = e^{-i(E_i t - p_i L)}|\nu_i(0)\rangle \tag{1.6}$$

The neutrino masses being very low, the following approximation on their energy can be made:

$$E_i = \sqrt{p_i^2 + m_i^2} = p_i(1 + \frac{m_i^2}{p_i^2})^{1/2} \approx p_i + \frac{m_i^2}{2p_i} \tag{1.7}$$

For the same reason, in natural units, $t \approx L$, which leads to the following expression:

$$|\nu_i(t)\rangle \approx e^{-i(m_i^2/2p_i)L}|\nu_i(0)\rangle \tag{1.8}$$

Considering $E \approx p$ for a relativistic neutrino of flavor α, the equation of propagation described in Equation 1.5 becomes:

$$|\nu_\alpha(L)\rangle \approx \sum_i U_{\alpha i} e^{-i(m_i^2/2E)L}|\nu_i\rangle = \sum_{i,\beta} U_{\alpha i}U^*_{\beta i} e^{-i(m_i^2/2E)L}|\nu_\beta\rangle \tag{1.9}$$

Still considering the flavor conversion $\nu_\alpha \rightarrow \nu_\beta$, the transition amplitude with the distance travelled is then given by:

$$A(\alpha \rightarrow \beta)(L) = \langle \nu_\beta|\nu_\alpha(L)\rangle = \sum_{i,\beta} U_{\alpha i}U^*_{\beta i} e^{-i(m_i^2/2E)L} \tag{1.10}$$

The transition probability is thus:

$$\begin{aligned} P(\alpha \rightarrow \beta)(L) = |A(\alpha \rightarrow \beta)(L)|^2 &= \sum_i \sum_j U_{\alpha i}U^*_{\alpha j}U^*_{\beta i}U_{\beta j} e^{-i(\Delta m_{ij}^2/2E)L} \\ &= \sum_i |U_{\alpha i}U^*_{\beta i}| + 2\text{Re}\left(\sum_{j>i} U_{\alpha i}U^*_{\alpha j}U^*_{\beta i}U_{\beta j} e^{-i(\Delta m_{ij}^2/2E)L}\right) \end{aligned} \tag{1.11}$$

with

$$\Delta m_{ij}^2 = m_i^2 - m_j^2 \tag{1.12}$$

Assuming CP invariance ($\delta = 0$), the PMNS matrix elements are real, hence:

$$P(\alpha \rightarrow \beta)(L) = \sum_i U_{\alpha i}^2 U_{\beta i}^2 + 2\sum_{j>i} U_{\alpha i}U_{\alpha j}U_{\beta i}U_{\beta j}\cos(\frac{\Delta m_{ij}^2 L}{2E}) \tag{1.13}$$

Equation 1.13 shows that for oscillations to exist, there must be at least one mass-squared difference different from zero and non-zero diagonal terms in the mixing matrix. It also requires the mass eigenstates not to be exactly degenerated. The transition probability only depends on Δm^2 which means that measuring the oscillations parameters does not give access to the absolute values of the mass eigenstates.

Considering the simple example where only two neutrino flavors exist ν_α and ν_β, which mixing is described by one angle θ and one mass difference $\Delta m^2_{12} = m^2_2 - m^2_1$ such that:

$$\begin{pmatrix} \nu_\alpha \\ \nu_\beta \end{pmatrix} = \begin{pmatrix} \cos\theta & \sin\theta \\ -\sin\theta & \cos\theta \end{pmatrix} \begin{pmatrix} \nu_1 \\ \nu_2 \end{pmatrix} \tag{1.14}$$

the transition probability is then:

$$P(\nu_\alpha \to \nu_\beta)(L) = \sin^2 2\theta \sin^2 \frac{\Delta m^2_{12} L}{4E} \tag{1.15}$$

Equation 1.15 is often expressed in units adapted to oscillation experiments:

$$P(\nu_\alpha \to \nu_\beta)(L) = \sin^2 2\theta \sin^2 \left(1.27 \Delta m^2_{12}(\mathrm{eV}^2) \frac{L(\mathrm{km})}{4E(\mathrm{GeV})} \right) \tag{1.16}$$

The Figure 1.3 shows the evolution of the transition probability as a function of the distance travelled and the energy of the neutrino, for arbitrary values of θ and Δm^2_{12}.

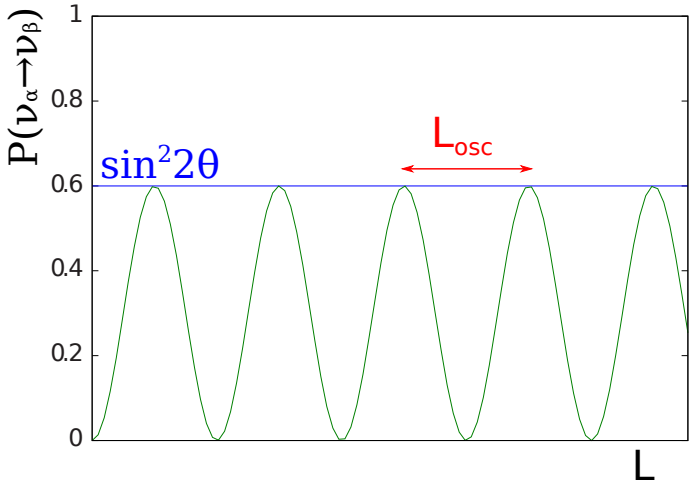

Figure 1.3 – Probability for a ν_α to be detected as a ν_β as a function of the distance traveled, where $L_{\mathrm{osc}} = \frac{4\pi \mathrm{E}}{\Delta m^2_{12}}$.

Oscillations in matter

The neutrino oscillations are affected by the presence of matter. This is known as the Mikheyev-Smirnov-Wolfenstein effect, already mentioned previously. All neutrino flavours interact with matter (protons, neutrons and electrons) through neutral currents.

This effect is identical for all flavours so the transition probabilities between them are unchanged. Only ν_e, however, react with the electrons in the matter through charged current interactions. This effect is proportional to the electrons density and the neutrinos energy. It is consequently substantial for neutrinos going through the Sun, the Earth or supernovae for instance. A similar description to that of Equation 1.15 can be adopted by taking into account this extra potential and replacing the mass-squared differences and mixing angles by new effective parameters.

Oscillation parameters

Solar, atmospheric, reactor and accelerator based neutrinos experiments have been studying neutrino oscillations for the past few decades and have now constrained the parameters of the PMNS matrix. In particular, the three mixing angles θ_{ij} have been measured and two mass-squared differences have been determined. Table 1.4 sums up the latest best fits values for these parameters.

Parameter	Hierarchy	Best fit	1σ
Δm^2_{12} [10^{-5}eV^2]	NH or IH	7.37	7.21 – 7.54
$\sin^2\theta_{12}$	NH or IH	0.297	0.281 – 0.314
Δm^2 [10^{-3}eV^2]	NH	2.50	2.46 – 2.54
Δm^2 [10^{-3}eV^2]	IH	2.46	2.42 – 2.51
$\sin^2\theta_{13}$	NH	0.0214	0.0205 – 0.0225
$\sin^2\theta_{13}$	IH	0.0218	0.0206 – 0.0227
$\sin^2\theta_{23}$	NH	0.437	0.417 – 0.470
$\sin^2\theta_{23}$	IH	0.569	0.518 – 0.597
δ/π	NH	1.35	1.13 – 1.64
δ/π	IH	1.32	1.07 – 1.67

Table 1.4 – The best-fit values and 1σ allowed range of the 3-neutrino oscillation parameters. Δm^2 is defined as $m^2_3 - (m^2_1 + m^2_2)/2$, with $+\Delta m^2$ for NH and $-\Delta m^2$ for IH. This table is adapted from [15].

Since all three mixing angles appear to have non-zero values, current and future oscillations experiments should be able to better constrain, or even measure, the value of δ, by looking at the difference between $P(\nu_\mu \to \nu_e)$ and $P(\overline{\nu_\mu} \to \overline{\nu_e})$. Since only the sign of Δm^2_{12} can be determined experimentally and not that of the larger mass-squared difference, an ambiguity still remains regarding the ordering of the mass eigenstates.

Mass hierarchy

The study of solar neutrinos, leaving the Sun's surface in a pure ν_2 eigenstate due to matter effects, provided the sign of Δm^2_{12} ($m_1 < m_2$). However, two different mass eigenstates orderings are still possible:

- the normal hierarchy: $m_1 < m_2 < m_3$

- the inverted hierarchy: $m_3 < m_1 < m_2$

These two possibilities are illustrated in Figure 1.4.

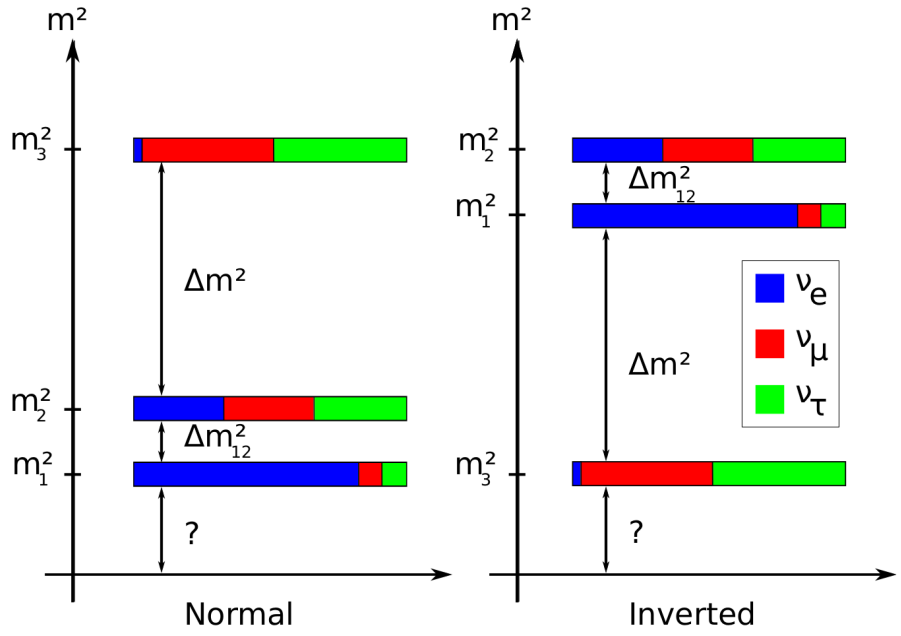

Figure 1.4 – Neutrino mass scale in the normal hierarchy *(left)* and inverted hierarchy *(right)* scenarios. The flavour contributions to each mass eigenstate are also displayed.

In the normal hierarchy, similarly to their lepton counterparts, the lightest mass eigenstate would be mainly composed by the electron-flavoured neutrino. Some hints on the hierarchy could be provided by current oscillation experiments while some future experiments plan on solving this ambiguity.

1.2.3 Neutrino mass and nature

The observation of neutrino oscillations proved that neutrinos are massive particles, in contradiction with the Standard Model, thus proving its incompleteness and manifesting the existence of physics beyond the Standard Model. There are several ways of extending the Standard Model to explain how neutrinos acquire their masses.

Dirac mass terms

Similarly to how quarks acquire their masses through Yukawa coupling to the Higgs field, one can introduce three singlets $\nu_{\alpha,\mathrm{R}}$ with $\alpha = \mathrm{e}$, μ or τ, corresponding to one right-handed neutrino per generation. The neutrino fermionic field $\nu = \nu_\mathrm{L} + \nu_\mathrm{R}$ is thus composed of two chiral fields which are two-components spinors. Indeed, noting m_ν^D the Dirac neutrino mass, one finds back a Lagrangian similar to the quark sector:

$$\mathcal{L}^{\mathcal{D}} = -m_\nu^D \overline{\nu}\nu = -m_\nu^D(\overline{\nu}_R\nu_L + \overline{\nu}_L\nu_R) \tag{1.17}$$

These neutrinos would then acquire a mass:

$$m_i = g_{Y,i}\frac{v}{\sqrt{2}} \tag{1.18}$$

This seems like a simple and natural extension of the Standard Model but several shortcomings arise. As a matter of fact, the Standard Model does not explain why the coupling constant $g_{Y,i}$ would need to be so small (>10^6 lower than for electrons). In addition, there is no genuine justification as to why there should be exactly 3 right-handed neutrinos. Finally, these neutrinos would be almost impossible to detect because they would only interact gravitationally.

Majorana mass terms

Considering the chiral decomposition of the fermionic field $\nu = \nu_{\mathrm{L}} + \nu_{\mathrm{R}}$, if, as the Standard Model predicts, neutrinos are massless particles, the Dirac equation becomes:

$$i\gamma^\mu \partial_\mu \nu_L = 0 \quad \text{and} \quad i\gamma^\mu \partial_\mu \nu_R = 0 \tag{1.19}$$

This means that a massless neutrino (or fermion in general), can be described by a single two-component chiral field. The ν_{L} and ν_{R} spinors are called Weyl spinors. However, if neutrinos are massive particles, the equations of motion are now coupled *via* the neutrino mass m_ν:

$$i\gamma^\mu \partial_\mu \nu_L = m_\nu \nu_R \quad \text{and} \quad i\gamma^\mu \partial_\mu \nu_R = m_\nu \nu_L \tag{1.20}$$

Instead of using four-components spinors to describe a massive particle, Ettore Majorana proposed to consider that the two chiral fields ν_{L} and ν_{R} are not independent [16]. This way, the two previous equations would actually be two different expressions of the same equation, assuming the Majorana relation:

$$\nu_R = \xi \mathcal{C} \overline{\nu}_L^T \tag{1.21}$$

where ξ is an arbitrary phase factor and C is the charge conjugation matrix.
Hence,

$$\nu = \nu_L + \nu_R = \nu_L + \mathcal{C}\overline{\nu}_L^T \tag{1.22}$$

In addition, since:

$$\mathcal{C}\overline{\nu}_L^T = (\nu_L)^C \tag{1.23}$$

It follows that:

$$\nu = \nu_L + (\nu_L)^C \quad \text{and thus} \quad \nu = \nu^C \tag{1.24}$$

This condition imposes Majorana fermions to be their own antiparticles. This is only possible for neutral fermions like neutrinos. Actually, the Majorana description of neutral fermions as two-component spinors is a more simple approach because it does not assume

the existence of antiparticles. For the left-handed chiral field allowed in the Standard Model, the associated Lagrangian becomes:

$$\mathcal{L}_L^M = -\frac{1}{2} m_\nu^M (\overline{\nu}_L^C \nu_L + \overline{\nu}_L \nu_L^C) \tag{1.25}$$

This description of the neutrino mass is in fact the most natural extension of the Standard Model.

Seesaw mechanism

Assuming a right-handed chiral field also exists, it is possible to combine the Dirac and Majorana descriptions, such that:

$$\mathcal{L}^{D+M} = \mathcal{L}_{\text{Dirac}} + \mathcal{L}^L_{\text{Majorana}} + \mathcal{L}^R_{\text{Majorana}} \tag{1.26}$$

which can be written:

$$\mathcal{L}^{D+M} = \begin{pmatrix} \overline{\nu}_L & \overline{\nu}_L^C \end{pmatrix} \begin{pmatrix} m_L & m_D \\ m_D & m_R \end{pmatrix} \begin{pmatrix} \nu_R^C \\ \nu_R \end{pmatrix} + h.c \tag{1.27}$$

where m_D is the Dirac mass as defined in Equation 1.17, and m_L and m_R are the Majorana masses for the left-handed and right-handed neutrinos, as defined in Equation 1.25 for the left-handed neutrino but equivalent for the right-handed neutrino. The mass eigenstates are then:

$$m_\pm = \frac{1}{2} \rho_\pm (m_L + m_R \pm \sqrt{(m_L - m_R)^2 + 4m_D^2}) \tag{1.28}$$

where $\rho_\pm$ ensures that the masses are positive. The mass eigenstates are composed of a mixing of the ν_L and ν_R fields with a mixing angle θ such that:

$$\tan(2\theta) = \frac{2m_D}{m_R - m_L} \tag{1.29}$$

Depending on the value of these parameters, several cases are possible:

- the Dirac limit: if $m_L = 0$ and $m_R = 0$ (or $m_L \ll m_D$ and $m_R \ll m_D$) and $\theta \approx \pi/4$, this is the Dirac description with two degenerate mass eigenstates $m_\pm = m_D$ of opposite CP parity.
- the Majorana limit: if $m_D = 0$, one finds back the pure Majorana description.
- the seesaw mechanism: $m_L = 0$ and $m_D \ll m_R$. This extension of the Standard Model explains how neutrinos acquire their small masses. Indeed, the Standard Model symmetries forbid a non-zero Majorana mass term for the left-handed field ν_L but predict nothing for the ν_R singlet. This way, two mass eigenstates are predicted:

$$m_+ \approx m_R \quad \text{and} \quad m_- \approx \frac{m_D^2}{m_R} \tag{1.30}$$

This could give a very heavy neutrino mass m_+ and a very light one m_-, which small mass is due to the high value of m_R, hence the name of "seesaw mechanism". The light

neutrino ν_- corresponds to the observed active neutrino, compatible with the Standard Model, while the heavy neutrino ν_+ corresponds to a new sterile singlet.

To sum up, the seesaw mechanism explained here in its simplest version (type I seesaw) introduces one very heavy neutrino for each flavor. It explains how neutrinos acquire their low masses other than with an inexplicably low Yukawa coupling for the neutrinos. The Dirac mass is generated through the Higgs mechanism, as for the other fermions. Considering a Dirac mass of the order of the lightest quark, *i.e.* $m_D \approx 1$ MeV, and the observed small neutrino masses (< 1eV), this would require the ν_R mass to be of the order of the Grand Unified Theory scale *i.e.* 10^{14}-10^{16} GeV, which makes it a very interesting Beyond the Standard Model theory. This very high mass also explains why these right-handed neutrinos have not been observed yet. This model requires the neutrinos to be Majorana particles.

Direct mass measurement

Some experiments, like Katrin [17], Project 8 [18] and MARE [19] aim at measuring directly the neutrino mass by studying the beta decay. Indeed, if the available energy E_0 of the decay is known precisely and the electron energy is measured with a high precision, one could infer the neutrino mass by evaluating how much the electron spectrum is affected at the endpoint as illustrated in Figure 1.5.

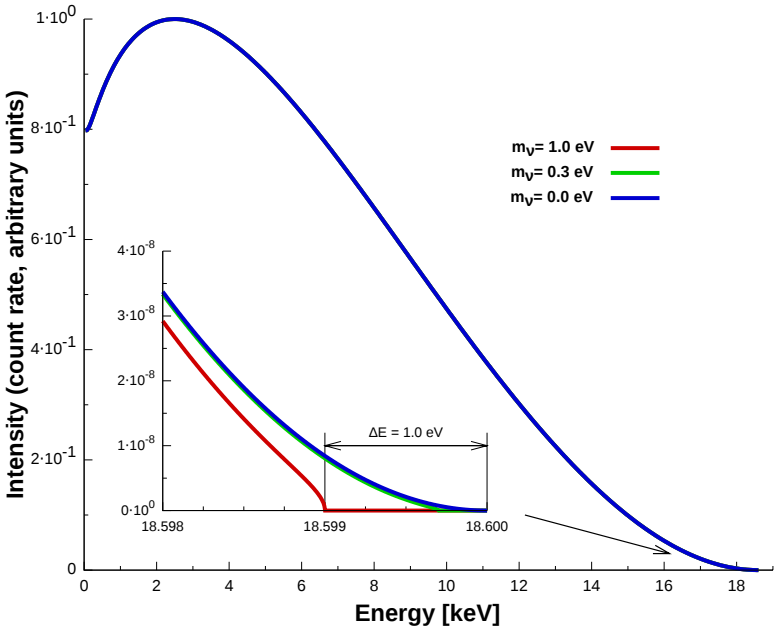

Figure 1.5 – Beta spectrum of Tritium. The neutrino mass can be evaluated by the distortion of the spectrum at the energy endpoint. The spectra for different neutrino mass assumptions are displayed near the endpoint.

Neutrino mass constraints from cosmology

Even if neutrinos are very light particles, their very high abundance means they played a quantifiable role in the development of the Universe as we know it today. Researchers have looked at different ways to measure the influence of the neutrino mass on the Universe evolution:

- Baryon Acoustic Oscillation from the 6dFGS, SDSS-MGS, BOSSLOWZ and CMASS-DR11 measurements.
- Supernovae neutrinos time of arrival.
- Cosmic Microwave Background (CMB) lensing potential power spectrum with Planck
- CMB temperature anisotropy angular power spectrum from the Planck and WMAP data.
- Lyman-α forest power spectrum with BOSS and XQ-100 data.

From these observations, limits on the sum of the neutrino masses can be derived. However, these computations are based on the Λ-CDM model which assumes a flat universe, a cosmological constant and adiabatic primordial perturbations. Some of the more recent studies place limits as low as $\Sigma m_\nu < 0.14$ eV 95 % C.L. [20] which is low enough to start testing the neutrino mass hierarchy.

Nature of the neutrino

Today, one of the main question in neutrino physics, and particle physics in general, is the nature of the neutrino. The neutrino can either be a Dirac or a Majorana particle. If, as proposed by Paul Dirac in 1928 for electrons and generalized to the other fermions, it is a Dirac particle, then neutrinos are different from antineutrinos. However, in 1937, Ettore Majorana proposed a new theory describing fermions [16]. He revisited the Dirac equation and developed the Majorana equation, containing only real factors:

$$-i\gamma^\mu \partial_\mu \psi + m\psi_C = 0 \quad \text{with} \quad \psi \doteq i\psi^* \tag{1.31}$$

This equation describes neutral particles, such as neutrinos, as being identical to their antiparticle. To this day, the best experimental way to unveil the nature of the neutrino is to look for the neutrinoless double beta decay.

1.2.4 Double beta decay

As mentioned previously, the search for a new process, the neutrinoless double beta decay ($0\nu\beta\beta$), is recognized as the best experimental way to determine the nature of the neutrino and to test the lepton number conservation. If the neutrino is found to be a Majorana particle it could open leads for the explanation of lepton number violation, the small masses of the neutrinos through the See-Saw mechanism and the matter/antimatter asymmetry in the Universe through Leptogenesis.

Standard double beta decay $2\nu\beta\beta$

For some nuclei with a high number of nucleons and an even number of protons and neutrons, the beta decay is energetically impossible (the large difference in angular momentum would make the energy of the daughter nucleus higher than the parent one as shown in Figure 1.6).

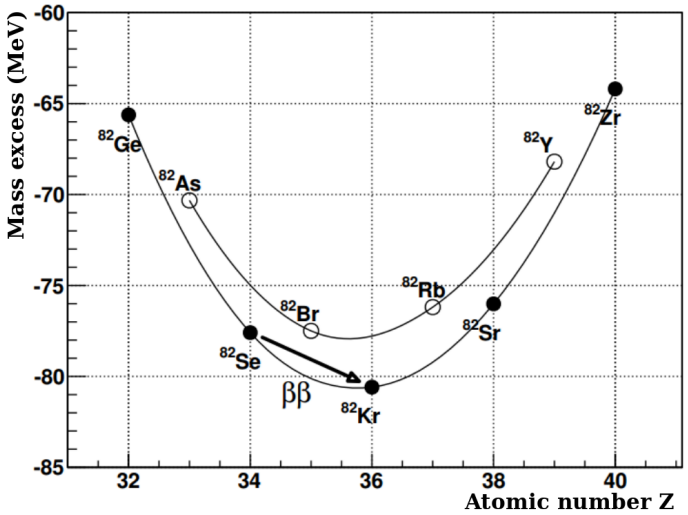

Figure 1.6 – Mass excess as a function of the atomic number for ^{82}Se.

In this case, a double beta decay, akin to two simultaneous beta decay within the same nucleus, is still possible (see Equation 1.32).

$$ {}^{A}_{Z}X \rightarrow {}^{A}_{Z+2}Y + 2e^{-} + 2\overline{\nu}_{e} \tag{1.32} $$

It has first been proposed by M. Goeppert-Mayer in 1935 [22] and has since been observed in numerous nuclei like ^{76}Ge, ^{82}Se, ^{100}Mo or ^{136}Xe, among 35 isotopes capable of double beta decay. Two electrons and two electron antineutrinos are emitted, leading to the measurement of a continuous beta-like energy spectrum extending to the maximum available energy $Q_{\beta\beta}$, the mass difference between the two nuclei (see Figure 1.7).

The Feynman diagram illustrating this decay is presented on Figure 1.8. It is a second-order weak process, making it one of the rarest phenomenon with measured half-lives of the order of 10^{20} years, only second to the hypothetical proton decay (>10^{34} years [23]). This process half-life $T^{2\nu}_{1/2}$ is linked to the phase space factor $G_{2\nu}$ [24] and the nuclear matrix element $M_{2\nu}$ according to:

$$ (T^{2\nu}_{1/2})^{-1} = G_{2\nu}(Q_{\beta\beta}, Z)|M_{2\nu}|^{2} \tag{1.33} $$

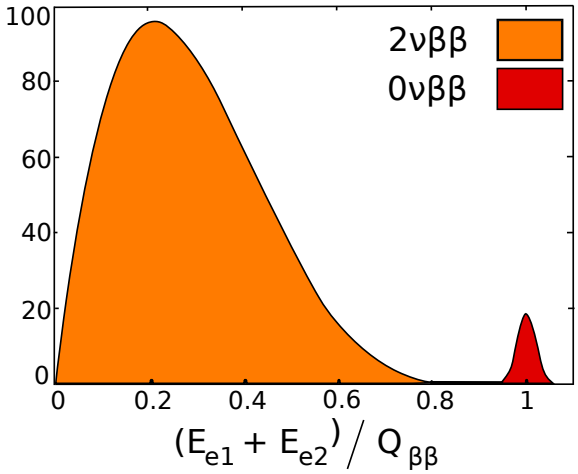

Figure 1.7 – Energy spectra of the $2\nu\beta\beta$ decay in orange and the $0\nu\beta\beta$ in red. The energy resolution applied here is arbitrary and leads to a smearing of the $0\nu\beta\beta$ peak.

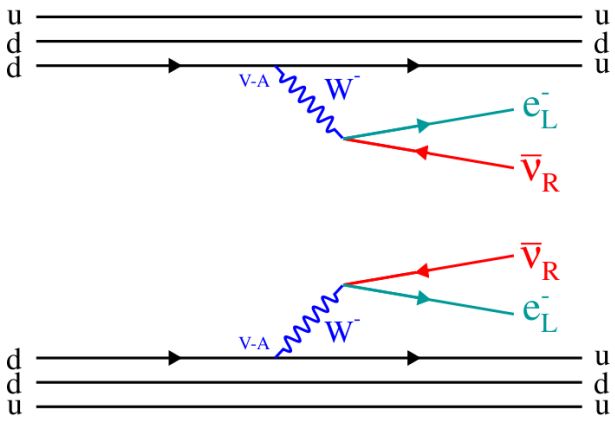

Figure 1.8 – Double beta decay process.

The four particles phase space factor can be accurately computed theoretically while uncertainties on the nuclear matrix elements are still large, as it will be explained later. That's why studying several isotopes is important, as it will constrain the nuclear models and bring some inputs to help reduce the uncertainties on the Nuclear Matrix Elements computation.

Neutrinoless double beta decay $0\nu\beta\beta$

The neutrinoless double beta decay or $0\nu\beta\beta$ was first proposed by W.H. Furry in 1939 [25]. Here, two neutrons decay simultaneously in the same nucleus but neutrinos are not emitted, thus violating the lepton number conservation by 2 units.

$$ {}^{A}_{Z}X \rightarrow {}^{A}_{Z+2}Y + 2e^{-} \tag{1.34} $$

This process is forbidden by the Standard Model but its observation would prove the Majorana nature of the neutrino, regardless of the underlying mechanism, as shown by

the Schechter-Valle theorem [26] (see Figure 1.9).

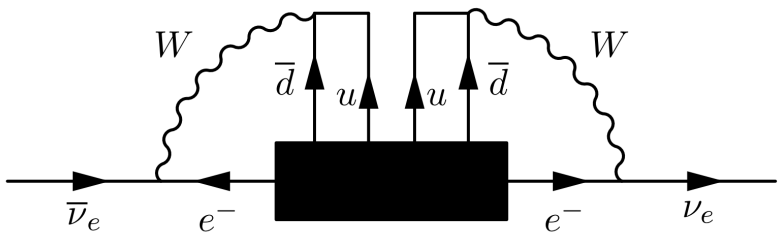

Figure 1.9 – Illustration of the Schechter-Valle theorem with the contribution of the Black Box operator to the Majorana neutrino mass.

Indeed, the mechanism through which the neutrinoless double beta decay could occur is still uncertain and several theories have been proposed (light Majorana neutrino exchange *a.k.a* mass mechanism, Right-Handed currents, Majoron emission, R-parity violating Supersymmetry or Extra Dimensions). The mass mechanism is regarded as the most natural mechanism to which other more exotic mechanisms could contribute. This mechanism is illustrated in Figure 1.10 and can be understood as a regular beta decay *i.e.* the emission of an electron and a right-handed antineutrino, followed by the immediate absorption of this right-handed antineutrino as a left-handed neutrino through a second beta decay occurring at the same time in the same nucleus. Indeed, neutrinos are actually in a superposition of a right-handed state and a left-handed state and despite their very low masses, they travel slower than the speed of light. Thus, there exists some referential in which a left-handed neutrino appears as a right-handed neutrino. Then, the required "transformation" of a neutrino into an antineutrino is natural if neutrinos are Majorana particles. Since the two emitted electrons can be detected, the neutrinoless double beta decay spectrum is expected to be a peak (smeared by the detector energy resolution) located at the maximum available energy $Q_{\beta\beta}$. The nuclear recoil energy is here negligible. The energy spectrum of this process is presented in Figure 1.7.

In addition, the decay rate for the light Majorana exchange mechanism is given by:

$$(T^{0\nu}_{1/2})^{-1} = G_{0\nu}(Q_{\beta\beta}, Z)|M_{0\nu}|^2|m_{\beta\beta}|^2 \tag{1.35}$$

where $G_{0\nu}(Q_{\beta\beta}, Z)$ is the two particles phase space factor, $M_{0\nu}$ is the nuclear matrix elements for the $0\nu\beta\beta$ process and $m_{\beta\beta}$ is the effective Majorana neutrino mass defined as:

$$\langle m_{\beta\beta}\rangle = \left|\sum_i m_i U_{ei}^2\right| \tag{1.36}$$

This effective mass takes into account the neutrino mixing. Consequently, observing the neutrinoless double beta decay would not only prove the Majorana nature of neutrinos but, assuming the mass mechanism, could also constrain the absolute neutrino masses.

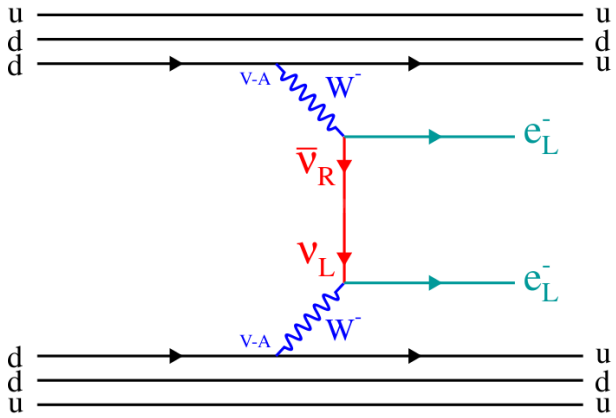

Figure 1.10 – Double beta decay process.

It is worth noting that other processes exist in which the absence of neutrino emission, if detected experimentally, would also prove the Majorana nature of the neutrino.

The double beta decay to excited states of the daughter nucleus, with or without the emission of neutrinos, is different from the $0\nu\beta\beta$ to the ground state in that γ's are also emitted with the electrons. Instead of decaying to the ground state, the nucleus decays, *via* double beta decay, to an excited state of the daugther nucleus, which then decays to its ground state by emitting γ particles. The electrons consequently carry less of the transition energy, which is shared with the γ's. This process has never been observed, neither for the $2\nu\beta\beta$ decay nor for the $0\nu\beta\beta$ decay, but observing it in the latter would also mean the neutrino is a Majorana particle.

Some different processes are:

- The double β^+ decay:

$$ {}^{A}_{Z}X \rightarrow {}^{A}_{Z-2}\,Y + 2e^+ + (2\nu_e)(\beta^+\beta^+) \tag{1.37} $$

- The electronic capture and β^+ decay:

$$ {}^{A}_{Z}X + e^- \rightarrow {}^{A}_{Z-2}\,Y + e^+ + (2\nu_e)(\beta^+/EC) \tag{1.38} $$

- The double electronic capture:

$$ {}^{A}_{Z}X + 2e^- \rightarrow {}^{A}_{Z-2}\,Y + (2\nu_e)(EC/EC) \tag{1.39} $$

The double β^+ decay has the highest predicted half-life of the three processes while the double electronic capture, though more likely, is more challenging to observe experimentally (only X-rays can be detected).

As explained previously, assuming the observation of the neutrinoless double beta decay *via* the mass mechanism and *a fortiori* the measurement of the process half-life, an

accurate computation of both the nuclear phase space factor and especially of the nuclear matrix elements (for each isotope) is required in order to aptly measure or at least constrain the absolute neutrino masses.

- Phase space factor

  Since the first calculations of phase space factors in the late 1950s, more accurate descriptions and fewer approximations of the scattering electron wave functions have lead to some improvements on the phase space factors calculations precision. In particular, taking into account relativistic corrections, the finite nuclear size and the effect of the atomic screening on the emitted electrons have provided updates of the order of a few percent for light nuclei and up to 90 % for U(Z=92). Today, the calculations provided by the different references are all compatible with each other and the main uncertainties come from the nuclear matrix elements.

- Nuclear matrix elements

  The mass mechanism assumes the exchange of a massive neutrino within the nucleus. A proper description of the phenomenon requires understanding the nucleon-nucleon interactions at short distances. These interactions can be described by a many-body Hamiltonian. But the difficulty in solving these equations lies in the need to consider a very large number of energy states possible for the nuclei and to add up all their contributions to accurately predict the transition rate. Several approaches, based on different approximations, have been developed to address this issue [27].

  - Nuclear Shell Model [28]: This model describes the nucleus with 2-body interactions, where the nucleons follow the non-relativistic Schrödinger equation. Here, nucleons are considered to behave independently in a mean field created by all the nucleons. In the same fashion as for electrons, protons and neutrons are each organized in discrete energy levels or shells. This empirical approach proved successful at justifying experimental observations such as the existence of magic numbers (responsible for the very high stability of some nuclei). This approximation is used to fully describe the interactions in a few nuclear orbitals in the valence shell. However, considering only a few nuclear orbitals might be the reason why this model predicts smaller than average values for the nuclear matrix elements. This method is better suited for smaller nuclei. In addition, the Hamiltonian can be adjusted to better describe the spectroscopy of the nucleus.
  - Quasiparticle Random Phase Approximation (QRPA) [29]: This approach aims at describing a large number of nuclear orbitals but considering simpler interactions between nucleons. The nucleus is described using nucleon-nucleon pairs. These quasiparticles are then treated as bosons. The coupling constant of the isoscalar particle-particle interaction, quantifying the proton-proton interaction, is a free parameter of the model but can be constrained experimentally

thanks to the measurements of the $2\nu\beta\beta$ rates. Experimental inputs help reduce uncertainties on the model but it might not describe accurately the $0\nu\beta\beta$ process. This model is more adapted for large nuclei.

- Interacting Boson Model (IBM-2) [30]: The calculations are performed under the shell-model approximation but considers only bosons made of pairs of nucleons with a total momentum of 0 or 2.
- Projected Hartree-Fock Bogoliubov [31]: The transition is calculated using PHFB wave functions and only describes neutron pairs with even angular momenta and positive parity. It includes only quadrupole interactions. Several parameterizations are employed and the resulting nuclear matrix elements are averaged.
- Energy Density Functional [32]: It is based on the PHFB method but aims at improving the latter by including the Gogny interaction [33].

All these models are tested on several isotopes and on similar processes like $2\nu\beta\beta$ decay, β^- decay and β^+ decay but the computations remain very different for the neutrinoless double beta decay because the processes do not share the same intermediate states. Figure 1.11 sums up the predictions on the nuclear matrix elements for the $0\nu\beta\beta$ decay in the main isotopes studied, using the five approaches described above. The predictions can vary greatly for a single isotope but the average values also depend on the isotope. That's why, like the phase space factor, the nuclear matrix elements play a non-negligible role in the choice of the isotope. Assuming a given effective Majorana neutrino mass and that the mass mechanism is responsible for the neutrinoless double beta decay, an isotope with a higher phase space factor and a higher nuclear matrix element would yield more signal events and would consequently be more favorable for the study of the $0\nu\beta\beta$ decay.

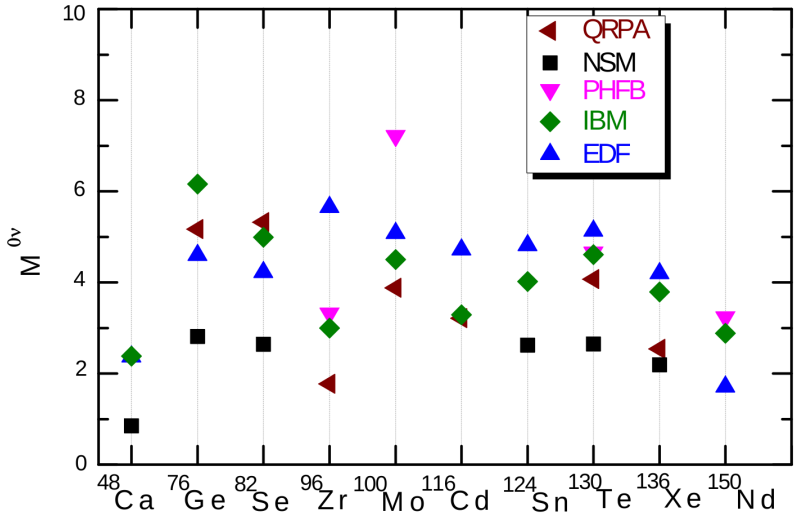

Figure 1.11 – Comparison of the Nuclear Matrix Elements computed for the main isotopes used in double beta decay experiments, using different approaches. Adapted from [34].

- Considerations on the g_A factor

  In the computations of NME for the single β decay (and electron capture EC) and the $2\nu\beta\beta$ decay, the axial vector coupling constant g_A of weak interactions is renormalized. The two main reasons for this renormalization are the interference or omission of non-nucleonic degrees of freedom (mainly Δ but also N^*,...) and the truncations in the nuclear structure calculations. The first reason would produce a quenching of g_A independent of the mass number A while the second reason would yield a quenching depending on the mass number A and model dependent (the larger the mass number A, the larger the quenching). The comparison of the models with the experimental measurements of the β decay/EC and the $2\nu\beta\beta$ decay half-lives can help investigate the effective value $g_{A,\text{eff}}$, defined for $2\nu\beta\beta$ as:

$$M_{2\nu}^{\text{eff}} = \left(\frac{g_{A,\text{eff}}}{g_A}\right)^2 M_{2\nu} \tag{1.40}$$

  Assuming the models are the same for the $0\nu\beta\beta$ decay, a quenching of 0.5 would represent a loss of a factor $(0.5)^4 = 1/16$ on the half-life sensitivity and a reduction by a factor 4 of the effective mass sensitivity. This would seriously impact the possibility for $0\nu\beta\beta$ experiments to probe the inverted hierarchy in the near future. It was estimated [35] that this quenching could be significant depending on the nuclear model: $g_{A,eff} \sim 0.6 - 0.5$ for IBM-2 and $g_{A,eff} \sim 0.8 - 0.7$ for ISM (nuclear shell model). This quenching scales with the mass number $1.269A^{-0.18}$, which means the quenching is more important in heavier nuclei. Several approaches in nuclear field theory have been considered to address the renormalization problem. However, while the renormalization is similar for β and $2\nu\beta\beta$ decays because the vertices can be renormalized separately, the intermediate neutrino propagator in $0\nu\beta\beta$ makes the calculations nonseparable. This means the quenching of g_A for $0\nu\beta\beta$ is still an open question which may or may not impact dramatically on the experimental sensitivities.

1.3 Experimental state of the art in $0\nu\beta\beta$ searches

Historically, three approaches have been considered for the study of the double beta decay: the geochemical detection, the radiochemical detection and the direct detection. The geochemical detection consists in measuring the abundance of double-beta decay daughter nuclei in a natural sample. This method allowed the first detection of the double beta decay in a ^{130}Te sample, back in 1950 [36]. The abundance of daughter nuclei in a dedicated $\beta\beta$-enriched sample can also be measured radiochemically, as was the case for ^{238}U. However, these two methods can only measure the sum of the $2\nu\beta\beta$ and $0\nu\beta\beta$ contributions. In order to unequivocally detect the neutrinoless double beta decay, an experiment should be able to also measure the energy of the electrons in the hope to distinguish between the two processes: this is the direct detection. Several experiments, spanning a wide variety of strategies, have been competing over the last decades without

any clear evidence for a $0\nu\beta\beta$ signal. The challenge for any neutrinoless double beta decay experiment is to observe an excess of events on the total energy spectrum, close to the transition energy $Q_{\beta\beta}$. The $0\nu\beta\beta$ half-life can be expressed as:

$$T_{1/2}^{0\nu} = \ln 2 \cdot \epsilon \cdot t \cdot \frac{\mathcal{N}_A \cdot m}{M} \frac{1}{N_{0\nu}} \tag{1.41}$$

where $\mathcal{N}_\mathcal{A}$ is the Avogadro number, ϵ is the 0ν detection efficiency, m is the total mass of isotope studied, t is the observation time, M is the isotope's molar mass and $N_{0\nu}$ is the number of 0ν events. If no significant excess of events is observed, a limit on the process can be set according to:

$$T_{1/2}^{0\nu,\text{lim}} = \frac{\ln 2 \cdot \epsilon \cdot t \cdot \mathcal{N}_\mathcal{A} \cdot m}{M \cdot N_{\text{exc}}} \tag{1.42}$$

where N_{exc} is the excluded number of 0ν events. If no background is expected, regardless of the exposure, the excluded number of events is constant and then:

$$T_{1/2}^{0\nu,\text{lim}} \propto \epsilon \cdot m \cdot t \tag{1.43}$$

However, if a large number of background events N_b is expected, the number of excluded events is in good approximation:

$$N_{\text{exc}} \propto \sqrt{N_b} \tag{1.44}$$

and with a number of background events proportional to the exposure mt and the width of the energy window ΔE defined by the detector resolution:

$$N_b = b \cdot m \cdot t \cdot \Delta E \tag{1.45}$$

where the background rate b is usually expressed in counts.keV^{-1}.kg^{-1}.y^{-1}. As a result, the best experimental sensitivity now only scales with the square root of the exposure:

$$T_{1/2}^{0\nu,\text{lim}} \propto \epsilon \cdot \sqrt{\frac{m \cdot t}{b \cdot \Delta E}} \tag{1.46}$$

Consequently, the ideal experiment would:

- have a high detection efficiency.
- have the highest isotope mass possible.
- have a good energy resolution. This helps reduce the impact of the natural radioactivity in the Region Of Interest (ROI) and especially the spreading of the 2ν high energy tail in the latter.
- identify the nature of each particle to reject background events.
- have a good spatial resolution to ensure the two electrons come from the same nucleus and reduce the background stemming from random coincidences.

- identify the daughter nuclei to ensure the process observed is indeed a double beta decay.

The background from the natural radioactivity decreases exponentially with the energy. That's why isotopes with high double beta decay transition energies, typically above 2 MeV, are prefered. The materials used by experiments are screened (HPGe measurements, etc.) and the source purified in order to achieve the highest radiopurity possible. Typical radiopurity levels are mBq/kg and even μBq/kg for the most harmful backgrounds or for materials closest to the source. In addition, experiments are operated in underground laboratories to shield them against cosmic rays. Muons can produce neutrons or γ particles from Bremsstrahlung radiation and be mistaken for $0\nu\beta\beta$ events. The deepest laboratories are located in mines or under mountains, providing several kilometers of shielding. Since the shielding power depends on the nature of the overburden, the effective shielding is often expressed in meter water equivalent (m.w.e.).

The choice of isotope, as discussed earlier, often drives the technological solution. Experiments either use an active source or a passive source. Active sources are both the signal provider and the detection means. Such experiments rely on semiconductors, scintillating liquids as well as bolometers. These experiments often have an excellent energy resolution and a high detection efficiency but only give access to the total energy of the transition. Passive source experiments use dedicated subdetectors to study a $\beta\beta$ source. They possess the advantage of measuring the full event kinematics and of identifying the nature of the particles, at the cost of a lower energy resolution and detection efficiency. Such experiments are liquid and gaseous Time Projection Chamber (TPC) or the NEMO experiments, combining tracking and calorimetry techniques.

1.3.1 Germanium experiments

Pure germanium is a semiconductor, which is an interesting property for energy measurement. Indeed, by applying an electric field to a germanium diode thanks to electrodes, it is possible to collect the charges created by a particle interacting in the crystal. These charges are then amplified and converted to a voltage pulse proportional to the energy deposited. Such diodes are usually enriched at about 86 % in ^{76}Ge, a $\beta\beta$ emitter. The drawbacks of this isotope are its low nuclear phase space and its quite low transition energy, $Q_{\beta\beta}$ = 2039 keV, which makes ^{208}Tl, with a γ emitted at E = 2.615 MeV, a problematic background. However, this vulnerability is compensated with an excellent energy resolution, reaching a few keV at the $Q_{\beta\beta}$ when operated at low temperature thanks to a liquid argon cooling system. Several designs have been used by double beta decay experiments. Two designs, namely semi-coaxial diodes and Broad-Energy Germanium (BEGe), are described in the following (see Figure 1.12).

- Semi-coaxial: These detectors consist of a cylinder of Ge crystal with an axial well in its center. The surface of the detector is covered with electrodes. In particular, the outer surface is coated with an n-type contact, having an excess of electrons over

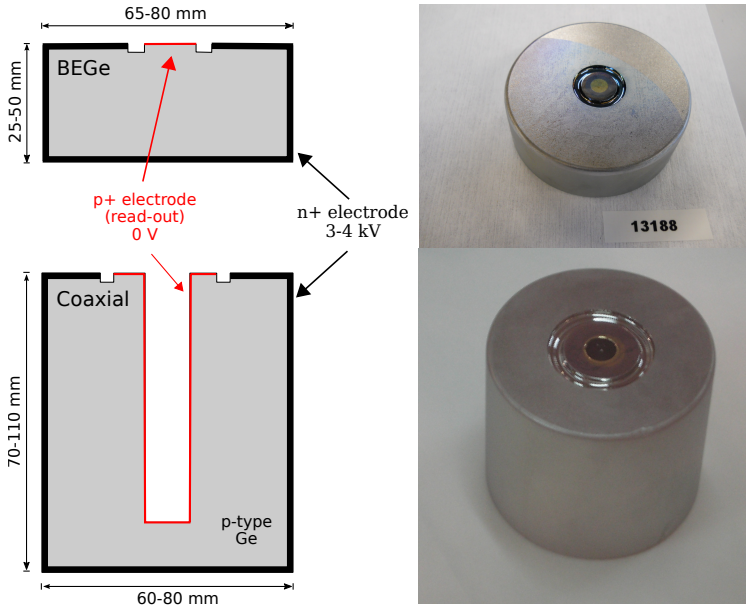

Figure 1.12 – Schematics *(left)* of a BEGe and a coaxial detector from GERDA [37] and their corresponding photos *(right)*.

holes, whereas the well surface is coated with a p-type contact, having an excess of holes over electrons. As a result, the charge carriers (basically electrons and holes) will migrate in the diode and create a detectable current.

- BEGe: the principle is essentially the same but the geometry is different. The p-type electrode is localized on a single face. This new type of detector provides a better energy resolution and better peak shapes, thanks to the use of germanium with enhanced charge collection. This improved design is also more stable (no charge collection loss) and has lower background levels than the coaxial detectors.

Although this experimental approach does not allow particle identification, it can still discriminate between 2 electrons events and γ backgrounds thanks to Pulse Shape Discrimination. Indeed, 2 electrons events create localized energy deposits while γ particles are more likely to be multi-site events since they only deposit energy via Compton scattering. By looking at the amplitude over energy ratio, it is possible to distinguish between single-site and multi-sites events. This technique can also be used to identify electrons or alpha particles from or close to the surface. Finally, looking at coincidences between cristals can help identify probable γ particles.

Heidelberg-Moscow

Heidelberg-Moscow [38] was an experiment in Laboratori Nazionali del Gran Sasso (LNGS, 3500 m.w.e), which ran between 1990 and 2003. It used coaxial germanium detectors enriched at 86 % in ^{76}Ge, totaling almost 11 kg of active source. Its energy resolution was 3 keV at $Q_{\beta\beta}$ and the background level in the ROI was 0.113 ± 0.007 cts.keV^{-1}.kg^{-1}.y^{-1}. In a first analysis, no excess was observed and a limit on the $0\nu\beta\beta$ decay of ^{76}Ge was

set at $T^{0\nu}_{1/2} > 1.85\ 10^{25}$ y with 90 % C.L. However, part of the collaboration, including the spokesperson Hans Klapdor-Kleingrothaus, later claimed the evidence of a 4.2 σ signal with $T^{0\nu}_{1/2} = 1.19\ 10^{25}$ y with 90 % C.L. (Figure 1.13). In the latest analysis, he claims the discovery of the neutrinoless double beta decay with a 6σ significance with $T^{0\nu}_{1/2} = 2.23^{+0.044}_{-0.31}\ 10^{25}\ y$ 90 % C.L. corresponding to $m_{\beta\beta} = 0.32 \pm 0.03$ eV with a 71.7 kg.y exposure.

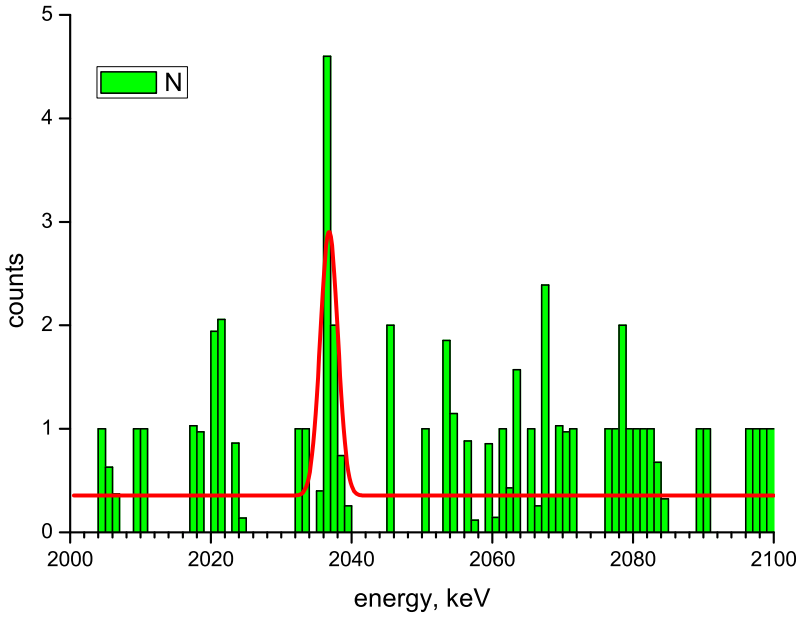

Figure 1.13 – Pulse-shape selected spectrum of single site events in Heidelberg-Moscow, motivating the claim for $0\nu\beta\beta$ discovery in the Heidelberg-Moscow experiment [39].

IGEX

The **I**nternational **G**ermanium **Ex**periment [40] took data from 1991 to 2000 in the Laboratorio Subterráneo de Canfranc (LSC, 2450 m.w.e). It also used semiconductors enriched at 86 % in ^{76}Ge with a 8.9 kg effective mass. It reached a 4 keV energy resolution at the $Q_{\beta\beta}$ and a background level of 0.10 cts.keV^{-1}.kg^{-1}.y^{-1} after Pulse Shape Discrimination. With a 8.88 kg.y exposure (see Figure 1.14), it did not observe any excess and consequently produced a limit $T^{0\nu}_{1/2} > 1.57\ 10^{25}$ y at 90 % C.L. translating to $m_{\beta\beta} < 0.33 - 1.35$ eV.

GERDA

Germanium **D**etector Array is an ongoing experiment located in LNGS. The first phase of the experiment aimed at verifying the Klapdor claim. To do this, it combined the semi-

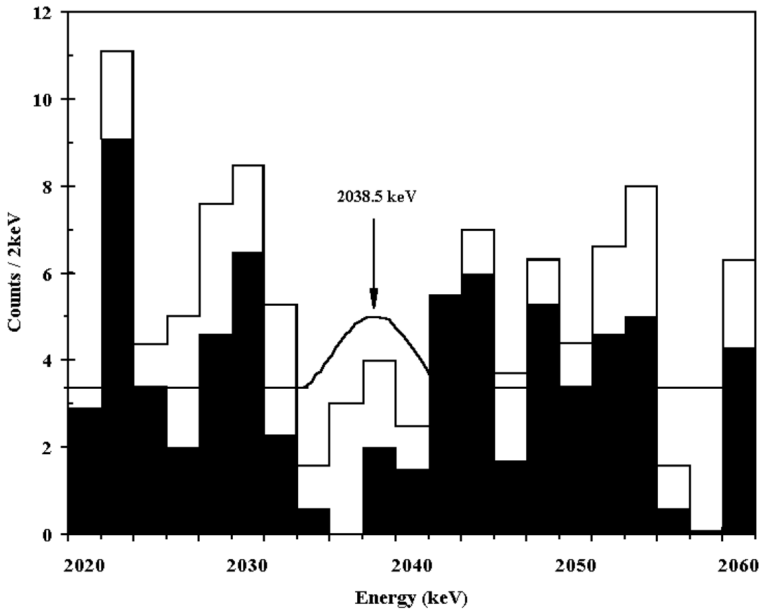

Figure 1.14 – Measured energy spectra before (white) and after (black) Pulse Shape Discrimination with IGEX. The 90 % C.L. constraint on the $0\nu\beta\beta$ process is represented as a gaussian of 3.1 events with a FWHM of ∼4 keV [40].

coaxial detectors from the Heidelberg-Moscow and IGEX experiments, thus gathering 17.7 kg of ^{76}Ge. It collected data between November 2011 and May 2013 for an exposure of 21.6 kg.y. In the absence of a signal, it set a limit $T^{0\nu}_{1/2} > 2.1\ 10^{25}$ y, thus strongly disfavoring the $0\nu\beta\beta$ discovery claim from the Heidelberg-Moscow data (and excluding their previous claim at $T^{0\nu}_{1/2} > 1.19\ 10^{25}$ y). In the second phase of the experiment, the mass was increased and the background rejected more efficiently, thanks to a liquid Argon veto system and pulse shape discrimination. Five new Broad Energy Germanium (BEGe) diodes have been added in 2012 as a test for the Phase II, for a total mass of 3.6 kg. The energy resolution of the coaxial and BEGe detectors was measured to be 4.8 ± 0.2 keV and 3.2 ± 0.2 keV respectively (FWHM at the $Q_{\beta\beta}$). The design of the experiment is illustrated in Figure 1.15.

Compared to the two previous experiments, the shielding was improved and the amount of material close to the detector, in particular, the support of the Germanium diodes, was minimized. The cryostat is a 4 m-diameter stainless steel vessel with a copper lining to reduce the γ flux from the vessel itself. It holds tens of tons of liquid Argon, acting as an external γ shield and a scintillating veto system. A 3 m-thick water shielding surrounds the cryostat in order to absorb neutrons and further reduce the external γ flux. This also provides a Cherenkov medium, to be used as a muon veto. The detector is protected against Radon thanks to a copper shroud located inside the cryostat. The first results of Phase II are presented on Figure 1.16. By combining the two phases, a new lower limit was deduced: $T^{0\nu}_{1/2} > 5.3\ 10^{25}$ y at 90 % C.L, converting to $m_{\beta\beta} < 0.15 - 0.33$ eV (90 % C.L.). The background level measured in the BEGe was $0.7^{+1.1}_{-0.5}\ 10^{-3}$ cts.keV^{-1}.kg^{-1}.y^{-1}, which is an encouraging result for the Phase II target of 10^{-3} cts.keV^{-1}.kg^{-1}.y^{-1}. The target sensitivity is $1.4\ 10^{26}$ y, with the hope to stay a background-free experiment.

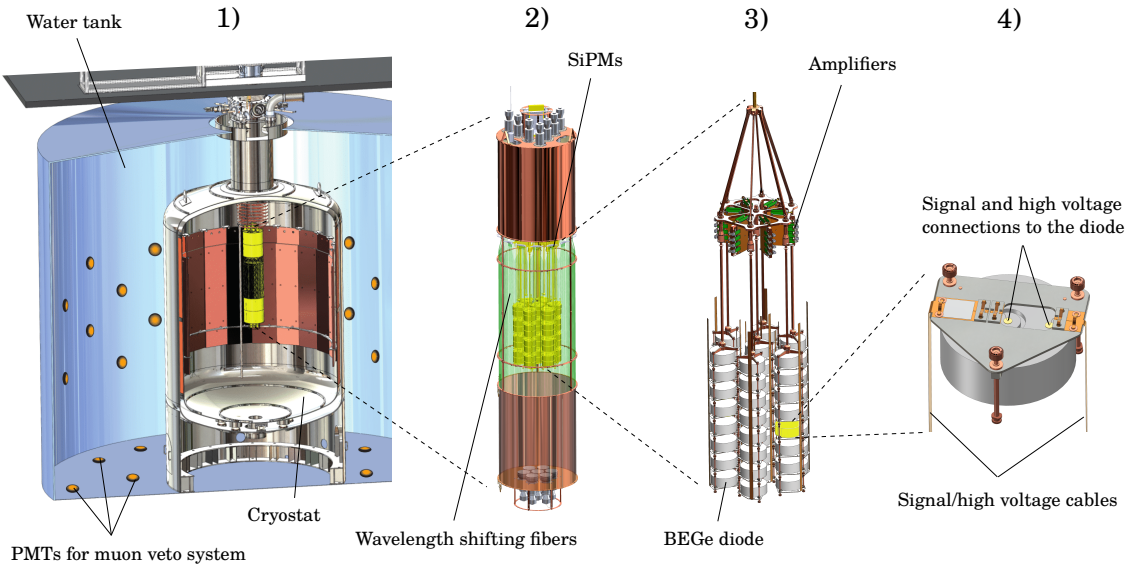

Figure 1.15 – The GERDA experiment. 1) Overview 2) LAr veto system 3) Detector array composed of 7 strings 4) Detector module (bottom view). Adapted from [37].

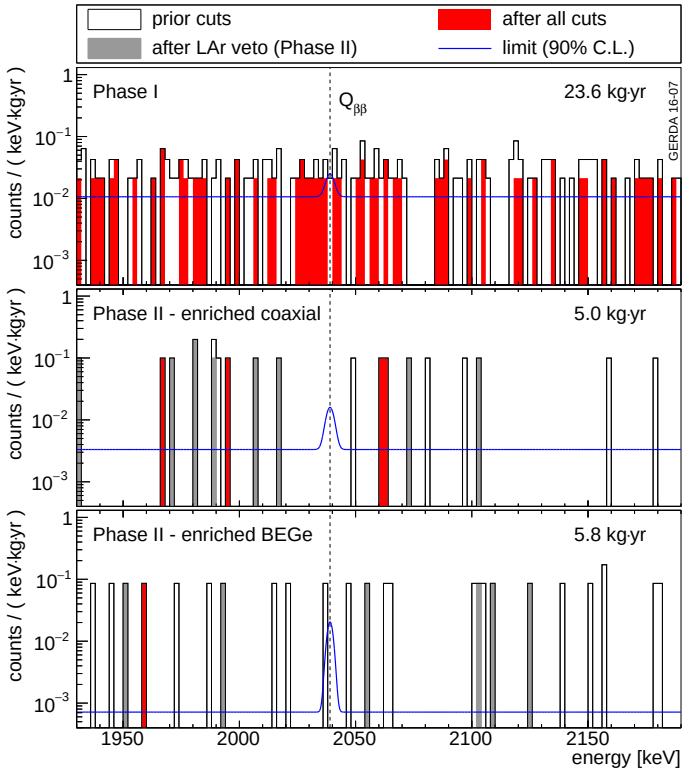

Figure 1.16 – Gerda spectra from the Phase I (top), Phase II coaxial (middle) and BEGe detectors (bottom), along with their respective exposure. The white histogram represents all events before the argon veto cut and the grey one before the pulse shape discrimination cut. The red histogram is the final spectrum. The blue line is the sum of the fitted spectrum and an hypothetical signal corresponding to the limit $T^{0\nu}_{1/2} > 5.3\ 10^{25}$ y at 90 % C.L. [37].

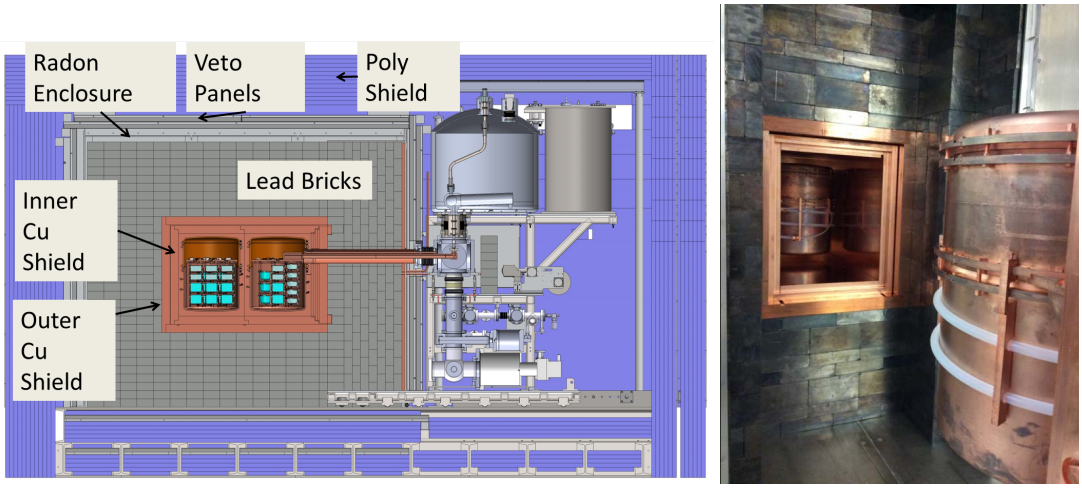

Figure 1.17 – *(left)* Overview of the Majorana Demonstrator with two cryostats in the center. *(right)* Photo of the two Majorana cryostats, one installed within the shield, the other just before insertion [41].

Majorana

The Majorana demonstrator contains [41] almost 30 kg of ^{76}Ge (Figure 1.17) and is located at the Sanford Underground Research Facility (SURF) in Lead, South Dakota, USA. It started taking data in April 2016. Its goal is to determine whether a future 1-tonne experiment can achieve a background level of 1 count per tonne-year in a 4 keV region around the $Q_{\beta\beta}$ (2039 keV), in particular by using electroformed copper for their cryostat. The Majorana and GERDA collaborations should then join their effort for a tonne-scale $0\nu\beta\beta$ search.

1.3.2 Bolometers

Bolometers are calorimeters operating at very low temperatures. When a particle interacts within its sensitive part, it creates heat, quantified by phonons, in proportion to the energy deposited. The heat is then collected by an absorber, like a semiconductor thermistor for instance, and the temperature increase is measured. This temperature increase is proportional to the ratio of the energy deposit over the material heat capacity. That's why such detectors are cooled down to 10 mK, in order to reduce this heat capacity. This experimental approach provides a high energy deposition detection efficiency but the heat signal is quite slow (making events pile-ups more likely). As for germanium detectors, the energy resolution is very good (a few keV). The 2-electrons topological signature is not available either. However, a pulse shape analysis can be performed. The main background sources come from the electronics noise, the thermal noise, natural radioactivity and cosmic rays.

CUORICINO, CUORE-0, CUORE

CUORICINO [42] was an experiment which ran from March 2003 to July 2008 in LNGS. The isotope studied was ^{130}Te, in the form of TeO_2 crystals enriched at 75 % and natural

TeO_2 crystals containing 33.8 % of ^{130}Te. The transition energy of ^{130}Te is $Q_{\beta\beta}$ = 2527.5 keV, which makes ^{208}Tl, with its 2.615 MeV γ, a harmful background. As a consequence, the main backgrounds originated from ^{208}Tl inside the detector as well as from α's from the ^{238}U and ^{232}Th chains daughter nuclei, located on the surface of the detector and from the copper structure holding the crystals. The resulting background levels were measured at 0.104 cts.keV^{-1}.kg^{-1}.y^{-1} for α's and 0.16 cts.keV^{-1}.kg^{-1}.y^{-1} for γ's. The detector was composed of 62 crystals (big and small crystals) for a total mass of 40.7 kg and an average energy resolution of 6.3 ± 2.5 keV (FWHM at $Q_{\beta\beta}$) . With an exposure of 19.75 kg.y, it did not observe the $0\nu\beta\beta$ decay (Figure 1.18) and thus set a limit of $T^{0\nu}_{1/2} > 2.8\ 10^{24}$ y at 90 % C.L. or $m_{\beta\beta} < 0.30 - 0.71$ eV. It also investigated the double beta decay of ^{130}Te to the excited states of ^{130}Xe, both for the two-neutrino and the neutrinoless decays. The limits deduced from this study are $T^{2\nu}_{1/2} > 1.3\ 10^{23}$ y and $T^{0\nu}_{1/2} > 9.4\ 10^{23}$ y, respectively.

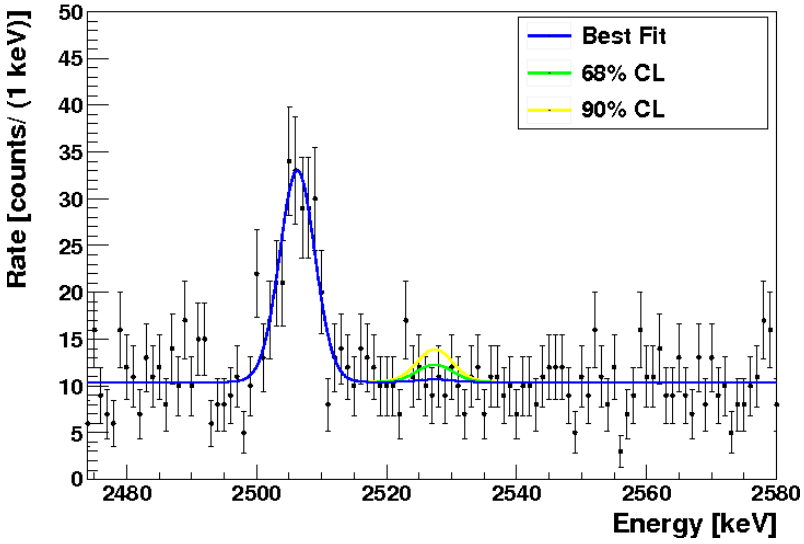

Figure 1.18 – CUORICINO energy spectrum (the different sub-detectors data are combined). In blue, the best fit and in yellow the excluded signal for $T^{0\nu}_{1/2} = 2.8\ 10^{24}$ y at 90 % C.L. [42].

CUORE-0 [43] is the next step towards the final project CUORE [44]. It consists of one CUORE-like tower made of 52 crystals, totaling 39 kg (see Figure 1.19).

The goal was to test the improvements brought over CUORICINO, especially concerning the background reduction thanks to very strict cleanliness conditions during the assembly, before scaling up to the full CUORE detector. After the cool down of the cryostat, the data taking started in March 2013. The data unblinding occurred in April 2015. The α background was reduced by a factor 6. The γ background is still present, but should be reduced with a new cryostat. The energy resolution was measured to be 4.9 keV (FWHM at 2.615 MeV). Combining CUORICINO and Cuore-0 results, a lower limit was set at $T^{0\nu}_{1/2} > 4.0\ 10^{24}$ y and $m_{\beta\beta} < 0.27 - 0.76$ eV.

CUORE is a scaled-up version of CUORE-0, which itself was built on the experience accumulated with CUORICINO. It comprises 19 towers (*i.e.* 988 TeO_2 crystals) for a total

mass of 741 kg, which represents 206 kg of ^{130}Te (see Figure 1.20). The expected resolution is 5 keV (FWHM) at $Q_{\beta\beta}$. Only ultra-pure materials were selected and a more efficient γ shielding was designed in an effort to reduce the background by a factor 2 and reach a background level of 0.01 cts.keV^{-1}.kg^{-1}.y^{-1}. The cryostat was installed and commissioned in spring 2016. After reaching a stable temperature of 6.3 mK, the detector was inserted and the cryostat closed at the end of 2016. The data taking started and the expected sensitivity after 5 years is $T^{0\nu}_{1/2} > 9.5\ 10^{25}$ y translating to $m_{\beta\beta} < 0.05 - 0.13$ eV.

The CUPID project plans to build on the experience and expertise acquired with CUORE to further improve the mass and reduce the backgrounds in the region of interest. This can be achieved by using scintillating bolometers as explained in the next part.

Figure 1.19 – The CUORE-0 tower with 52 TeO_2 crystals.

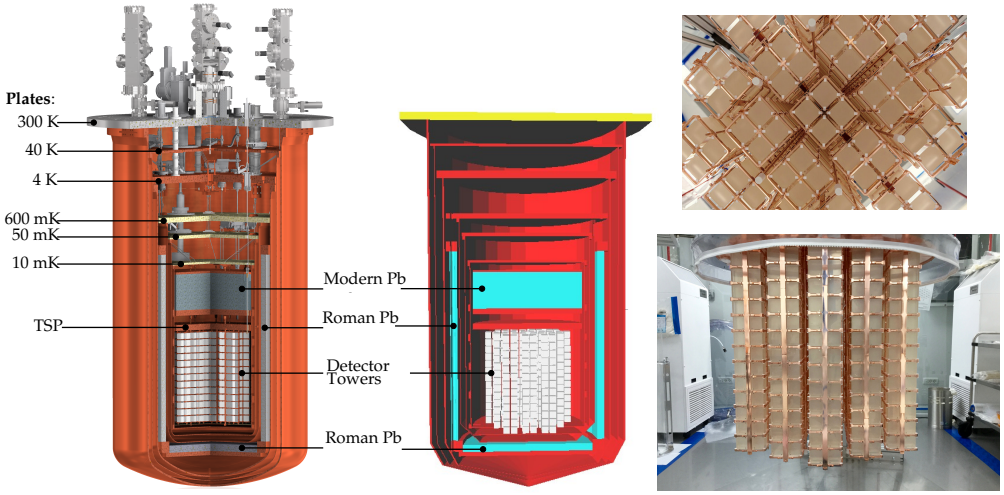

Figure 1.20 – *(left)* Overview of the CUORE experiment, 3D drawing and Monte-Carlo implementation respectively. *(right)* Photos of the CUORE 19-tower array from the bottom and from the side. [44]

LUCIFER, LUMINEU

LUCIFER [45] (Low Background Cryogenic Installation for Elusive Rates) is an experiment relying on bolometers made of ZnSe crystal. ^{82}Se has a higher transition energy $Q_{\beta\beta}$ = 2.995 MeV compared to ^{130}Te, which means the $0\nu\beta\beta$ search is almost free from the ^{208}Tl contamination. The principle is the same as CUORE but in addition to the heat, a small fraction of the energy deposited is converted into scintillation light. Since the scintillation quenching factor is different for α particles and γ/β particles, this property can be used to improve the background reduction. This technology has already been studied in Dark Matter searches and is not possible with Te-based crystals because of its low light yield. The demonstrator will count 36 crystals, representing 15 kg of ^{82}Se. This granularity will also help the background identification because γ's can deposit energy in several crystals at the same time. The expected sensitivity after 5 years and a background level of 10^{-3} cts.keV^{-1}.kg^{-1}.y^{-1} is $T^{0\nu}_{1/2} > 6.0\ 10^{25}$ y and $m_{\beta\beta} < 0.07 - 0.19$ eV.

The LUMINEU [45] experiment (Luminescent Underground Molybdenum Investigation for NEUtrino mass and nature) also plans on using scintillating bolometers but made of $Zn^{100}MoO_4$ and $Li_2^{100}Mo0_4$ crystals (see Figure 1.21). The first crystals produced achieved a 6 keV energy resolution (FWHM at 2.615 MeV) and the production process guarantees an excellent radiopurity. There is now plan for a pilot experiment using 7 kg of ^{100}Mo as part of the CUPID [45] experiment.

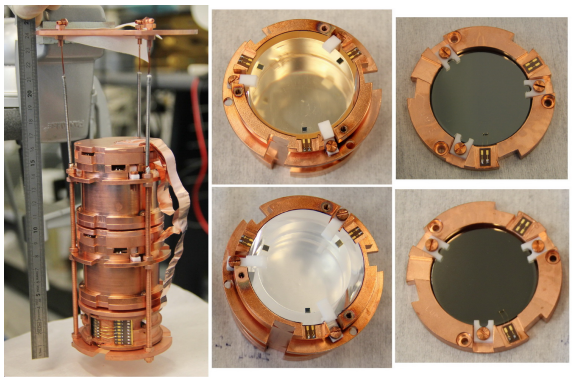

Figure 1.21 – *(left)* Photo of a LUMINEU tower suspended by 3 springs. *(top middle)* 334 g $ZnMoO_4$ bolometer. *(bottom middle)* : 186 g $Li_2^{100}MoO_4$ bolometer. *(right)* : Germanium light detectors. [45]

1.3.3 Time Projection Chamber

Time Projection Chambers are popular detector used in several physics fields, providing a 3-dimensional reconstruction of a particle trajectory. Several designs of TPCs have been developed but the principle stays essentially the same. When a particle goes through a sensitive gas or liquid, it ionizes the medium. The electrons from the ionization drift towards a position-sensitive electron collection system under the effect of an electric field applied to the chamber. The drift time measurement is what allows the reconstruction of

the third coordinate. In addition, if a prompt signal is available (from scintillation light for instance), it is possible to reconstruct the absolute position of the event in the detector.

EXO-200

EXO-200 [46] is a liquid Xenon TPC located in the Waste Isolation Pilot Plant (1585 m.w.e.), New Mexico, USA. It studies 200 kg of ^{136}Xe (enriched at 80.6 %) which transition energy is $Q_{\beta\beta}$ = 2.458 MeV. The design of the detector is presented in Figure 1.22. The detector adopts a cylindrical geometry (40 cm wide and 44 cm long) with a cathode grid held at a negative high voltage in the mid-plane, effectively making it a double TPC. This design aims at minimizing the surface to volume ratio and thus reduces the background contribution from the vessel. The shielding is composed of 50 cm of cryogenic fluid at 167 K in a vacuum-insulated copper cryostat, as well as 25 cm of lead to reduce the external γ flux. Cosmic rays are vetoed by plastic scintillating panels. The ionization and scintillation light produced by the two β particles are read by wire grids and avalanche photodiodes respectively, located at each end of the chamber. The wire grids give access to the 2D-transverse profile of the track and to the energy deposited, while the longitudinal coordinate is deducted from the time difference between the prompt scintillation light measured by the photodiodes and the wire grid signal. The sensitive volume being liquid, electrons will not leave tracks as they would in a gas. However, the possibility to reconstruct the energy deposits positions help discriminate between different topologies of events, namely single-site events (generated by electrons and alpha particles) or multi-site events (generated by gamma particles). As a result, this helps reduce the background induced by γ particles. Moreover, a fiducial volume of 76.5 kg of ^{136}Xe excluding the walls of the TPC was defined in order to lower the background level. Combining the ionization and scintillation signals, EXO-200 can obtain a 3.3 % energy resolution (FWHM at the $Q_{\beta\beta}$). It started taking data in May 2011 and in their latest results they set a limit $T^{0\nu}_{1/2} > 1.1\ 10^{23}$ y and $m_{\beta\beta} < 0.19 - 0.45$ eV. They measured a background level of 1.7 ± 0.2 10^{-3} cts.keV^{-1}.kg^{-1}.y^{-1} and plan on reducing this value for a ton-scale experiment. Some leads on how to increase to the sensitivity are the tagging of ^{136}Ba nuclei, the daughter of ^{136}Xe through double beta decay, and the switch to a gaseous TPC which would add tracking information.

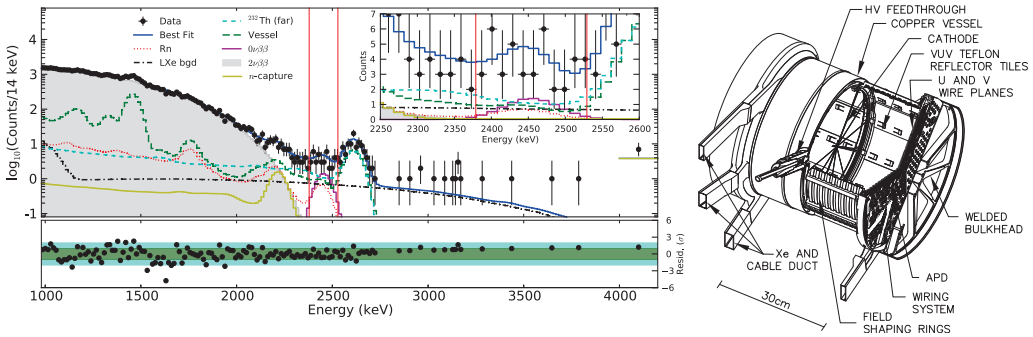

Figure 1.22 – *(left)* EXO-200 energy spectrum of single-site events. *(right)* Design of the EXO-200 TPC. [47]

NEXT-100

NEXT-100 [48] plans to use high pressure gaseous Xenon. The two main advantages are a better energy resolution and the possibility to identify the $\beta\beta$ topology from the track reconstruction. As a matter of fact, β particles can travel around 20 cm in a gas at a 15 bar pressure. An electron signature would be a tortuous track, due to multiple scattering, ending with a characteristic higher energy deposit or blob. The experiment will be hosted in the Laboratorio Subterráneo de Canfranc in Spain. They propose to use electroluminescence to enhance the energy resolution (see Figure 1.23). As for liquid TPC, the scintillation light is the prompt signal providing the reference time used for the spatial reconstruction. It is measured by 60 PMTs located behind a transparent cathode. The ionization electrons drift towards the anode. An extra grid is placed in front of the anode and held at a much higher voltage. This creates an intense field in a 0.5 mm-thick region called the electroluminescence gap. Electroluminescence is then produced by the deexcitation of the gas. This secondary light is emitted isotropically and is measured by the same PMTs used for the prompt signal. The emission possesses a very linear gain and thus provides an accurate calorimetric measurement. The light collection is improved by a reflective coating of the inner surface. Regarding the spatial reconstruction, a tracking plane placed behind the anode and composed of 7500 SiPMs measures the electrons arrival times. NEXT-100 consists in a stainless steel vessel with a 2 m drift length and a 1.3 m diameter. This creates a 2 m^3 volume which, under a 10-15 bar pressure, can hold 100-150 kg of Xe gas. Two prototypes have been developed. The NEXT-DBDM prototype was a smaller version of NEXT-100 (but in the same proportions) which showed it was possible to reach a good energy resolution (1 % FWHM at 662 keV with a ^{137}Cs γ source) using electroluminescence with high-pressure gaseous Xenon. The NEXT-DEMO, in addition to obtaining a good energy resolution also managed to reconstruct tracks with some blobs using a 30 cm drift region. Another prototype, the NEW detector, is currently being commissioned in LSC. It uses the materials planned for NEXT-100 but is only half its size and contains only a tenth of its mass. It plans to characterize the backgrounds and to measure the $2\nu\beta\beta$ decay half-life. The main backgrounds for the $0\nu\beta\beta$ search is the rare 2447 keV γ ray from ^{214}Bi which is close to the ^{136}Xe $Q_{\beta\beta}$ of 2462 keV. Assuming a 4 10^{-4} cts.keV^{-1}.kg^{-1}.y^{-1} background level, a 0.75 % FWHM energy resolution at the $Q_{\beta\beta}$ and a 28 % signal efficiency, NEXT-100 with a 275 kg.y exposure would reach a sensitivity of $T^{0\nu}_{1/2} > 6\ 10^{25}$ y.

1.3.4 Liquid scintillator

Two large liquid scintillator experiments, Kamland and SNO, originally built to detect neutrinos emitted by nuclear reactors or coming from the Sun respectively, are now looking for the neutrinoless double beta decay. By dissolving $\beta\beta$ isotopes to the liquid scintillator they can easily reach large masses of source.

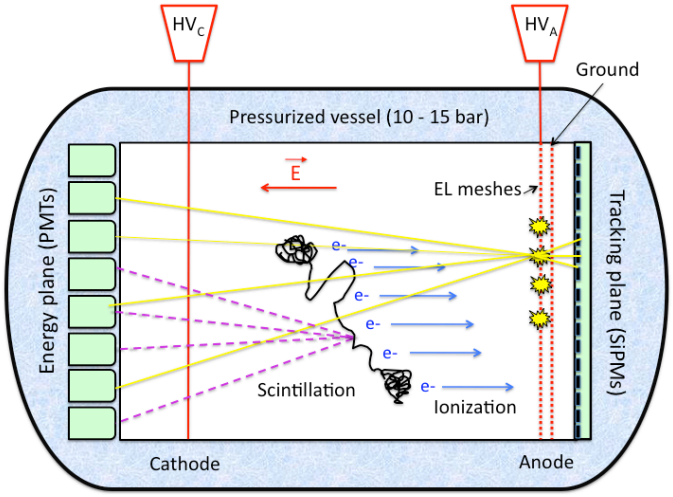

Figure 1.23 – Principle of the NEXT-100 experiment [48].

KamLAND-Zen

Kamland-**Ze**ro **n**eutrino [49] is an experiment located in the Kamioka mine (2700 m.w.e) in Japan. It employs 13 tons of liquid scintillator loaded with 330 kg of Xe enriched at 91 % in ^{136}Xe. Considering the mass of isotope involved, ^{136}Xe was chosen because of its low cost and easy enrichment. It also has a high $2\nu\beta\beta$ half-life and a good solubility (a few percents mass fraction). An overview of the experiment is given in Figure 1.24. The Xe-loaded liquid scintillator is contained in a 3 m-diameter spherical transparent balloon suspended in the existing Kamland experiment. The outer balloon is a 13 m-wide sphere surrounding the inner balloon and contains 13 ktons of liquid scintillator. It serves as an active shielding against γ particles and can detect the internal radiation coming from the inner balloon and its content. The two balloons are themselves contained in 18 m-wide stainless steel sphere filled with buffer oil which acts as an external shielding. This sphere is covered with 1325 17" PMTs and 554 20" PMTs ensuring a 34 % solid angle coverage of the inner balloon. These photodetectors measure the scintillation light emitted by the electrons in the liquid scintillator. This setup provides a 4.1 % energy resolution (FHWM) at the $Q_{\beta\beta}$. Finally, the detector is placed in 3.2 kton water tank used as a water Cherenkov veto detector.

It started taking data in Summer 2011. A fiducial volume, keeping only the innermost 129 kg of ^{136}Xe, was defined. However, an unexpected background was observed in the $0\nu\beta\beta$ region. This background was found to be a contamination in ^{110n}Ag coming from the Fukushima fallout of March 2011. The liquid scintillator and the Xenon were purified and a reduction by a factor 10 of the ^{110m}Ag contamination was achieved. However, an increase in ^{214}Bi events was observed on the lower half of the inner balloon and a more stringent fiducial volume was defined, keeping only 88 kg of ^{136}Xe from a 1 m sphere in the center of the inner balloon. The second phase started in December 2013 and ended in October 2015. The energy spectrum from phase 2 is displayed on Figure 1.24. Combining the results from the two phases, they obtained a lower limit $T^{0\nu}_{1/2} > 1.07\ 10^{26}$ y at 90 %

C.L. and $m_{\beta\beta} < 61 - 165$ meV. This represents the best current limit on the effective Majorana neutrino mass. In a third phase, 600 kg of Xenon should be diluted in the liquid scintillator.

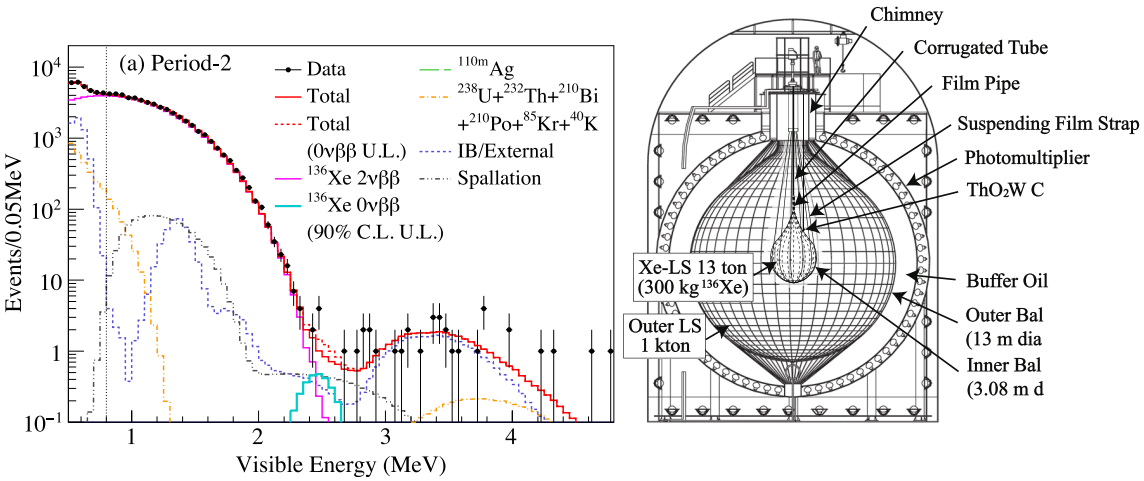

Figure 1.24 – *(left)* Kamland-Zen energy spectrum of selected $0\nu\beta\beta$ candidates in a 1 m-radius spherical volume during Phase 2. The best fit is drawn in red and the spectra corresponging to the 90 % C.L. limit for the $0\nu\beta\beta$ process is drawn in cyan. *(right)* Design of the Kamland-Zen detector. [47]

SNO+

The Sudbury Neutrino Observatory [50] is the world's largest liquid scintillator detector. It is located in SNOLAB (6000 m.w.e.) in Sudbury, Canada. It was originally filled with heavy water to study the solar neutrinos and contributed to the discovery and understanding of neutrino oscillations. SNO+ uses a spherical acrylic vessel with a 12 m diameter to hold the liquid scintillator (see Figure 1.25). They replaced the heavy water with 780 tonnes of scintillating solution (Linear AlkylBenzene) mixed with a wavelength shifter (PPO). This mixing was chosen because of its compatibility with the acrylic vessel, its high light yield (10000 photons/MeV), its good optical transparency, its fast decay time and its low scattering properties. They chose to dope the liquid scintillator with ^{130}Te in the form of natural Tellurium at a 0.3 % mass fraction which represents 800 kg of $\beta\beta$ isotope. A spherical stainless steel frame holds the 9500 8" PMTs employed to measure the scintillation light. This frame has a 18 m diameter and encompasses the acrylic vessel, leaving a 3 m water shielding between the scintillator and the PMTs. This design provides a 6.4 % energy resolution (FWHM) at the $Q_{\beta\beta}$. A protection to shield the detector against the Radon gas emanating from the mine rocks was installed. The detector is currently being filled with water and commissioned. The addition of scintillator should occur during Summer 2017. This will allow to test the detector and assess the background level. The loading with ^{130}Te is scheduled for early 2018. The expected sensitivity on the effective Majorana mass is better than 0.1 eV.

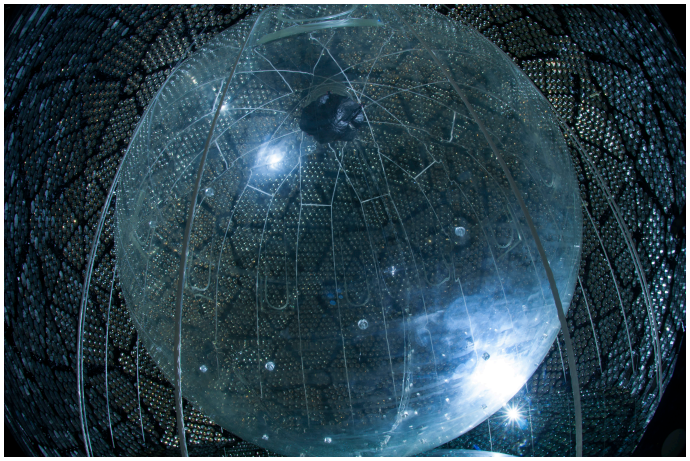

Figure 1.25 – Photo of the SNO+ detector. The acrylic vessel can be seen in the center with the PMTs all around [51].

1.3.5 Tracko-calo experiment: NEMO-3

NEMO-3 [52] is currently the only experiment which has been able to reconstruct both the individual energies and the tracks of the electrons from the double beta decay. It ran between 2003 and 2011 in the Laboratoire Souterrain de Modane (LSM, 4800 m.w.e.). The design of the experiment is illustrated in Figure 1.26.

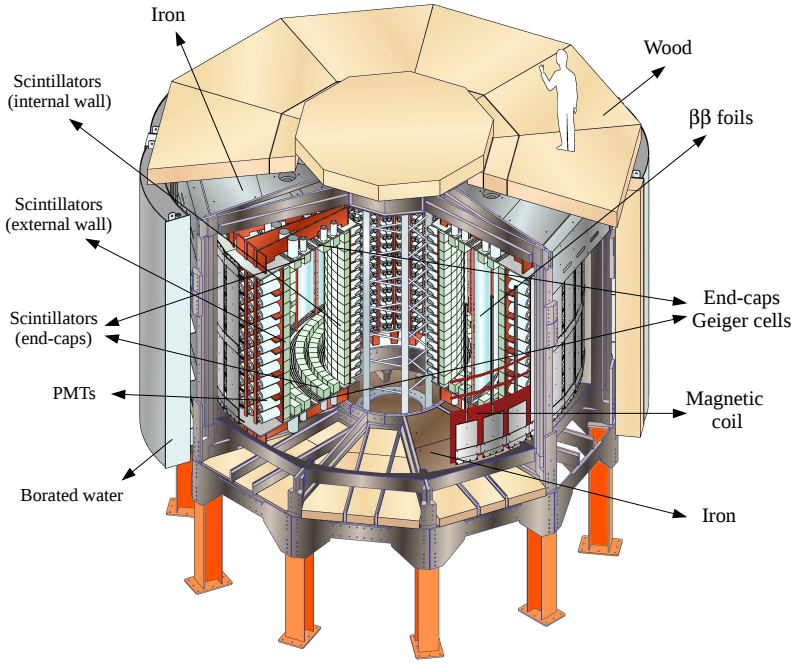

Figure 1.26 – The design of the NEMO-3 experiment.

Unlike other experiments, it uses a passive source, segmented in source foils, enriched in different $\beta\beta$ emitters. They are placed inside a vertical drift wire chamber, providing a three dimensional track reconstruction of the charged particles. The energy of the particles was measured by the calorimeter, which was made of plastic scintillators coupled to low radioactivity 3" and 5" photomultipliers via light guides. A 25 G magnetic field was applied to the tracking volume in order to distinguish electrons from positrons. In addition to the careful material screening, in an effort to improve the experiment's radiopurity, the experiment was protected against external backgrounds with pure iron and borated water shieldings (against the γ's and the neutrons respectively). An anti-radon tent was deployed during the running of the experiment, which reduced the radon contamination in the tracker by a factor 6. It studied, among several isotopes, 6.914 kg of ^{100}Mo. With a 34.3 kg.y exposure to the latter, it did not observe the neutrinoless double beta decay and thus set a limit on the half-life of the process $T^{0\nu}_{1/2} > 1.1\ 10^{24}$ y, corresponding to a limit on the effective Majorana neutrino mass of $m_{\beta\beta} < 0.33 - 0.62$ eV [52]. The two-electron energy sum, focused on the region of interest for this isotope, is displayed in Figure 1.27. No background events were observed above 3.2 MeV, which is an encourageing result for this technique and augurs well for isotopes with a higher transition energy (^{150}Nd, ^{48}Ca or ^{96}Zr).

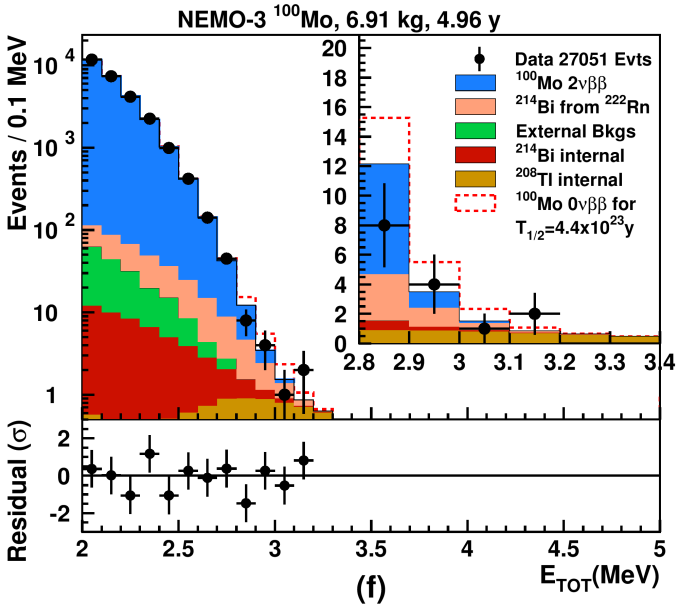

Figure 1.27 – Two-electrons energy spectrum in the region of interest for a 34.4 kg.y exposure to ^{100}Mo [52].

1.3.6 Summary of the present and future experiments

The experiments described above all have their advantages and disadvantages. A wide variety of experimental approaches has been explored and still remains to be developed. If the neutrinoless double beta actually exists, only time will tell which design

proved to be the most succesful. What is certain is that several isotopes need to be studied and several experimental solutions need to be tested. A selection of the current and future main experiments, as well as their projected sensitivity, is presented in Table 1.5.

Experiment	Mass (kg)	Timescale (y)	Sensitivity $T_{1/2}^{0\nu\beta\beta}$ (y)	Sensitivity $\langle m_{\beta\beta} \rangle$ (meV)
GERDA	35	3 (2016 – 2019)	$1.0\ 10^{26}$	110 - 270
LEGEND	200	4 (2022?-2026)	$1.0\ 10^{27}$	75
CUORE	200	5 (2017-2022)	$9.5\ 10^{25}$	53 - 200
CUPID-Mo	7	3 (2017-2021)	$1.7\ 10^{25}$	70 - 200
CUPID	200	10 (2022?-2032)	$2.2\ 10^{27}$	6 - 17
EXO	200	5 (2016- 2021)	$4\ 10^{25}$	100 - 270
nEXO	5000	10 (2025?-2035)	10^{27} - 10^{28}	6 - 53
KamLAND-Zen	750	3 (2017?-2021)	$2.0\ 10^{26}$	45 - 120
	1000	3 (2020?- 2023)	$6.0\ 10^{26}$	26 - 69
SNO+	800	5 (2018-2023)	$9\ 10^{25}$	55 - 205
	8000	5 (2020?-2025)	$7\ 10^{26}$	20 - 73
SuperNEMO	7	2.5 (2017-2020)	$6\ 10^{24}$	200 - 550
	100	5 (2025?-2030)	$1.0\ 10^{26}$	40 - 110

Table 1.5 – Summary of the results of some of the current experiments and the projected sensitivities of their upgrade.

Assuming the mass mechanism is responsible for the neutrinoless double beta decay, SuperNEMO might not be the first experiment to determine the nature of the neutrino. However, thanks to its tracking capabilities and segmented calorimeter, SuperNEMO is currently the only experiment which would be able to identify the underlying mechanism and thus unveil which new physics is responsible for the lepton number violation. The SuperNEMO demonstrator aims at showing that a tracko-calo experiment can reach a very favorable background index, despite a modest energy resolution, as illustrated by Figure 1.28. In fact, this allows competitive sensitivities to be reached while the mass of isotope studied is more than one order of magnitude less than that of experiments with similar energy resolutions.

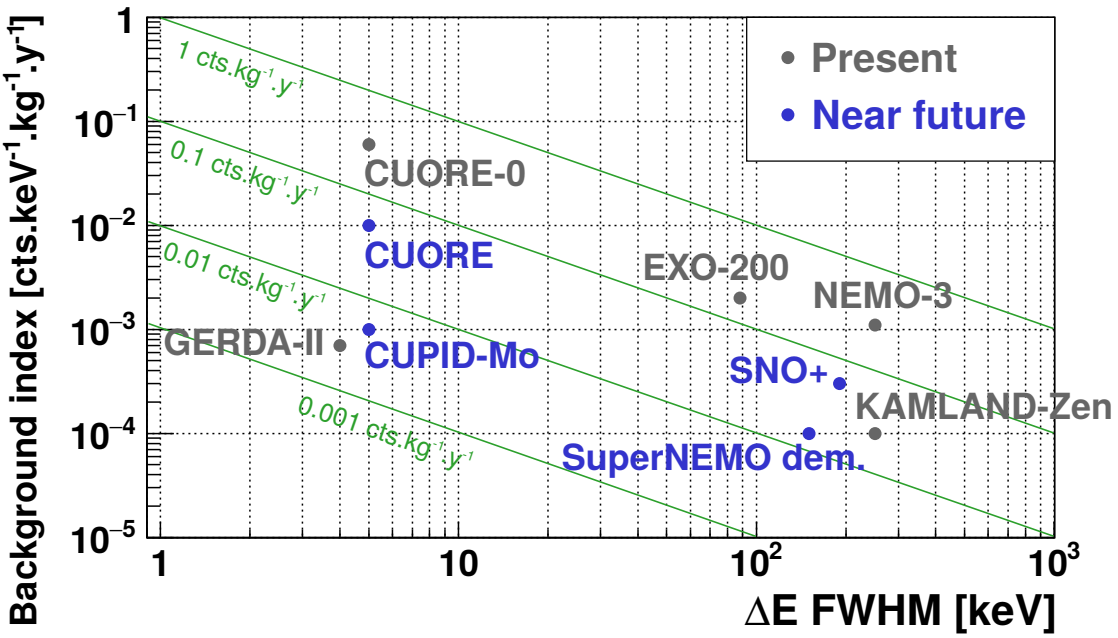

Figure 1.28 – Main experiments' background indices and regions of interest. The latter are directly related to their energy resolution.

Chapter 2

The SuperNEMO experiment

SuperNEMO builds upon the experience acquired with the NEMO-3 experiment. The experimental principle is similar and combines tracking and calorimetry techniques. It uses a segmented calorimeter to measure the individual energies of the particles and a tracker to reconstruct the tracks of charged particles. The source is shaped in foils enriched in $\beta\beta$ emitters, totaling 7 kg of ^{82}Se. A magnetic field is applied to the tracking volume in order to distinguish electrons from positrons. The detector is located in a deep underground laboratory to stop most of the cosmic muons. A combination of an anti-radon tent, a pure iron shielding and a water shielding protects the detector against the natural radioactivity from the laboratory. Two calibration systems are designed to monitor the aging of the calorimeter. A description of the main backgrounds expected in the SuperNEMO demonstrator is provided at the end of the Chapter, before concluding on a comparison with the NEMO-3 experiment.

2.1 The SuperNEMO demonstrator

SuperNEMO is the successor of the NEMO-3 experiment [52]. Unlike other neutrinoless double beta decay experiments, NEMO-3 and SuperNEMO are tracko-calo experiments. This means they are not only able to measure the energy of the particles thanks to a calorimeter, but they can also reconstruct the trajectory of the charged particles with a tracker. This way, the individual particles can be identified and the kinematics of the event recorded. There are many benefits to this technique:

- All the particles from the natural radioactivity, namely e^-, e^+, γ and α, can be detected and identified. SuperNEMO can also identify muons crossing the detector. This provides a powerful background rejection and gives access to channels dedicated to the background measurement.
- Other processes, like the double beta decay to the excited states of the daughter nuclei, can be investigated in dedicated channels (*e.g.* two electrons and one/two gamma particles) .
- Assuming the observation of the $0\nu\beta\beta$ decay, the reconstruction of the kinematics

variables could help discriminate between the different hypothesized underlying mechanisms.

- The source can be exchanged with any other isotope, provided it can be manufactured in a foil shape. This is especially useful if, for instance, new enrichment techniques are developed for more interesting isotopes with a higher transition energy, like ^{48}Ca, or with a greater phase space factor, like ^{150}Nd.

Despite all these advantages, the design of tracko-calo experiments means that only a relatively low mass (compared to liquid scintillator and liquid TPCs experiments) can be studied at once. The $0\nu\beta\beta$ detection efficiency is also reduced and the energy resolution is modest compared to germanium and bolometers experiments.

2.1.1 Principle of a tracko-calo experiment

Unlike all the experiments mentioned in the previous chapter, tracko-calo experiments use passive sources *i.e.* the source only emits the particles, which are then studied with dedicated sub-detectors. The principle of the NEMO experiments is illustrated in Figure 2.1. The source is a thin foil enriched in $\beta\beta$ emitters. It is surrounded by a planar wire chamber which records the tracks of charged particles in the three spatial dimensions. A magnetic field is applied to the tracker to curve the charged particle tracks and thus determine their electric charge (at the exception of α particles and muons). The individual energy and time of arrival of the particles are measured by a segmented calorimeter. The design of the demonstrator is presented in Figure 2.2. The demonstrator is the first SuperNEMO module, out of the 20 planned. The different sub-detectors are presented in details in the following sections.

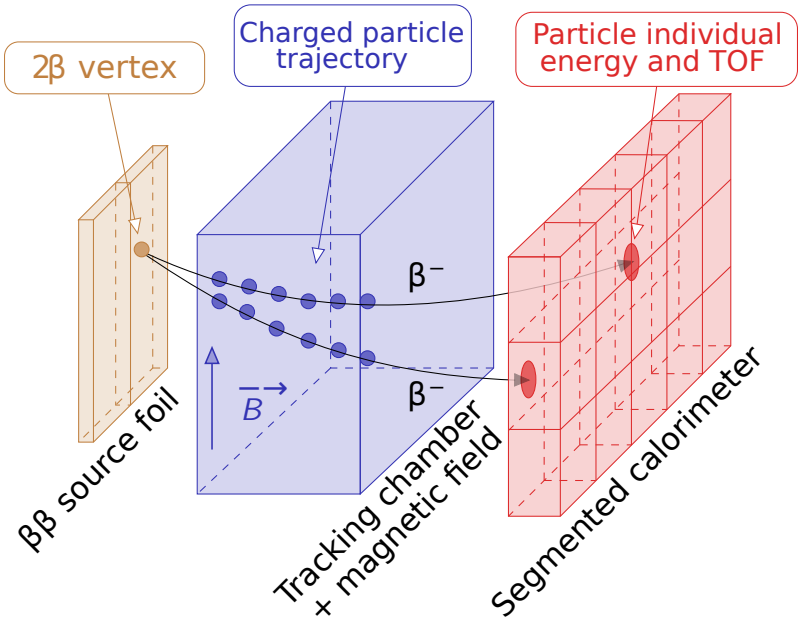

Figure 2.1 – Detection principle of the NEMO experiments.

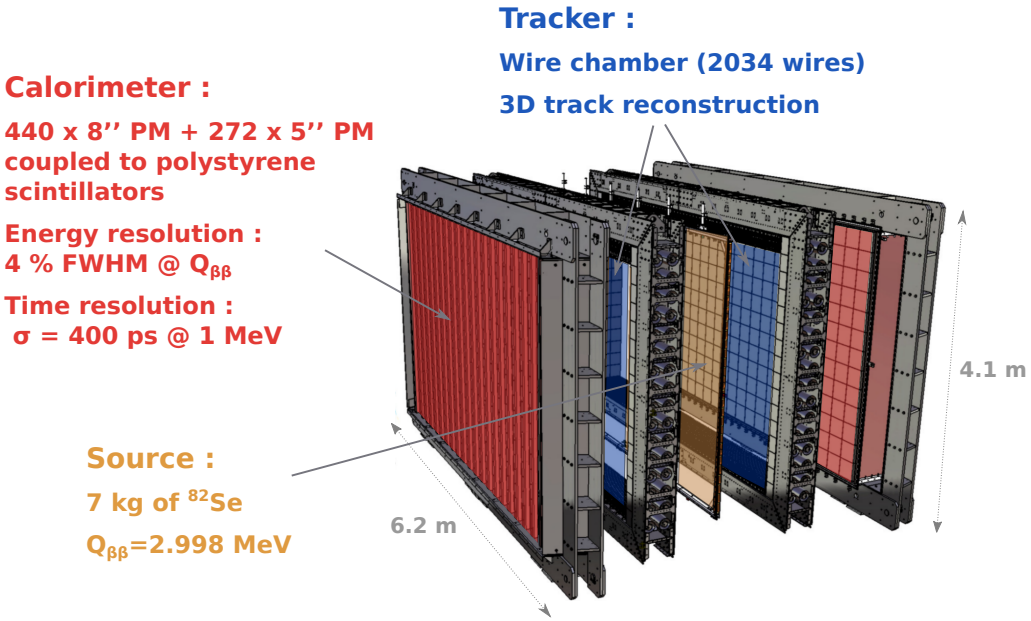

Figure 2.2 – Overview of the demonstrator module. The color choice echoes the colors from Figure 2.1.

2.1.2 The calorimeter

Requirements

In every neutrinoless double beta decay experiments, the sensitivity of the search is directly linked to the background rate in the energy region of interest. The lower it is, the better. This background rate can, of course, be reduced by selecting radiopure materials. Even if this is especially true for materials close to the source foil[a], this is also very important for the calorimeter, considering the mass percentage it accounts for. Furthermore, despite its full event reconstruction capabilities, SuperNEMO cannot distinguish neutrinoless double beta decay events from standard double beta decay events because they share the same signature. Only the reconstructed energy can differentiate the two $\beta\beta$ processes. One way to improve the experiment sensitivity is to decrease the overlap of these two spectra by improving the energy resolution. The $2\nu\beta\beta$ high energy tail will thus be reduced in amplitude and extend less to the $Q_{\beta\beta}$ region, where the $0\nu\beta\beta$ peak would, in addition, be narrowed down. Besides a good energy resolution, the calorimeter must also have a good time resolution as well as an efficient γ detection efficiency (> 50 % at 1 MeV) for background suppression purposes. Mechanical and financial constraints also come into play when choosing the calorimeter design. A sufficiently high granularity is required to be able to measure individual electrons energies and reduce the pile-up probability. This is outbalanced by the need to minimize the dead zone area but also, and mainly, to keep the number of channels to a reasonable amount, financially speaking.

[a] As will be shown later, comparing the time of arrival of the two electrons can help discriminate between the events coming from or close to the source and those emitted in the tracker or the calorimeter.

The calorimeter should also be mechanically easy to manufacture and assemble, robust and long lasting. To reach the target sensitivity while taking all these constraints into account, the goal was set at a 7 % FWHM (Full Width at Half Maximum) resolution for 1 MeV electrons. Table 2.1 shows this resolution for 3 MeV electrons and their equivalent in standard deviation σ. This represents a factor 2 improvement compared to NEMO-3, hence the need for an R&D phase.

Resolution	1 MeV	3 MeV
FWHM	7 %	4 %
σ_E/E	3.0 %	1.7 %

Table 2.1 – Calorimeter energy resolution requirement for SuperNEMO.

R&D

A phase of R&D was carried out in order to improve the calorimeter performance compared to NEMO-3 and establish its final design [53]. SuperNEMO, like NEMO-3, employs plastic scintillators coupled to photomultipliers (PMTs). The principle of the energy measurement is the following:

- An electron, an alpha particle, or a γ particle through Compton scattering, interacts with the scintillator, which in response, emits scintillation photons proportionally[b] to the energy of the incoming particle.
- The scintillation photons propagate through the scintillating medium until they reach the photomultipliers' photocathode.
- This photocathode will absorb the photons and emit photoelectrons *via* the photoelectric effect.
- Each photoelectron will derive towards the first dynode of the PMT under the influence of a high electric potential difference.
- When an electron reaches the first dynode, it will create multiple other electrons by ionization. The number of electrons is further amplified as they cascade through several dynodes. The number of electrons created finally generates a measurable electric current (the typical gain of a PMT being 10^6, which means that for one incoming electron, about a million more electrons are created).

Due to the detection method, the energy resolution is driven by the stochastic fluctuations in the number of photoelectrons, according to:

$$\frac{\Delta E}{E} \approx \frac{2.35\sigma}{E} = \frac{2.35}{\sqrt{N_{\text{pe}}}} \tag{2.1}$$

[b] The quenching of α particles and low energy electrons in the scintillator alter this proportionality.

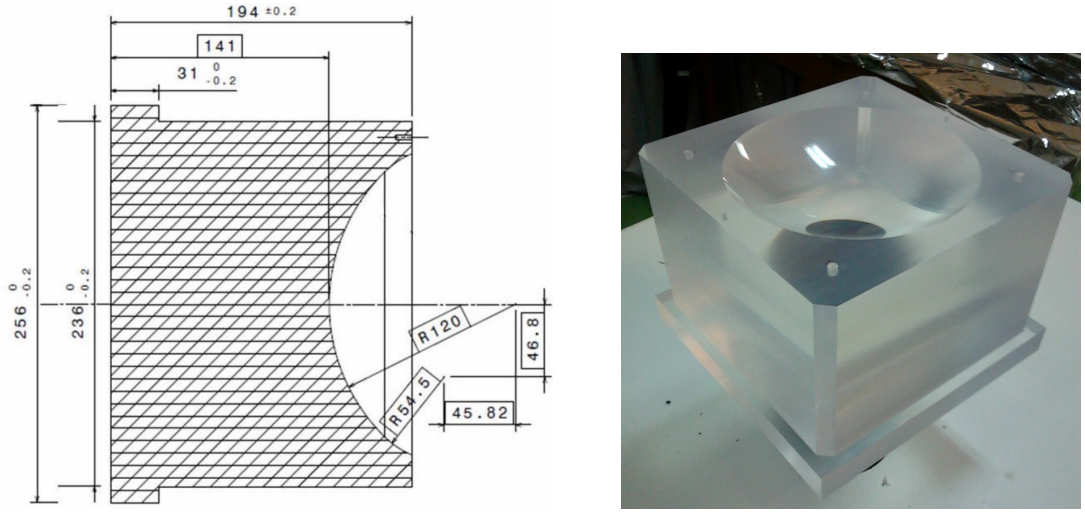

Figure 2.3 – *(left)* Geometry of a polystyrene scintillator block. *(right)* The scintillator block is carved out to receive the PMT bulb. The front face is wider and extends outside the magnetic shielding to increase the calorimeter coverage.

The number of photoelectrons N_{pe} depends, in turn, on the characteristics of the detector, according to:

$$N_{\text{pe}} = \frac{E}{1\text{MeV}} \cdot N_{\text{ph}}^{0} \cdot \epsilon_{\text{col}}^{\text{scint}} \cdot QE_{\text{PMT}} \cdot \epsilon_{\text{col}}^{\text{PMT}} \tag{2.2}$$

In the order in which they are involved in the process: E is the energy of the particle, N_{ph}^{0} is the number of scintillation photons created per MeV of energy deposited (it depends on the scintillator light output), $\epsilon_{\text{col}}^{\text{scint}}$ is the collection efficiency of the scintillation light from the scintillator to the PMT photocathode, QE_{PMT} is the quantum efficiency of the PMT photocathode and $\epsilon_{\text{col}}^{\text{PMT}}$ is the collection efficiency of the photoelectrons from the photocathode to the first dynode.

To help characterize and compare the different solutions considered, a test bench was developed in parallel with a GEANT4 [73] optical simulation. The electron source used is an electron spectrometer (a ^{90}Sr/^{90}Y radioactive source placed inside a magnetic field, operating a precise energy selection) providing electrons with an energy ranging between 0.4 and 1.8 MeV. The time resolution is measured by sending the same 420 nm signal-shaped LED pulse to two identical optical modules. The choice of the scintillator material is driven by the need for a high light yield, a good timing, a low Z (to reduce the low energy electrons backscattering probability), a high radiopurity and a low cost. Several scintillating materials and geometry were considered, including liquid scintillators, but a polystyrene scintillator, which design is shown in Figure 2.3, was retained.

The scintillator depth choice, in addition to the γ detection efficiency, is motivated by the presence of a magnetic field. A study showed that a magnetic shielding needs to extend at least 10 cm beyond the PMT photocathode for it to be efficient. Otherwise, depending on the orientation of the dynode system with respect to the magnetic field, the gain would be noticeably reduced and the resolution worsened relatively by up to 50 %. In order to improve the light collection efficiency, a reflective wrapping and a surface treat-

ment are applied. The scintillator is wrapped with Teflon (600 μm thick or 0.024 g/cm^2) on its sides and Mylar (12 μm) on the sides and the front face (Figure 2.4).

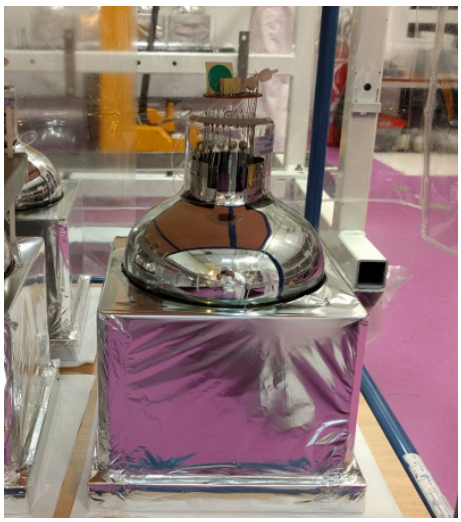

Figure 2.4 – Optical module without magnetic shielding. The shiny wrapping around the scintillator is aluminized Mylar.

The front face wrapping is different because it needs to be thin, with a low Z, in order to reduce the electrons energy losses and the electron backscattering probability, while still shielding against UV photons coming from outside. As shown in Figure 2.3, the scintillator is carved to receive the PMT bulb. A surface polishing and an optical gel with a refractive index comprised between the indices of the PMT glass and the scintillator also helps the optical coupling. The choice of PMT model is motivated by the need for a high quantum efficiency, a good photoelectron collection efficiency, a linear gain with energy, a good time resolution, low dark currents and of course a low radioactivity. The R&D program was carried out in partnership with Hamamatsu and Photonis. This lead to an improvement of the quantum efficiency for 400 nm light (the peak emission of SuperNEMO scintillators), now equal to 35 %, compared to the 25 % quantum efficiency in NEMO-3. The high voltage divider ratios between dynodes were also optimized to increase the photoelectrons collection efficiency and linearity (less than 0.5 % deviation on the 0 – 4.5 MeV range). These improvements should increase the number of photoelectrons to the 1100 required to reach the 7 % energy resolution. This configuration actually provides a mean resolution of 8.3 % for 1 MeV electrons. The Figure 2.5 shows the energy resolution of one of the best optical module tested, as a function of the electron energy.

The scintillators and the PMTs equally impact the calorimeter time resolution. In scintillators, the main factors are the random decay time of the excited states of the scintillator molecules and the propagation time of the photons. For the PMTs, the time resolution can

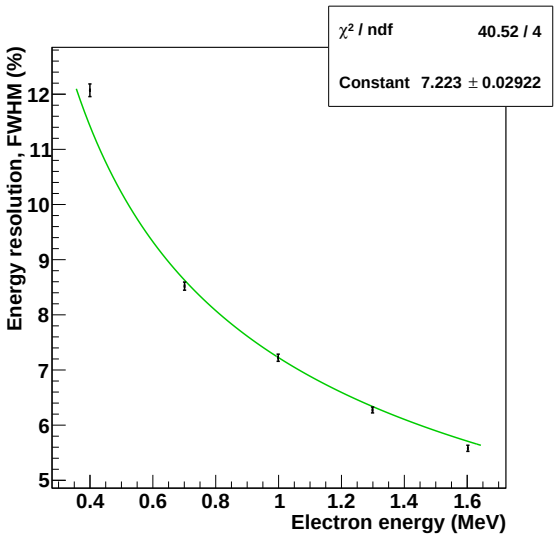

Figure 2.5 – Energy resolution of a SuperNEMO optical module as a function of the electron energy, using a ^{90}Sr beam.

be improved by reducing the number of dynodes so as to reduce the transit time spread. The hemispherical design offers equal distance trajectories from the photocathode to the dynode system. In light of these requirements and the developments accomplished, SuperNEMO selected the 8-inch R5912-MOD Hamamatsu PMTs. The time resolution measurement, using a LED light as explained earlier, gives a 400 ± 90 ps resolution. The Figure 2.6 sums up the share of the different improvements, compared to NEMO-3. Concerning the radiopurity, measurements carried out on the PMTs glass yield the following contamination: A(^{40}K) = 850 mBq/kg, A(^{214}Bi) = 380 mBq/kg and A(^{208}Tl) = 150 mBq/kg. The targets for the PMTs glass radiopurity are thus reached (and better than NEMO3), except for the ^{208}Tl level, which is few times higher than expected.

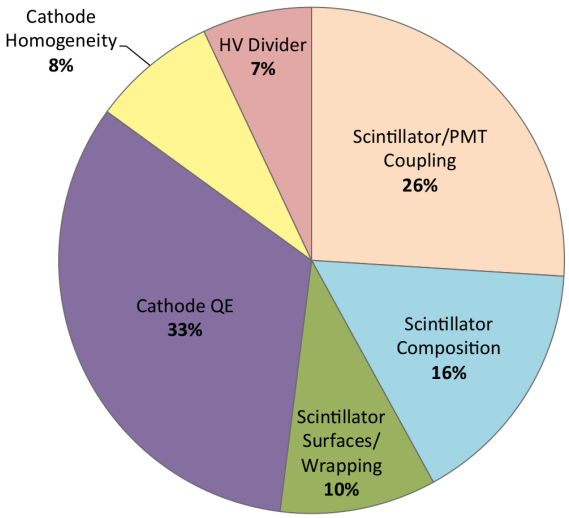

Figure 2.6 – Contribution of the different developments to the energy resolution improvement of a SuperNEMO optical module compared to NEMO-3.

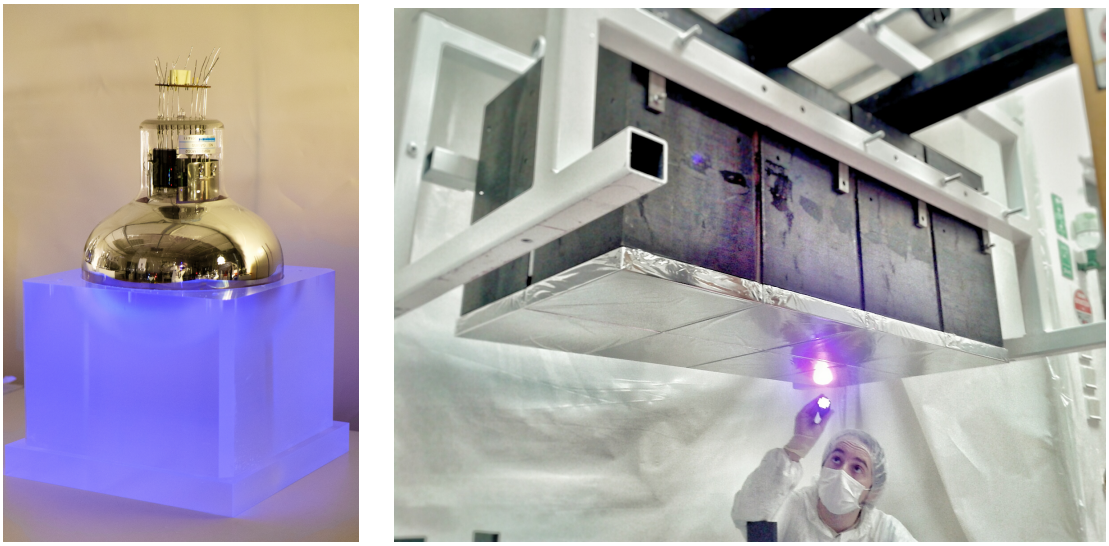

Figure 2.7 – *(left)* PMT coupled to a scintillator illuminated by a UV light. *(right)* Eight optical modules inserted into their magnetic shielding and assembled together into a brick.

Mechanical design

Some photos of a photomultiplier coupled to a scintillator (before wrapping) as well as a calorimeter brick, composed of 8 optical modules (OMs), are shown in Figure 2.7.

The magnetic shielding is made of pure iron and fulfills a mechanical role. Indeed, the optical modules are inserted in the magnetic shielding and pre-assembled in bricks of 8 to ease the integration in LSM. These bricks, also called calobricks, are then stacked to form the main calorimeters walls. A wall is 20 OMs long and 13 OMs tall. The first and last rows of optical modules use 5" PMTs recovered from NEMO-3. These PMTs have a lower energy resolution but most of the associated scintillator entry face is masked by the calorimeter modules which are built with the tracker. These optical modules would thus barely detect any electrons. They are, however, present to ensure a 4π coverage for γ particles. One of the two main calorimeter walls assembled in LSM can be seen in Figure 2.8. All the interfaces and gaps between the individual calorimeter modules are sealed with Stycast, a radon-tight glue [55]. This glue also prevents the helium from coming to contact with the PMTs and damaging them. In addition, a Nylon film is wrapped around the calobricks to stop the possible migration of radon, coming from outside or emanating from the calorimeter, inside the tracker volume.

Construction and assembly

The pure iron magnetic shieldings were manufactured by a company and shipped to the Laboratoire de l'Accélérateur Linéaire (LAL) to be cleaned and pre-assembled in calorimeter bricks. They were plunged into an ultrasonic bath and rinsed by hand with

Figure 2.8 – One of the two calorimeter main walls assembled in LSM.

acetic acid, water and isopropyl alcohol in order to remove the grease, ink or dust which could have deposited on the surface of the magnetic shielding during their manufacturing. A significant fraction of them was subjected to a 25-30 G magnetic field in order to check their magnetic shielding power and their consistency from one production batch to the other. They were then pre-assembled in calobricks of 8 shieldings and the laser-welded interfaces were coated with Styrene Butadiene Rubbers (SBR) and Stycast to ensure the radon tightness.

They were then shipped to the Centre d'Etudes Nucléaires de Bordeaux-Gradignan (CENBG) where the bricks were populated with the optical modules. The plastic scintillators were tested individually, as they arrived from the Czech Republic where they were produced. The plastic scintillators were then coupled to the photomultipliers with RTV 600 (a silicone adhesive sealant providing also a satisfying optical coupling) and wrapped with Teflon and aluminized Mylar to isolate the optical module from the external light. Eight optical modules are added to the magnetic shielding to form a complete calobrick, ready to be shipped to LSM.

All the calobricks are tested in Modane before being installed in the main wall. The brick is supplied with a high voltage and placed in a light-tight environment. The two gammas, resulting from the annihilation of a positron emitted by a ^{22}Na source, are detected in coincidence by a reference calorimeter module and every individual module of the brick to be tested. If, fed with the optimum voltage determined beforehand, all 8 mod-

ules of the brick detect the annihilation gammas at the expected output voltage, the brick can be installed.

The main improvement regarding the calorimeter electronics with respect to NEMO-3 is the digitization of the calorimeter signals. While this approach generates significantly more raw data, the offline analysis could greatly benefit from these information thanks to a pulse shape analysis. These new digitization functionalities are illustrated in Figure 2.9. A calorimeter signal can be accurately recorded thanks to the 1 Ghz sampling frequency, corresponding to one measurement every 1 ns. Being able to reconstruct several points of the leading edge also provides a 100 ps time stamping resolution. This solution was already implemented in the BiPo-3 detector.

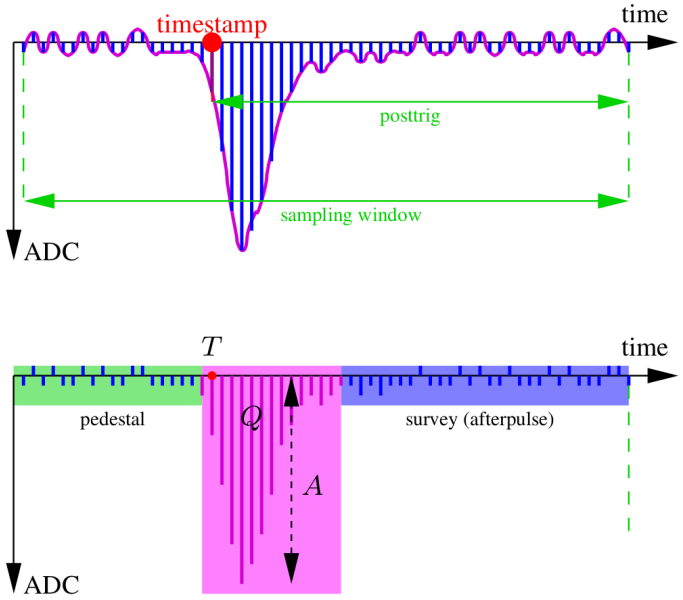

Figure 2.9 – *(top)* Schematic view of sampled calorimeter signal. *(bottom)* The pulse shape analysis can take advantage of the charge over amplitude ratio to identify the presence of γ's for instance (since mutliple interactions would produce wider signals). Monitoring the afterpulses also permits a signal quality survey.

The energy is then deduced from this electric signal using the following equation :

$$E = a \cdot (Q_{\mathrm{ADC}} - P) + b \tag{2.3}$$

where Q_{ADC} is the charge measured, P is the pedestal, while a and b are parameters determined by the calibration. This formula makes it possible to correct for the non-linearity of the photomultipliers appearing above 4 MeV. The time measurement is provided by the time stamp of the signal leading edge.

In order to process the signals generated by the 712 optical modules, 45 front-end boards, divided in 3 crates, will be required, as illustrated in Figure 2.10. Each board holds eight 2-channel SAMLONG ASICs, which makes them capable of processing 16 channels at once. A dedicated backplane ensures the control, trigger and data communication.

Three control boards, one per crate, ensure the communication of the crate with a central control/trigger board which then provides the data transfer interface for the DAQ system.

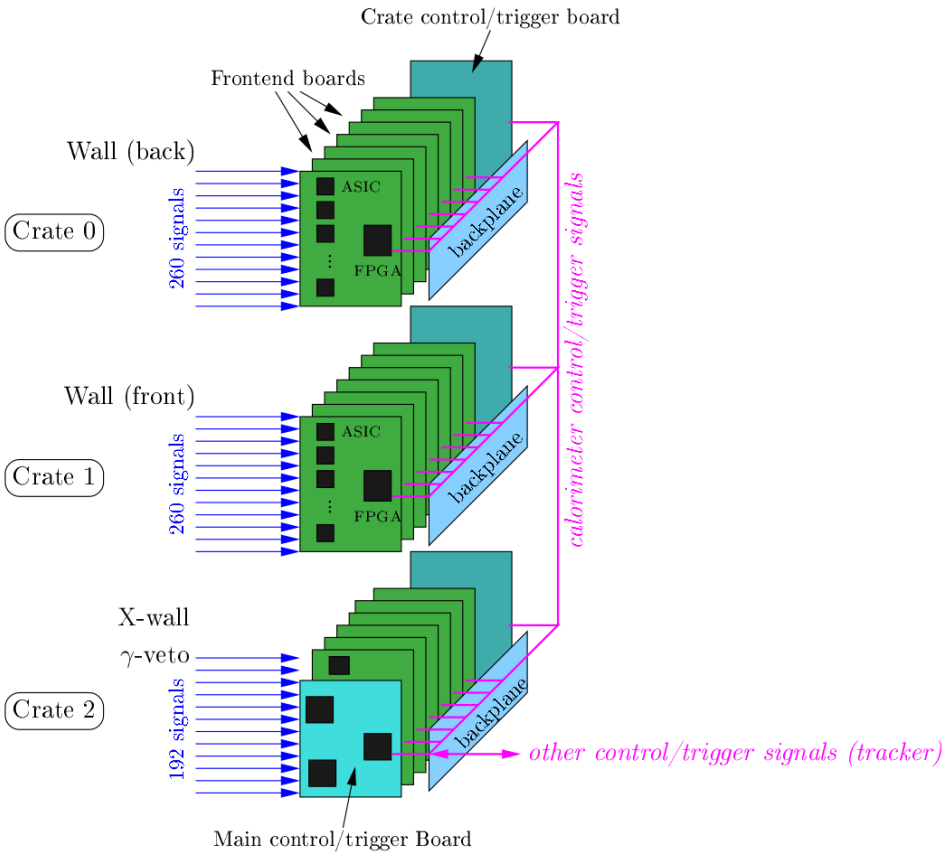

Figure 2.10 – Architecture of the calorimeter electronics.

2.1.3 The tracker

As explained earlier, the ability to reconstruct individual particle tracks is a key feature of SuperNEMO. This not only allows for a powerful background rejection, by making sure the event is composed of exactly two electrons (with each a single energy deposit associated and a compatible time-of-flight), but can also help disambiguate between several hypothesized mechanisms in case of a signal observation thanks to the ability to measure the full kinematics of the event (the angle and energy distribution between the two electrons being different from a mechanism to another).

Requirements

The choice of technology is dictated by the need for a low Z medium and a minimal amount of materials so as to minimize the energy losses occurring through multiple scattering. Of course, the radiopurity is, once again, paramount, especially for the materials closest to the source, where it becomes harder to distinguish the background events from

the signal events at the analysis stage. A good spatial resolution, mainly for the vertex reconstruction, is also crucial to make sure two electrons come from the same vertex or, at least, the same source strip. The reconstruction of the vertices on the source makes it possible to identify highly contaminated areas, also called hotspots, and to reject them with fiducial cuts. The accuracy of the reconstruction of the impact points on the calorimeter is also important : some inhomogeneity in the scintillator and optical module, depending on the electron entry point, can be compensated by applying energy corrections. These considerations led the collaboration to revisit the NEMO-3 technology, consisting of an array of Geiger counters operating in the Geiger regime.

The wire chamber

The principle of a Geiger counter is the following. When a charged particle passes through the medium in which the cell is immersed, it ionizes it. A high electric potential is applied between the central wire, the anode, and the peripheral grounded wires. This potential makes the freed electrons drift towards the anode and the heavier ions drift more slowly towards the field-shaping wires. In this strong electric field, the electrons are accelerated and further ionize the gas, creating an avalanche (Figure 2.11).

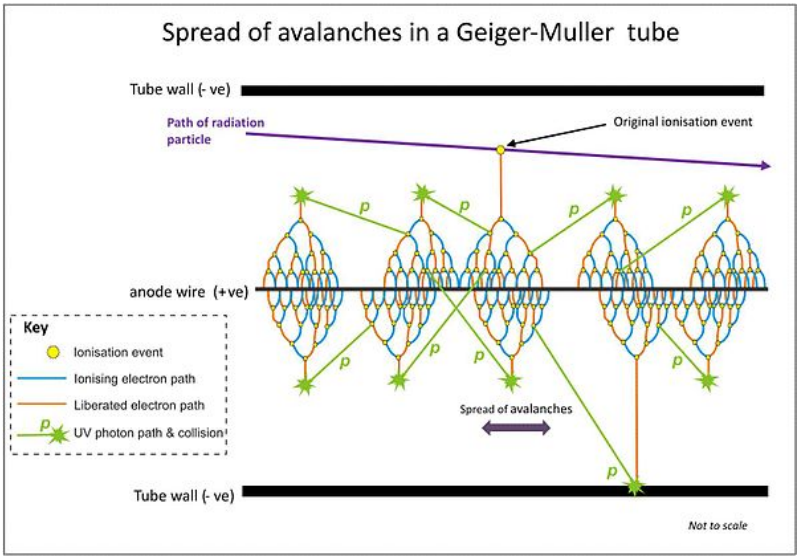

Figure 2.11 – The principle of a Geiger cell is illustrated here.

This avalanche, also known as a Townsend discharge, propagates until it reaches the anode wire. These moving charges induce a current in the latter, from which the distance to the first electron-ion pair can be inferred (provided a separate prompt reference time measurement is performed by the calorimeter). These avalanches can be contained by tuning the electric field and gas composition. Indeed, as the avalanche wraps around the anode wire, it screens the electric field such that newly freed electrons do not have enough energy to further ionize the medium. The avalanche is said to be saturated, this is the

Geiger regime. However, the emission of de-excitation and recombination UV photons can seed new avalanches and make the plasma propagate along the cell. By measuring the time the avalanche reaches both ends of the cell, it is possible to reconstruct the longitudinal position where the initial particle crossed the wire. Once a cell is triggered and the avalanches have burned out all the sensitive gas mixture, a recovering time is necessary before new avalanches can be created. This dead time is of the order of μs - ms, which means this technology is not well suited for high-rate applications. Another pivotal point is the need for a quenching agent in the gas mixture. This quenching agent, often an organic vapor, will absorb secondary photons and prevent the avalanche from becoming self-sustained, which would induce a continuous electric current and render the detector useless. The same end, though more complicated, can be achieved by reducing the voltage when the first avalanche is detected. Nonetheless, the use of a quenching agent may induce premature aging. As the organic molecules are dissociated after absorption of a secondary photon, the polymers drift towards the wires and form polymer chains. These chains disrupt the electric field, stop the avalanches and generate spurious signals through the ejection of electrons from the conductor's surface (*a.k.a.* Malter effect). This aging effect can be attenuated by adding oxygen-rich molecules, such as CO_2, which will react with the polymers and be flushed away before they can aggregate.

The design chosen by SuperNEMO consists in an array of cells in Geiger mode immersed in a helium-based gas mixture. The Geiger mode operation not only provides a very high detection efficiency (>99 %) but the current created is high enough that no preamplification is required. This translates into cheaper electronics and better radiopurity because the electronics can be set up outside the detector shielding.

The SuperNEMO tracker is divided into two halves, one on each side of the source foil, in a 9x113 configuration, for a total of 2034 cells. A cell is made up of 1 central anode wire (stainless steel, 40 μm in diameter) surrounded by 12 field-shaping wires (stainless steel 50 μ m in diameter), shared with its neighbors (Figure 2.12).

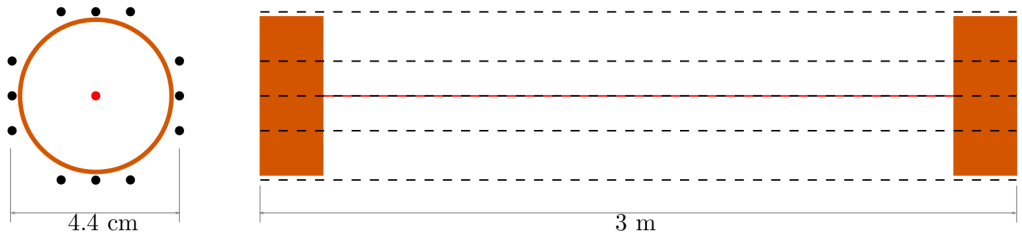

Figure 2.12 – Sketch of a SuperNEMO Geiger cell. *(left)* Transverse view: the anode wire is drawn in the center and the 12 field shaping wires are all around. *(right)* Side view: the anode is drawn in red in the center, the field wires are the dashed lines and the copper rings appear in red on both ends of the cell [56].

A cell is 3 m long and 4.4 cm in diameter. The large diameter minimizes the aging effect and limits the amount of material present inside the tracking chamber (better radiopurity and decrease of the energy losses due to scattering on the wires, compared to NEMO-3

and its 3 cm diameter cells). Two copper rings, 4.2 cm in diameter, 4 cm long and placed on both ends of the cells, permit the readout of the avalanches. The gas mixture is almost the same as in NEMO-3: Helium, Argon (1 % in volume) and ethanol (4 % in volume). Helium is the main component of the gas mixture. It is an inert gas, which means it will not react with the sensitive part of the detector but will still be ionized by electrons (24.6 eV ionization energy). A small fraction of Argon was found to enhance the propagation of avalanches in NEMO-3 thanks to its lower ionization energy (15.8 eV). Ethanol is used as the quenching agent. Water vapor was also used in NEMO-3 but since it did not appear to bring significant improvements, it will not first be considered.

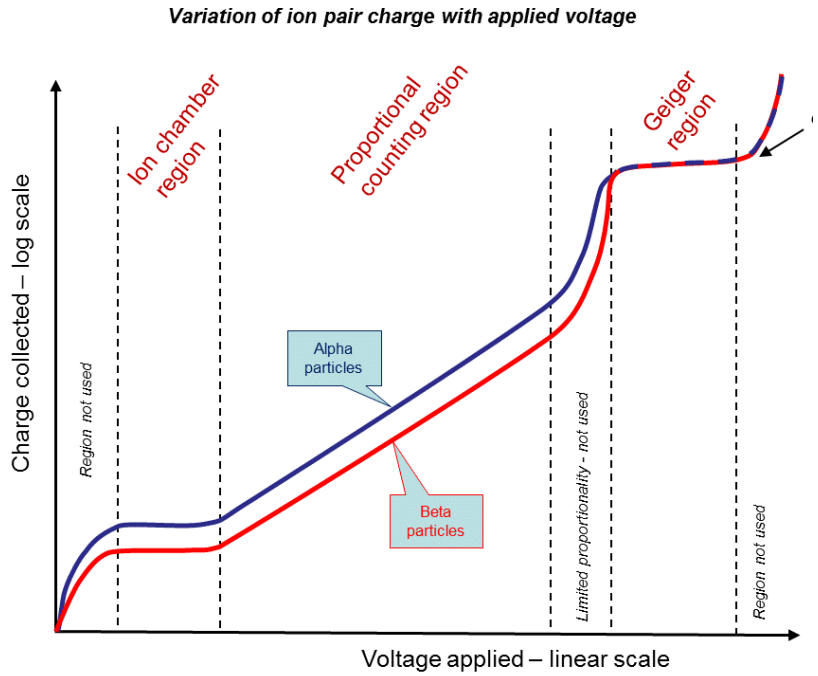

Figure 2.13 – Charge collected by the wire as a function of the voltage applied, for α particles, in blue, and β particles, in red. The different regimes are indicated.

The behavior of a Geiger cell depends on the voltage applied, as shown in Figure 2.13. At lower voltage, the charge collected scales with the voltage and is proportional to the energy deposited in the medium by the particle. At a higher voltage, there is a range where, as mentioned before, the medium is saturated and increasing the voltage will not increase the collected charge: this is the Geiger plateau. After this plateau, the cell becomes unstable. The optimal operating mode for SuperNEMO is thus to sit in the middle of this 200-300V-wide plateau, typically around 1800 V, but this depends on the intrinsic properties of each cell. Under these operating conditions, the avalanches are estimated to spread through the 3m long cells in about 50 μs while the dead time is estimated at around 3 ms (with noticeable but harmless effects up to 10 ms).

As explained above, an array of Geiger cells allows for a 3D track reconstruction where each individual cell is capable of measuring the radial distance (the distance of the particle

from the anode) and the longitudinal distance (the position along the cell axis). This can be achieved by looking at the electric signals measured by the cell readout. The apparition of avalanches is detected from the anode signal, in red, in Figure 2.14.

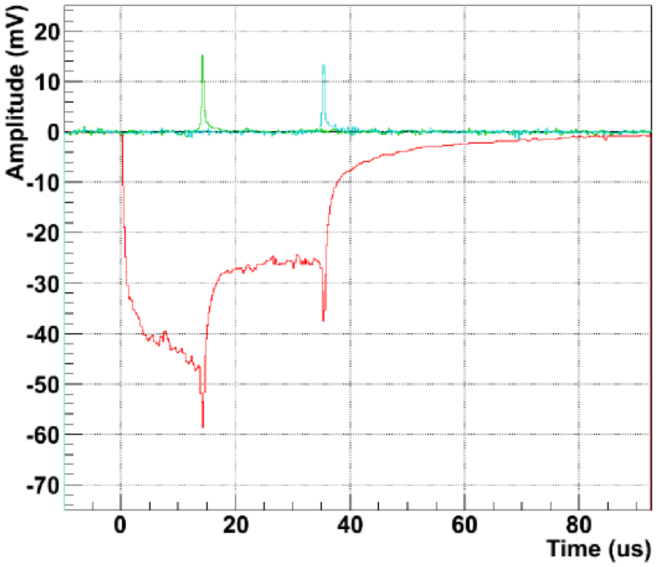

Figure 2.14 – The anode signal is displayed in red while the two copper rings signals are green and blue.

The anode signal rises quickly until the medium becomes saturated, drops by half when one of the two avalanche fronts reaches the end of a cell and dies after the second avalanche front reaches the other end of the cell, once the medium has recovered. The arrival time of the two avalanche fronts is measured by looking at the signal seen by the two copper rings. When the avalanches go through the rings, they induce a current, detected as two short pulses (in blue and green in Figure 2.14). We will call t_a the time measured on the leading edge of the anode signal, and t_{C1} and t_{C2} the time of the two cathode pulses. The reference time is given by the much faster calorimeter signal. The anode time being proportional to the distance of the first ionization point and knowing the drift model, the radial distance is given by:

$$r = \frac{A \cdot t_a}{t_a^B + C} \tag{2.4}$$

where A, B and C are parameters determined from the data.

The longitudinal position z, with respect to the middle of the wire of length L and assuming positive values of z towards the end labeled 2, is given by:

$$z = \frac{L}{2} \cdot \frac{t_{C2} - t_{C1}}{t_{C1} + t_{C2} - 2t_A} \tag{2.5}$$

Construction and assembly

As explained previously, a tracker frame is composed of 1017 cells in a 9x113 configuration. One tracker frame is divided in C-sections (named after the C-shape formed by the structural frame), each containing 9x56 cells. The last 9 cells are inserted at the joining of two C-sections during their integration in Modane. To ensure a 4π calorimetric coverage (at least for γ particles), the tracker frame also comprises calorimeter modules. The calorimeter modules located on the sides make up the X-wall. These 32 optical modules (2 columns of 16) are directly exposed to the tracker volume and can thus detect electrons. On the other hand, tracker cells are anchored to the top and bottom of the frame, which means some materials will screen the 16 calorimeters modules located behind it. The amount of material is minimized such that γ particles can still be detected. The top and bottom calorimeter modules are only used as a veto system against external γ's. The calorimeter modules used for the tracker are composed of the best 5" PMTs recovered from NEMO-3, coupled to custom made scintillators. Their energy resolutions are consequently more modest than the rest of the calorimeter with 10 % FWHM at 1 MeV for the X-wall blocks and 16 % FWHM at 1 MeV for the veto blocks.

The tracker cells were produced in cassettes (2x8 cells) in the University of Manchester. All the pieces used during the production or which will come in contact with the tracker gas underwent a strict cleaning procedure. The stainless steel wire used for the tracker was tested by sections in a test tank submitted to the SuperNEMO operating conditions. Cosmic rays werre used to test the wire performance and to select sections without areas creating spurious discharges or, on the contrary, blocking the propagation of avalanches. The cassettes were then strung by a dedicated robot and conditioned for two days. The conditioning period consists in placing the cassettes in a tank with the SuperNEMO tracking gas mixture and applying a high voltage to the anodes. If the cassette remained unstable after this period, it was rejected. This conditioning ensures that all tracker cells have a uniform hit rate, satisfying signal amplitudes and avalanche propagation times, an avalanche propagation efficiency higher than 95 % and that plateaus are wider than 50 V. This procedure limited the production rate to 2 cassettes per week. University College London was in charge of assembling and testing the calorimeter modules. The tracker frames were built and populated with the calorimeter modules and the tracker cassettes in the Mullard Space Science Laboratory (MSSL). Once a section was fully assembled, the ^{222}Rn activity inside it was measured. It was then commissioned using cosmic rays. The 4 C-sections were finally delivered to LSM, where they were coupled in pairs to form the two tracker frames (Figure 2.15).

Concerning the electronics, some improvements on the tracker high voltage supply and data acquisition system have been made compared to NEMO-3. The optimum voltage can be applied to the cells individually. A new data acquisition (DAQ) approach could help reduce the number of DAQ channels. The arrival time of pulses on the pick-up rings are recorded and a differentiating circuit is used to record the three peaks of the anode signal (Figure 2.16). The first peak represents the arrival of the avalanche on the anode wire, while the two other peaks indicate the arrival of the avalanche to the end of the

Figure 2.15 – *(left)* Delivery of a tracker C-section to LSM in its special transport box. *(right)* A full tracker module assembled in LSM. The nine layers of wires and the cathode rings are visible.

cells. This should provide enough information to reconstruct the radial and longitudinal positions of the tracker cells hits.

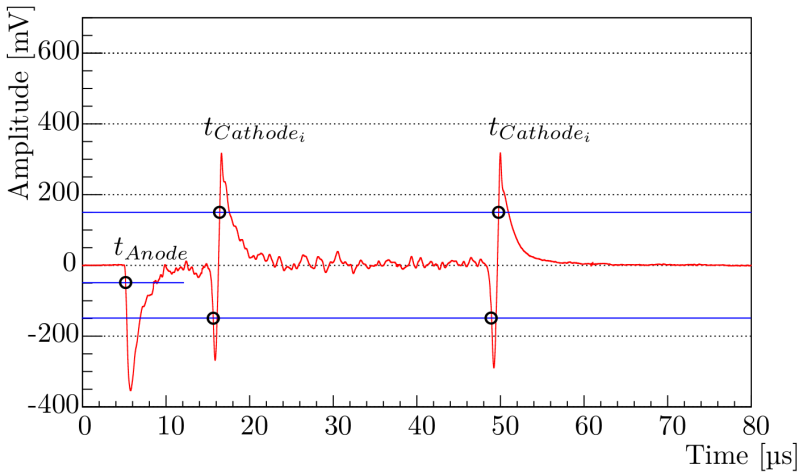

Figure 2.16 – Derivative of the anode signal. The arrival of the avalanche on the anode is measured on the leading edge of the pulse as t_{Anode}. The time of arrival of the avalanche to the two ends of the cell is labeled t_{Cathode_i} [56].

2.1.4 The source

The choice of isotope is driven by several factors:

- The higher the transition energy $Q_{\beta\beta}$, the better. Preferably, the isotope needs to have a transition energy larger than 2.615 MeV, which is the energy of a γ emitted by ^{208}Tl. But ^{150}Nd with its 3.367 MeV transition energy, and even more so ^{48}Ca and its 4.273 MeV transition energy, would guarantee a background free search.

- The phase space factor and the nuclear matrix elements link the half-life of the $0\nu\beta\beta$ process to the effective Majorana neutrino mass. This means that, for a given effective mass, the larger these parameters, the more signal events are expected.

- The higher the $2\nu\beta\beta$ half-life, the less the high energy distribution tail will extend to the region of interest and contribute to the background. Some Coulomb corrections can also play out in favor of some isotopes, like ^{150}Nd, because it will modify the shape of the energy spectrum, such that less events are expected in the spectrum high energy tail.

- The higher the natural abundance, the easier high enrichment levels can be reached. The known purification techniques must also be applicable to the isotope considered. Most of the enrichment is done by centrifugation of a gaseous form of the isotope to be enriched. Since this technique is not available for ^{48}Ca, it is, to this day, the only reason why this isotope is barely studied in double beta decay experiments. Enrichment techniques using lasers to separate isotopes are being developed.

The most promising isotopes studied by current experiments, as well as their characteristics, are summarized in the Table 2.2.

Isotope	$Q_{\beta\beta}$ (MeV)	$G_{0\nu}$ ($10^{-15}y^{-1}$)	$T^{2\nu}_{1/2}$ (y)	η (%)	Experiment
^{48}Ca	4.273	24.81	$6.37^{+0.56}_{-0.69}\ ^{+1.21}_{-0.89}\ 10^{19}$ (NEMO-3)	0.187	Candles
^{76}Ge	2.039	2.363	$1.926\pm 0.094\ 10^{21}$ (GERDA)	7.8	Gerda, Majorana
^{82}Se	2.995	10.16	$9.6 \pm 0.3 \pm 1.0\ 10^{19}$ (NEMO-3)	9.2	SuperNEMO, Lucifer
^{96}Zr	3.350	20.58	$2.35 \pm 0.14 \pm 0.16\ 10^{19}$ (NEMO-3)	2.8	
^{100}Mo	3.035	15.92	$6.93 \pm 0.04\ 10^{18}$ (NEMO-3)	9.6	Amore, Moon
^{116}Cd	2.809	16.70	$2.8 \pm 0.1 \pm 0.3\ 10^{19}$ (NEMO-3)	7.6	Cobra
^{130}Te	2.530	14.22	$6.9 \pm 0.9\ 10^{20}$ (NEMO-3)	34.5	Cuore, Sno+
^{136}Xe	2.458	14.58	$2.165 \pm 0.016 \pm 0.059\ 10^{21}$ (EXO-200)	8.9	Exo, KamlandZen, Next
^{150}Nd	3.367	63.03	$9.11^{+0.25}_{-0.22} \pm 0.63\ 10^{18}$ (NEMO-3)	5.6	SuperNEMO, DCBA

Table 2.2 – Characteristics of the isotopes studied in current experiments. $Q_{\beta\beta}$ is the transition energy, $G_{0\nu}$ ($10^{-15}y^{-1}$) is the phase space factor for the $0\nu\beta\beta$ decay, $T^{2\nu}_{1/2}$ is the half-life of the $2\nu\beta\beta$ process (the experiment responsible for the measurement is quoted in parenthesis) and η is the natural abundance. The last column lists the experiments studying the corresponding isotope.

^{82}Se was chosen for SuperNEMO because of its high transition energy, and preferred to ^{100}Mo because of its higher $2\nu\beta\beta$ half-life. Its nuclear phase space factor and natural abundance are satisfying and the enrichment of ^{82}Se does not pose any problems.

The source measures 4.857 m x 2.7 m and is broken down into 36 strips (34 main strips plus one on each extremity). ITEP, in Russia, took care of the enrichment and purification of ^{82}Se. Approximately 2 kg of ^{82}Se have been purified industrially via double distillation and can be used to produce 11 strips. Another 3 kg have been purified in Dubna *via* reverse chromatography and should make up 15 strips. A last batch of ^{82}Se was also purified by double distillation, for a total of 1.5 kg, which should be used to produce 8 source strips.

Two source designs have been tested. In both cases, the selenium powder is ground down to a fine powder (50 μm grains) then mixed with PVA glue to form sheets of 52 $\mu g/cm^2$. With the ITEP design, these selenium sheets are sandwiched between two backing films made of Mylar, before the mixture has even dried out. The Mylar sheets have

been perforated by irradiation beforehand. This allows the mixture to dry and to better adhere to the backing film. Another solution was developed in the Laboratoire d'Annecy le Vieux de Physique des Particules. Instead of proposing a 3 m-long selenium strip, one strip is split up in several pads. Two mylar sheets are then heat welded together to host the several pads. The Figure 2.17 shows a photo of the source pads design.

Figure 2.17 – A source strip made up of several selenium pads.

Similarly to NEMO-3, it might be useful to place some strips of ultra radiopure copper in the detector. These reference sources can be used to independently measure the external background and reduce the overall systematics of the analysis.

2.1.5 The magnetic coil and the shieldings

The magnetic coil is built with copper rods surrounding the detector. The copper rods are recycled from the NEMO-3 experiment and need to be reshaped to fit the new detector geometry. The coil should contain 200 turns with a 16 mm step. This design should provide a 25 G magnetic field without generating too much heat. The mechanical design is presented in Figure 2.18.

The anti-radon tent will surround the magnetic coil. The tent, composed of PMMA panels, is designed to prevent the laboratory air, relatively rich in radon, from migrating inside the detector. The volume inside the tent will be flushed with radon-free air, to avoid the stagnation of radon, emitted mainly by the PMTs, around the detector. The air will

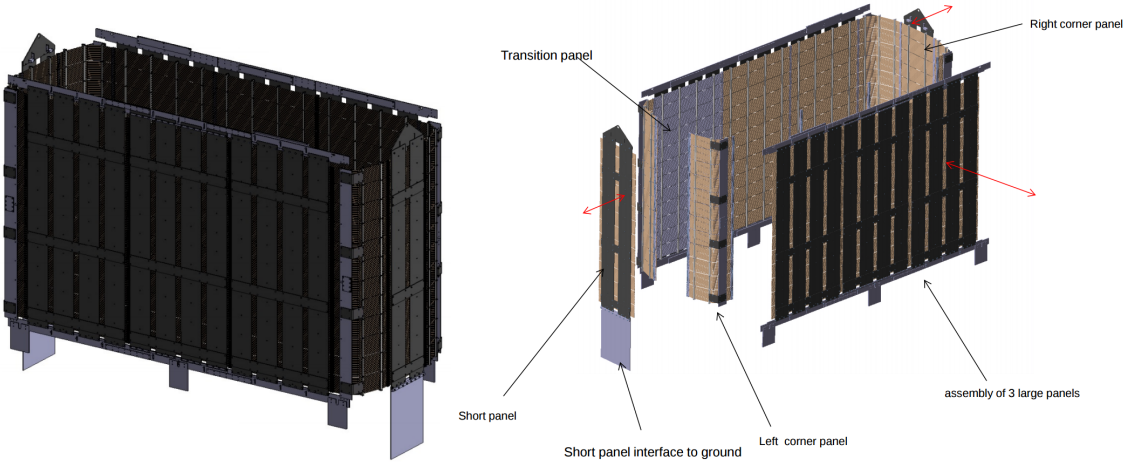

Figure 2.18 – *(left)* Overview of the magnetic coil assembled. *(right)* Details of the magnetic coil design. The overall dimensions are 6097 x 2198 x 3483 mm for a total weight of 9 tonnes [57].

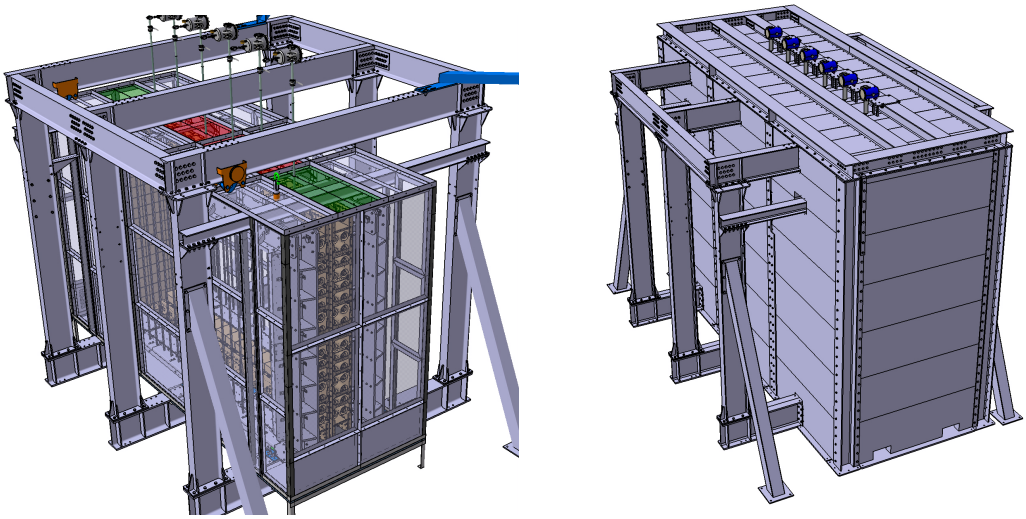

Figure 2.19 – *(left)* Design of the SuperNEMO anti-radon tent. *(right)* Design of the SuperNEMO pure iron shielding.

be purified by a dedicated anti-radon factory which uses a charcoal column to trap the radon atoms, at least long enough for them to decay. The design of the anti-radon tent is presented in the left part of Figure 2.19.

The demonstrator will be protected from external γ's by a pure iron shielding (about 20 cm thick) surrounding the anti-radon tent (right part of Figure 2.19). Outside this pure iron shielding, some water shielding will stop the external neutrons. Some studies showed that borated water or sheets of borated polyethylene would constitute a better shielding against neutrons [58], but is also more expensive. This water shielding could take the form of plastic tanks stacked on top of each other.

2.1.6 The underground laboratory

The SuperNEMO demonstrator is hosted in an underground laboratory, the Laboratoire Souterrain de Modane (LSM). LSM is located midway in the Fréjus tunnel, under the Alps, between France and Italy (Figure 2.20). It is one of the deepest laboratory in the world with a 1700 m rock overburden or 4800 m.w.e. (Figure 2.21) This lowers the cosmic ray flux by a factor 10^6, down to 4 per m^2 per day. This laboratory was built in the early 80s to host an experiment looking for the proton decay. It has been hosting the successive NEMO experiments since the late 80s, as well as a variety of astrophysics experiments, biology experiments, etc.

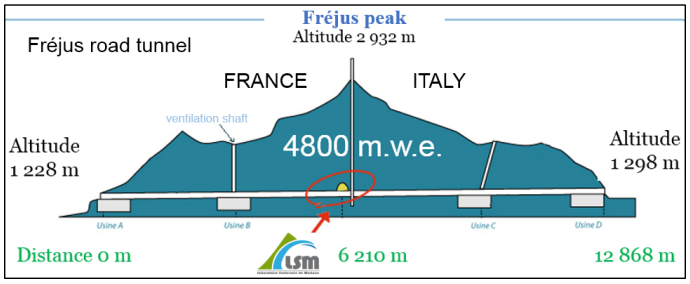

Figure 2.20 – Location of the LSM in the Fréjus tunnel.

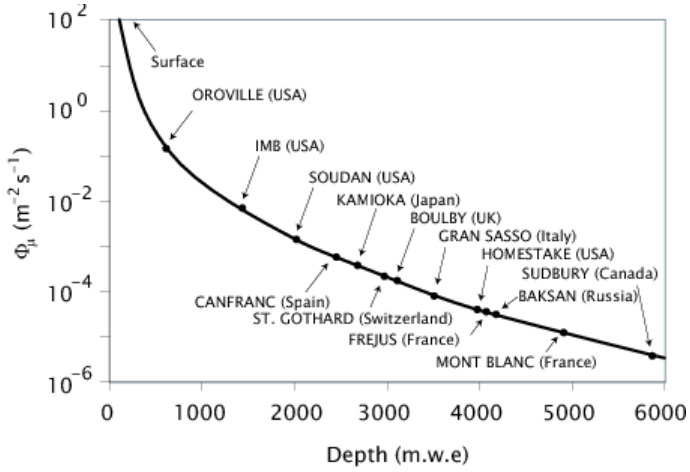

Figure 2.21 – Cosmic ray flux in different underground laboratories as a function of the overburden expressed in meter water equivalent units.

2.1.7 Calibration strategy

Two complementary calibration strategies should be implemented to make sure the energy measured by the calorimeter is as close to the genuine energy as possible.

Source Deployment System

The first approach, called the Source Deployment System, permits an absolute energy measurement. The idea is to measure standard candle sources of electrons of known energy and correct the calorimeter modules accordingly. An electron source satisfying several constraints must be chosen. These constraints include:

- a limited activity, such that the tracker cells trigger rate stays below 20 Hz (above this trigger rate, a premature aging or even damage to the wires can occur). To help decrease the trigger rate, the sources should not be aligned with a row of tracker cells.
- all the calorimeter blocks should receive enough electrons (in a reasonable amount of time) to compensate for the stochastic nature of the measurement *e.g.* detect enough electrons to fit an energy peak.
- the sources need to be removed between calibration runs and the space occupied on the source plane needs to be minimized (to optimize the mass of isotope studied).

The design selected consists of 6 columns of 4 sources of ^{207}Bi, deployed vertically between the source strips, as shown in Figure 2.22.

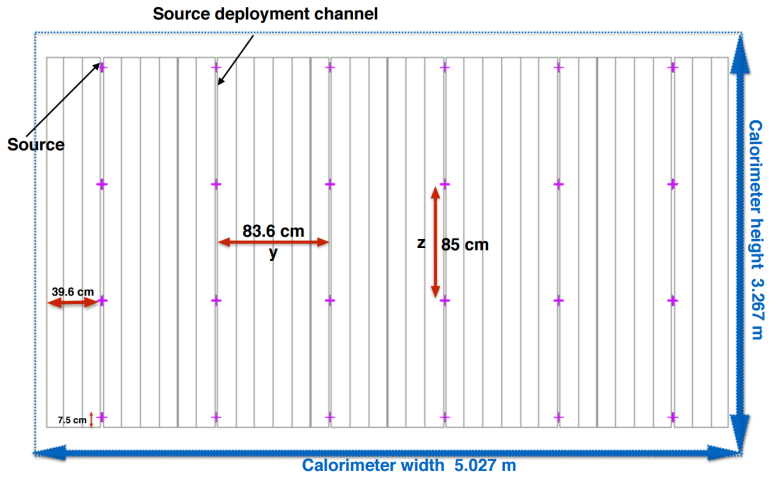

Figure 2.22 – Front view of the source strips. The 24 ^{207}Bi sources locations are indicated with a pink cross. [59]

As in NEMO-3, ^{207}Bi was chosen because of the three conversion electrons it can emit, at 482 keV, 976 keV (the most frequent decay of the three) and 1682 keV (Figure 2.23). Measuring these three peaks, what's more, at different energies, provides an absolute energy measurement and helps follow and correct the response of the calorimeter modules with time.

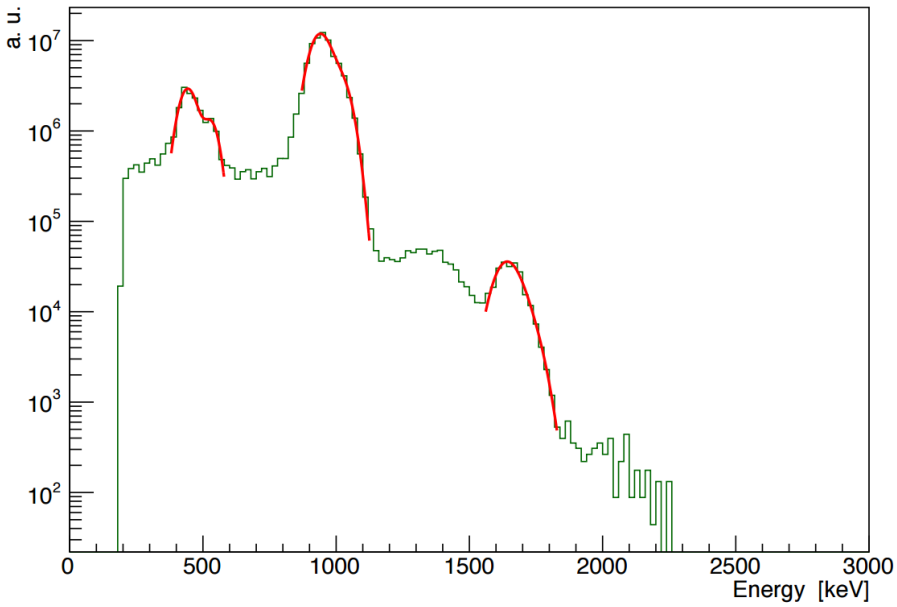

Figure 2.23 – Reconstructed energy spectrum from a simulation of a calibration run. The three peaks from electron conversions of ^{207}Bi are clearly visible [59].

These sources can be automatically deployed during dedicated calibration runs. The frequency at which such calibration runs should be performed is not determined yet but two main scenarios are under consideration:

- A long run ($\approx$ 18 hours) can be performed twice a month, long enough to measure the three energy peaks positions with an uncertainty lower than 1 %.
- A short run (1 hour) carried out daily to monitor the daily PMT gain variations, using only the 976 keV peak.

The available sources, with a 318 Bq activity, could suffice but 2 kBq sources would bring a better precision, provided the first layer of Geiger cells can be switched off (because the trigger rate would be too high).

Ligh Injection Monitoring System

A second calibration system should run in tandem with the system explained above. Here, some UV LED light is injected in every calorimeter module via optical fibers in order to monitor and calibrate the response of the calorimeter over its lifetime. As a matter of fact, the gain of a PMT depends upon the applied high voltage (which can fluctuate) and the temperature. These deviations can be tracked by injecting known light levels periodically and compensate for these effects at the 1 % level. This system also makes it possible to check the linearity of the optical module as a function of the energy. While calibration sources can generate electrons up to 1682 keV, some electrons, should they come from $0\nu\beta\beta$ decays or from the background, are expected to carry almost twice that energy. At these energies, the optical modules could start exhibiting some non-linearities. The gain curve can, therefore, be mapped using a tunable light source (from the equivalent

of a few tens of keV to the $Q_{\beta\beta}$ and beyond). Each optical module receives a LED signal from 2 fibers, but this signal can vary too. That's why a separate PMT receives the exact same signal. This separate PMT can then compare the LED signal it receives with a source of ^{241}Am of known energy. A sketch summarizes the setups of the two calibration systems in Figure 2.24. This LED calibration system can also be used to perform time calibrations of the calorimeter.

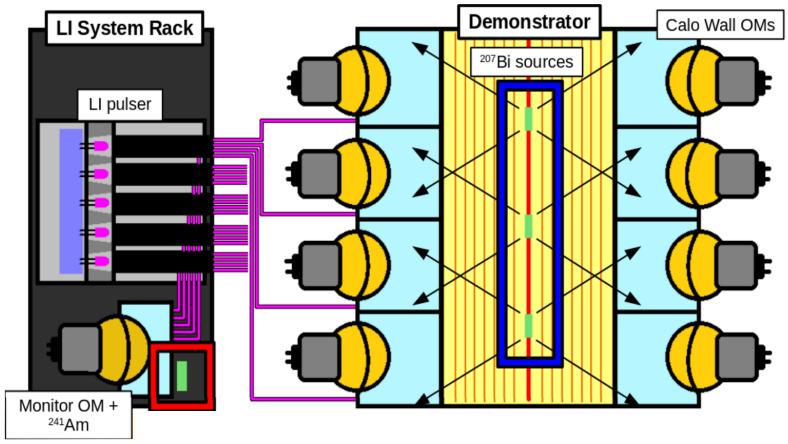

Figure 2.24 – Sketch of the Source Deployment System and the Light Injection Monitoring system for the SuperNEMO demonstrator. [60]

2.2 The backgrounds

The background for the $0\nu\beta\beta$ search comes from any process which can produce two electrons of high energy *i.e.* close to $Q_{\beta\beta}$ = 2.998 MeV. The main contribution comes from natural radioactivity and in particular high energy β/γ emitters. Such isotopes are produced during the successive decays of long-lived isotopes, like ^{238}U, ^{232}Th or ^{235}U[c] (Figure 2.25).

These isotopes are present everywhere in nature in small quantities. ^{40}K does not originate from these decay chains but it is a background for the $2\nu\beta\beta$ decay measurement. The most troublesome decay products are grayed out in Figure 2.25. ^{208}Tl, with a transition energy Q_β = 4.992 MeV, and ^{214}Bi, with a Q_β = 3.270 MeV, are the only isotopes which can produce two electrons of high enough energies to mimic a $0\nu\beta\beta$ event. Radon (^{222}Rn or ^{220}Rn, also known as Thoron), is a radioactive gas emanating from the detector materials but also from the laboratory rocks. This gas can migrate inside the detector and, in particular, in the tracker volume. Its alpha decay is not an issue for the $0\nu\beta\beta$ decay search, but the resulting ionized daughter nuclei will deposit on the surface of the field wires or even on the source. These nuclei will then decay until they reach ^{214}Bi, which, as mentioned earlier can be harmful to the experiment.

[c] ^{235}U is less troublesome because it has a low abundance (0.72 %) and none of its decay products have high enough transition energies to be a background for the $0\nu\beta\beta$ decay search.

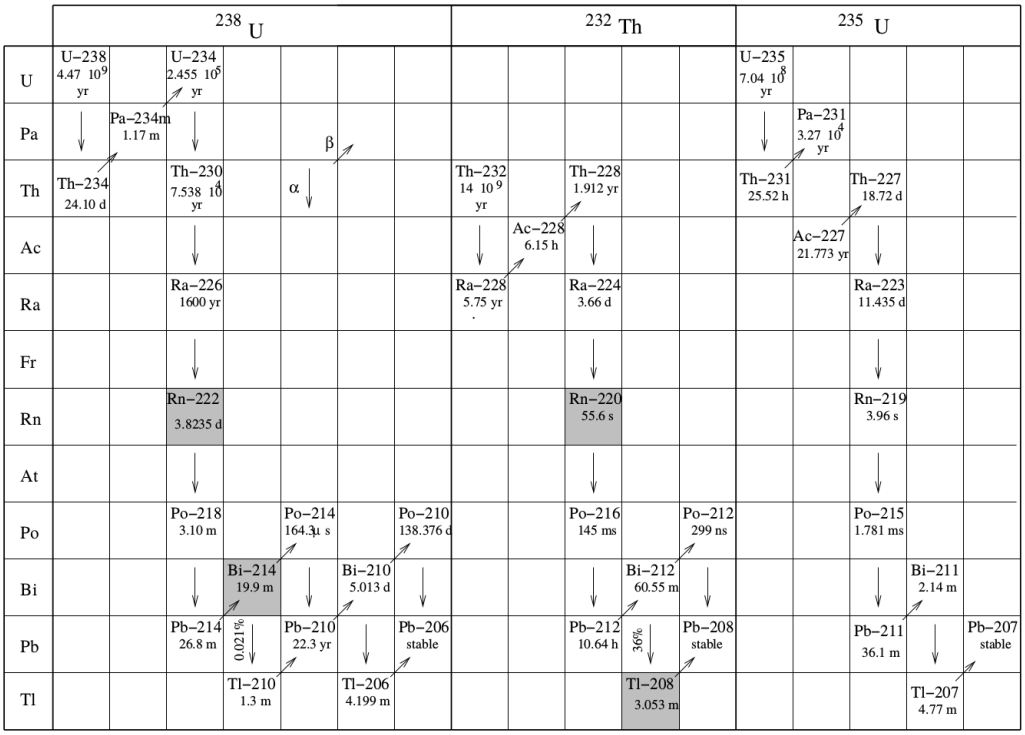

Figure 2.25 – Natural radioactivity decay chains. The most harmful isotopes for SuperNEMO are grayed out.

The background can be classified as internal or external depending on its origin. If it originates from the source, it is called internal, otherwise, it is qualified as external. The main processes leading to the production of two electrons from a contamination of the source are illustrated in Figure 2.26. The first one is a β decay accompanied by the emission of an electron resulting from an internal conversion. The emission occurs when, following a β decay for example, an excited nucleus interacts electromagnetically with an orbital electron. This electron is then expelled from its orbit with a discrete energy corresponding the transition energy minus the binding energy of the electron shell. The rearrangement of the electrons from the outer shells, to fill the hole left by the electron from an inner shell, produces X-rays. Another way to produce two electrons with a β/γ emitter is when the β particle generates a second electron via Möller scattering. Finally, a β decay followed by the creation of an electron via Compton scattering of a γ of deexcitation also produces two electrons.

All the possible transitions for the ^{208}Tl and the ^{214}Bi isotopes are presented in Figure 2.27. This shows that ^{208}Tl always β-decays to an excited state of the daughter nuclei. This means that between 1 and 3 γ's (at least 2 in more than 99 % of the decays) are expected immediately after the β emission, which represents as many chances for a Compton scattering to occur. However, with ^{208}Tl, the most dangerous mode of $\beta\beta$-like

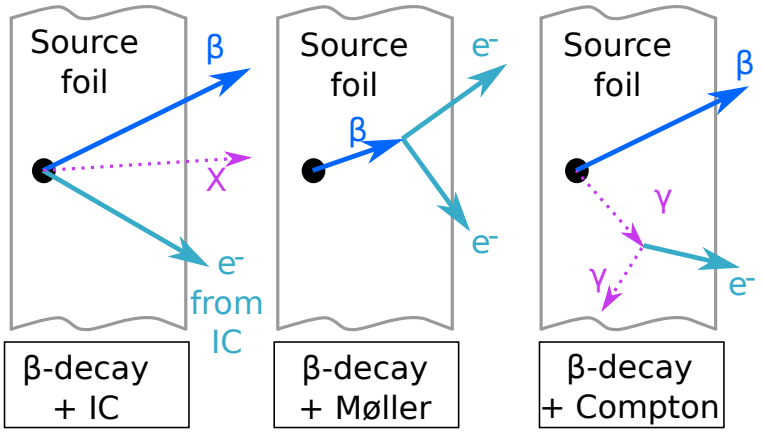

Figure 2.26 – The internal background is defined as the background originating from the source foil, like a contamination of the source with β/γ emitters. Different processes can lead to the emission of two electrons.

events production comes from the internal conversion of the 2.615 MeV-γ, resulting in two electrons emitted with a high energy sum. Concerning ^{214}Bi, between 0 and 2 γ's are expected. Since it has a transition energy of $Q_{\beta\beta}$ = 3.270 MeV, any of the processes illustrated in Figure 2.26 can also generate two electrons with an energy close to the $Q_{\beta\beta}$ of ^{82}Se.

External backgrounds can also generate two electrons, as illustrated in Figure 2.28. A γ particle coming from outside the source can create an electron/positron pair and, if the positron charge is badly reconstructed, this process can fake a $\beta\beta$ event. In this case, the two γ's emitted during the annihilation of the positron must escape the detection. Furthermore, a γ particle can undergo two successive Compton scatterings in the source, thus creating two electrons. A single Compton scattering is also enough to produce two electrons if the Compton electron produces another electron via Möller scattering. The last two processes make up background events only if the original γ is not detected.

The three processes described here require a single high energy γ. That's why, in light of Figure 2.27, external ^{208}Tl and ^{214}Bi do not impact the $0\nu\beta\beta$ decay search (the γ particles do not have sufficient energies). These isotopes will, however, undermine the sensitivity of the search for the double beta decays to the excited states. Still, high energy γ's (up to 10 MeV) can be produced by radiative capture of neutrons in matter. These neutrons come from natural radioactivity and, to a lesser extent, from cosmic radiations.

In order to keep these background levels as low as possible, a careful screening of all the materials used in the detector was performed with the help of High Purity Germanium detectors. The requirements for the source radiopurity, at the level of a few μBq/kg, are so stringent that it is impossible to measure it with standard germanium detectors. That's why a dedicated detector called BiPo-3 was developed [61]. This detector can measure 4 source strips at the same time and is specially designed to look for the decay of ^{212}Bi to ^{212}Po, hence its name.

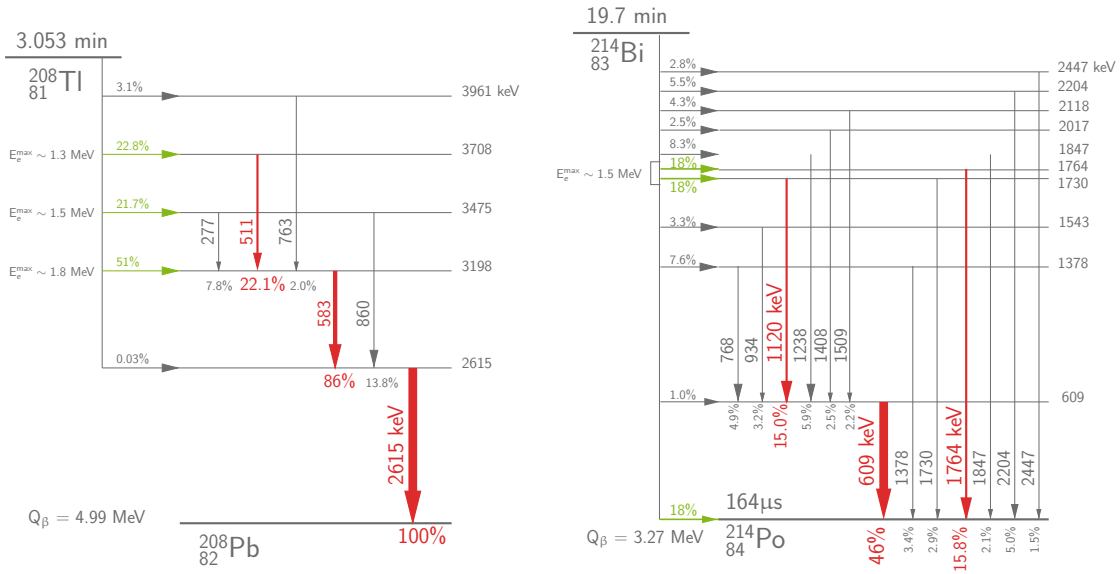

Figure 2.27 – Decay schemes of ^{208}Tl *(left)* and ^{214}Bi *(right)*. The most frequently emitted γ's, along with their percentage of occurrence, are highlighted in red.

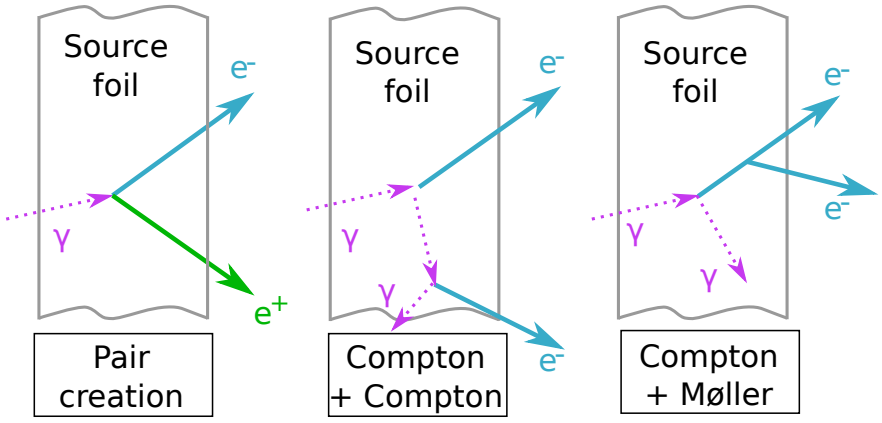

Figure 2.28 – Mechanisms of production of two electrons from an external γ particle.

2.3 Goals and comparison with NEMO-3

The main improvements over NEMO-3 are summarized in Table 2.3.

While NEMO-3 studied several isotopes at the same time, the SuperNEMO demonstrator will focus on ^{82}Se. The first module will host 7 kg of this isotope and might study ^{150}Nd in a second phase. The R&D program carried out for the calorimeter was successful since a factor 2 improvement on the energy resolution has been achieved. A special care was taken during the enrichment and purification of the source in order to reduce the contamination in ^{208}Tl and ^{214}Bi by a factor 50 and 30, respectively. The experience acquired from NEMO-3 also helped realize that radon can and should be signifi-

	NEMO-3	SuperNEMO target specifications	SuperNEMO demonstrator
Mass	7 kg	7 kg | 100 kg	✓
Isotopes	^{100}Mo among 7 isotopes	^{82}Se (^{150}Nd, Copper,...)	✓
Calo. energy res. @ $Q_{\beta\beta}$ FWHM - σ	8 % - 3.4 %	4 % - 1.7 %	4.6 % - 2.0 %
Backgrounds:			
A(^{208}Tl)	$\sim$ 100 μBq/kg	$\leq$ 2 μBq/kg	50 (20-137) μBq/kg*
A(^{214}Bi)	60-300 μBq/kg	$\leq$ 10 μBq/kg	< 300 μBq/kg**
A(Radon) in tracker	$\sim$ 5 mBq/m^3	$\leq$ 0.15 mBq/m^3	TBD
0ν efficiency (all energies)	18 %	30 %	27 %
Exposure	35 kg·y	17.5 kg·y | 500 kg·y	
Sensitivity			See Chapter 7
$T_{1/2}^{0\nu 2\beta}$ (90% C.L.)	> 1.1 10^{24}	> 6 10^{24} y | > 10^{26} y	
$\langle m_{\beta\beta}\rangle$	< 0.33 - 0.87 eV	< 0.2 - 0.55 eV | < 0.04 - 0.1 eV	

Table 2.3 – Main improvements brought by SuperNEMO over NEMO-3
* The ^{208}Tl contaminations range from 20 to 137 μBq/kg depending on the purified powder batches. The weighted average is around 50 μBq/kg.
** No positive measurement has been reached with the BiPo3 detector for the ^{214}Bi contamination, only an upper limit (9 % C.L.) can be established.

cantly reduced. The different design adopted should increase the signal reconstruction efficiency. The demonstrator plans to run for 2.5 years. It should reach the NEMO-3 sensitivity in 6 months and, with a 17.5 kg·exposure, assuming no signal is observed, could set a limit $T_{1/2}^{0\nu}$ > 6 10^{24} y at 90 % C.L. or $\langle m_{\beta\beta}\rangle < 0.2 - 0.55$ eV. By extrapolating to the 20 modules running for 5 years, i.e. a 500 kg.y exposure, SuperNEMO could start probing the inverted mass hierarchy. The demonstrator aims at proving SuperNEMO can be a background free experiment in the region of interest.

Chapter 3

Simulation, reconstruction and analysis tools

A basic simulation can sometimes be used to test the design of a detector, obtain a rough estimation of its potential in terms of sensitivity, and therefore help figure out if an experiment is worth building or not. In a genuine experiment, however, having a very detailed simulation of the detector is paramount. A faithful simulation can motivate experimental choices, like the optimum magnetic field in SuperNEMO (see Chapter 4). It is also used to test the reconstruction algorithms, so that the agreement between the simulated data and the recorded data is the best possible. Actually, some parameters, like the $0\nu\beta\beta$ decay reconstruction efficiency in SuperNEMO, can only be evaluated through advanced simulations and are essential for obtaining experimental results. If the experimental data, regardless of how good the detector is, cannot be explained and reproduced by the simulation, these measurements are worthless. This Chapter describes the SuperNEMO simulation and reconstruction software. It also details the use of channels, dedicated to the search for new processes or to the measurement of the internal and external backgrounds. Finally, the analysis tools employed in this thesis are presented.

3.1 The SuperNEMO software

SuperNEMO developed its own simulation, reconstruction and analysis software. The software is divided into three main components: Cadfael [62], Bayeux [63] and Falaise [64]. They are available to all and their installation is eased thanks to the use of the Brew [65] package manager. Cadfael is a software development kit. It gathers all the software packages needed for the development of the SuperNEMO software, namely Boost [67], ROOT [68], Camp [69] (to be replaced by Ponder [70]), CLHEP [71], XercesC [72], Geant4 [73], Doxygen [74] and Qt5 [75]. These programs are popular and well known among the nuclear and particle physics community. Bayeux is a C++ library for experimental nuclear and particle physics. It is a collection of C++ classes and functions designed for the simulation, recording and analysis of data. Some of its features include:

- data handling: in particular, the data structure (`datatools`), the data processing (`dpp`),

the data serialization (`datatools` for the Boost serialization towards `brio`, which stands for Boost/serialization over ROOT I/O) and the data selection (`cuts`).

- numerical tools: a C++ wrapper of the GNU scientific library (`mygsl`) [66]
- a variety of utilities for the Geant4 simulation (the latter being wrapped by the `mctools` program): definition of the primitive geometrical volumes (`geomtools`), database of the elements and isotopes composing the detector (`materials`), modelling of the electromagnetic field inside a detector (`emfield`), nuclear database to describe the kinematics of the radioisotopes (`genbb_help`, a C++ port of Genbb/Decay0 from Vladimir Tretyak [76]) and a random vertex generator (`genvtx`).

Cadfael and Bayeux were originally developed by and for the SuperNEMO collaboration but are now used by other nuclear and particle physics experiments as well as some industrial partners.
Falaise, though depending on Cadfael and Bayeux, is specific to the SuperNEMO experiment. It holds the C++ library and the data models allowing the reconstruction and data analysis of the SuperNEMO experiment. In particular, it contains the geometry and materials of the detector, the event data model, the reconstruction algorithms and the analysis tools. Falaise is where most of the software contributions of this thesis have been made.

A collection of modules forms a pipeline, through which the events successively pass, starting with the simulated/recorded data, followed by the reconstructed data and ending with the analyzed data. Indeed, using the same software for the reconstruction and analysis of both the simulated and the recorded data reduces the biases and systematic errors introduced by the latter. The philosophy adopted for the simulation, reconstruction and analysis of the SuperNEMO data with a dedicated software is explained in the next sections.

3.1.1 The event simulation

The first step is the event simulation. The detector geometry, its materials as well as the physical conditions (electromagnetic field, etc) are reproduced virtually. Any physical process can then be simulated in this environment. Considering the example of the double beta decay coming from the ^{82}Se source strips bulk, a vertex of origin is randomly generated in the source volume. The kinematics of the events (the momenta carried by the two electrons, the angle between them, etc) is randomly generated according to some probability distribution functions defined in the database for each process. The propagation of the two electrons in the detector volumes is operated following a Monte-Carlo procedure, as implemented in Geant4. Each particle is propagated one step after the other. The length of each step depends on the materials and the physical conditions in which the particle propagates. This length is drawn randomly according to the effective physical interactions implemented in the software (the Bethe formula for instance). At each step, the interaction probability, should it come from a scattering or simply a spontaneous decay, is computed and the simulation is modified accordingly (creation of new particles, energy losses, etc.) The choice of the minimal length is a trade-off between the need for accuracy

(the shorter the steps, the more accurate the propagation is) and the computation power and time required (more steps also means more lengthy computations). The simulation stops once a criterion defined beforehand is reached: the energies of the particles involved have decreased below a cutoff value, the particles all left a predefined volume, etc.

Of course, though theoretically conceivable, all the physical processes occurring in a real life event cannot be simulated this way. For instance, the plasma propagation in a Geiger cell or the photoelectrons avalanches in a photomultiplier are not simulated for each event, since it would be very demanding computationally. Instead, an effective model is adopted in these sensitive volumes. This does not mean, however, that such simulations would be pointless. At this stage of the simulation software development, the calorimeter signals are not simulated but having access to the digitized pulses could help identify the γ's piling up with the electrons hits through pulse shape analysis for instance.

Coming back to our example, a successful simulation will describe the path of our two electrons (from the source, where they were emitted, to the scintillator blocks, where they deposited all their energy), as well as the path of the secondary particles they might have generated (*e.g.* a Möller electron or γ from Bremsstrahlung). Obviously, all the electrons will not reach the calorimeter and some might not even leave the source foil. But this is precisely how an experiment is able to predict its detection efficiency and, later, to successfully explain the data it has acquired. By generating and reconstructing very large amounts of Monte-Carlo simulations for all the physical processes expected in the detector (signal events and, especially, background events), an experiment should be able to understand and explain the data it has observed *i.e.* as a compound of all these backgrounds (and possibly signal) simulations. An example of a $0\nu\beta\beta$ event simulated in the SuperNEMO detector is displayed in Figure 3.1.

The colored circles visible in Figure 3.1 are centered on the anode wire and their radii correspond to the minimum distance between the particle track and the anode wire. The color of these circles depends on the time at which the electrons entered the sensitive volume associated with the cells. This assumes an ideal detection of the particle tracks, with a perfect time resolution of the tracker. In practice, considering the stochastic nature of the measurement by a Geiger cell, the radii are only known with an associated uncertainty which makes it impossible to order the tracker cells in time (the electrons go through the tracker in a matter of nanoseconds, which is almost instantaneous compared to the few microseconds it takes for the avalanche to be created and the plasma to propagate towards the cell). In addition, the efficiency of the tracker cell is considered perfect in the simulation, while in reality, the further from the anode a charged particle passes, the lower the detection efficiency[a]. The same electrons, in a genuine detector, might not actually trigger all the tracker cells considered by the simulation.

The calorimeter energy deposits are represented by small red boxes and occur within the first millimeters of the scintillator. As mentioned earlier, the scintillation photons and, *a fortiori*, the following processes involved in the energy measurement, are not simulated here; only the amount of energy deposited in the scintillator volume is recorded. How-

[a]The efficiency decreases with the distance to the anode wire but still remains very high (above 99 %).

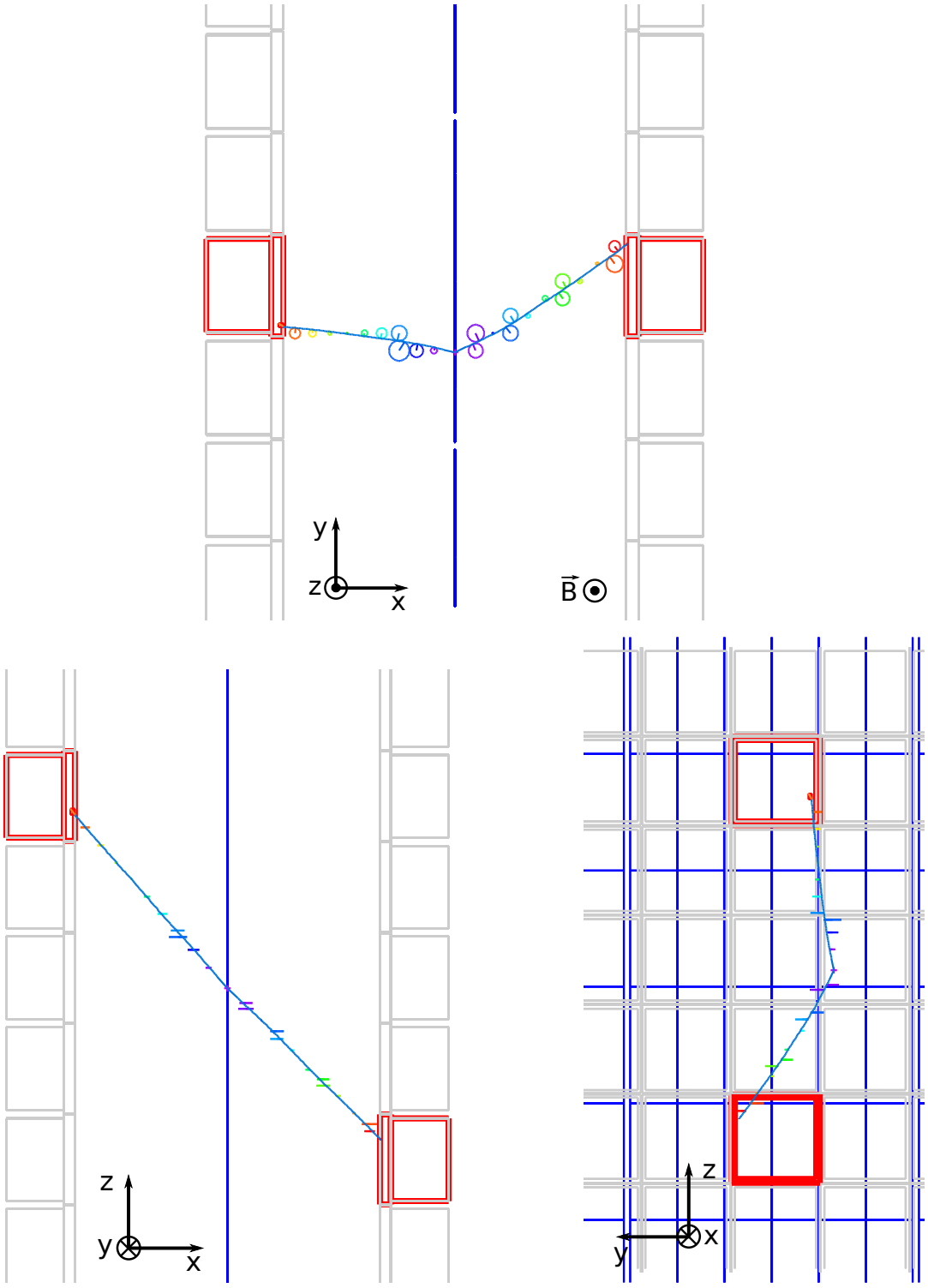

Figure 3.1 – Display of a simulated $0\nu\beta\beta$ event in the SuperNEMO demonstrator. *(left)* Top view. *(middle)* Side view. *(right)* Front view. The calorimeter PMTs, the side and top scintillator blocks and the tracker cells are not represented for sake of readibility. The source is displayed in blue and the different source pads are distinguishable. The scintillators are displayed in gray. The two simulated electrons tracks are blue and the colored circles represent the tracker cells they have crossed.

ever, a dedicated optical simulation of the propagation of the scintillation photons can and has been developed in order to evaluate the collection efficiency of the scintillator design and, in particular, how it varies depending on the position of the energy deposit on the scintillator entry face [77]. This information, as represented in Figure 3.1, compose the Simulated Data bank (SD).

Once a full event is simulated, it is possible to take into account the limitations of the different subdetectors. Some corrections are applied on the perfect simulated data in order to obtain true-to-life data, on which the reconstruction can be performed. Such corrections are, for instance, a smearing of the energy deposited in a scintillator, according to the resolution of the calorimeter measured experimentally, or a smearing of the detection time. The time of an energy deposit is known absolutely in the simulation and is expressed relatively to t = 0 ns, the time of emission. In a real event this time in unknown. This is not an issue because, as will be explained later, the reference time used in the reconstruction is the first calorimeter hit, which is almost the same as the emission time considering the time scale of a tracker measurement. Some corrections are also applied on the tracker simulated response. The Geiger cell trigger efficiency as a function of the distance of the incoming particle with respect to the anode is measured experimentally. This behavior can be simulated by generating Monte-Carlo draws on this probability distribution. This way, tracker hits furthest from the center are less likely to be detected and will sometimes be missed. Finally, an uncertainty, determined by the resolution of the different detector, is associated with each measurement. It follows that the resulting event is indistinguishable from a real event and the information remaining are exactly what will be available with a genuine recorded event. The same simulated event, presented in Figure 3.1, is now displayed after this pseudo-calibration in Figure 3.2.

The chronological information from the tracker cells are no longer available and the radii now have an uncertainty which translates into a ring rather than a circle (a longitudinal uncertainty, visible on the side view, is also assigned to each tracker hit). Moreover, one can notice that one of the tracker hit from the left electron track (negative values of x), present in the simulated data, is no longer available in the corrected data because it was too far from the cell center. Finally, the energy and time measurements from the calorimeter are displayed with their uncertainties.

The energy pseudo-calibration is performed by considering a Gaussian function centered on the simulated energy and which width is the calorimeter energy resolution. The new corrected energy is then randomly generated according to this Gaussian function.

The time measurement is randomized too and is related to the energy deposited. It is drawn from a Gaussian distribution centered on the time of the simulated deposit and which width is given by the following empirical parametrization:

$$\sigma_t = \frac{\tau_{\text{scint}} \cdot \sigma_{\text{E}}}{E[\text{MeV}]} \tag{3.1}$$

where τ_{scint} is the scintillator relaxation time, σ_{E} is the uncertainty on the energy measurement and E is the simulated energy deposit. The SuperNEMO plastic scintillator relaxation time is around 12 ns. As a matter of fact, the scintillator excited state can be

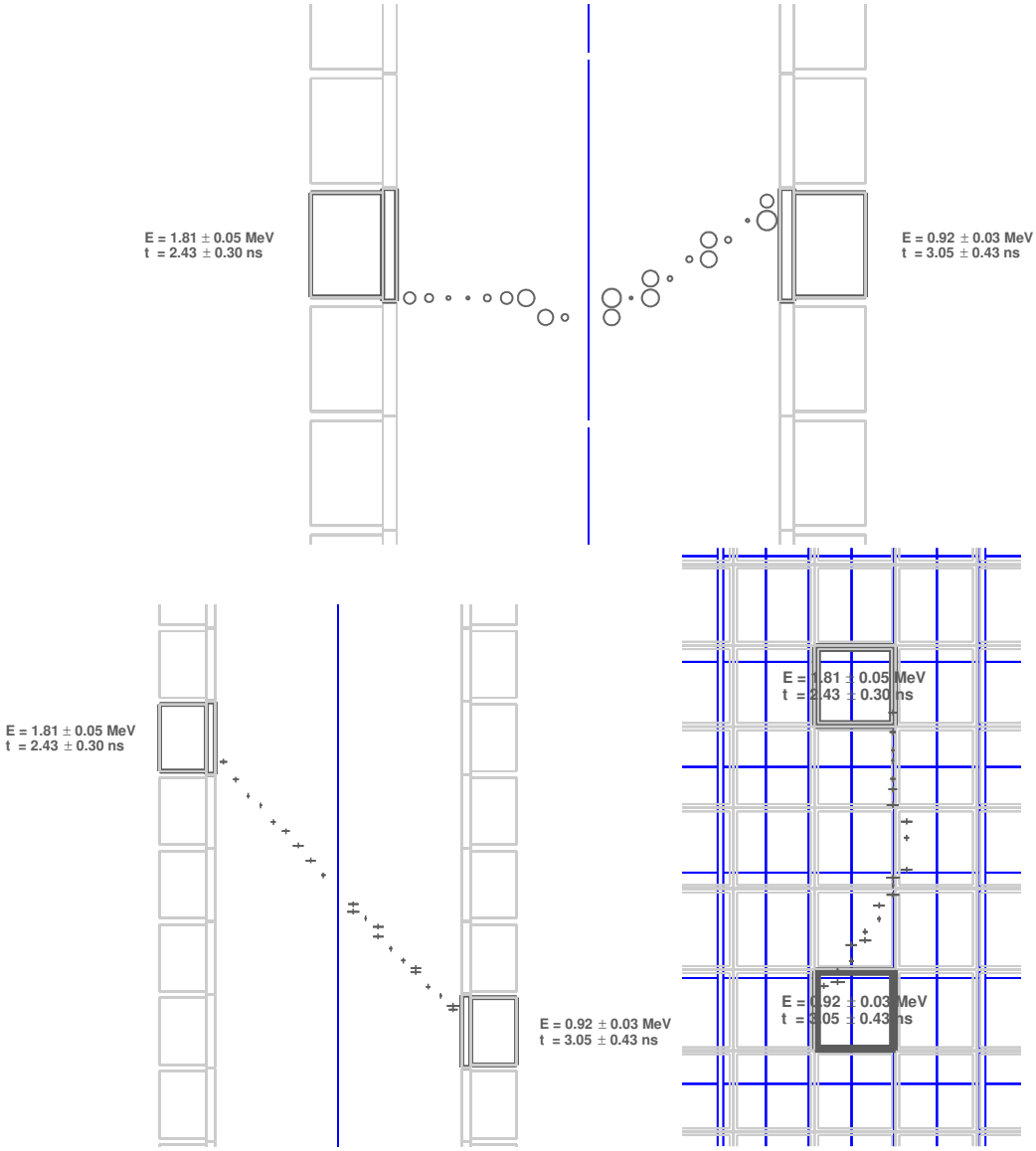

Figure 3.2 – Display of the same simulated event as in Figure 3.1 after a pseudo-calibration is applied. *(top)* Top view. *(bottom left)* Side view. *(bottom right)* Front view. The chronological information from the tracker is lost and all measurements have an associated uncertainty. The primary particles are not visible anymore and need to be reconstructed.

metastable, so this value represents the delay between the excitation and the emission of the de-excitation light.

To match more faithfully the real data, the simulation can also take into account the running conditions as well as the aging that may occur over the experiment lifetime. The PMTs gains will be monitored, corrected if possible, and recorded in a database. The dead PMTs and dead Geiger cells will also be listed. These alterations can be easily taken into account in the simulation. The information resulting from the pseudo-calibration are visible in Figure 3.2 are saved in a bank called Calibrated Data bank (CD).

At this stage of the simulation, the data generated is identical to genuine recorded data and the reconstruction tools can thus be developed, before even having access to the recorded events.

3.1.2 The event reconstruction

The simulated or recorded events go through a succession of algorithms which each strive to improve our comprehension of the events and to accurately reconstruct them.

The tracker clustering

The first step of the reconstruction is to identify the number of charged particles present in the event, based solely on the tracker hits. A cellular automaton tracker (CAT) algorithm is used to gather neighboring hits into clusters until all tracker hits are part of a cluster. It starts from a tracker hit in the layer closest to the source and adds the neighboring hits, layer after layer. Once it reached the last layer closest to the calorimeter, if some triggered tracker hits remain unclustered, it starts a new cluster search. By construction, a cluster cannot extend across the source foil, so particles going through the foil will generate two clusters and will only be identified as crossing particles later in the reconstruction. This algorithm is, however, able to discriminate clusters induced by delta rays, Moller electrons or backscattering electrons, from a primary electron cluster. The tracker cells triggered more than 10 μs after the prompt calorimeter signal will be identified as delayed cells. This time window is dictated by the electronics. A second trigger and acquisition system is dedicated to the recording of the tracker hits occurring after this time period. In the event visualization, each cluster is identified by a color, as illustrated in Figure 3.3, showing once again the same event. This information make up the Tracker Clustering data bank (TCD).

The tracker trajectory fitting

The clusters gather the tracker cells likely to have been triggered by a single charged particle. Therefore, the next step is to try to fit a trajectory through these collections of tracker hits. The patterns tested are, of course, helices (of negative and positive curvature) but also lines. Indeed, the magnetic field is not high enough to bend high energy muons or alpha particles tracks. Only the best trajectory, which is the fit with the lowest χ^2/ndof, is kept for each cluster, as illustrated in Figure 3.4. Delayed clusters are temporarily fitted with a straight line, where the cells are attributed a default radius of one fourth of their

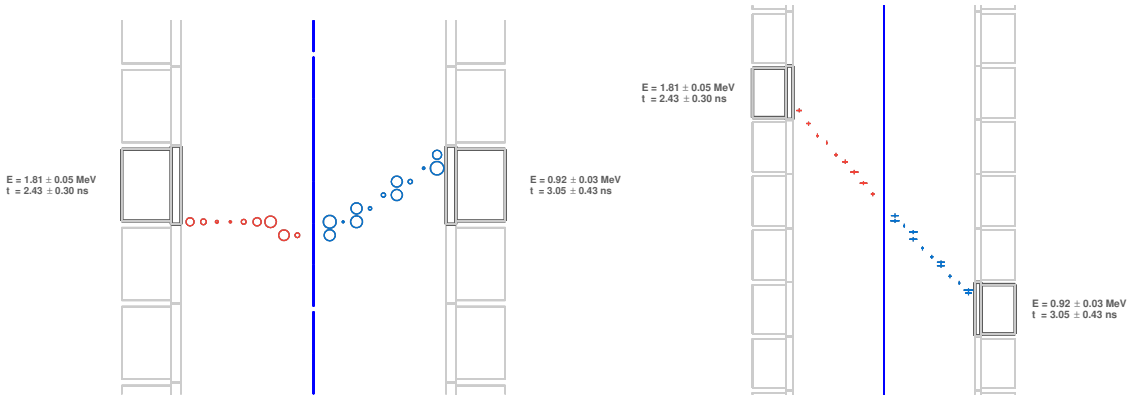

Figure 3.3 – Display of the same simulated event as in Figure 3.1 after application of the tracker clusterization algorithm. *(left)* Top view. *(right)* Front view. Two collections of tracker hits, or clusters, are identified, a blue and a red one.

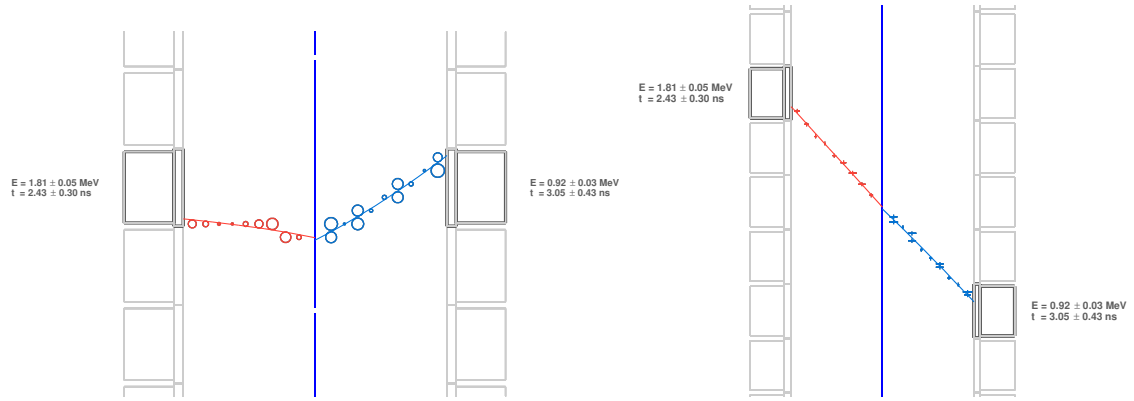

Figure 3.4 – Display of the same simulated event as in Figure 3.1 after application of the tracker trajectory fitting algorithm. *(left)* Top view. *(right)* Front view. Two helices are identified as the best fits for the two clusters.

total radius. The new bank associated with this procedure is called the Tracker Trajectory Data bank (TTD).

The charged particle tracking

The reconstruction algorithms used until this point are somewhat independent of SuperNEMO and could be used in any experiment using a wire chamber. The next step of the reconstruction will resituate the reconstructed tracks in the context of the SuperNEMO detector. The tracks are extrapolated to the calorimeter walls to check if a calorimeter hit can be associated with it. The tracks are also extrapolated to the source, in an attempt to locate the vertex of origin of the event. The spatial resolution provided by the tracker is expected to be better than $\sigma_y = 4$ mm (horizontally *i.e.* perpendicularly to the wires) and $\sigma_z = 11$ mm (vertically *i.e.* along the cells), as shown in Figure 3.5.

It will be measured thanks to the ^{207}Bi calibration sources. The reconstructed source vertices from the conversion electrons will be compared to the real positions of the source known to within 1 mm. The particles electric charges are determined from the curvature of the tracks, assuming they come from the source and end up in the calorimeter. This

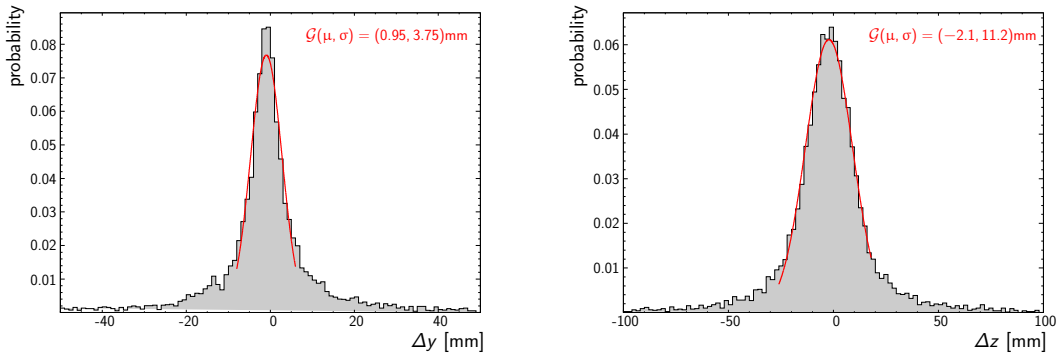

Figure 3.5 – Distributions of the horizontal *(left)* and vertical *(right)* spatial differences between the simulated and the reconstructed vertices on the source for single electrons events with a uniformly distributed random energy between 0 and 3 MeV [78].

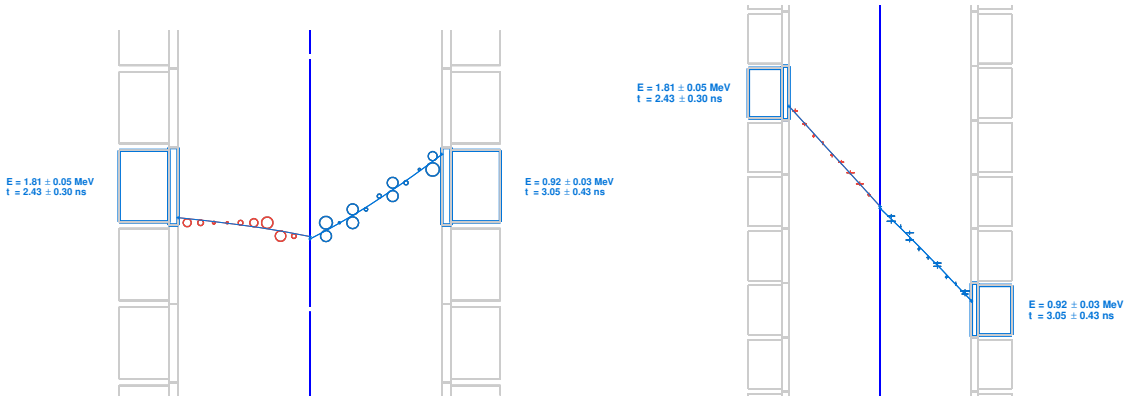

Figure 3.6 – Display of the same simulated event as in Figure 3.1 after application of the charged particle tracking algorithm. *(left)* Top view. *(right)* Front view. A calorimeter hit is associated with each negatively-curved particle track. A vertex is also extrapolated on the source for each track.

approach is what constitutes the charge identification in SuperNEMO. Coming back to our example, at this stage of the reconstruction, two negatively charged particles with each an associated calorimeter hit and a vertex on the source are identified (Figure 3.6).

This reconstruction module is also able to identify the alpha particles in the events. Most of the α particles detected in the tracker (from the ^{214}Bi-Po cascade) will be delayed with respect to a prompt electron. This generates delayed tracker hits which, because they are delayed, are not considered by the clustering algorithm. In addition, the absence of a reference time (usually provided by the calorimeter) does not give access to the drift radii of such tracker cells. The longitudinal coordinate can nonetheless be reconstructed (the reference time is taken as the anode time *i.e.* the moment the initial avalanche reaches the anode).

The alpha tracks are consequently reconstructed by fitting straight tracks to the delayed tracker cells to which a default drift radius is assigned (one-fourth of the cell radius for instance). An example of an event with a delayed alpha particle is shown in Figure 3.7.

The new information provided by this module compose the Particle Track Data bank (PTD). SuperNEMO can thus reconstruct charged particles tracks, generated by electrons,

positrons or α particles but, as advertized in Section 2.1, it is able to detect γ particles too.

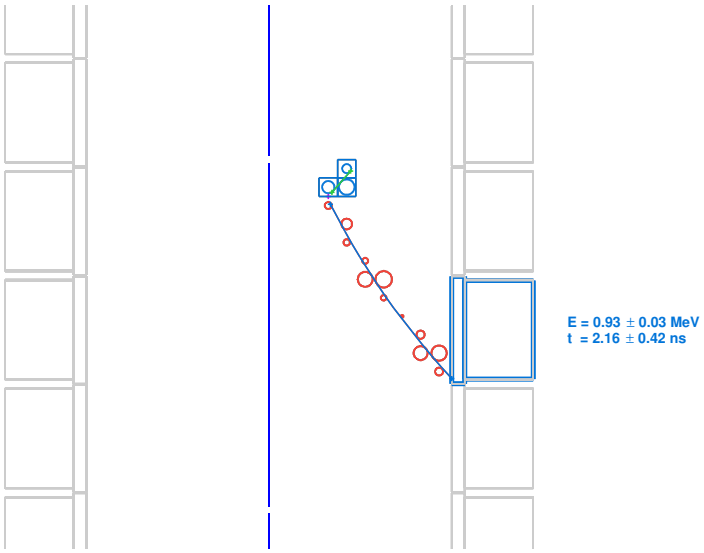

Figure 3.7 – Display of a ^{214}Bi decay from the tracker wires. The delayed cells, belonging to the α particle, are indicated by a square around them.

The gamma reconstruction

The γ particles, being neutral, are not detected by the tracking chamber. Their signature is one or several calorimeter hits to which no track is associated. Indeed, γ particles can bounce around in the detector and trigger several calorimeter modules. A dedicated algorithm employs geometrical and Time-Of-Flight information to follow the γ's in the detector and reconstruct the event as faithfully as possible. The next chapter is devoted to the implementation and validation of this algorithm. An event with an electron and two γ's, one of which bounces and triggers two calorimeter hits, is displayed after application of the algorithm in Figure 3.8. The reconstructed γ tracks are added to the Particle Track Data bank.

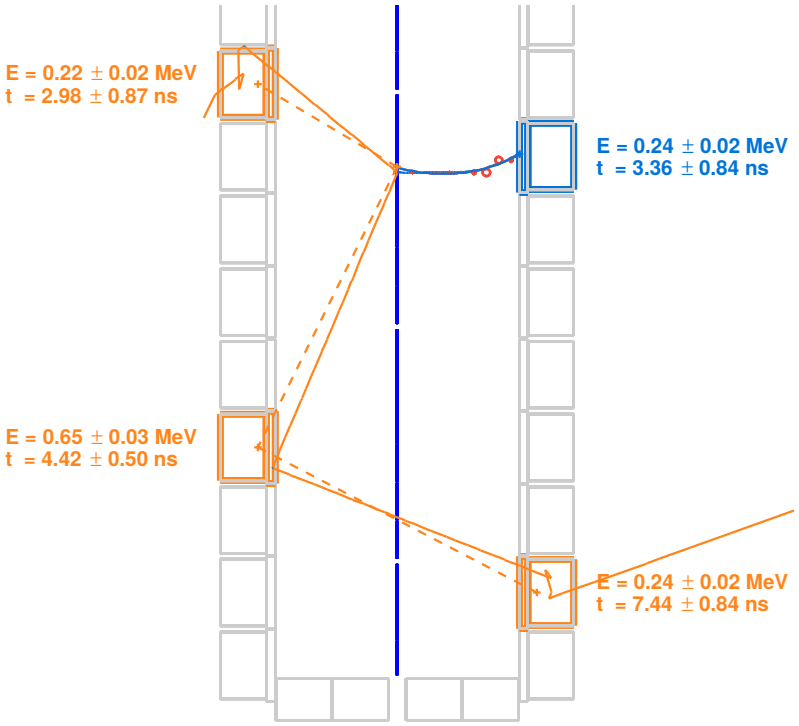

Figure 3.8 – Display of an event with one electron and two γ's emitted. The simulated γ tracks are the solid orange lines. One of them scatters in a first scintillator and deposits energy in a second calorimeter block. The tracks reconstructed with the γ reconstruction algorithm are the dashed orange lines. By default, since the interaction point of the γ particle in the scintillator cannot be reconstructed, the tracks link the barycenter of the scintillators to the vertex of the event.

3.1.3 The particle identification

At this stage of the reconstruction, the particle tracks have been reconstructed individually. The next step is to identify the nature of the particles involved and to relate them at the level of the event. The different particle signatures are illustrated in Figure 3.9 and are the following:

- **Electron**: a negatively[b] curved track with an associated calorimeter hit.
- **Positron**: a positively curved track with an associated calorimeter hit.
- **Alpha**: a short straight track (sometimes delayed).
- **Gamma**: One or more unassociated calorimeter hits.

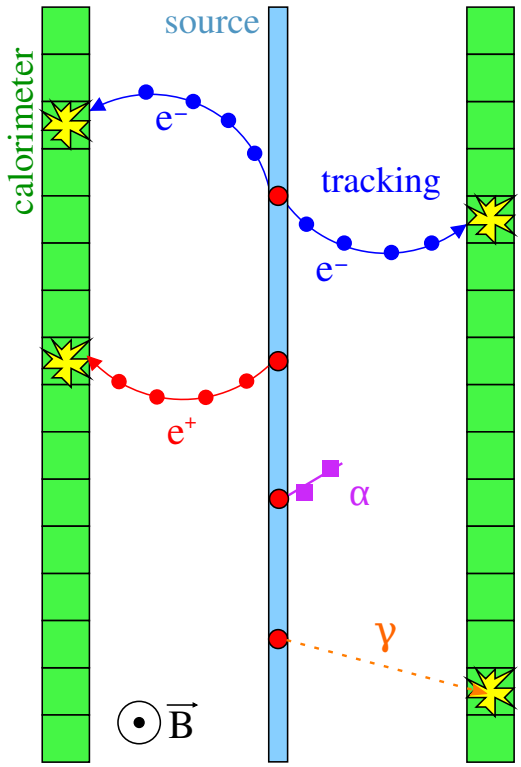

Figure 3.9 – Sketch of the different particle signatures in the SuperNEMO detector.

The Particle Identification module, developed in the context of this Ph.D., first tags each tracks according to the criteria listed above. These criteria are the same across this thesis and are the one used in the different analyses performed in this thesis. However, the possibility is left to the user to provide its own particle definitions and the tracks will be tagged accordingly.

[b] A negative, resp. positive, curvature refers to the curvature a negatively, resp. positively, charged particle would produce in the tracker as it travels from the source to the calorimeter.

The charge of the particle is inferred from the track curvature, induced by the magnetic field and assuming the particle travels from the source to the calorimeter. The electrons and positrons, among other reasons, are thus required to have an associated calorimeter hit (it is indeed very unlikely to observe an electron originating from the calorimeter, depositing energy as it leaves, and dying in the source foil, rather than the opposite). In addition, if no calorimeter module is triggered, the event would not have passed the trigger conditions and been recorded in the first place. Yet, in our definitions, the charged particles are not required to have a vertex on the source foil. This can be useful to study the events originating from the tracker volume. Concerning α particles, they are, on the contrary, required to have no associated calorimeter hits. An α particle is indeed not expected to travel long distances in the tracker gas and, *a fortiori*, to penetrate the tens of μm of nylon and aluminized mylar separating the tracker from the scintillator.

The tracks which do not match any definitions are tagged as undetermined. Once all the particles in the event are identified, an event topology can be defined. Such topologies are for instance: two electrons events (labeled $2e$), one electron plus one γ events (1e1γ) or even one electron and one alpha event (1e1α).

Therefore, this module identifies the particles and classifies the events according to their topologies. This can be considered the first step towards the analysis but this module does not perform any event selection and lets the user proceed as he/she pleases. Nonetheless, this module does prepare the analysis work by performing all the topological measurements relevant to the event. Such measurements are:

- the angle between the particles. This angle is measured for two charged particles, as the angle between the tangent of the two helices at the vertex of origin (the source foil for instance). The angle between a charged particle and a γ is also computed, where the earliest γ calorimeter hit is considered for the measurement and the γ energy deposit is assumed to occur in the center of the scintillator block. The angle of a single charged particle is recorded as well and is the angle between the tangent of the track at the origin and the $0x$ axis, perpendicular to the foil.

- the distance between the source vertices of charged particles. Each track has its own vertex extrapolated on the source, this distance can thus be later used to decide if the two particles share the same vertex of origin. The construction of a probability, similar to that of the internal probability based on the TOF, was considered. The hypothesis tested being whether the two vertices, given their associated spatial uncertainties, are compatible with a single vertex, defined as the barycenter of the two vertices, where the weight is inversely proportional to the uncertainty on the vertex. The χ^2 associated with this computation did not follow a Gaussian distribution, such that the probability distribution was not flat. In this particular case, this meant that the uncertainties were overestimated. This approach was set aside until a better estimation of the vertices uncertainties is developed. Some answers can come from the software, which does not provide the uncertainty associated with the reconstruction, or by waiting for the results of the calibration runs in the demonstrator.

- the internal and external probabilities, based on the Time-Of-Flight computation,

between two particles. This measurement can only be performed if both particles have at least one associated calorimeter hit, and that one of them is charged (a vertex is needed to formulate a hypothesis.)

The internal and external probabilities are more elaborate measurements and deserve a more detailed explanation, even if the concept will be addressed again in the next chapter. The internal probability is used to quantify the likelihood of the hypothesis that two particles were emitted simultaneously from the source foil. The external probability, however, is built to test if one of the two particles (an electron or, more likely, a γ) first deposited some energy in the calorimeter, crossed the tracker to reach the source foil and, either created a second particle, or carried on to trigger a second calorimeter module. First a χ^2 is computed for each hypothesis:

$$\chi^2_{\text{int}} = \frac{\left((t_2^{\text{exp}} - t_1^{\text{exp}}) - (\frac{\ell_2}{\beta_2 c} - \frac{\ell_1}{\beta_1 c})\right)^2}{\sigma^2_{t_1} + \sigma^2_{t_2} + \sigma^2_{\beta_1} + \sigma^2_{\beta_2} + \sigma^2_{\ell_1} + \sigma^2_{\ell_2}} \tag{3.2}$$

$$\chi^2_{\text{ext}} = \frac{\left(\left|t_1^{\text{exp}} - t_2^{\text{exp}}\right| - (\frac{\ell_1}{\beta_1 c} + \frac{\ell_2}{\beta_2 c})\right)^2}{\sigma^2_{t_1} + \sigma^2_{t_2} + \sigma^2_{\beta_1} + \sigma^2_{\beta_2} + \sigma^2_{\ell_1} + \sigma^2_{\ell_2}} \tag{3.3}$$

where t_i^{exp} is the time measured experimentally by the calorimeter for the particle i, ℓ_i is the reconstructed track length of the particle i (for γ particles, this is the distance between the source vertex tested and the center of the scintillator of the earliest or the latest calorimeter hit, for the internal and external probabilities respectively), $\beta_i = v_i/c$ is deduced from the measured energy and is equal to 1 for γ particles, c is the speed of light, σ_{t_i} is the uncertainty on the time measurement for the particle i, σ_{β_i} is the uncertainty on β_i (which is linked to the uncertainty on the energy measurement) and σ_{ℓ_i} is the uncertainty on the track length of the particle i, translated into a time uncertainty assuming a speed c.

For the internal probability, the experimental time difference is compared to the theoretical time difference to see if it can be explained only by the difference in track lengths. If it is compatible, which means of the order of the experimental uncertainties, the associated χ^2 will be low *i.e.* close to 1 or lower. The same approach is used for the external probability, except the time difference is compared to the time it would have taken a particle to fly from one calorimeter module to the other.

In both cases, the χ^2 is translated into a probability according to:

$$P(\chi^2_{\text{int}}) = \frac{1}{\sqrt{2\pi}} \int_{\chi^2_{\text{int}}}^{+\infty} x^{-\frac{1}{2}} e^{-\frac{x}{2}} \mathrm{d}x = 1 - \frac{1}{\sqrt{2\pi}} \int_0^{\chi^2_{\text{int}}} x^{-\frac{1}{2}} e^{-\frac{x}{2}} \mathrm{d}x$$

One may recognize here the error function. This formula transforms a Gaussian distribution into a flat distribution between 0 and 1. This approach presents several advantages. Not only is it more convenient to manipulate hypothesis probabilities rather than χ^2, but this transformation will also bring out any underestimation or overestimation of the experimental uncertainties which would translate into skewed or even bumpy probability distributions.

The new information brought by the Particle Identification module are recorded in the Topology Data bank. Considering the example of a two electrons events, the information stored are the individual energies (tagged as minimum and maximum energies), the energies sum and difference, the internal and external probabilities, the angle between the two tracks on the source, the distance between the two vertices in the three spatial dimensions, the 3D location of the two vertices barycenter (as explained earlier) and the category of the vertex *i.e.* whether it is reconstructed on the source, in the tracker, on the main calorimeter walls surface etc.

3.1.4 Summary of the simulation and reconstruction pipeline

A diagram summarizing the SuperNEMO simulation and reconstruction chain is provided in Figure 3.10.

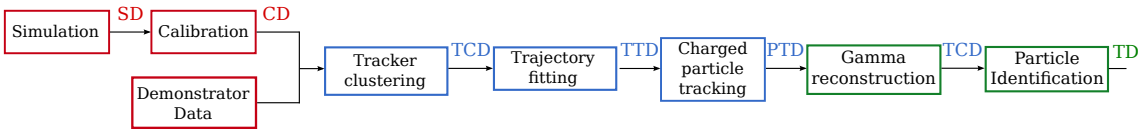

Figure 3.10 – Overview of the SuperNEMO simulation and reconstruction pipeline. The green modules were developed during this thesis.

This shows that the simulated data and the data recorded by the detector follow exactly the same reconstruction process. The end of the reconstruction chain, namely the γ reconstruction and the particle identification (and associated topological measurements) were developed during this thesis.

3.2 The analysis channels

One of the strengths of SuperNEMO is its ability to identify the particles. The reconstruction process explained above makes possible the definition of event topologies. The most interesting event topologies are $2e$, $1e$, $1e\mathrm{N}\gamma$, $2e\mathrm{N}\gamma$, $1e1\alpha$ and, to a lesser extent $1e1p$ (one electron and one positron). These topologies can be further classified into analysis channels based on the measurements performed during the reconstruction. These channels can then be used to identify and measure the different background contributions, independently from the main channel, devoted to the search of the neutrinoless double beta decay. The different channels used during the analysis, as well as the backgrounds they are mainly dedicated to, are described in this section.

3.2.1 The signal channels

Two internal electrons

This is the main analysis channel. In addition to the $2e$ topology, this channel requires the two electrons to come from the same vertex and to have a good internal probability.

In practice, "same vertex" means that the two electrons source vertices should not be separated by more than a few mm, while an internal probability is considered as "good" above a few percents. The exact selection values are determined during the analysis and depend on the background levels. If more background is present, more stringent cuts need to be applied. Most of the $0\nu\beta\beta$ signal events should fall in this category of events. The main contribution will come from the $2\nu\beta\beta$ decay but some backgrounds events are also expected in this channel, as explained in Section 2.2. A $0\nu\beta\beta$ event falling into this channel is shown in Figure 3.11.

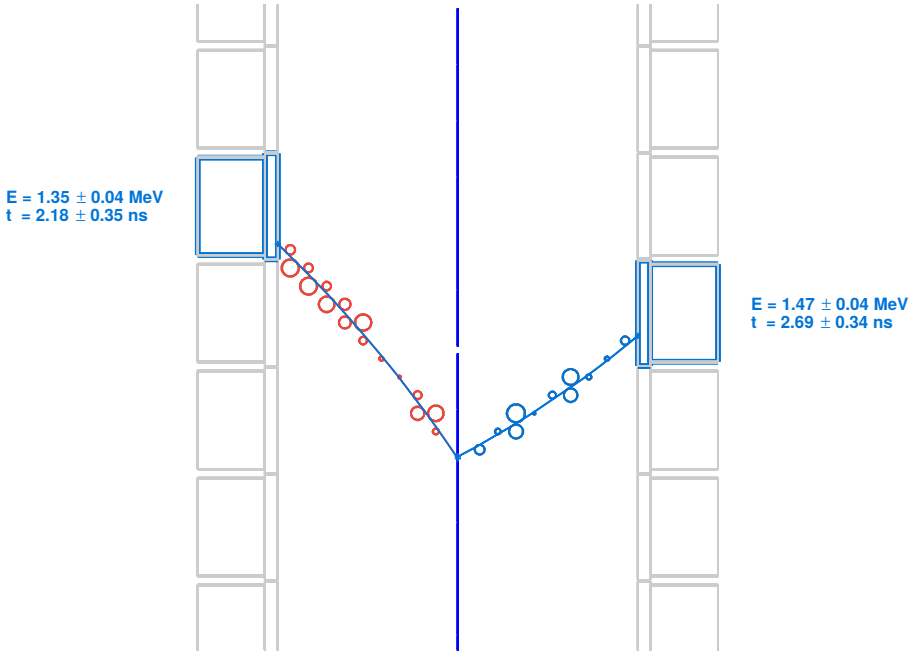

Figure 3.11 – Display of a $0\nu\beta\beta$ event satisfying the criteria of two internal electrons channel.

Two internal electrons and any internal γ's

This channel is dedicated to the search for the double beta decay to the excited states, with or without emission of neutrinos. All the particles are required to have a good internal probability with each other (or at least with one or both the electrons). The electrons are, of course, required to have matching source vertices. Since more particles are sharing the energy, this channel has a lowered detection efficiency. Particles of lower energy will have a harder time leaving the source, crossing the tracking chamber and depositing enough energy to pass the trigger threshold. On the other hand, it is also harder for the beta/γ emitters sources to fake this kind of event. Therefore, the background will mainly come from the double beta decay to the ground state, where one or more γ are created *via* Bremsstrahlung or are faked by noisy PMTs and random coincidences. An example of an event of ^{82}Se double beta decay to the excited states with the emission of neutrinos can be seen in Figure 3.12.

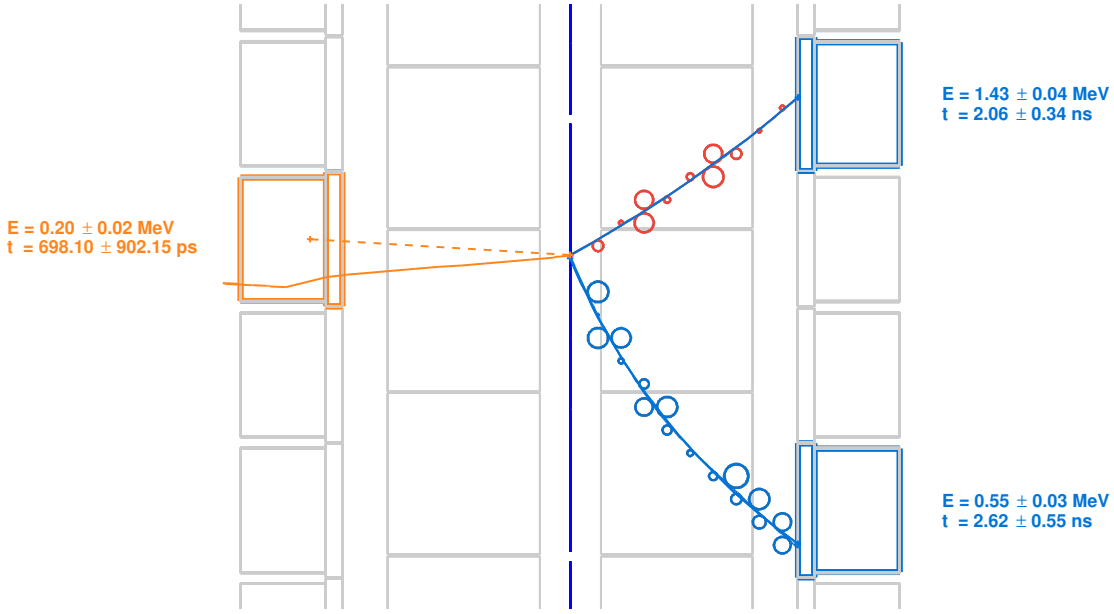

Figure 3.12 – Display of a $2\nu\beta\beta$ decay to the excited states, matching the two internal electrons and one internal γ channel.

3.2.2 The internal background channels

The main backgrounds for the neutrinoless double beta decay search come from a contamination of the source in ^{208}Tl and ^{214}Bi, as well as from Radon gas in the tracker. As explained earlier, one of the key feature of the SuperNEMO demonstrator is its ability to measure its own background in dedicated channels, which are independant from the main signal channels.

One electron and one α in the tracker

This channel requires an electron and an α particle to share a vertex in the tracker volume. There is a very limited mass of wires present in the tracker. In addition, the materials used for their construction were screened and measured to be radiopure. Consequently, most of the events coming from the tracker are expected to be radon-induced events. The most harmful of its decay product is ^{214}Bi. This nucleus β-decays to ^{214}Po which, soon after, decays to ^{210}Pb, *via* α decay, with a half-life of 164.3 μs, as reminded in Figure 2.25. This β-decay, followed by a delayed α decay, provides a clear signature of radon-induced events. An example of radon event was already shown in Figure 3.7.

One electron and one α from the source

This channel is almost identical to the previous one, except for the shared vertex which must be located on the source foil. The only events expected in this channel come from two background contaminations: a contamination of the source in ^{214}Bi or a contamination of

the tracker with radon. Indeed, radon can either deposit[c] on the surface of the source foil, in which case the event vertex actually comes from the source, or it can deposit on the field wires of the cells closest to the source. An α track can be mistakenly extrapolated to the source foil but there is no way to prevent this. However, α's coming from a source contamination will go through much more materials before being detected by the tracker. Consequently, their tracks will be, on average, shorter than for radon events. This channel thus allows the measurement of the ^{214}Bi source contamination and the confirmation of the radon level measurement. Figure 3.13 shows an example of a ^{214}Bi decay in the source.

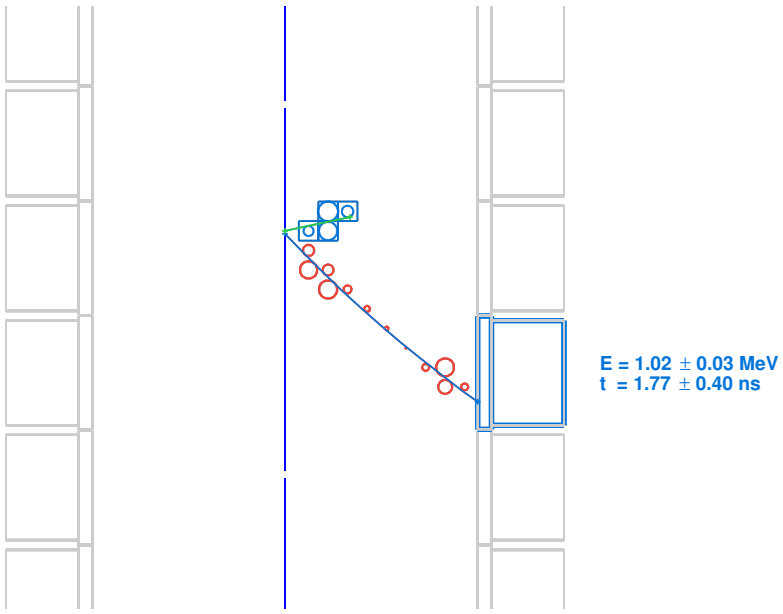

Figure 3.13 – Display of a ^{214}Bi β decay followed by an α decay of ^{214}Po, coming from the source foil. This event is reconstructed in the channel 1e1α from the source.

One electron and any internal γ's

In this channel, every γ ray must have a good internal probability with the electron, which is required to come from the source. Indeed, looking at Figure 2.27, the ^{208}Tl and ^{214}Bi nuclei, present in the source, are β and γ emitters. In particular, as explained before, ^{208}Tl emits one electron and between 1 and 3 γ's while ^{214}Bi emits one electron and between 0 and 2 γ's. Assuming an efficient γ reconstruction, the $1e3\gamma$ channel appears to be ideal for the ^{208}Tl measurement. However, since the particles need to share the same fixed energy, the more particles there are, the less energy they will carry. Considering the calorimeter non-perfect γ detection efficiency, it is less likely for three γ to be detected at the same time. In addition, assuming a γ is detected, it seldom deposits all its energy in a single calorimeter block. This means the more γ's there is, the less likely they are to all pass the energy trigger threshold. Consequently, though the $1e3\gamma$ channel is a

[c] Actually, only the radon daughter nuclei deposit on the wires, and in particular ^{214}Pb nuclei since ^{218}Po nuclei form a complex with the alcohol in the tracker gas.

pure channel for the measurement of the ^{208}Tl source contamination, it is not very efficient and is expected to provide fewer statistics than other channels. On the contrary, the $1e2\gamma$ and $1e1\gamma$ channels can be used to measure both the ^{208}Tl and ^{214}Bi activities from the source. Because the transition energy is higher and that more γ's are emitted, ^{208}Tl is best measured in the $1e2\gamma$ channel. A significant contribution to these channels is however expected from other radiocontaminants, like ^{40}K, but also from the $2\nu\beta\beta$ decay and from radon events. An example of ^{208}Tl decay in the source, reconstructed in the $1e2\gamma$ channel, is provided in Figure 3.14.

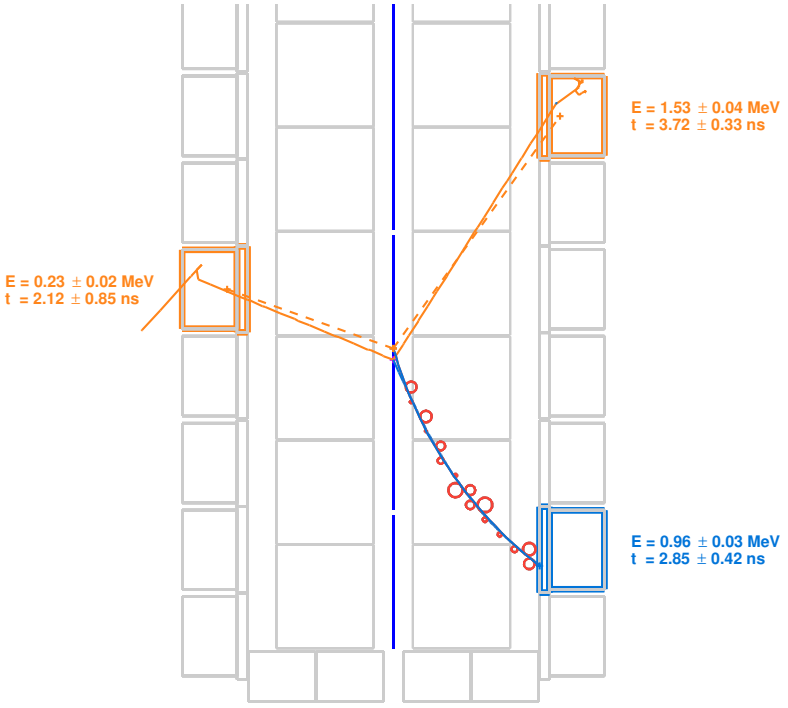

Figure 3.14 – Display of a ^{208}Tl decay from the source foil, reconstructed in the 1e2γ internal channel.

One electron channel

The 1e electron channel is one of the simplest channels as it only requires an electron coming from the source. However, since many contributions are expected, the identification and measurement of the different background origins can become challenging. It can still be used together with other channels to better constrain the background model (and identify some background sources which could not be measured with HPGe detectors).

3.2.3 Hot spots: $1e$ and $1e1\gamma$ internal channels

The $1e$ electron and $1e1\gamma$ internal channels are useful for the localization of so-called "hot spots" on the source foils. These hot spots are composed of contaminants with a

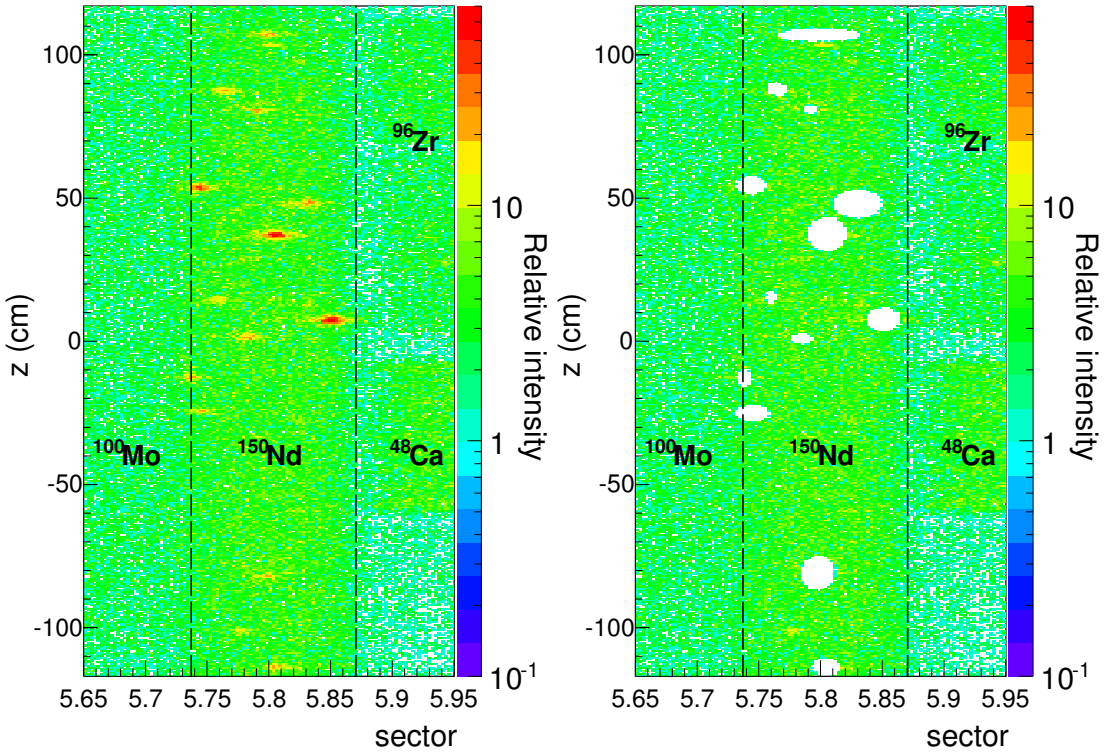

Figure 3.15 – Distribution of the 1e1γ event vertices reconstructed by NEMO-3 in the ^{150}Nd source foil. *(left)* Before and *(right)* after the removal of the hot spot regions. [79]

very high level of activity[d] and which might have been introduced during the production, transport or installation of the source. The $1e$ channel will help identify β decays to the ground state while the $1e1\gamma$ internal channel will help identify decays to the excited states. The energy distribution of the electron and the γ particle can provide some input as to the composition of these hot spots in order to find out how they could have been introduced. The basic idea is to divide the source in regions, of the order of the spatial resolution of the tracker, and to exclude the ones with an event rate higher than a 3σ fluctuation from the mean rate, for instance. These fiducial cuts are applied in an effort to enhance the signal-to-background ratio, not only for the search of the $0\nu\beta\beta$ decay but also for the measurement of the $2\nu\beta\beta$ half-life. A picture of the ^{150}Nd source as seen by NEMO-3 is presented in Figure 3.15.

3.2.4 The external background channels

As explained in Section 2.2, the background can come from β/γ emitters located outside the source, *e.g.* ^{208}Tl and ^{214}Bi in the PMTs glass or on the surface of the scintillators. This can impact the search for the $0\nu\beta\beta$ decay but it is especially harmful to the search of the double beta decay to the excited states. Fortunately, some analysis channels are dedicated to the characterization of this background.

[d] A very high activity compared to the overall source activity which is quite low.

Crossing electron

This channel aims at selecting events where an electron is emitted from a triggered calorimeter module, goes through the source foil and triggers a second calorimeter block. One could also select, without distinction, the events where the electron bounced on the source foil and stayed in the same half of the detector but in that case, a significant part of the electron's energy might have been lost during the backscattering. This channel requires two tracks of opposite curvature, with a good external probability and a compatible vertex on the source. Such events can be generated by a γ particle, creating a Compton electron in the last millimeters of the scintillator. The electron can also come from the surface of the calorimeter. In that case, the first energy deposit can occur through the backscattering of the electron or through the emission of a γ particle, triggering the calorimeter block close to the electron emission vertex. Such event can also be faked by ^{212}Bi present on the scintillator surface or in the calorimeter wrapper. A ^{212}Bi nucleus can undergo a β decay to ^{212}Po which then decays to ^{208}Pb via α decay with a 300 ns half-life. The two tracks would be generated by the electron and the α decay would occur promptly, a few ns after the β decay, in order to induce a good external probability. For the same reason, if the electron's charge is misidentified and if the α decay time is compatible with an internal event, this process can mimick a $\beta\beta$ event. An example of crossing electron event is displayed in Figure 3.16.

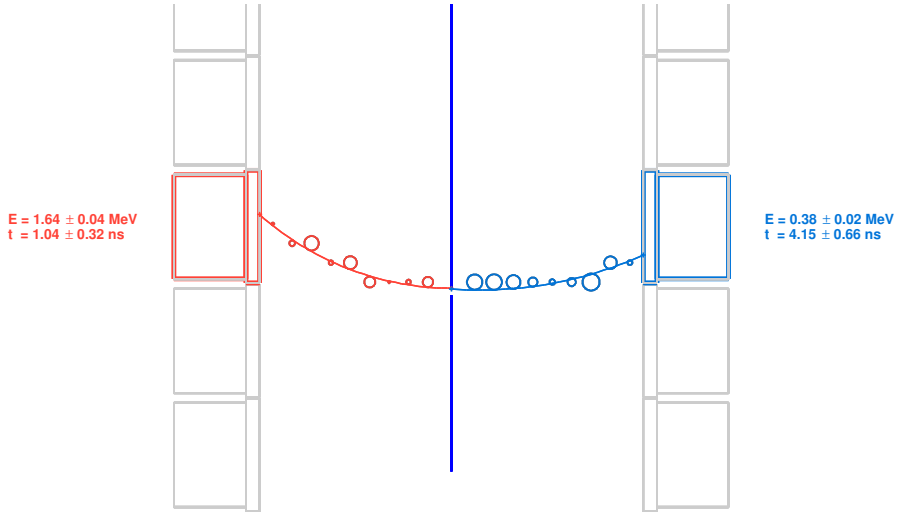

Figure 3.16 – Display of a ^{214}Bi event from the scintillator surface, reconstructed in the crossing electron channel.

One external γ and one electron

Another channel can be used to build the external background model. The $1e1\gamma$ external channel is less accurate than the crossing electron channel (SuperNEMO being dedicated to the electron detection) but can still be used as a cross-check of the background measurement. This channel selects events where a γ first interacted in a scintillator block

and then created an electron in the source foil. A good external probability between the electron and the γ is thus required. Since two successive Compton scatterings are necessary, this channel provides fewer statistics than the crossing electron channel. Figure 3.17 shows such an event.

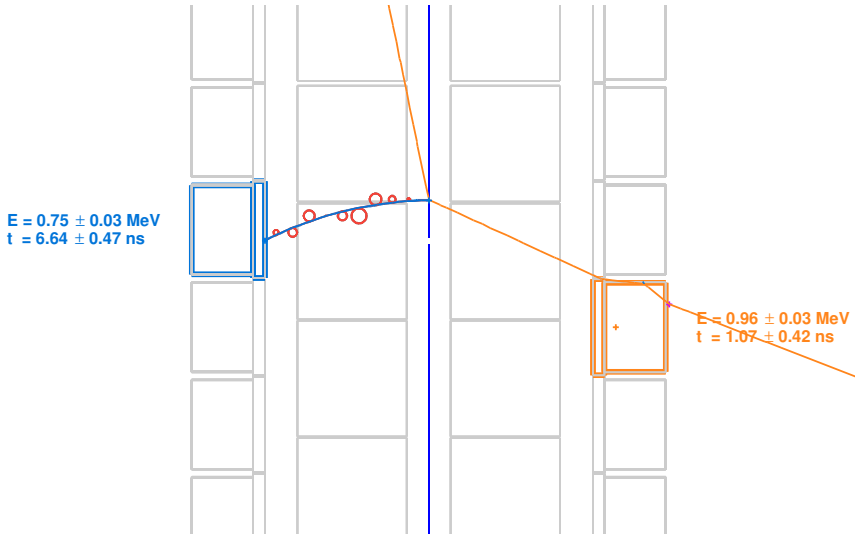

Figure 3.17 – Display of ^{208}Tl decay from the PMTs glass. A γ particle triggers a calorimeter module, creates a Compton electron in the source and leaves the detector without being detected.

The origins of such events, and of the external background in general, are more varied than that of the internal background. In these two last channels, the external γ particle can come from any isotope from the natural radioactivity or from the radiative capture of neutrons in any part of the detector. If an accurate description of the external background model cannot be achieved, an effective model can prove sufficient, like in NEMO-3, since it does not significantly impact the search for the neutrinoless double beta decay.

3.2.5 Summary of the analysis strategy

SuperNEMO does not rely on a single channel to perform its analysis. Moreover, the multiple channels described above, each provide a variety of information (the particles individual energies, the angular distribution, the internal and external probability distribution, etc) to help discriminate between signal and background events and even to discriminate between the different background processes. This approach allows an accurate and independent *in situ* determination of the background model, both internal and external. The channels selection criteria provided here are representative of the different studies performed in NEMO-3. However, in any of these channels, some cuts can be loosened or even removed if it benefits the analysis. On the contrary, depending on the detector performance, more stringent cuts may be introduced (high PMTs counting rates, self-triggering tracker cells, etc.).

3.3 The analysis tools

Having introduced the simulation and reconstruction tools, this part will focus on the analysis tools used to process both the data generated by the Monte-Carlo simulations and the future data recorded by the demonstrator.

3.3.1 Fitting the data

After their reconstruction and their classification, the events and their characteristics are recorded to generate distributions used to discriminate signal from background events. This does not mean, however, that this discrimination can be performed on an event-by-event basis. Instead, these distributions, like the total energy of the event, will help highlight regions in the parameters space where signal events tend to accumulate. The Monte-Carlo simulations strive to reproduce such distributions and the goal of the analysis is to manage to fit the Monte-Carlo templates to the real data. In the absence of data from the demonstrator, the analyses performed in this thesis were carried out on simulations which we will call pseudo-data, or simply data, in the following.

The fit of Monte-Carlo templates to pseudo-data was performed using a binned log-likelihood fit. Let's assume, first, a single variable distribution, divided into bins, populated by events following the Poisson statistics. The probability p_i of observing in a bin i, a number of data events d_i, explained by a Monte-Carlo prediction on the number of signal events s_i and background events $\sum_j b_{i,j}$ (the sum over all j background sources), is expressed:

$$p_i = \frac{e^{-(s_i+\sum_j b_{i,j})}(s_i + \sum_j b_{i,j})^{d_i}}{d_i!} \tag{3.4}$$

The likelihood $\mathcal{L}$ is defined as the product of probabilities in all i bins:

$$\mathcal{L} = \prod_i \frac{e^{-(s_i+\sum_j b_{i,j})}(s_i + \sum_j b_{i,j})^{d_i}}{d_i!} \tag{3.5}$$

This construction yields a maximum likelihood for the parameters s and b_j that best describe the data. This expression can be extended to include several channels k in the same fit:

$$\mathcal{L} = \prod_{i,k} \frac{e^{-(s_{i,k}+\sum_j b_{i,j,k})}(s_{i,k} + \sum_j b_{i,j,k})^{d_{i,k}}}{d_{i,k}!} \tag{3.6}$$

Including several channels at once helps ensure the predicted model is compatible with data observed and improves the stability of the measurement against statistical fluctuations. It is often convenient to use a logarithm to turn the product into a sum. The logarithm is a monotonic function and, as such, will not change the maximum of $\mathcal{L}$. In addition, this quantity is multiplied by a factor -2 so that the significance of a change in its value can be calculated using a χ^2 distribution:

$$-2\ln(\mathcal{L}) = 2\prod_{i,k}\left[s_{i,k} + \sum_j b_{i,j,k} - d_{i,k}\ln(s_{i,k} + \sum_j b_{i,j,k}) + \ln(d_{i,k}!)\right] \tag{3.7}$$

Thus, minimizing -2ln$\mathcal{L}$ is equivalent to finding the best normalizations of the Monte-Carlo templates (for both the signal and the backgrounds). These normalizations are translated into a number of events, assigned to each of the sources composing the model. The computation of the likelihood for a large parameter space and its subsequent minimization is performed with the help of the TMinuit package from ROOT [68].

3.3.2 Computing the half-life from the decay rate

The decay rates are measured as the normalizations of the different backgrounds (and possibly signal) that best explained the observed data. But a decay rate, expressed as a number of events, depends on the experimental conditions, namely the mass of isotope studied and the duration of the measurement. Instead, the computation of half-lives from these decay rates allows a comparison with other experiments, the theoretical predictions and the values found in the literature.

The well-known law of radioactive decay gives the number of nuclei remaining in a sample of an unstable isotope:

$$N(t) = N_0 \cdot e^{-\lambda \cdot t} \tag{3.8}$$

where N_0 is the number of nuclei present in the sample at the time $t = 0$ and λ is the decay constant, related to the half-life of the isotope $T_{1/2}$ according to:

$$\lambda = \frac{\ln 2}{T_{1/2}} \tag{3.9}$$

The half-lives involved in double beta decays are larger than 10^{18}y which means $\lambda \ll 1$ and a Taylor expansion of Equation 3.8 can be performed around t, such that:

$$N(t) \approx N_0(1 - \lambda \cdot t) \quad \text{or} \quad N_0 - N(t) \approx \frac{N_0 \cdot \ln 2 \cdot t}{T_{1/2}} \tag{3.10}$$

If N_0 is the number of nuclei at the beginning of the experiment and $N(t)$ is the number of nuclei remaining after the time elapsed t, their difference represents the number of decays which occurred during the lifetime of the experiment. Taking into account the detection efficiency ϵ of the experiment, Equation 3.10 becomes:

$$N_{\text{obs}} = \frac{\epsilon \cdot N_0 \cdot \ln 2 \cdot t}{T_{1/2}} \tag{3.11}$$

where N_{obs} is the number of events observed during the lifetime of the experiment. The number of nuclei in a sample of mass m and molar mass M is given by the relation:

$$N_0 = \frac{m \cdot N_{\text{A}}}{M} \tag{3.12}$$

where N_A is Avogadro's number.

Substituting in Equation 3.11, one finds back Equation 1.41, the expression of the half-life in terms of the decay rate measured by the experiment:

$$T_{1/2} = \frac{\ln 2 \cdot \epsilon \cdot m \cdot N_{\text{A}} \cdot t}{N_{\text{obs}} \cdot M} \tag{3.13}$$

This equation is only valid if some signal events are observed. Otherwise, a lower limit on the half-life of the process studied can be derived thanks to a proper statistical treatment.

3.3.3 Setting limits in low statistics physics experiments

Physics experiments searching for new physics all proceed alike. They are built to measure one or several final variables which are expected to be sensitive to a parameter of interest. The analysis of the data produced by these experiments, combined with proper statistical calculations, help physicists test their models and hypotheses.

Glossary

Before going into more details, a few concepts should be defined in the context of a search for new physics.

- **Final variable**: A final variable is a quantity measured by an experiment which should enable the observation of a new signal among various expected backgrounds. Such variable in SuperNEMO is, for instance, the two electrons energy sum.
- **Null or background-only hypothesis**: As suggested by its name, the null/background-only hypothesis represents the model where no signal is expected.
- **Test hypothesis or signal-plus-background hypothesis**: This model assumes the existence of a new process (the neutrinoless double beta decay for instance) translated into a non-zero number of signal events and is to be tested against the null hypothesis.
- **Test statistic**: The test statistic is constructed to quantify how well the data match either the Null or the Test hypothesis. Frequent test statistics are for instance the negative log-likelihood ratio or the profile likelihood ratio.
- **Parameter of interest**: The parameter of interest is the model parameter driving the difference between the Null and the Test hypothesis. In our search for the neutrinoless double beta decay, it would be the half-life of the process.
- **Nuisance parameter**: Some parameters of the model are unspecified but will be required for the measurement of the parameter of interest. For instance, when searching for the neutrinoless double beta decay, the half-life is the parameter of interest but it cannot be measured without knowing the efficiency of the process (reconstruction and selection). And since the efficiency is not specified by the model (it depends only on the experiment), it is a nuisance parameter. Such parameters may or may not have associated uncertainties.
- **Conditional probability**: It is the probability to observe an outcome A given the occurrence of another outcome B (also written P(A | B)).

- **Marginal probability**: Conversely, the marginal probability is the probability to observe the outcome A, regardless of the outcome B:

$$P(A) = \int P(A|B)P(B)dB \tag{3.14}$$

- **Prior probability**: The prior probability is the assumption made on the probability of a parameter before performing a measurement.

- **Confidence interval**: It is the interval in which the parameter is said to lie with a specified confidence, whether this confidence is interpreted as a relative frequency or as a degree of belief (respectively known as the frequentist or the Bayesian interpretation).

- **Confidence level**: In a frequentist interpretation, it is the minimum fraction of intervals containing the true value of the parameter, while in a Bayesian interpretation, it is the degree of belief that the quoted interval contains the true parameter value.

Several solutions have been developed by physicists and statisticians to answer the problem of proper limit setting. A few of these solutions are presented in the following pages while their application to our search will be addressed later.

CL_S method with COLLIE

COLLIE, which stands for Confidence Level Limit Evaluator, is a software package developed by the D∅ collaboration. It is used to construct confidence levels and evaluate exclusion limits and was extensively used in the NEMO3 analysis. It uses a modified-Frequentist approach to construct confidence levels, also known as CL_S, for the parameter of interest.

As previously mentioned, physics experiments will record and present data events as a binned distribution (or histogram) of the final variable. This distribution of the number of events observed will then be compared to those expected in the Null and Test hypotheses. In order to quantify how well the data match either hypothesis, one of the test statistic used in COLLIE is the Poisson Log-Likelihood Ratio (ratio between Test and Null hypothesis probabilities). Indeed, a likelihood-ratio test statistic is proven to be especially indicated for searches with small statistics [80].

First, if both hypotheses are treated as Poisson counting experiments, a Poisson likelihood ratio can be defined as:

$$Q(s, b, d) = \frac{e^{-(-s+b)}(s+b)^d/d!}{e^{-b}b^d/d!} \tag{3.15}$$

wherein s and b are the expected number of signal and background events and d is the observed number of data events. This formulation can be generalized to consider multiple

bins and multiple channels. The joint likelihood is built by multiplying each individual probability, such that it becomes:

$$Q = \prod_{i=1}^{N_{\text{channels}}} \prod_{j=1}^{N_{\text{bins}}} \frac{e^{-(s_{ij}+b_{ij})}(s_{ij}+b_{ij})^{d_{ij}}/d_{ij}!}{e^{-b_{ij}} b_{ij}^{d_{ij}}/d_{ij}!} = \prod_{i=1}^{N_{\text{channels}}} \prod_{j=1}^{N_{\text{bins}}} e^{-s_{ij}} \left(\frac{s_{ij}+b_{ij}}{b_{ij}}\right)^{d_{ij}} \tag{3.16}$$

A standard operation is to recast this expression as a negative log-likelihood ratio. It follows:

$$\Gamma = -2\ln(Q) = 2 \sum_{i=1}^{N_{\text{channels}}} \sum_{j=1}^{N_{\text{bins}}} (s_{ij} - d_{ij}\ln(1 + s_{ij}/b_{ij})) \tag{3.17}$$

This test statistic has the advantage of being accurate for small numbers of expected events and approximates a Gaussian χ^2 function for large numbers of events. For large systematic uncertainties *i.e.* of the order of the Poisson variance, an alternative test statistic, namely a Profile Likelihood Ratio, can be used in COLLIE. A description of this test statistic can be found in the COLLIE User Guide [80].

Using this test statistic definition, one can compare the test statistic value of the data with the test statistic values of the Null and Test hypotheses. However, the two latter represent only two possible outcomes and it is very unlikely for an experiment to match exactly either hypotheses. In addition, this approach is not sufficient to derive confidence intervals, hence the need to construct the probability distribution function (PDF) of the test statistic for the Null hypothesis and the Test hypothesis. To do that, the expected number of events for each hypothesis are sampled from a Poisson distribution which mean value is the original expected number of events. Furthermore, in order to take into account the uncertainties on the nuisance parameters, such as the selection efficiency, the Poisson PDF is marginalized by assuming different values of these nuisance parameters, which translates into different values of the expected number of events used as the mean value of the previous Poisson distribution. By specifying the distribution of the possible values for the selection efficiency, *a.k.a.* prior, the marginal PDF can be obtained by integration. COLLIE performs this integration via Monte-Carlo sampling of the specified priors. As a result, each hypothesis is now described by a distribution of possible outcomes, which is also referred to as the prior predictive ensemble for the hypothesis. Each of this outcome can be evaluated by a test statistic Γ, which, in the end, describes the PDF for this ensemble P(Γ). An example showing the Null and Test PDF is presented in Figure 3.18.

Though not rigorous, confidence levels and p-values have similar interpretations in our use case (where processes are physically bounded by zero). Thus, a confidence level CL can be computed by considering all the outcomes, in the pseudo-data, less signal-like than a reference value (the observed data for instance):

$$\text{CL}_\text{H} = \int_{\Gamma_{\text{ref}}}^{\infty} P(\Gamma)\text{d}\Gamma \tag{3.18}$$

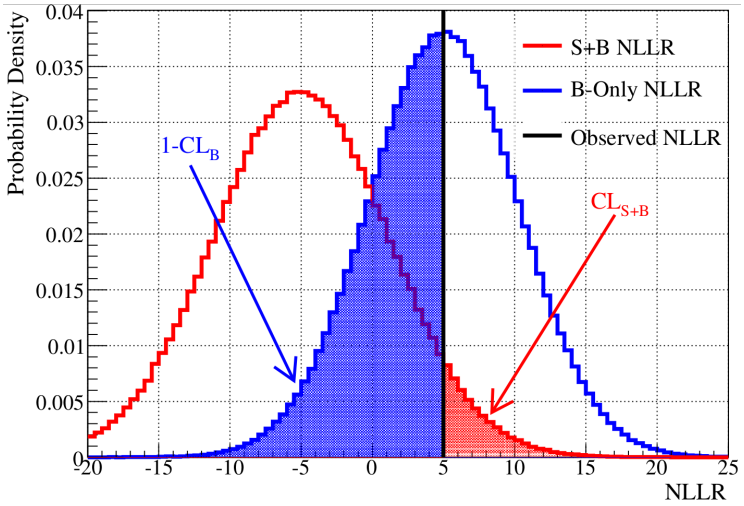

Figure 3.18 – Probability distribution function of a Negative-Log Likelihood Ratio test statistic (or Γ) for the Test hypothesis (in red) and the Null hypothesis (in blue). The values of the confidence levels CL_{S+B} and 1-CL_B for an observed outcome are equal to the blue and red shaded areas respectively.

In other words:

- CL_{S+B} or p-value for the Test hypothesis, is the probability for the Test hypothesis to produce an outcome more background-like than the observed data. On Figure 3.18, it represents the fraction (in red) of the Test (S+B) PDF with a test statistic value higher than that of the observed data (by construction in COLLIE, background-like outcomes have higher/positive test statistic values than signal-like outcomes).
- CL_B is the probability for the Null hypothesis to produce an outcome more background-like than the observed data. However, the p-value for the Null hypothesis, or 1-CL_B, is used to quantify the significance of a signal excess and to reject the background only hypothesis. This is represented, in blue in Figure 3.18, by the fraction of the Null (B-only) PDF with a test statistic value lower than that of the observed data.

In order to extract exclusion limits for model parameters, COLLIE made the choice to rely on the modified-Frequentist construction or CL_S. This more conservative approach helps guard against large downward data fluctuations or poor background modeling. Instead of basing the exclusion on a constraint on CL_{S+B} only, the quantity to constrain is the following:

$$CL_S = \frac{CL_{S+B}}{CL_B} \tag{3.19}$$

However, CL_{S+B}, as well as CL_B, both depend indirectly on the signal rate s through the test statistic definition. That's why the PDFs of the prior predictive ensembles must be re-evaluated for different values of the signal parameters. Actually, the definition of the signal exclusion at a confidence level 1-α is defined as:

$$CL_S(s(x_{\text{limit}})) < \alpha \tag{3.20}$$

where x_{limit} is the value of the signal parameter satisfying the condition. In our search for the neutrinoless double beta decay, the exclusion limit is often expressed as a limit on the process half-life $T^{0\nu}_{1/2}$, quoted with a 90 % Confidence Level.

The different methods used by COLLIE to evaluate x_{limit}, as well as more details on the generation of pseudo-data and the treatment of uncertainties can be found in the COLLIE User Guide [80].

More recent tools, sharing the same purpose, have been developed and used by other physics experiments.

RooStats

RooStats [81] is a package for ROOT [68] based on RooFit [82]. RooStats gathers high-level statistics tools which utilization is eased by the use of the RooFit framework. A few of the tools used to compute confidence intervals and limits are described below but before, the general philosophy of a Bayesian analysis for low statistics experiments [83] is presented.

- The Bayesian approach

  Here, the hypotheses tested are H, the hypothesis that the data observed comes only from the backgrounds contributions, and its negation $\overline{H}$, meaning the contribution from the signal process to the data is nonzero. The conditional probability for the hypothesis H (resp. $\overline{H}$) given the data is written $p(H|\text{data})$ (resp. $p(\overline{H}|\text{data})$) and can be computed according to Bayes' theorem:

$$p(H|\text{data}) = \frac{p(\text{data}|H) \cdot p_0(H|I)}{p(\text{data})} \qquad (\text{resp. for } p(\overline{H}|\text{data})) \tag{3.21}$$

  where $p(\text{data}|H)$ is the conditional probability of observing these data assuming the hypothesis H to be true and $p_0(H|I)$ is the prior probability for H (I represents additional information, known from other experiments and model predictions). In addition, $p(\text{data})$ can be rewritten as:

$$p(\text{data}) = p(\text{data}|H) \cdot p_0(H) + p(\text{data}|\overline{H}) \cdot p_0(\overline{H}) \tag{3.22}$$

  If S is the expected number of signal events and B the expected number of background events, one can decompose $p(\text{data}|H)$ and $p(\text{data}|\overline{H})$ as follows:

$$p(\text{data}|H) = \int p(\text{data}|B) \cdot p_0(B) dB \tag{3.23}$$

$$p(\text{data}|\overline{H}) = \int p(\text{data}|S, B) \cdot p_0(S) \cdot p_0(B) dS dB \tag{3.24}$$

  wherein $p_0(S)$ and $p_0(B)$ are the prior probabilities of observing S signal events and B background events, respectively.

As aforementioned, the final variable is a binned distribution of the two electrons energy sum but it can be any binned distribution, like a BDT score. Either way, the expected number of events in the i-th bin is:

$$\lambda_i = \lambda_i(S, B) = S \cdot \int_{\Delta x_i} f_S(x)dx + B \cdot \int_{\Delta x_i} f_B(x)dx \tag{3.25}$$

where $f_S(x)$ and $f_B(x)$ are the normalized Monte-Carlo templates (*i.e.* expected signal and background distributions) for the variable x, and Δx_i is the width of the i-th bin. Assuming the number of events in each bin fluctuates according to a Poisson distribution:

$$p(\text{data}|B) = \prod_{i=1}^{N} \frac{\lambda(0, B)^{n_i}}{n_i!} e^{-\lambda_i(0,B)} \tag{3.26}$$

$$p(\text{data}|S, B) = \prod_{i=1}^{N} \frac{\lambda(S, B)^{n_i}}{n_i!} e^{-\lambda_i(S,B)} \tag{3.27}$$

Hence,

$$p(H|\text{data}) = \frac{\left[\int \prod \frac{\lambda_i^{n_i}}{n_i!} \cdot p_0(B)dB\right]_{S=0} \cdot p_0(H)}{\left[\int \prod \frac{\lambda_i^{n_i}}{n_i!} \cdot p_0(B)dB\right]_{S=0} \cdot p_0(H) + \left[\int \prod \frac{\lambda_i^{n_i}}{n_i!} \cdot p_0(B)p_0(S)dBdS\right]_{S=0} \cdot p_0(\overline{H})} \tag{3.28}$$

The uncertainties can be taken into account by marginalizing over the nuisance parameter k such that:

$$p(\text{data}|B) = \int \left[\prod_{i=1}^{N} \frac{\lambda_i(0, B|k)^{n_i}}{n_i!} e^{-\lambda_i(0,B|k)}\right] p_0 dk \tag{3.29}$$

$$p(\text{data}|S, B) = \int \left[\prod_{i=1}^{N} \frac{\lambda_i(S, B|k)^{n_i}}{n_i!} e^{-\lambda_i(S,B|k)}\right] p_0 dk \tag{3.30}$$

where $p_0(k)$ is the probability density for the nuisance parameter (*e.g.* a Gaussian distribution).

In practice, for the neutrinoless double beta decay search, given the unknown nature of the neutrino, the prior on either hypotheses are chosen to be $p_0(H) = 0.5$ and $p_0(\overline{H}) = 0.5$. A possible prior for the background contribution is a Gaussian centered on the expected number of events. The prior distribution on the number of signal events can be a flat distribution, ranging from 0 (the absence of signal) to S_{max}, which is derived from the current best experimental limit. Another choice of prior can be $1/T^{0\nu}_{1/2}$ (instead of $T^{0\nu}_{1/2}$), which presents the advantage of also being bounded by 0 (if $T^{0\nu}_{1/2} \to \infty$) and $1/T^{0\nu}_{1/2,\text{max}}$ (one over the best experimental limit[e]).

[e] If the best experimental limit was not obtained with the same isotope, the choice can be made to translate it into an effective neutrino mass (assuming the light Majorana neutrino exchange mechanism) and then back into the equivalent half-life for the isotope of interest.

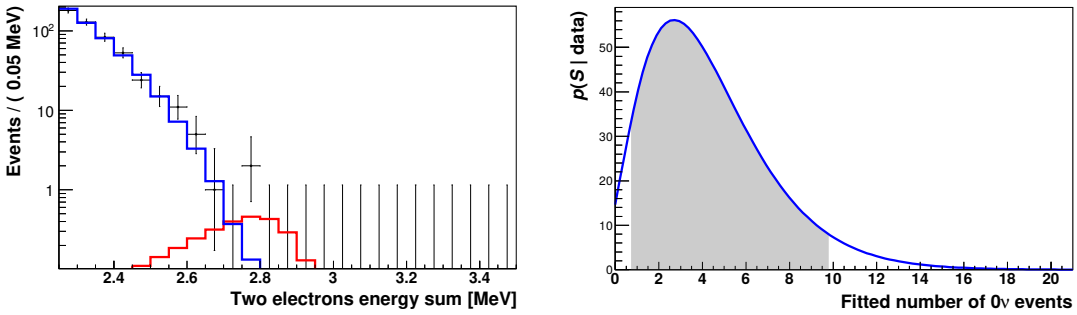

Figure 3.19 – *(left)* A pseudo-experiment with 3 $0\nu\beta\beta$ events at the end of the $2\nu\beta\beta$ spectrum. The red histogram represents the fitted signal contribution while the blue one represents the fitted background contribution. *(right)* Distribution of the posterior probability for different number of signal events hypothesized. The gray area represents a 90 % confidence interval around the maximum probability.

- Examples with pseudo-experiments

  Let's illustrate this Bayesian approach with two simple examples, composed of a $0\nu\beta\beta$ signal and a $2\nu\beta\beta$ background.

  In a first example, illustrated in Figure 3.19, we generate a pseudo-experiment containing 3 signal events, to be identified amidst the dropping $2\nu\beta\beta$ spectrum.

  As explained before, using Bayes' theorem, the probability to explain the observed data with our parameters S and B is:

$$p(S, B|\text{data}) = \frac{p(\text{data}|S, B) \cdot p_0(S) \cdot p_0(B)}{\int p(\text{data}|S, B) \cdot p_0(S) \cdot p_0(B)\ dS\ dB} \tag{3.31}$$

  This probability is then marginalized with respect to B in order to estimate the signal contribution to the observed data:

$$p(S|\text{data}) = \int p(S, B|\text{data})\ dB \tag{3.32}$$

  This formula is used to generate the posterior function shown in the right plot in Figure 3.19. The probability is maximum between 2 and 3 signal events. In this pseudo-experiment, the maximum of the posterior function is not closer to $S = 3$ because, while the two events in the [2.75;2.8] MeV bin are clearly raising above the $2\nu\beta\beta$ high energy tail, the single signal event in the [2.65;2.7] MeV bin could also very well have been explained by the background. Still, in this pseudo-experience the absence of signal can be excluded with a 90 % confidence since $S = 0$ is not included in the 90 % confidence interval, represented by the gray area under the posterior function. The two bounds, S_{lower} and S_{upper}, of this 90 % confidence interval are

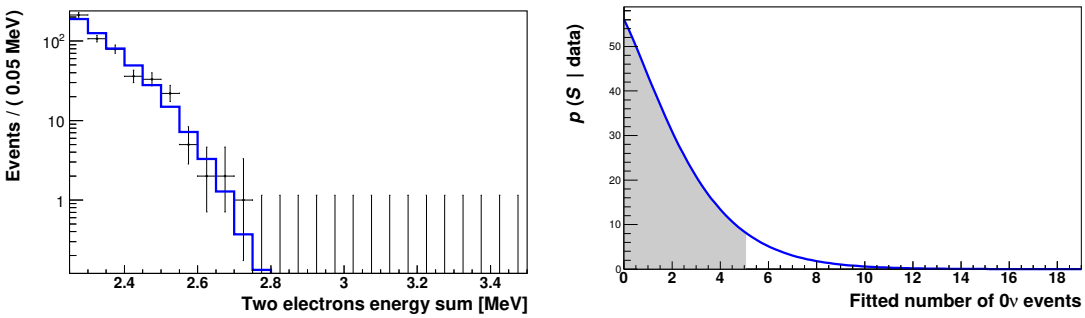

Figure 3.20 – *(left)* A pseudo-experiment with the $2\nu\beta\beta$ background but no $0\nu\beta\beta$ signal events. The blue histogram represents the fitted background contribution. *(right)* Distribution of the posterior probability for different number of signal events hypothesized. The gray area represents a 90 % confidence upper limit on the number of signal events.

defined, for a central and symmetrical interval, as :

$$\int_0^{S_{\text{lower}}} p(S|\text{data})\, dS = 0.05 \quad \text{and} \quad \int_0^{S_{\text{upper}}} p(S|\text{data})\, dS = 0.95 \tag{3.33}$$

The second example illustrates the eventuality where no signal is observed. Such pseudo-experiment can yield the spectrum visible in Figure 3.20.

In that case, a 90 % upper limit on the number of signal events can be derived by finding S_{90} which statisfies :

$$\int_0^{S_{90}} p(S|\text{data})\, dS = 0.90 \tag{3.34}$$

This integration of the posterior probability is represented by the gray area in the right plot of Figure 3.20. In this example, the positive fluctuation of the background events in the last bin ([2.7;2.75] MeV) means that the limit we would be able to set would be raised to slightly more than 5 signal events.

Coming back to RooStats, this package proposes a framework to ease the computation of limits. Several algorithms, including the Bayesian approach, are implemented and described below.

- Bayesian Calculator

  The computation of a confidence interval is done using a Bayesian approach. As explained above, the user needs to provide its model (expected signal and background distributions, the prior probability density function, etc) and the posterior probability is computed by integrating the likelihood function. The nuisance parameters are marginalized in the computation of the posterior function. The posterior function is integrated and normalized using numerical integration methods and the interval is obtained by inverting the cumulative posterior distribution.

- Monte-Carlo Markov Chain Calculator

This calculator also follows the Bayesian approach but uses the Monte-Carlo Markov Chain method to integrate the likelihood function with the prior to obtain the posterior function.

- Profile Likelihood Calculator

  It works similarly to COLLIE[f], but instead, uses a profile likelihood ratio to construct intervals based on the p-values.

- Feldman-Cousins Calculator

  The Feldman-Cousins approach is a specific case of the Neyman construction, using a likelihood ratio as its test statistic[g]. This method successfully reproduces the famous tables published by Feldman and Cousins [84], which are especially indicated for low statistics experiments.

3.3.4 Multivariate analysis

Multivariate analyses are increasingly more popular in physics data analysis. The SuperNEMO experiment, thanks to its full event reconstruction and the several inherent topological measurements, is probably the double beta decay experiment that could benefit the most from a multivariate analysis. Since the dawn of machine learning and multivariate analysis, a variety of software libraries have been developed, from Google's TenserFlow and Scikit-learn, which are versatile solutions applicable to a variety of problems, to TMVA [85], developed by and for physicists in the famous ROOT framework. The latter solution was used in this work since it proved reliable in previous particle physics classification problems and is still relevant today, despite not hosting the latest and most powerful algorithms.

Presentation of TMVA

TMVA, which stands for Toolkit for Multivariate Data Analysis, is a toolkit, integrated into the data analysis framework ROOT. It provides a large variety of multivariate classification and regression algorithms, improved by statisticians and physicists over time. A common physics data analysis concern is the discrimination of signal events from background events. This challenge is a typical classification problem, where the algorithms learn to discriminate two populations of objects based on the input variables they are given. The different classifiers proposed by TMVA are widely configurable and a user interface makes the performance evaluation easier. The choice to focus on Boosted Decision Trees (BDTs) is motivated in the next section.

---

[f] Wilk's theorem, stating that -2log(Q) follows a χ^2 distribution, is assumed to be valid.

[g] Like COLLIE, this choice is motivated by the Neyman-Pearson lemma, which states that the likelihood ratio test for two hypotheses is the most powerful test in achieving a given significance. In other words, it is the criterion providing the highest signal purity for a given signal efficiency.

Motivation for the choice of BDTs

All classification algorithms available in TMVA were tested on a simplified model: identification of a 0ν signal among a 2ν background. The algorithms were configured with the tutorial out-of-the-box settings. The results are reported on Figure 3.21.

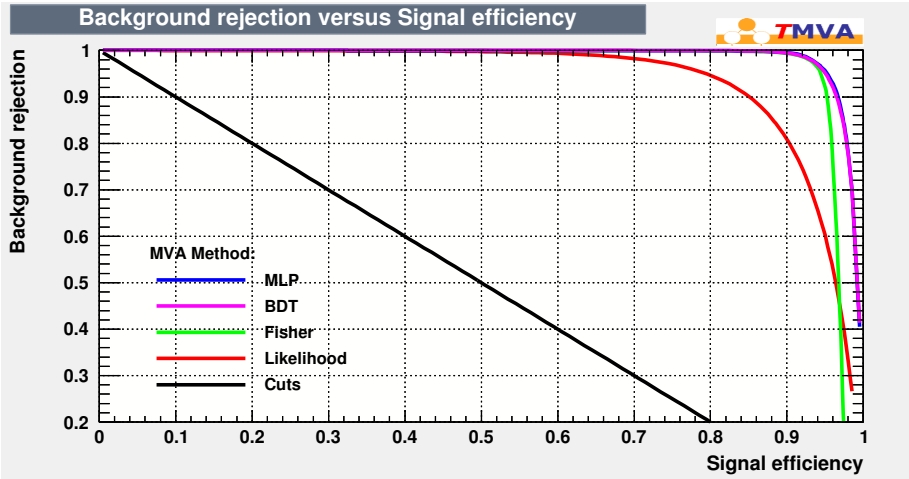

Figure 3.21 – Comparison of the background rejection as a function of the signal efficiency for different classifiers. The values of the confidence levels CL_{S+B} and 1-CL_B for an observed outcome are equal to the blue and red shaded areas respectively.

The curves presented in Figure 3.21, are also called ROC curve (Receiver Operating Characteristic), and, in classification problems, displays the background rejection power of the algorithm as a function of the signal efficiency. The ideal classifier would have a maximum rejection efficiency for a maximum signal efficiency. The comparison of these ROC curves shows that for any given signal efficiency, the BDT and MLP[h] (neural network) algorithms would yield the highest background rejection. It boils down to these two algorithms. However, neural networks, though notoriously more efficient, may require a fine tuning of the algorithm to yield the best results. BDTs are much more stable and the simplest configurations can sometimes already greatly improve the physics analysis. BDTs are also much more convenient if one wants to check the selection process since individuals trees are readable and easily understandable.

Explanation of the BDT

The first step in training a BDT is to provide an ensemble of events composed of signal and background events, each described by a set of variables. For the neutrinoless double beta decay search, such a variable is the two electrons energy sum for instance (which distribution is expected to be different for signal and background processes). The algorithm

[h]MLP stands for MultiLayer Perceptron and is the fastest and most flexible of the three neutral network implementations proposed in TMVA.

then looks for the cut on a variable which optimizes the signal/background separation. This separation can be quantified by a variety of criteria. The available criteria are:

- Gini index: $p \cdot (1-p)$ [i]
- Cross entropy: $-p \cdot ln(p) – (1–p) \cdot ln(1–p)$
- Misclassification error: $1 - max(p, 1-p)$
- Statistical significance: $S/\sqrt{S+B}$

The cut value is chosen as the one providing the highest increase in the separation index between the original sample and the sum of the indices of the two resulting subsets, weighted by their relative fraction of events. The granularity of the search for the optimal cut value is configurable. This process is then repeated on the two resulting samples, thus developing a tree-like structure, as illustrated in Figure 3.22. The subsets of events at each step are also called nodes. The tree is developed this way until it reaches a maximum specified depth or the number of training events in the node becomes too low. Finally, the events are classified as signal or background based on the majority of events in the final node (or leaf) to which they belong.

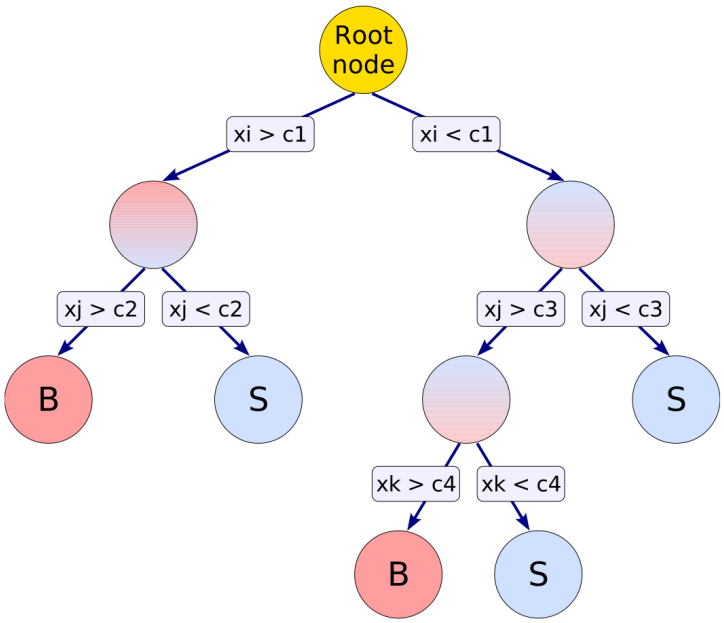

Figure 3.22 – Principle of a decision tree. At each node, the data is split based on the discriminating variable that best separates signal from background events. This process is repeated until a stopping criterion is reached. The final nodes are considered as signal or background nodes, depending on the majority of events they contain.

[i] The purity is defined as $\frac{S}{S+B}$ but all criteria are symmetric: they are maximum for p=0.5 (perfectly mixed) and fall to 0 for pure subsets.

However, such a tree is quite sensitive to statistical fluctuations in the training sample. For instance, if two cuts on different variables yield equivalent separation gain for the first node but one is favored due to statistical fluctuations, this can result in a whole different cut sequence for the rest of tree. That's why constructing a forest of trees helps the algorithm to be more robust against statistical fluctuations. To do so, the events misclassified in a first tree are assigned higher weights with the hope that a new tree, using the same sample but with different event weights will better classify these events. This procedure is called boosting. There are several ways to set the misclassified event weights, the most popular being the AdaBoost algorithm (Adaptive Boosting). This method consists in multiplying the misclassified events by a boost weight α depending on the previous tree misclassification rate ϵ, as follows:

$$\alpha = \frac{1-\epsilon}{\epsilon} \tag{3.35}$$

Several hundreds of classifiers can thus be constructed, considerably improving the stability and separation performance, compared to a single decision tree. Indeed, instead of relying on a single binary decision, an event will be tested against all classifiers and a weighted average will be computed, called the score:

$$\text{BoostScore}(\mathbf{x}) = \frac{1}{N_{\text{trees}}} \sum_{i}^{N_{\text{trees}}} \ln(\alpha_i).h_i(\mathbf{x}) \tag{3.36}$$

where $\mathbf{x}$ is the set of input variables and $h_i(\mathbf{x})$ is the result of the i-th classifier, equal to +1 if the event ends up in a signal leaf and -1 if it ends up in a background leaf. Consequently, signal-like events will have positive scores (ideally equal to 1) while background-like events will tend to have negative scores. In addition, the user can configure the learning rate β, which modifies the boost weight $\alpha \to \alpha^{\beta}$ and often improves the performance by forcing a "slower learning". Alternatively, the signal purity of the node can be used as the weight, this is the Real-AdaBoost algorithm. Other boosting approaches, like the Gradient Boosting or the Bagging, are described in details in the TMVA User Guide [85].

Though boosting makes the algorithm lose in interpretability, it is still possible to look at individual classifiers to get a better grasp on the process. Furthermore, the variable ranking can help understand the choices made by the algorithm. Indeed, one of the advantages of BDTs is that the user can provide a large number of input variables, but the variables offering little to no discrimination power will be ignored. A variable ranking is proportional to how often the variable is used to split a node, to the separation gain-squared it has achieved and to the number of events in the node. However, caution should still be kept when comparing variables ranking. For instance, if two variables offer similar separation power but one is only slightly better, the second may rarely be used because it discriminates against the same population of events. The high ranking achieved by the first variable could also have been achieved by the second if it had been removed. In other words, a good variable might get a low ranking because it is eclipsed by a slightly better variable.

Check for overtraining

One of the shortcomings of machine learning algorithms is the overtraining. This phenomenon can seem paradoxical at first and occurs when the algorithms are trained on samples with too few events compared to the many degrees of freedoms they are provided. In practice, it means that a BDT performance can be degraded if too many parameters are available to the trees or that these trees are too deep. In this case, the algorithm trains on statistical fluctuations of the training sample which are not statistically significant, as illustrated in Figure 3.23. This training, if applied on a similar sample, but with different statistical fluctuations, would not perform well.

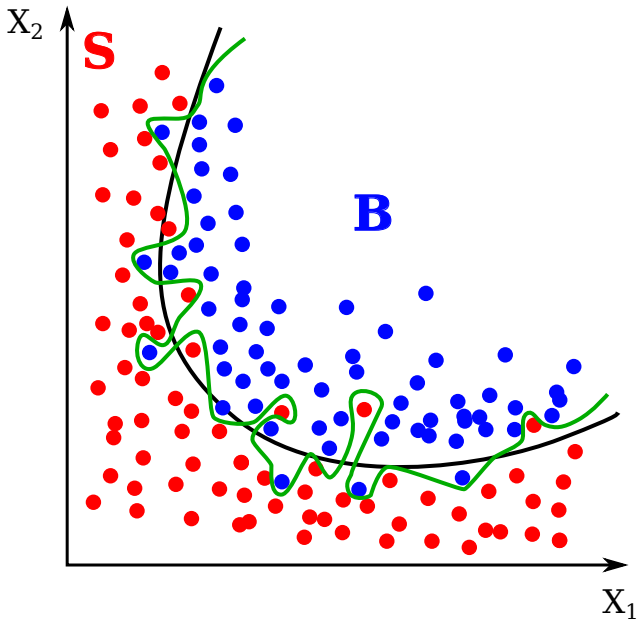

Figure 3.23 – Illustration of the overtraining. The signal events, in red, and the background events, in blue, are distributed in the parameter space. The black line represents a reasonable choice of cuts while the green line shows a combination of cuts resulting in overtraining.

One way to be protected against overtraining is to divide the data sets into different samples and to check that the results of the training are stable, regardless of the samples used for the training or the application. In particular, TMVA compares the response of the BDT, when applied to two different samples (the training sample and a test sample), thanks to a Kolmogorov-Smirnov test. This test determines the probability that the two samples come from the same distribution. If two BDT responses are dissimilar, which is the case when overtraining occurs, the Kolmogorov-Smirnov test will detect it as a low probability. Overtraining can be limited by increasing the size of the training samples or, alternatively, by reducing the complexity of the trees.

Chapter 4

Study of the magnetic field in the SuperNEMO demonstrator

This Chapter summarizes a variety of studies related to the magnetic field in SuperNEMO. The use of a magnetic field is first motivated. The technical implementation of the magnetic field, as well as the design of the magnetic shieldings, are reminded. The results of a study, based on Monte-Carlo simulations, aiming at finding the optimum value of the magnetic field, are then presented. The magnetic shieldings properties were investigated in more details. In particular, their effectiveness and impact on the external magnetic field were evaluated using small scale magnetic coils. Finally, the impact of a non-uniform magnetic field, confirmed by dedicated simulations, on the event reconstruction is estimated.

4.1 The SuperNEMO magnetic field

4.1.1 Motivation

A magnetic field, together with a tracking chamber, was already implemented in NEMO-3. The 25 G magnetic field applied in the SuperNEMO tracking volume will provide an electron/positron discrimination. Indeed, this magnetic field is high enough to bend the paths of the few MeV electrons and positrons of interest for SuperNEMO, without preventing them from reaching the calorimeter. It is, however, not high enough to impact significantly neither the few muons nor the α particles expected to be detected by the tracker. Due to their much higher momenta, they will instead leave straight tracks in the wire chamber. In practice, this magnetic field is mainly used to identify and reject the electron-positron pairs created by high energy γ's, themselves emitted after a neutron capture. It is also very useful to better identify the crossing electron events, mostly coming from a ^{212}Bi contamination on the surface of the calorimeter, as explained in Section 3.2.4. For instance, as shown in Figure 4.1, NEMO-3 observed three events in the [2.8;3.2]MeV region of interest in the one electron one positron channel and two events, induced by high energy γ's from neutron capture, with energies higher than 4 MeV.

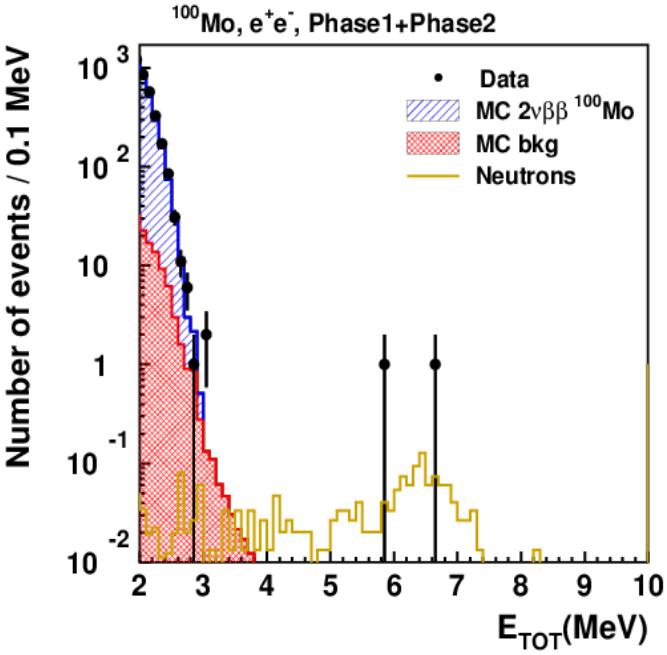

Figure 4.1 – Total energy spectrum in the one electron one positron channel from NEMO-3 with a 35 kg.y exposure to ^{100}Mo [86]. Three events were observed in the [2.8;3.2]MeV energy window and two events with energies higher than 4 MeV.

4.1.2 Design of the magnetic coil

The design of the SuperNEMO magnetic coil was briefly addressed in Section 2.1.5 and a drawing of the coil and its support frame was presented in Figure 2.18. The coil is composed of 200 turns of 10×10 mm square copper rods, with a 16 mm step. It is surrounded by 10 mm thick pure iron plates, serving as magnetic field return yokes. Its overall dimensions are 6097×2198×3483 mm, for a total weight of around 9 tonnes.

4.1.3 The magnetic shielding

The photomultipliers are highly sensitive to the presence of a magnetic field. As will be shown later, even a magnetic field as low as 1 G can greatly impair the performance of the photomultipliers by preventing the low energy photoelectrons from reaching the first dynode. That's why magnetic shieldings were designed to protect the optical modules. Two similar designs, one for 5" PMTs and one for 8" PMTs were developed. The mechanical design of the 8" calorimeter blocks is presented in Figure 4.2. They are made from 3 mm thick pure iron sheets then folded and laser-welded in their final form. The iron was machined using only laser cutting and welding to preserve the radiopurity of the materials. The shieldings have all underwent an annealing process in order to enhance their magnetic properties. As explained before, the calorimeter modules have been assembled to form the calorimeter walls. The magnetic shieldings are separated by 10 mm acrylic spacers (PMMA). The idea behind this approach is not to stop the magnetic field but instead to redirect it around the shielded volume, thanks to the shieldings high magnetic permeability. A better magnetic shielding could thus be achieved with mu-metal, which

has an even higher magnetic permeability, but which is also much more expensive and less radiopure.

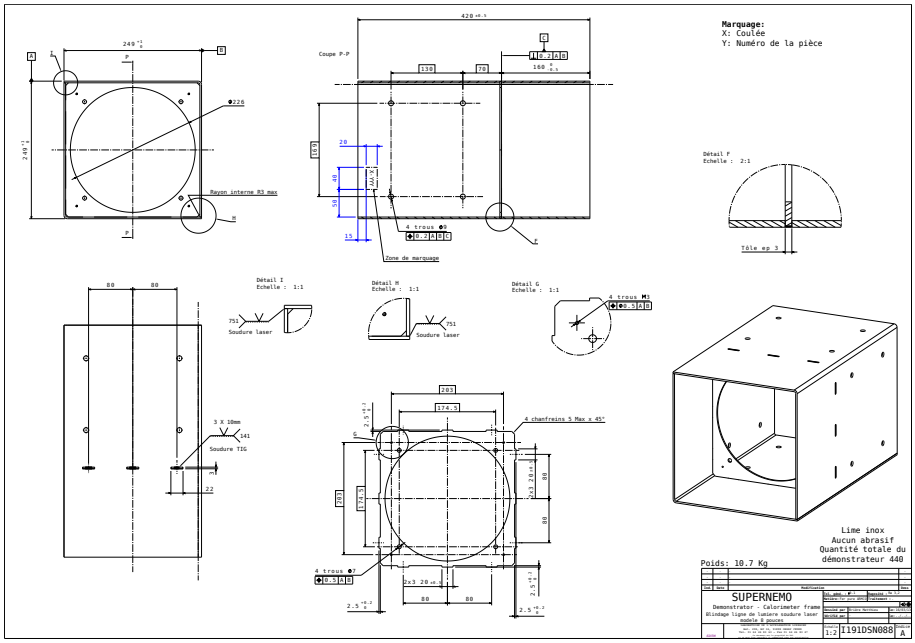

Figure 4.2 – Mechanical design of a magnetic shielding for 8" optical modules. A shielding has a 249 mm side and a 420 mm length.

4.2 Optimization of the SuperNEMO demonstrator magnetic field

The value of the magnetic field it is possible to apply is only limited by the electric current fed to the coil. With a dedicated power supply delivering a few tens of Amperes, the magnetic field applied could be as high as 50 G. Above this value, low energy electrons would struggle reaching the calorimeter and the coil would start to generate quite some heat. Using Monte-Carlo simulations, it is possible to find the value of the magnetic field that would optimize the detector sensitivity.

4.2.1 Conditions of the simulation

The simulations and the event reconstruction were performed with an earlier, yet very similar, version of the software presented in Section 3.1. The goal of this study was to evaluate the impact of the magnetic field on the $0\nu\beta\beta$ events reconstruction efficiency. In order to better understand the SuperNEMO charge identification capabilities, a first study was performed with single electron events.

4.2.2 Single electron charge reconstruction

The electrons are simulated with a uniformly distributed random energy between 0 and 3 MeV. The origin vertex is randomly generated in the source bulk and the electrons

are emitted isotropically. The events undergo the reconstruction procedure described in Section 3.1.2. The Particle Identification module was not yet developed at the time of this study so the event selection was performed with cuts on the final reconstructed event. One of the parameter of interest in this study is the reconstruction efficiency, which is defined as the fraction of events fulfilling a given set of criteria among the total number of events simulated. Simulating first 10^5 electrons in the absence of a magnetic field, the reconstruction efficiency, as a function of the selection criteria applied is presented in Table 4.1.

Selection criteria	Reconstruction efficiency
One calorimeter block triggered (>150 keV)	67 %
One cluster with more than 3 tracker cells	65 %
One reconstructed track with an associated calorimeter	52 %

Table 4.1 – Single electron reconstruction efficiency without magnetic field.

These criteria add up such that more than half of the electrons generate interesting events *i.e.* events where the particles energies can be measured. At this point, no requirement on the reconstructed charge is applied. As explained earlier, the clusters of tracker cells are fitted with helices and lines and only the best fit is considered. Assuming the electrons travel from the source to the calorimeter, the negative or positive helicity of fitted helices provides the charge of the particle. If the best track fit is a line, the particle charge is labelled as undefined. Among these 52 % of reconstructed events, it is then interesting to look at the distribution of the reconstructed charges. Figure 4.3 shows the proportion of electrons reconstructed with a negative, a positive or an undefined charge, as a function of their simulated energy. Since electrons should travel in straight lines in the absence of a magnetic field, the fact that only a minority of electrons are reconstructed as such can be surprising. However, looking at these events in more details reveals that multiple scatterings occur far more often than not. Thus, even if the electrons are only slightly deflected, it is enough for an helix fit to be preferred over a straight line fit (better χ^2/ndof). In addition, since scatterings equiprobably deflect electrons to the left or to the right, the electrons are reconstructed with a negative or a positive charge with the same probability. Finally, one can notice that percentage of tracks reconstructed as straight line increases with the electrons energy. This shows that scatterings are less likely for higher energy electrons and that even if they occur, electrons with greater momenta are less deflected by soft scatterings.

Performing the same procedure with a 25 G and a 50 G magnetic field yields the Figure 4.4 and 4.5, respectively. In a 25 G magnetic field, the charge identification is quite effective, with 83 % of the electrons reconstructed with a negative charge, regardless of their energies. The charge is reconstructed as positive for 11 % of the events because of the multiple scattering. Once again, even with a magnetic field, electrons are more likely to leave straight tracks if they have higher energies. With a 50 G magnetic field, the same

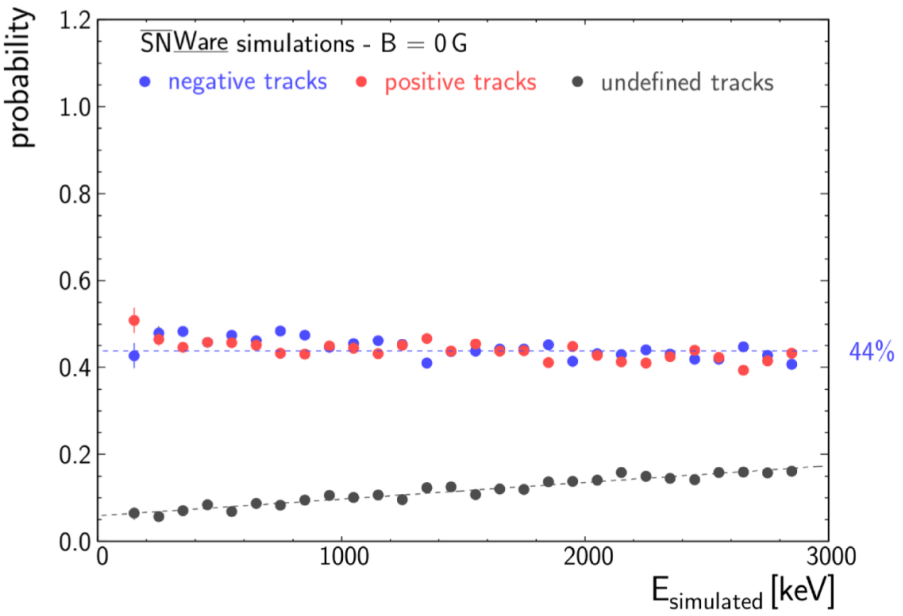

Figure 4.3 – Proportion of electrons reconstructed with a negative (blue), a positive (red) or an undefined charge (black) as a function of their simulated energy, in the absence of a magnetic field.

observations can be made, albeit amplified. From this preliminary study, it appears that the higher the magnetic field applied, the better the charge reconstruction. However, this does not take into account the reconstruction efficiency, which decreases with the magnetic field. As mentioned before, electrons submitted to a high magnetic field are less likely to reach the calorimeter walls or to even leave the source foil. The quantity of interest in SuperNEMO is rather the total electron reconstruction efficiency, which is the product of the reconstruction efficiency and the probability to reconstruct an electron with a negative charge. The evolution of these three quantities as a function of the magnetic field applied is shown in Figure 4.6.

This last Figure shows that, while the charge discrimination is better with higher values of the magnetic field, the reconstruction efficiency decreases with the latter. It results than the total electron reconstruction efficiency is optimum around 30 G (though very similar between 20 G and 50 G). Studying these single electrons events helped better understand the charge identification in SuperNEMO. However, the goal of the study is to eventually optimize the value of the magnetic field for the identification of $0\nu\beta\beta$ events.

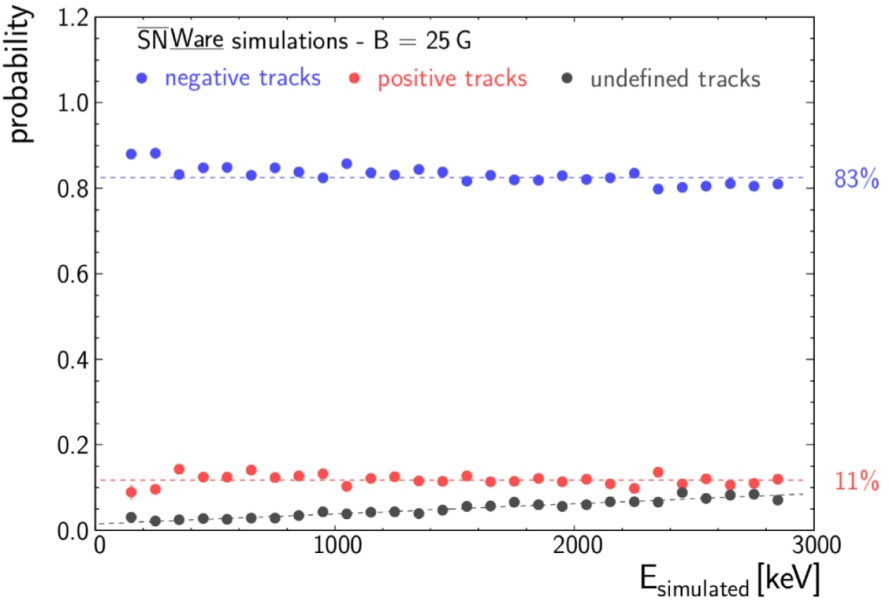

Figure 4.4 – Proportion of electrons reconstructed with a negative (blue), a positive (red) or an undefined charge (black) as a function of their simulated energy, in a 25 G magnetic field.

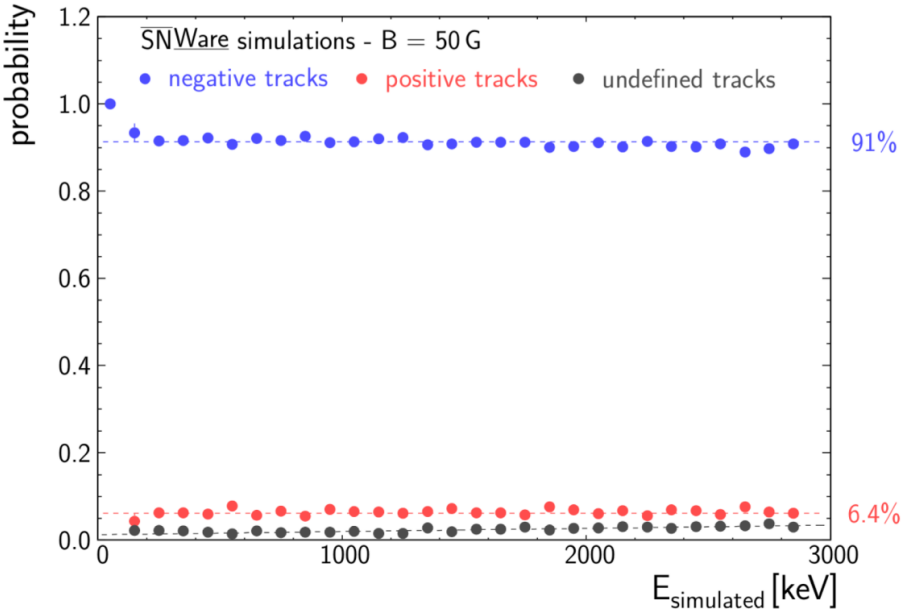

Figure 4.5 – Proportion of electrons reconstructed with a negative (blue), a positive (red) or an undefined charge (black) as a function of their simulated energy, in a 50 G magnetic field.

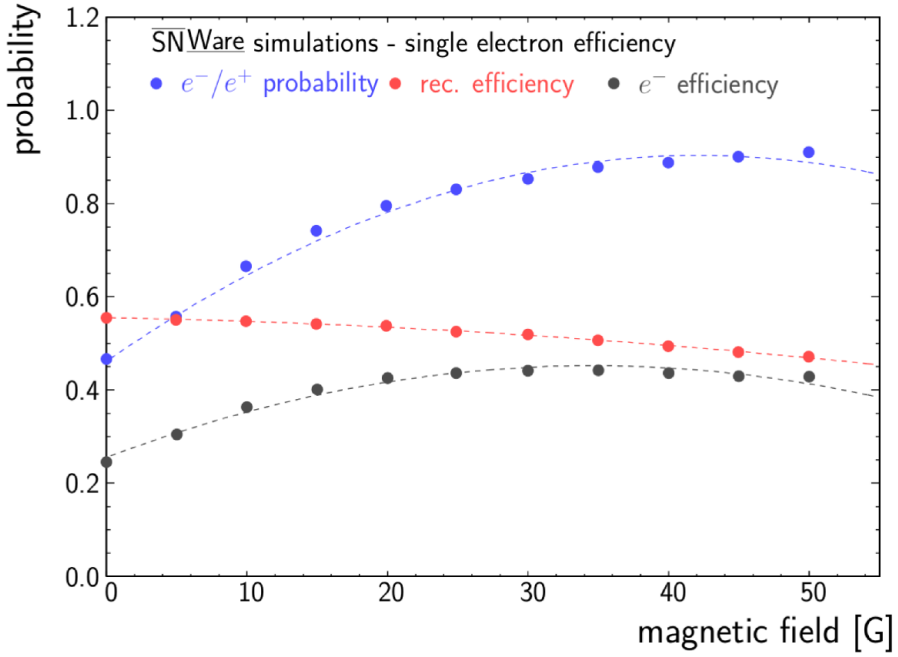

Figure 4.6 – Evolution of the negative charge identification probability (blue), the reconstruction efficiency (red) and the total electron reconstruction efficiency (black), as a function of the applied magnetic field.

4.2.3 $0\nu\beta\beta$ events reconstruction

The exact same study has thus been performed with $0\nu\beta\beta$ events. This time, we aim at correctly reconstructing both the electrons at the same time. The total reconstruction is thus expected to be lower than with single electrons events. The two electrons here share a fixed 2.998 MeV energy. Since the electrons energy is correlated, the optimum magnetic field cannot be inferred from the previous study. Figure 4.7 shows the evolution of the correct charge identification probability, the reconstruction efficiency and the total two-electron reconstruction efficiency, as a function of the magnetic field. As with single electrons, the probability to correctly identify the charge of the two electrons increases with the magnetic field, while the reconstruction efficiency decreases. It follows that the optimum magnetic field for the total $0\nu\beta\beta$ events reconstruction efficiency lies around 30 G. Very similar efficiencies can be achieved with a magnetic field ranging from 25 G to 40 G. The study presented in the next section motivated the choice for a 25 G magnetic field.

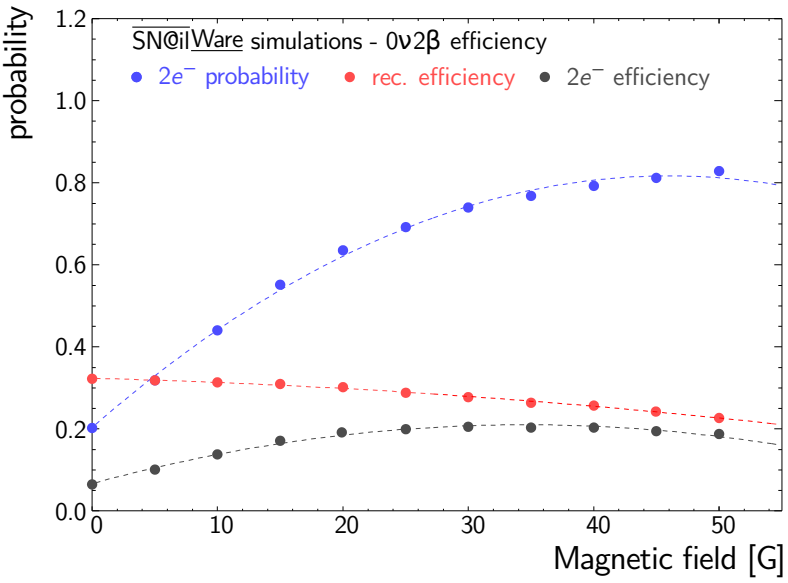

Figure 4.7 – Evolution of the correct charge identification probability (blue), the reconstruction efficiency (red) and the total two-electron reconstruction efficiency (black), as a function of the applied magnetic field.

4.3 Characterization of the magnetic shielding

As mentioned earlier, the magnetic shielding is designed to protect the photomultipliers from the magnetic field applied to the detector. A small magnetic coil was built in LAL in order to test the magnetic shielding properties.

4.3.1 The LAL coil

A photo of the magnetic coil built in LAL is shown in Figure 4.8. Its inner radius is 371 mm and its height is 898 mm. It can thus hold up to three magnetic shielding stacked vertically. The coil is made of about three hundreds turns of a 2.9 mm thick copper wire. It is closed on the top and bottom with 3 mm thick iron return yokes. A power supply can provide up to 19.5 A, translating into a maximum magnetic field of 65 G.

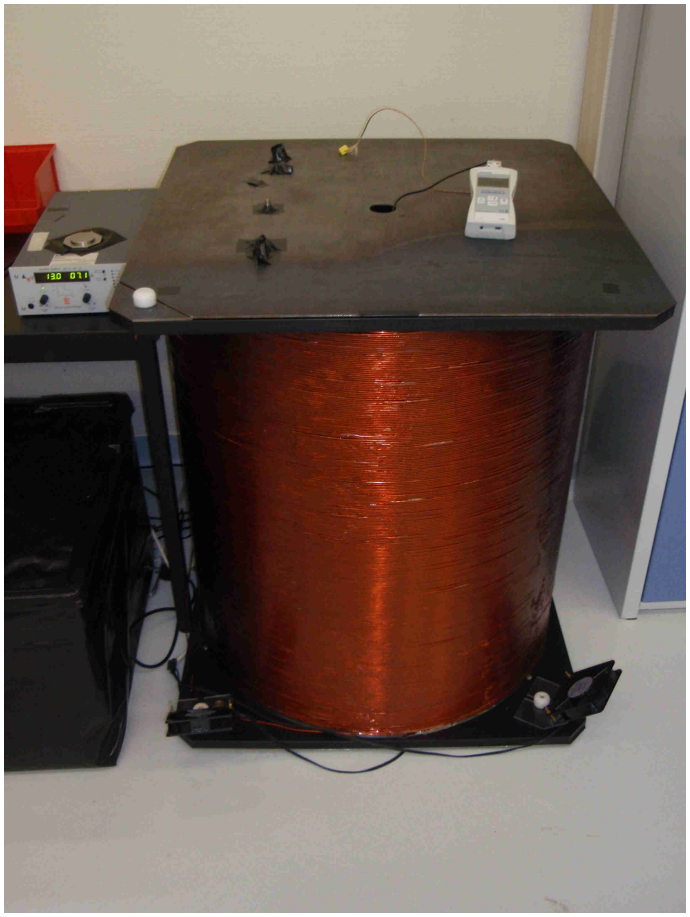

Figure 4.8 – The magnetic coild built in LAL to test the magnetic shieldings properties.

4.3.2 Effect of the magnetic field on an optical module

The coil was first used to check the shielding effectiveness of the magnetic shielding prototypes. A prototype of magnetic shielding with a design similar to the final one was equipped with an 8" PMT, coupled to a plastic scintillator wrapped in Mylar. A UV signal was generated thanks to a LED and transmitted to the plastic scintillator via an optical fiber plugged into the latter. The orientation of the PMT dynodes with respect to the magnetic field impacts the performances of the optical module. If the first dynode is oriented in parallel with the magnetic field, the photoelectrons are less likely to reach it, as illustrated in Figure 4.9. The photoelectrons collection efficiency is thus reduced and the

energy resolution is degraded as a result. To mitigate this effect, the PMT from this study, as well as every PMT from the demonstrator, were oriented dynode up *i.e.* perpendicular to the magnetic field.

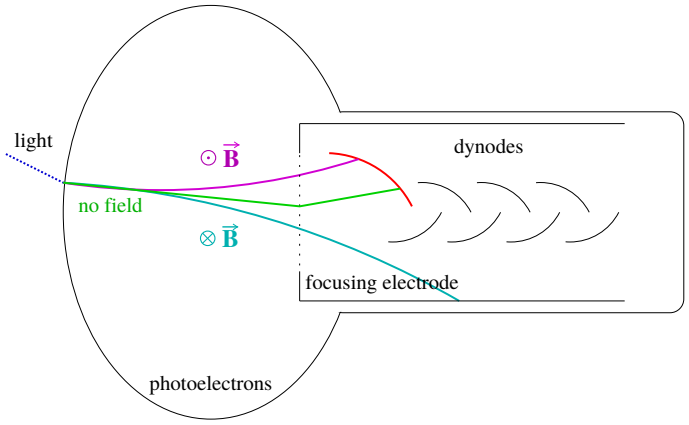

Figure 4.9 – Illustration of the photoelectrons collection in a PMT with and without a magnetic field parallel to the dynodes. The magnetic field disrupts the photoelectron collection. Adapted from [87].

The performances of the optical module described above when applying a magnetic field were measured with and without magnetic shielding. The results are presented in Figure 4.10. The left plot shows that without protection against the magnetic field, the charge collected by the PMT quickly drops as the magnetic field increases. Under barely 1 G, the collected charge is more than 3 times lower than the charge collected in the absence of a magnetic field. Thanks to the magnetic shielding, the charge collected when applying a 40 G magnetic field is only 15 % lower than the charge collected without magnetic field. The right plot shows the loss in energy resolution of an optical module protected by a magnetic shielding, as a function of the magnetic field applied. Applying a 30 G magnetic field makes the energy resolution decrease from 8 % to almost 8.5 % FHWM at 1 MeV. This loss in energy resolution can be in part compensated by increasing the PMT voltage (which we generally try to avoid because it increases the PMT noise). While the previous study showed that a 25 G or a 30 G magnetic field would yield very similar $0\nu\beta\beta$ reconstruction efficiencies, the loss in energy resolution is less important with a 25 G magnetic field. What's more, the original energy resolution can be retrieved by slightly increasing the voltage applied to the PMT. This motivates our preference for a 25 G magnetic field to be applied in the demonstrator.

4.3.3 Estimation of the magnetic shielding effectiveness

The next measurements performed aimed at quantifying the magnetic field inside the shielding, at the origin of the PMT performance decrease. The measurements were performed on genuine final magnetic shieldings without optical modules inside. A Hall magnetometer is placed in the center of the magnetic shielding, where the first PMT dynodes

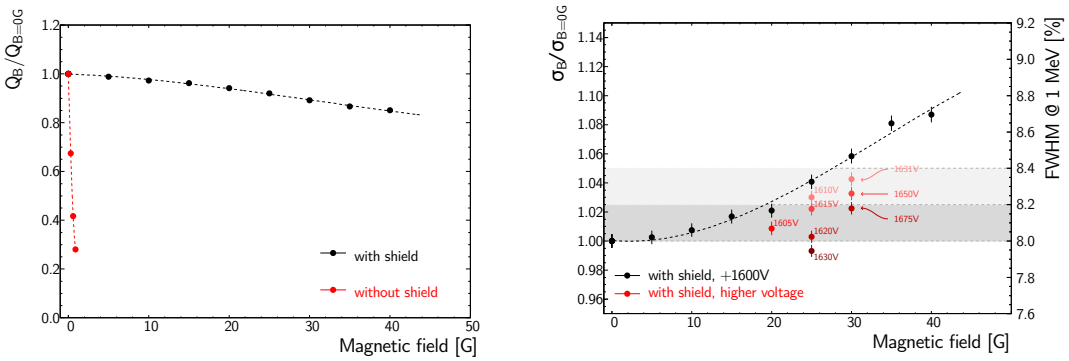

Figure 4.10 – *(left)* Ratio of the PMT charge collected for different magnetic field applied, over the charge collected at 0 G. The red line shows that the PMT performances without magnetic shielding plummet as the magnetic field barely reaches 1 G. The black line illustrates how the magnetic shielding is able to protect the PMT, even with magnetic fields as high as 50 G [89]. *(right)* The black line represents the evolution of the energy resolution of a PMT protected by a magnetic shielding, as a function of the magnetic field applied. The red dots show how the loss in energy resolution can be compensated by applying a higher voltage to the PMTs [89].

would be. The evolution of the magnetic field measured inside a single magnetic shielding, as a function of the magnetic field applied is shown in Figure 4.11. The blue curve, labelled first magnetization, shows this evolution for a shielding never exposed to a magnetic field before. It expectedly starts near zero when no magnetic field is applied and increases up to 0.9 G for the highest magnetic fields applied. The green curve, labelled second magnetization, shows the exact same measurement but performed after the first magnetization. This time, the magnetic field inside the shielding is no longer zero even if no magnetic field is applied. Instead, it starts at opposite values of the field to which it was previously subjected. Unfortunately, this phenomenon does not help to reduce the magnetic field seen by the probe as the applied magnetic field increases. Two main conclusions can be drawn from these measurements :

- the magnetic shieldings do not perfectly protect the PMTs from the external magnetic field. Up to 1 G can be measured inside the shieldings for a 40 G magnetic field applied.
- the pure iron shieldings unexpectedly exhibit what looks like a diamagnetic behavior. After being subjected to a magnetic field, the residual magnetic field measured inside the shielding is opposite to the original magnetic field.

A more logical explanation would originate from the iron natural ferromagnetism. As the external magnetic field is redirected through the shieldings walls, the iron becomes magnetized in the same direction. When the external magnetic field is removed, the iron shielding remains magnetized and part of its field lines, similarly to a magnet, loop through the shielding, thus inducing a small magnetic field, opposite to the originally applied magnetic field. This is illustrated in Figure 4.12.

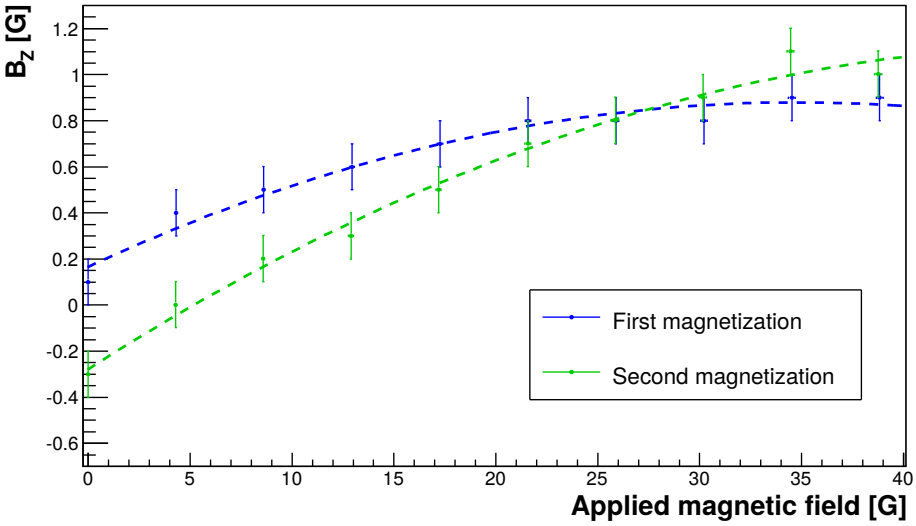

Figure 4.11 – Evolution of the magnetic field measured inside a single magnetic shielding as a function of the magnetic field applied.

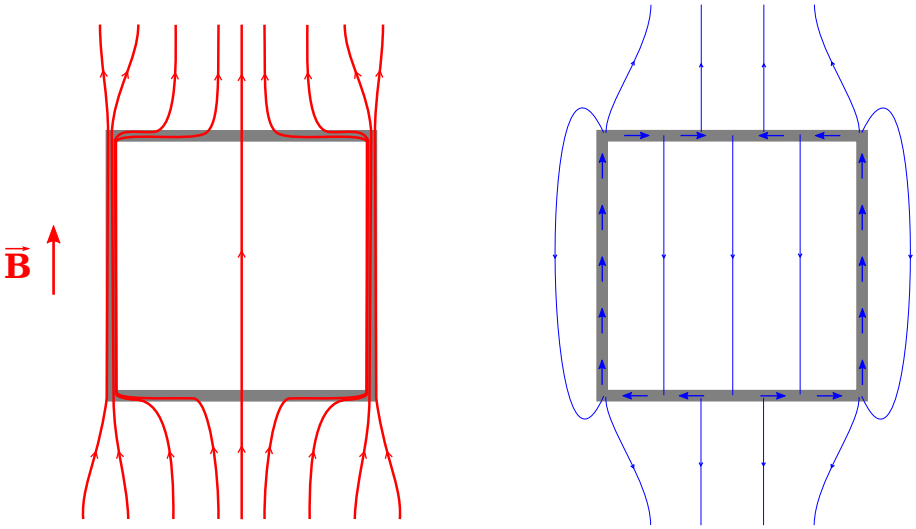

Figure 4.12 – The gray square represents the magnetic shielding seen from the front. *(left)* An external magnetic field is applied and the field is redirected through the shielding walls. *(right)* The external magnetic is removed. The iron acquired a magnetization (illustrated by the blue arrows). Similarly to a magnet, the shielding generates its own magnetic field. Part of this field loops through the shielding.

Fortunately, this ferromagnetic behavior means that we can take advantage of the magnetic hysteresis to cancel the field inside the shielding. The idea is shown in Figure 4.13. By first ramping up to a higher magnetic field and then ramping down to the desired external magnetic field, the residual magnetization can be amplified and used to cancel the magnetic field inside the shielding. This shows that despite their imperfect shielding power, the ferromagnetic properties of the pure iron shielding can in theory be used to obtain a perfect magnetic shielding. For instance, the red curve in Figure 4.13 shows that first ramping up to a ∼35 G magnetic field, then ramping down to the desired 25 G

magnetic field, allows the cancellation of the magnetic field inside of the shielding.

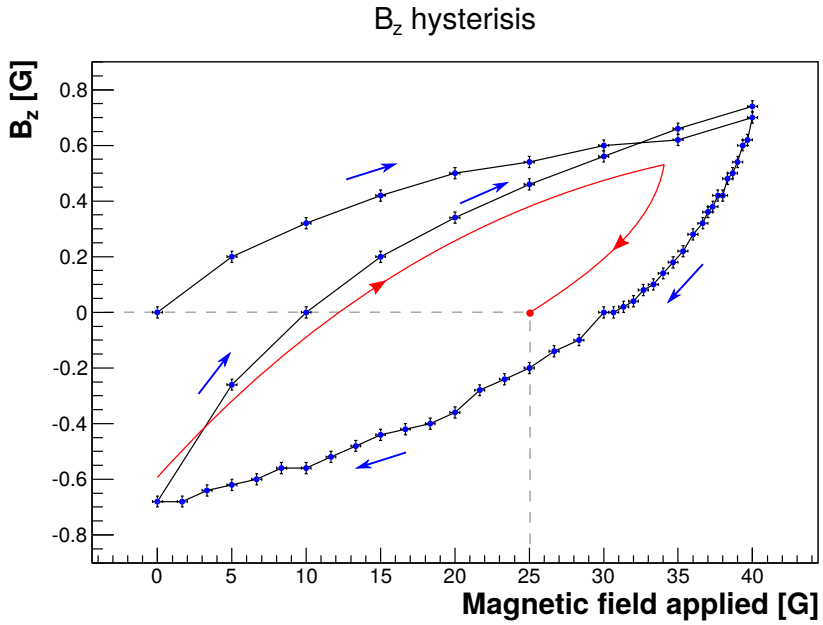

Figure 4.13 – Illustration of the hysteresis phenomenon in a pure iron magnetic shielding. The blue points represent the magnetic field measured inside the shielding as a function of the applied magnetic field. The blue arrows show the chronology of the measurement, starting at 0 G measured in the absence of a magnetic field. Ramping up to 40 G, the magnetic field measured inside the shielding reaches almost 0.8 G. Ramping down, the curve does not follow the same path due to the magnetization the shielding has acquired. This magnetization helps cancel the magnetic field inside the shielding. When the magnetic field applied is removed, a 0.7 G magnetic field in the opposite direction is measured. Ramping up again, the magnetization obtained with a 40 G magnetic field is maximum, so it cannot further oppose the internal magnetic field than during the first magnetization. Actually, once the first magnetization has occured, repeating this process of ramping the magnetic field up and down would yield the same measurements *i.e.* following the hysteresis loop. The red curve illustrates the procedure to follow to achieve a 0 G magnetic field inside the shielding while an external 25 G magnetic field is applied.

The measurements presented in this section were performed with a single magnetic shielding. Stacking the magnetic shieldings together, like they are in the calorimeter walls, might make things different.

4.3.4 The prototype coil in LPC

A prototype coil was built in LPC in order to check the mechanical feasibility of the design proposed (Figure 4.14). Incidentally, this fully functional prototype can host up to 9 magnetic shieldings. This is particularly useful to study the collective behaviour of the latter. The coil uses the NEMO-3 copper rods. It is composed of 80 loops with a 3 mm step. The return yokes are 10 mm thick iron plates. Its dimensions are 1255×756×1430 mm, which means it can host 9 magnetic shieldings in a 3×3 configuration. This setup allows to generate up to a 40 G magnetic field.

Figure 4.14 – Photo of the LPC prototype coil.

4.3.5 Shielding effectiveness with multiple shieldings

Once again, a Hall magnetometer is used to measure the field inside the shieldings when an external magnetic field is applied. The nine shields studied are spare shielding similar in all respects to the magnetic shieldings used for the construction of the calorimeter.

First, three magnetic shieldings are stacked vertically in a 1×3 configuration. The magnetic field is measured in the middle shielding, where the PMT dynodes would be, if equipped with an optical module. The results are presented in Figure 4.15. Three configurations are compared: a single shielding, three shieldings stacked vertically with 10 mm spacers (like in the demonstrator) and three shieldings stacked vertically without spacers. The evolution of the magnetic field inside a single magnetic shielding is similar to the measurements performed with the LAL coil. Adding shieldings above and below the same shielding appears to worsen the protecting power of the central shielding. With spacers, the magnetic field to which a PMT would be subjected when a 25 G is applied, reaches 1 G. For higher applied magnetic fields, the field inside the shielding starts diverging. This is even more true when the shieldings are not separated with spacers : in this configuration, the shieldings act as a single, less effective, protection against the magnetic field.

However, the protection seems to be improved when the shieldings are put side by side, in a 3×1 configuration, as illustrated in Figure 4.16. In this configuration, the magnetic field inside the central shielding is lower than with a single shielding, at around 0.2 G, regardless of the presence of spacers or not. It is thus interesting to see if the two different effects seen in the two three-shieldings configurations can compensate each other in a 3×3 configuration.

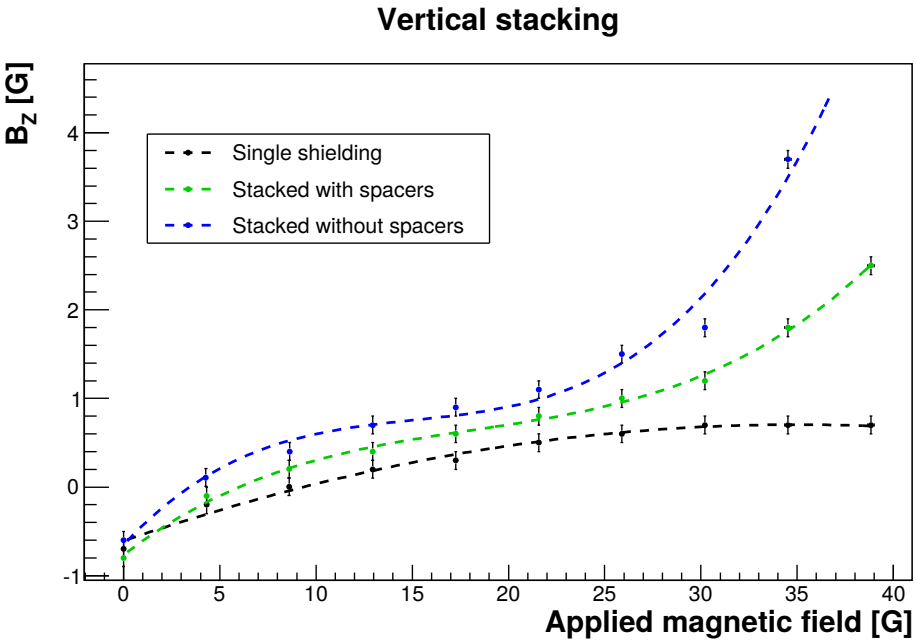

Figure 4.15 – Evolution of the magnetic field measured inside a shielding when subjected to an increasing magnetic field. The black curve represents this evolution for a single shielding. The green and blue curves show the same evolution in the middle shielding of three shieldings stacked vertically, with and without 10 mm spacers respectively.

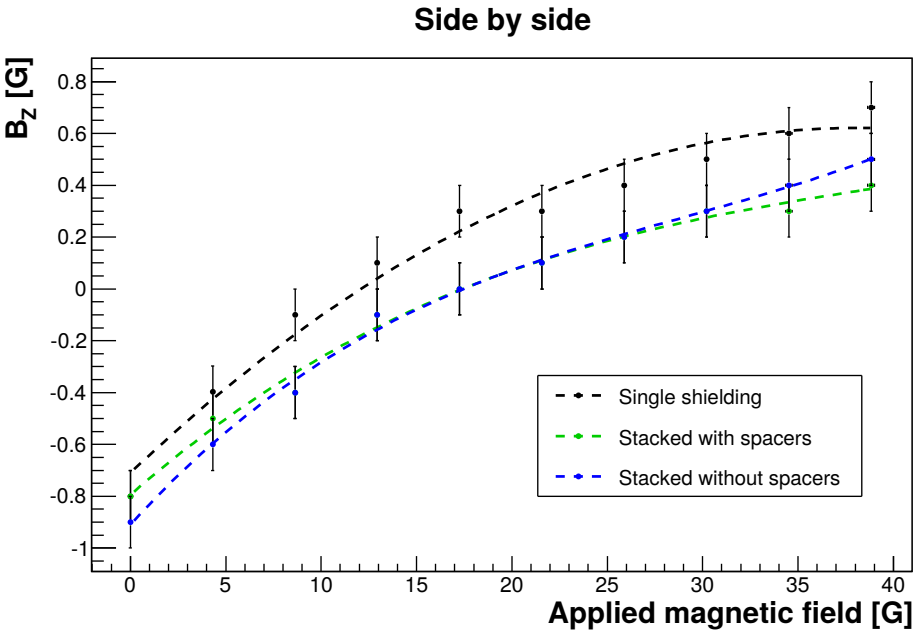

Figure 4.16 – Evolution of the magnetic field measured inside a shielding when subjected to an increasing magnetic field. The black curve represents this evolution for a single shielding. The green and blue curves show the same evolution in the middle shielding of three shieldings put side by side, with and without 10 mm spacers respectively.

The measurements inside a central magnetic shielding when surrounded by 8 others magnetic shieldings in a 3×3 configuration are reported in Figure 4.17. No divergence is

observed when high magnetic fields are applied. However, a 0.8 G magnetic field is measured inside the central shielding when a ∼25 G magnetic field is applied. Fortunately, this harmful magnetic field can still be cancelled by following the procedure described earlier.

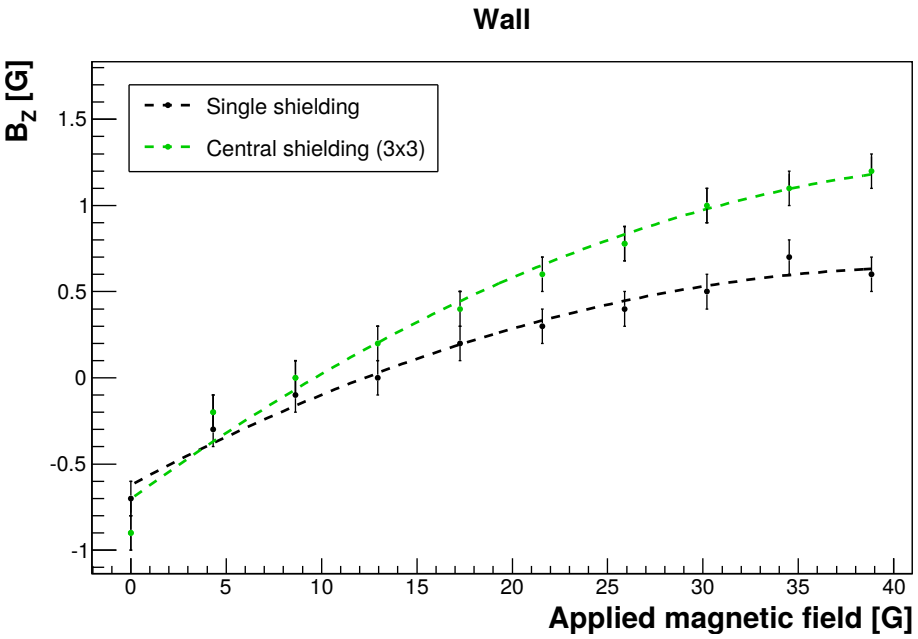

Figure 4.17 – Evolution of the magnetic field measured inside a shielding when subjected to an increasing magnetic field. The black curve represents this evolution for a single shielding. The green curve shows the same evolution in the central shielding of a 3×3 configuration, where the shieldings are separated with 10 mm spacers.

4.3.6 Influence of the magnetic shieldings on the external magnetic field

Another study allowed by this coil prototype is the estimation of the impact of the magnetic shieldings on the magnetic field outside of it. The coil is large enough so that the magnetic field in front of a single magnetic shielding, or even in front of three magnetic shieldings stacked vertically, can be measured. These measurements are summed up in Figure 4.18. The idea is here to estimate how a 25 G magnetic field is impacted by the presence of magnetic shieldings. Even a single shielding appears to affect the magnetic field up to a 30 cm distance. It evens drops as low as 10 G a few centimeters outside the shielding, where the scintillator stop. Stacking the shieldings vertically worsens the situation, especially when no spacers are used. In that case, even at distance close to where the source foil would be, the 25 G magnetic field cannot be kept. It can be assumed that adding more shieldings to the wall would impact the magnetic field even more. In addition, one must consider that the tracking volume is closed off by calorimeter walls, containing a total of 712 magnetic shieldings. These measurements portend that the magnetic field inside the demonstrator could be severely impacted.

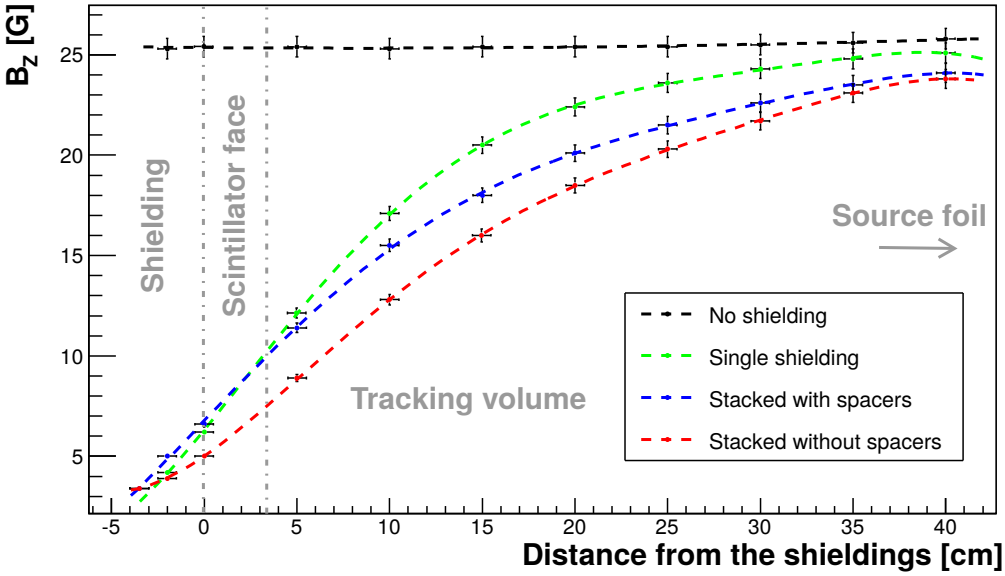

Figure 4.18 – Evolution of the magnetic field as a function of the distance from the magnetic shielding. The green curve represents the magnetic field at a distance from a single shielding. The blue and red curves represent the same evolution but with three shieldings stacked vertically, with and without spacers respectively.

4.3.7 Simulation of the magnetic field inside the demonstrator

Following the measurements presented in the previous sections, some simulations of the magnetic field inside the demonstrator were performed [90]. These simulations rely on number of approximations. Notably, the exact geometry cannot be simulated. The magnetic shieldings design is too complex for the volume required to be mapped. Instead, a few shieldings are simulated in details and the two main calorimeter walls are replaced by an equivalent homogeneous material. In addition, the saturation and the hysteresis expected to occur in the shielding material are ignored. This simulation consequently does not allow to predict the value of the magnetic field inside the shieldings. The main goal of this work was to provide a map of the magnetic field inside the tracker. A mapping of the resulting magnetic field is presented in Figure 4.19. The precision on the absolute scale is lesser than the precision on the overall shape. This shows that when a 25 G magnetic field is applied to the demonstrator, barely 10 G is expected near the source foil (red curve). What's more, the magnetic field drops at the vicinity of the calorimeter walls. This also shows that a few Gauss component of the magnetic field is to be expected perpendicularly to the calorimeter and oriented from the source foil towards the calorimeter walls. The latter should not significantly impact the electrons propagation. The lower than expected vertical magnetic field will however lessen the charge discrimination power of the demonstrator. A 25 G magnetic field near the source could in theory still be possible if the applied magnetic field is at least twice as high. Some Monte-Carlo

simulations are required to quantify the impact of this non-uniform magnetic field on the event reconstruction and the charge identification.

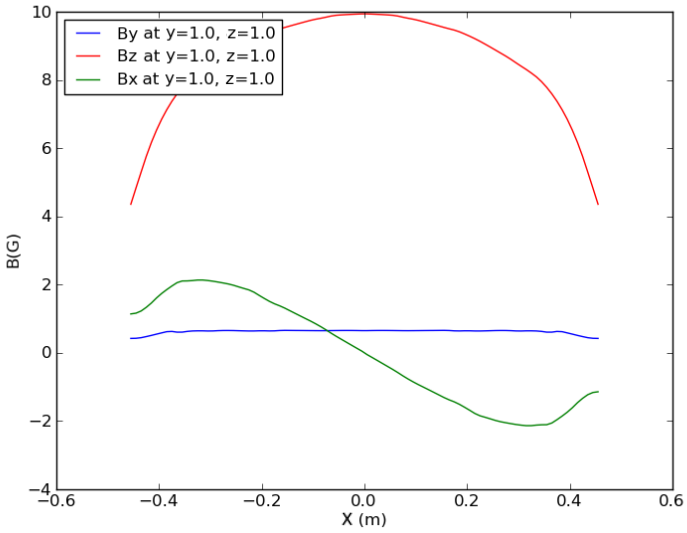

Figure 4.19 – Result of the magnetic simulation. The evolution of the vertical field B_Z along the X-axis (perpendicular to the source) is presented in red. The blue curve represents the same evolution for the horizontal component of the magnetic field parallel to the source. The green curves shows the component of the magnetic field perpendicular to the source. Adapted from [91].

4.4 Impact of a non-uniform magnetic field on the event reconstruction

Similarly to what has been presented in Section 4.2, Monte-Carlo simulations of $0\nu\beta\beta$ events have been generated under a uniform and a non-uniform magnetic field [92]. The idea is to compare the event reconstruction under these two different conditions. The study performed in this section uses a different version of the SuperNEMO software than the one used in Section 4.2. In particular, it relies on different versions of the GEANT4 software. Some differences, notably concerning the reconstruction efficiencies are thus expected. As before, $0\nu\beta\beta$ events are randomly simulated from the source foil. A 25 G uniform magnetic field is considered as well as a so-called polynomial magnetic field, which results from the fit of the measurements presented in Figure 4.18. The shape of this polynomial field is presented in Figure 4.20. The map provided in Figure 4.19 was not available at the time of this study but, scaled to a 25 G in the center of the detector, it would be similar to the shape considered here.

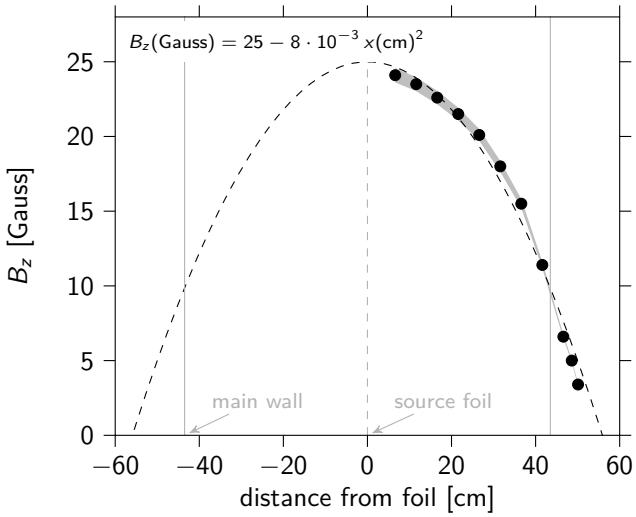

Figure 4.20 – Polynomial fit of the measured magnetic field (black dots) at a distance of the calorimeter (Figure 4.18) [92].

4.4.1 Reconstruction efficiency

First, the $0\nu\beta\beta$ reconstruction efficiencies depending on the selection criteria are presented in Table 4.2. The main difference between a uniform and a polynomial magnetic field is observed for the track extrapolation on the calorimeter. In a non-uniform magnetic field, where the field is much weaker near the calorimeter, the tracks are more likely to be successfully extrapolated to a triggered calorimeter hit. Since the field is weaker near the calorimeter, the end of electrons tracks are straighter and thus less likely to be tangent to the calorimeter wall, which actually improves the track reconstruction. Actually, the total $0\nu\beta\beta$ reconstruction efficiency turns out to be higher with a polynomial field than with a uniform field.

	Uniform field	Polynomial field
2 triggered calo. blocks (>150 keV and >50 keV)	58 % - 58 %	58 % - 58 %
2 clusters with more than 3 cells each	82 % - 47 %	83 % - 48 %
2 tracks with an associated calorimeter hit	77 % - 36 %	82 % - 40 %
2 tracks with a foil vertex	93 % - 34 %	95 % - 38 %
2 negatively charged tracks	83 % - 28 %	83 % - 31 %
Total $0\nu\beta\beta$ reconstruction efficiency	28 %	31 %

Table 4.2 – Relative and absolute $0\nu\beta\beta$ reconstruction efficiencies for different selection criteria.

4.4.2 Spatial resolution

However, since the electron tracks are still curved by the magnetic field, the best fit remains an helix fit. But if the magnetic field is not uniform, the electrons curvature are not going to be constant with the distance from the source foil. The spatial resolution for the vertices extrapolated on the source and the calorimeter is thus expected to be

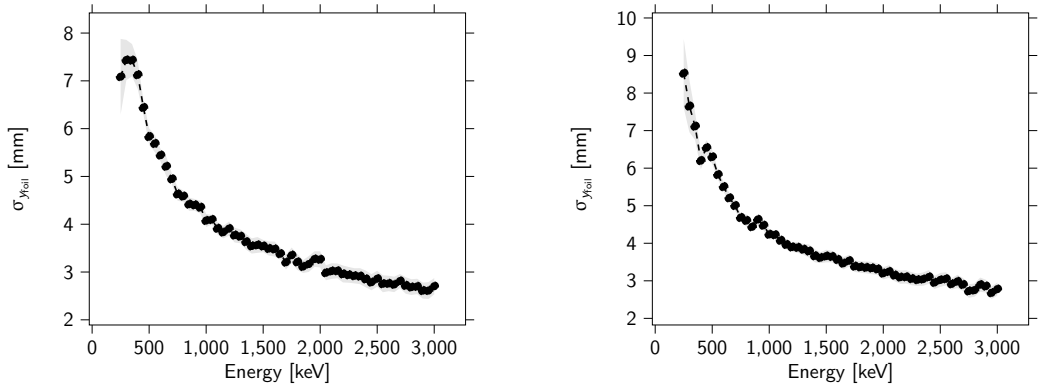

Figure 4.21 – Horizontal spatial resolution of the source vertex, as a function of the reconstructed electrons energy, with a uniform magnetic field *(left)* or a polynomial magnetic field *(right)* [92].

degraded. Figure 4.21 compares the horizontal spatial resolution of the source vertices reconstruction, obtained with two different magnetic fields. Like in Section 3.1.2, the resolution is obtained from the distribution of the distance between the simulated and the reconstructed source vertices. First of all, with both magnetic fields, the higher the reconstructed electron energy, the more accurate the source vertex reconstruction. Indeed, not only high energy electrons are less likely to be significantly affected by scatterings in the tracker, but if these electrons managed to keep a high energy, this also means they did not scatter in the first place. The spatial resolution for these high energy electrons is as good regardless of the shape of the magnetic field. However, lower energy electrons appear to be less accurately reconstructed with a non-uniform field. This is expected since, in a non-uniform magnetic field, the variations of the curvature radius along the tracks are far greater for low energy electrons. These tracks are consequently less well fitted by the proposed helices. Similar results are observed in the source vertical spatial resolution.

Figure 4.22 compares the horizontal spatial resolution of the calorimeter vertices reconstruction, obtained with two different magnetic fields. Once again the difference is only significative for low energy electrons and once again, the spatial resolution is worse with a non-uniform field. In the case of the polynomial magnetic field, a better spatial resolution could be achieved by fitting the tracks with helices of non-constant radii of curvature but this approach is non-trivial. Instead, one could contemplate fitting an helix for the first part of the track and finishing with a straight line fit near the calorimeter.

4.5 Conclusion

The first study presented in this Chapter showed that the optimum value of the magnetic field to be applied in the demonstrator is a compromise between the charge identification efficiency and the reconstruction efficiency: the particles curvature are better reconstructed in a high magnetic field but the latter also prevents more charged particles from reaching the calorimeter. The optimum magnetic field for the $0\nu\beta\beta$ events reconstruction ranges between 25 and 40 G. However, measurements performed with a small scale coil in LAL proved that the magnetic shieldings would not perfectly protect the op-

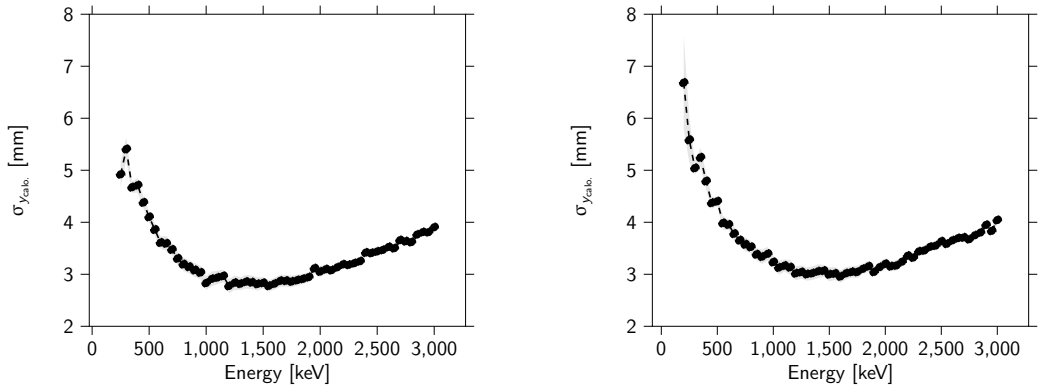

Figure 4.22 – Horizontal spatial resolution of the calorimeter vertex, as a function of the reconstructed electrons energy, with a uniform magnetic field *(left)* or a polynomial magnetic field *(right)* [92].

tical modules against the applied magnetic field. This could translate in a deterioration of the energy resolution. Thankfully, the iron magnetic properties can be taken advantage of in order to cancel the remaining field inside the shieldings. This remaining magnetic field is lower and more easily canceled if the external magnetic field is low. This motivates the preference for a 25 G magnetic field in the demonstrator. Yet, another undesired effect induced by the magnetic shielding was discovered from measurements performed with a coil prototype. The magnetic field outside the shieldings appears to be attenuated by the latter. A dedicated magnetic simulation confirmed that applying a 25 G magnetic field could result in a field as low as 10 G in the center of the detector and strongly decreasing when approaching the calorimeter walls. Nonetheless, Monte-Carlo simulations performed with a non-uniform magnetic field showed this could actually sensibly improve the $0\nu\beta\beta$ reconstruction efficiency. The spatial resolution is impaired by the fact that helices do not accurately describe the particle tracks anymore. This issue could, however, be addressed by adapting the trajectory fitting procedure.

Chapter 5

The γ reconstruction in SuperNEMO

A γ particle does not leave tracks in the detector but can trigger several calorimeter modules, hence the need for a dedicated reconstruction algorithm. Before focusing on the γ reconstruction, the principle of the γ detection in SuperNEMO is reminded. First, a γ-clustering algorithm *a la* NEMO-3 as well as a γ-tracking algorithm are presented. Both of them were tested on simple γ events, multiple γ-events and on ^{208}Tl and ^{214}Bi decay events in order to understand their performances and behavior regarding several parameters such as the calorimeter time resolution. These results led to the elaboration of a new algorithm, called γ-tracko-clustering, which brings some improvements by combining the clustering and tracking features.

5.1 The detection of γ's in SuperNEMO

The γ-particles, being neutral, do not ionize the gas at the vicinity of the tracker cells and, thus, no information on their trajectory can be obtained from the tracker. Furthermore, neutral particles need to interact with the scintillator blocks in order to be detected. However, the energy of the γ's of interest, should they originate from a γ-decay or follow an internal conversion, ranges from a few hundred keV up to a few MeV. In carbon-based materials, like SuperNEMO's plastic scintillators, considering the energies involved, γ particles will mostly interact through Compton scattering (Figure 5.1). The Compton electrons created inside the scintillators will ionize the medium and allow the indirect detection of the γ particles by the calorimeter.

At these particular energies, the γ's will mainly scatter forward (Figure 5.2) and, considering the detector design, will tend to escape the detector or deposit a small fraction of their energies. Nonetheless, a fraction of these γ's will scatter with a higher angle and interact in neighboring calorimeter blocks. As it will be explained later, these events are reconstructed using a γ-clustering algorithm. Actually, a smaller fraction of the γ's will backscatter: the γ-clustering cannot reconstruct these events, hence the need for γ-tracking algorithms.

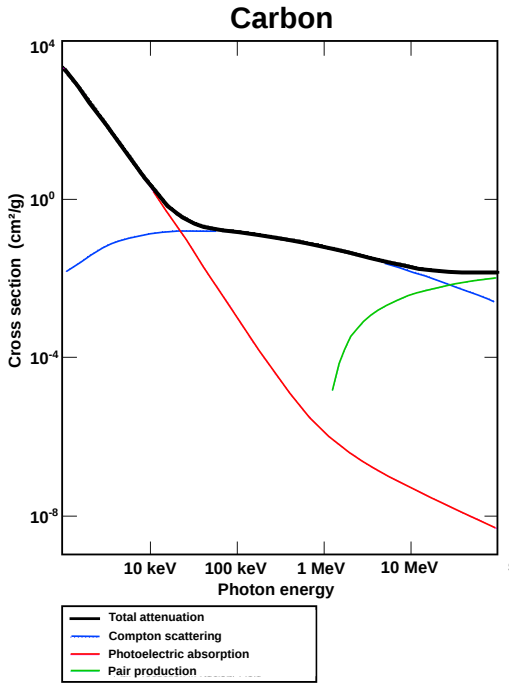

Figure 5.1 – γ cross-section on a Carbon target as a function of its energy. The Compton scattering dominates for SuperNEMO γ's energy range.

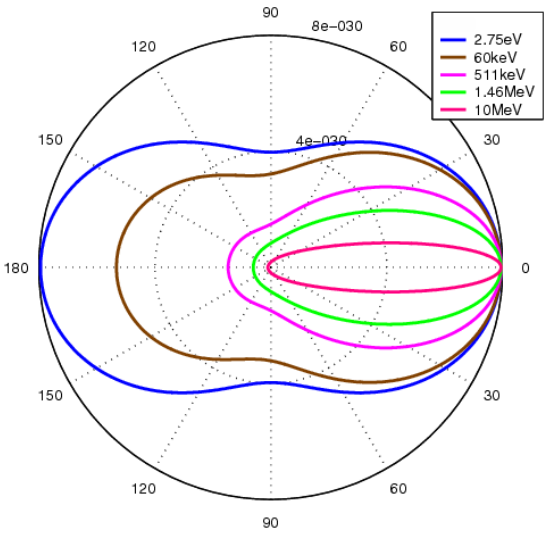

Figure 5.2 – Klein-Nishina distribution of Compton scattering angles for several γ energies. Each colored line represents the probability for a γ of a given energy to scatter with a certain angle. The further from the center the line is, the higher the probability for the γ to scatter with this angle is.

The amount of energy transferred E_e to the detection material (in the form of a Compton electron) depends on the angle of interaction θ which, being different for each inter-

action, will result in a broad and continuous energy spectrum. Equation 5.1 shows this dependence, where E_γ is the energy of the incident γ and E'_γ the energy of the scattered γ).

$$E_e = E_\gamma - E'_\gamma = E_\gamma - \frac{E_\gamma}{1 + \frac{(1-cos\theta)E_\gamma}{m_e c^2}} \tag{5.1}$$

$$E_{\text{max}} = E_{e|\theta=\pi} = E_\gamma(1 - \frac{1}{1 + \frac{2E_\gamma}{m_e c^2}}) \tag{5.2}$$

In addition, even at the maximum energy transfer, corresponding to θ=π *i.e.* a back-scattering, as shown in Equation 5.2, the energy deposited is always lower than the energy of the incident γ: this is the Compton edge. The resulting theoretical energy spectrum is presented in Figure 5.3. Fortunately, the scintillators were designed large enough so that several Compton scatterings can occur in a single calorimeter block. This design choice provides a higher γ detection efficiency and a more accurate γ energy measurement.

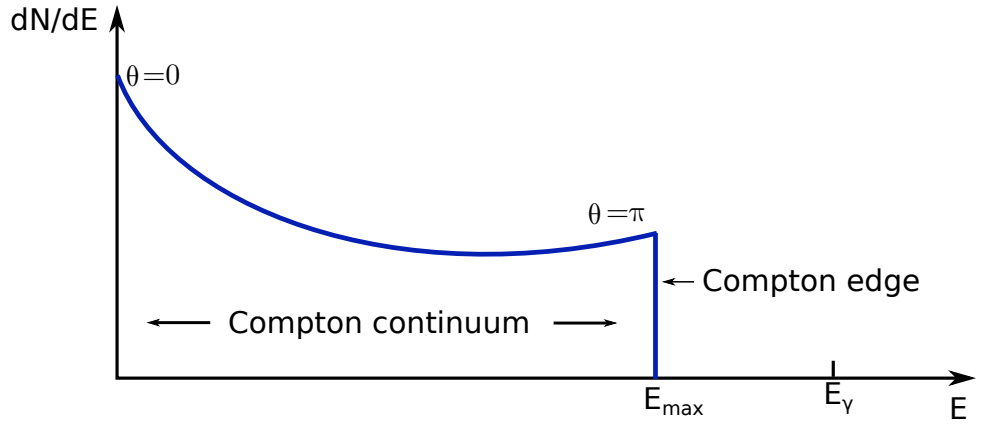

Figure 5.3 – Theoretical Compton scattering spectrum.

Without information from the tracker, the expected SuperNEMO experimental signature for γ-particles are unassociated calorimeter hits or collections of neighboring calorimeter hits called clusters. The simplest way to reconstruct them is to assign a γ to each calorimeter hit or, after a minor processing, to a cluster of calorimeter hits. A more sophisticated method relies on the calorimeter time measurements or more precisely on the Time-Of-Flight likelihood. These two methods have been implemented in the reconstruction software and are described in the following parts.

5.2 The γ-clustering

As mentioned previously, γ-particles can interact with nonzero scattering angles and subsequently interact with one or more neighboring calorimeter blocks. The clustering, a la NEMO-3, simply consists in gathering neighboring calorimeter hits into clusters of

calorimeter modules. The search for clusters is operated with an ersatz cellular automaton. A new γ-particle is then attributed to each cluster. Since the interaction point of a γ particle within a scintillator cannot be reconstructed, the γ calorimeter vertices are chosen as the center of the scintillators (12.8 cm from the sides and at 9.7 cm from the entry face). This choice is made for all the γ reconstruction algorithms addressed in this chapter.

An example of successful reconstruction of a ^{208}Tl event is presented in Figure 5.4. Three γ's are emitted, including the 2.615 MeV γ, which can be seen going up, in this side view of the detector. This particular γ illustrates the fact that the energy detected is higher and closer to the full γ energy when there are multiple interactions in the same scintillator. The middle γ, with two low energy deposits, triggers two neighboring calorimeter blocks and the algorithm successfully reconstruct a cluster of calorimeter hits as belonging to the same particle.

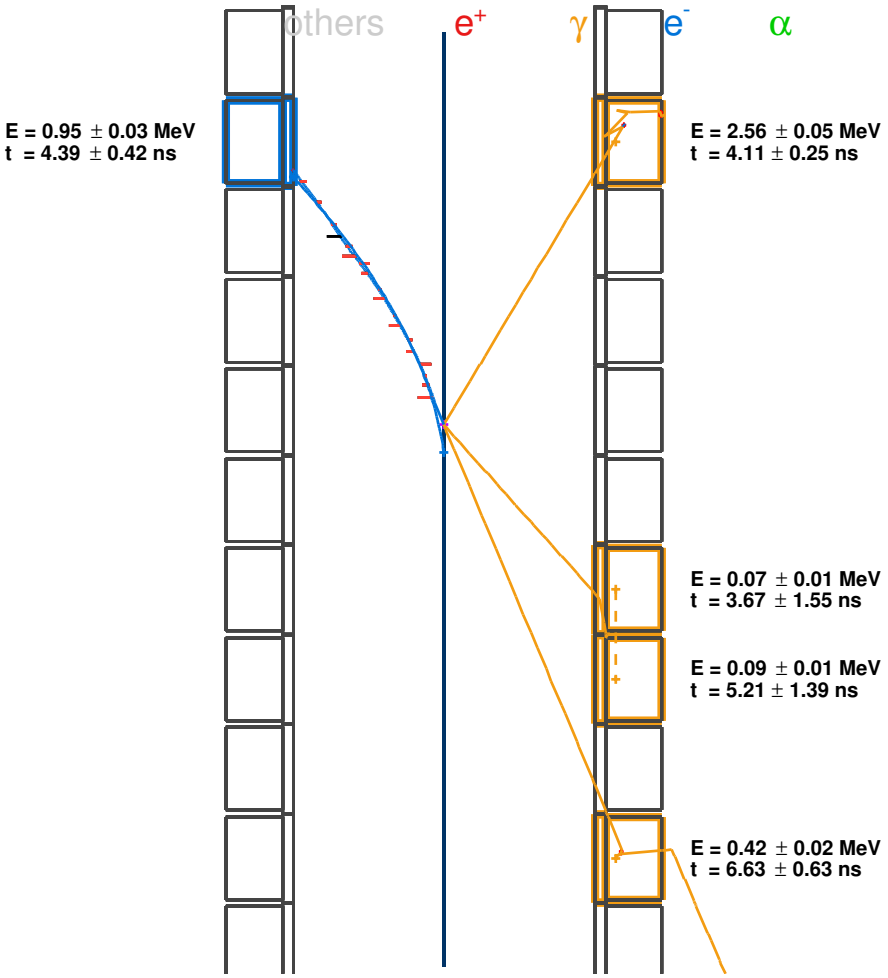

Figure 5.4 – Event display of a ^{208}Tl event using γ-clustering. The solid orange lines are the simulated γ tracks. The orange crosses in the scintillators are the reconstructed γ vertices, which need to be related to the electron, later in the reconstruction. The dashed orange line depicts the reconstructed γ tracks.

The clustering algorithm also requires that two consecutive calorimeter hits within a

cluster should not be separated by more than 2.5 ns. This value is high enough to allow the clusterization of two neighboring hits with a high time uncertainty (such as the cluster in Figure 5.4, where the two hits are separated by 1.54 ns, *i.e.* a travel distance of about 45 cm, whereas the two blocks are direct neighbors), but low enough to prevent the clusterization of two unrelated hits.

Considering the simplest event possible, namely a single γ, the algorithm fails to reconstruct the event every time the γ bounces in the detector and triggers a non-neighboring calorimeter module. Such event is displayed in Figure 5.5.

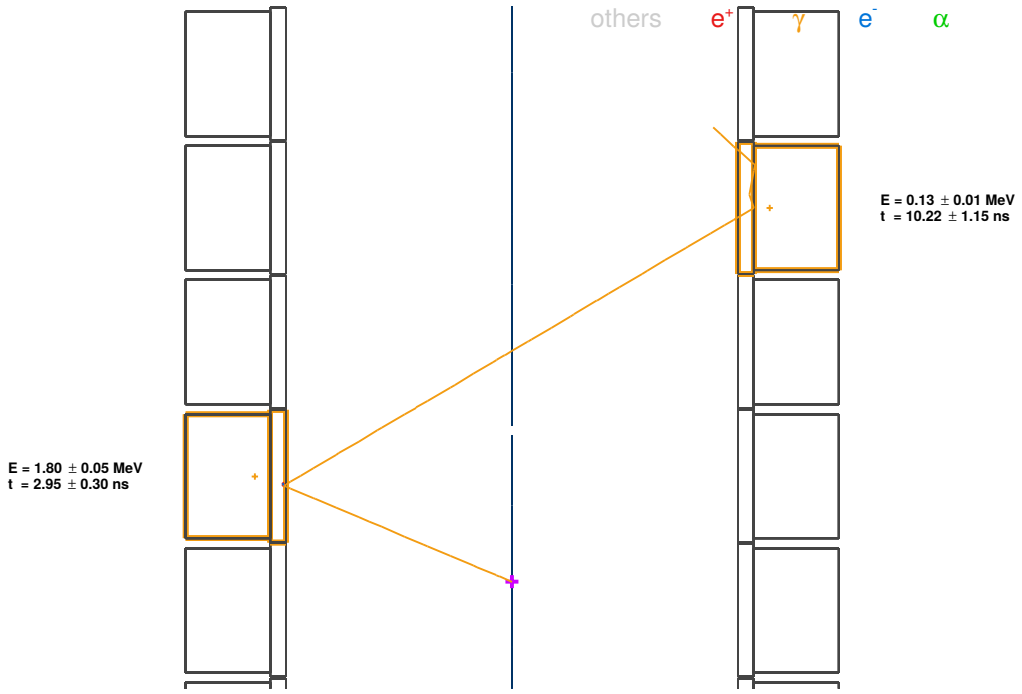

Figure 5.5 – Event display of a failed reconstruction using the γ-clustering algorithm.

In Figure 5.5, a 2 MeV γ originates from the foil (pink cross) and back-scatters on a first scintillator, thus depositing a high amount of energy. It then flies across the detector but the algorithm, not able to follow the γ, interprets the second hit as a second γ-particle.

The main advantage of the γ-clustering technique is that it is fairly simple and efficient, since only a minority of γ's actually bounce around the detector. It also performs relatively well when a high number of γ's are involved in an event (the γ's are usually spatially uncorrelated), even though the probability for at least one of them to scatter back in the detector increases with the number of γ's. These events with a high γ content will be discussed in more details when comparing the γ-tracking and the γ-clustering algorithms. The main limitation of the γ-clustering, however, is its inability to track γ's triggering distant calorimeter blocks, which is what the γ-tracking is designed for.

5.3 The γ-tracking

The purpose of the γ-tracking is to reconstruct the array of calorimeter blocks triggered by a γ particle by comparing if the time measurements are compatible with a given scenario. Indeed, a γ-particle, being a massless particle, travels at the speed of light c regardless of its energy. Thus, by comparing the theoretical Time-Of-Flight (TOF in the following) separating two triggered calorimeter blocks to the experimental time difference (and considering the experimental uncertainties), it is possible to evaluate the probability that a γ-particle could indeed be responsible for these hits.

5.3.1 Definition of the Time-Of-Flight probability

In practice, if one considers two calorimeter blocks, labeled 1 and 2, and assuming the γ interacts consecutively in both calorimeters blocks, the likelihood is computed by first evaluating a χ^2 quantity, presented in Equation 5.3, similarly to Equation 3.2. The probability extracted from this quantity, in the same fashion as in Equation 3.1.3, reflects the likelihood of the hypothesis that a γ actually flew from the calorimeter blocks 1 to 2 (Equation 5.4). Considering the similarities between the two equations, the hypothesis tested in the γ tracking will also be referred to as the "internal" hypothesis in the following.

$$\chi^2 = \frac{\left((t_2^{\text{exp}} - t_1^{\text{exp}}) - \frac{\ell_{1\to 2}}{c}\right)^2}{\sigma_{t_1}^2 + \sigma_{t_2}^2 + \sigma_\ell^2} \tag{5.3}$$

$$P(\chi^2) = 1 - \frac{1}{\sqrt{2\pi}} \int_0^{\chi^2} x^{-\frac{1}{2}} e^{-\frac{x}{2}} dx \tag{5.4}$$

For a track with more than two calorimeter hits involved, say $C_1 \to C_2 \to \ldots \to C_n$, the probability is not simply the product of each pair probability but rather $P_{C_1\to C_2\to\ldots\to C_n} = P(\sum_{i=1}^{n-1} \chi^2_{C_i\to C_{i+1}})$ with a degree of freedom $n-1$. In Equation 5.4, two hits are considered, so the degree of freedom is 1 and it does not appear explicitly in the probability. The uncertainties involved in the computation of χ^2 are the uncertainties on the time measurement σ_{t_i} and the uncertainty on the track length used for the computation of the theoretical Time-Of-Flight. The former uncertainties are related to the detector performances and more especially to the calorimeter response. As a matter of fact, the time uncertainty is linked to the calorimeter characteristics and its energy resolution through Equation 5.3.1:

$$\sigma_t = \frac{\tau \times \sigma_E}{E} = 400 \text{ ps at 1 MeV}$$

where τ is the scintillator relaxation time and the energy resolution is 8 % at 1 MeV (FWHM).

The uncertainty on the track length is due to the uncertainty on the interaction point. The assumed track is the line joining the center of both the scintillators but it is impossible to identify more precisely the region of the scintillator where the γ-particle interacted. The analysis of the signal shape might provide some hints but, given the symmetries of a

calorimeter block, it would not completely raise all spatial degeneracy. The next part is a proposal for the determination of this uncertainty based on simulations.

5.3.2 Evaluation of the track length uncertainty

From simulations

Assuming two calorimeter hits, where the γ went from a calorimeter block to the other without intermediate interactions *i.e.* went in a straight line from one calorimeter block to the other, it could be possible to evaluate conservatively, "by hand", the standard deviation of the track length distribution. Nevertheless, this assumption is arguably moot, since γ's can interact a substantial amount of times within the same calorimeter block, let alone between two calorimeter hits.

Thanks to the simulation software, it is possible to study the whole simulated γ track. The events of interest are obtained by simulating single monokinetic γ's and keeping only events where the γ triggered two calorimeter blocks *i.e.* the events for which a TOF computation is relevant. Among these events, it is worth considering two populations: either the two blocks are neighbors and make up a cluster or the two blocks are separated, meaning that the γ bounced back in the detector (or possibly went through a neighboring scintillator block without being detected). For these two populations, the distributions of the difference between the simulated track length and the reconstructed track length are shown in Figure 5.6 and Figure 5.7.

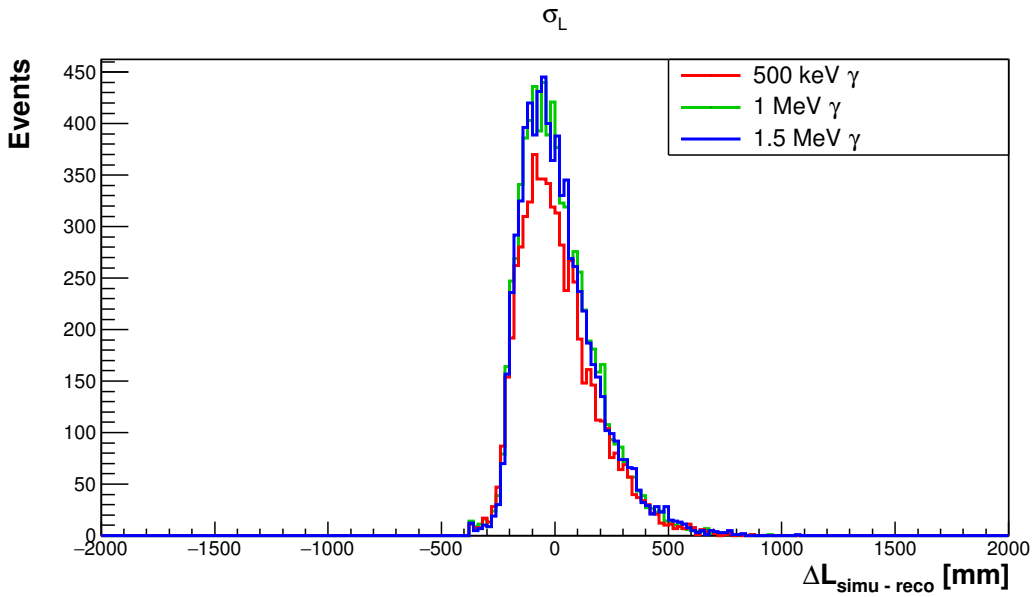

Figure 5.6 – Distribution of the difference between the simulated and reconstructed γ track lengths for events with neighboring calorimeter hits. The γ's are emitted isotropically from a random source vertex.

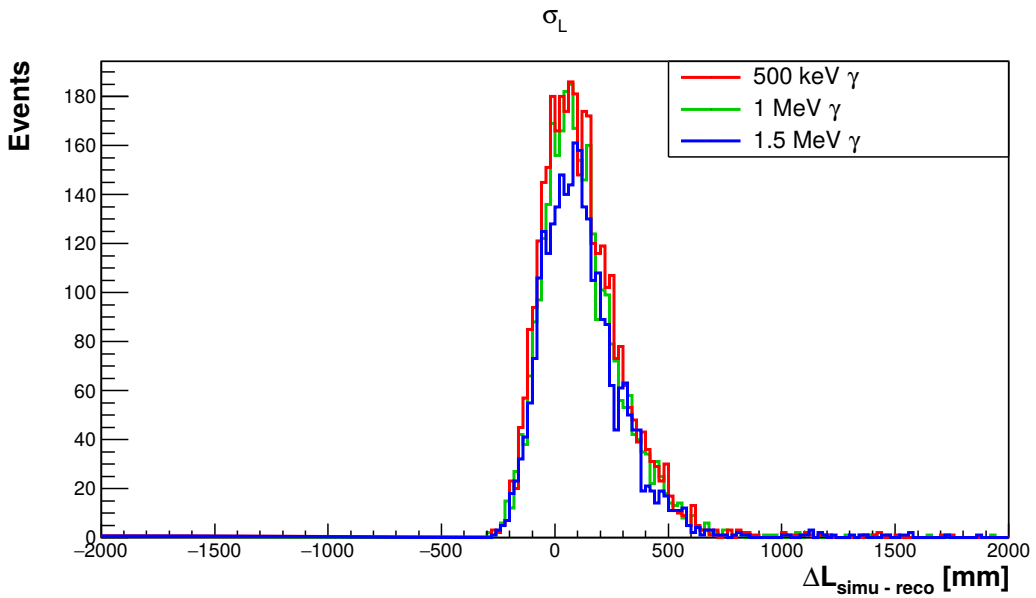

Figure 5.7 – Distribution of the difference between the simulated and reconstructed track lengths for events with distant calorimeter blocks. The γ's are emitted isotropically from a random source vertex.

First, one can notice that these two distributions are not perfectly Gaussian. Indeed, the assumed reconstructed track is a straightforward γ going from one scintillator center to the other. If the simulated track consisted simply in a straightforward path going from one random interaction point to another, one could expect a mathematically even distribution. In reality, the γ behavior is much more erratic and each scattering (on its way to the second calorimeter module or in the scintillator block) increases its track length. It is then quite instinctive to see that a γ has much more "opportunities" to increase its path length, making the right part of the distribution ($\Delta L \geq 0$) broader than the left one. This can also explain the shift of the average track lengths difference towards higher values, apparent in Figure 5.7, because the γ has even more opportunities to scatter on its way between the two distant calorimeter blocks than for neighboring calorimeter blocks. Another interesting thing to notice is the difference in amplitude for different energies, even though the number of events simulated for each energy was the same. As a matter of fact, the distant calorimeter blocks events consist mainly of events going from one wall to the other. However, such topology of events require larger scattering angles than the angles required to make clusters. According to Figure 5.2, the γ of smaller energies are indeed more likely to scatter with large angles (and even backscatter) than the γ's of higher energies, which tend to scatter forward (which favors clusters over back-scattering events). Eventually, fitting these distributions with a Gaussian function gives σ_{L} = 18 cm or, translated into a time, about $\sigma_{\mathrm{t_L}}$ = 0.6 ns then $\sigma_{\mathrm{t_L}}$ = 0.9 ns[a], taking into account the scintillator refractive index $n = 1.5$. Furthermore, this value does not appear to depend on the γ energy. The simulation might introduce a bias because the time measured in the genuine detector can be the time of any of the deposit in the scintillator. The first energy deposit detected by

[a] Assuming the track lengths differences are mainly generated in the scintillator volume.

the calorimeter will be the one generating the scintillations photons that will first induce a PMT signal. In the simulation, however, the track length is measured starting from the last step in the first scintillator to the last step in the second scintillator. If the γ behavior is on average the same in both the scintillators, no bias should be introduced. Yet, once a γ loses energy (a significant amount for back-scattering events), its cross-section increases and the particle is more likely to scatter multiple times in the second calorimeter blocks, thus extending its path length.

The track length uncertainty is an input of the Time-Of-Flight calculations. It is thus possible to validate this evaluation of the track length uncertainty by performing *a posteriori* checks.

Confirmation *a posteriori*

One way to check if σ_L=0.9 ns is a reasonable evaluation of the track length uncertainty is to look at the TOF probability distribution. Indeed, one of the benefits of using the probability distribution rather than the χ^2 distribution is that it brings extra qualitative information, especially useful to check the estimation of the uncertainties. The shape of the probability distribution can bring out an overestimation or, *a contrario*, an underestimation of the uncertainties, which would translate into a positive or a negative slope, respectively. On the other hand, a flat distribution signifies an appropriate estimation of the errors and confirms the Gaussian distribution of the original quantity measured. The confirmation of the previous result is performed with a pure set of 1 MeV γ's, triggering exactly two optical modules, such that the internal hypothesis is almost certain to be verified. Once again, two topological populations are considered, the events where the two triggered calorimeter blocks are neighbors and the others. As shown in Figure 5.8, the latter exhibits the expected flat distribution, characteristic of a good estimation of the errors. On the other hand, the events with clusters clearly do not follow the same distribution. This can be explained by the fact that for small traveled distances, the uncertainties are relatively and significantly more important than for a γ traveling for a few nanoseconds. Consequently, the χ^2 values will mechanically be smaller and the probabilities higher. This also shows the limited reliability of the γ-tracking algorithm for neighboring calorimeter blocks. Since the probabilities are overestimated and that a good probability is required between two hits, clusters will be more easily created. With genuine data, it might not be possible to notice this phenomenon because the background events will fill the low probability region.

5.3.3 NEMO-3 γ-tracking algorithm

All the parameters needed for the TOF probability computation are now available. The γ-tracking algorithm used in NEMO-3 [93] was implemented in Falaise. Given a collection of unassociated calorimeter hits, the algorithm will try to reconstruct as faithfully as possible the event, solely from the TOF information. One feeds the TOF probabilities between all the pairs of calorimeter hits possible and the algorithm computes all the

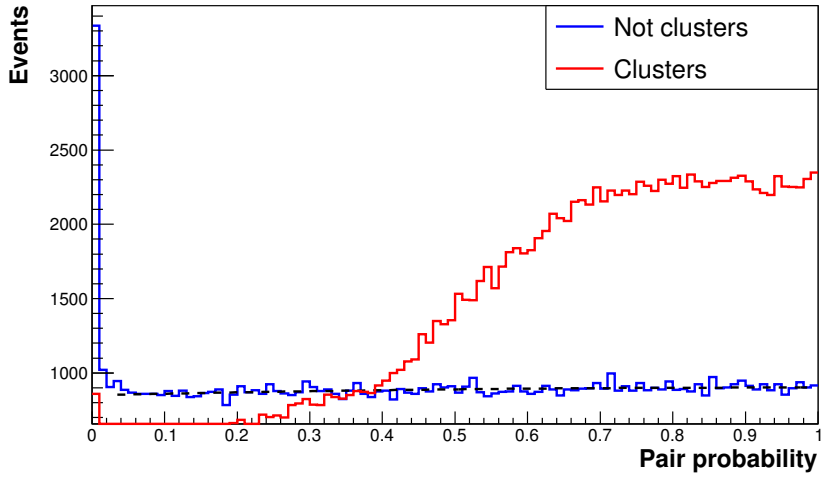

Figure 5.8 – Probability distribution for cluster and non-cluster events on a set of pure internal events.

possible paths and the probability associated with them. For example, if an event contains three unassociated calorimeter hits 1, 2 and 3 with $t_1 < t_2 < t_3$, one computes all the probabilities beforehand, in this case $P_{1\to2}$, $P_{1\to3}$ and $P_{2\to3}$ (for n calorimeters hits $\frac{n(n-1)}{2}$ probabilities must be calculated). These probabilities are then given as an input to the algorithm which computes the probability of all scenario possible, in our simple example: P_1, P_2, P_3, $P_{1\to2}$, $P_{1\to3}$, $P_{2\to3}$ and $P_{1\to2\to3}$. The reconstructed track will be the longest one, provided its probability satisfies a minimum value, typically 4 % in NEMO-3. If two possible tracks share the same length, the one with the highest probability is favored. This is the basic principle of the algorithm and its performance, compared to the γ-clustering will be presented later.

5.3.4 Limits of the algorithm

Once again, considering single γ events, the few events failing the γ-tracking are the events where the γ travelled for too long between the two calorimeters hits without being detected, either because it went outside the detection volume and came back (Figure 5.9) or because the intermediate energy deposits were not high enough to pass the energy threshold (Figure 5.10). The time difference between the two calorimeter hits is too large, making the χ^2_{int} too large and the probability too low for the event to be considered as one γ. In contrary to the γ-clustering, the γ-tracking is highly vulnerable to the presence of multiple γ's because the calorimeter hits from the different sequences can be mixed up more easily. This particular case, along with more complex events, will be studied in the next part.

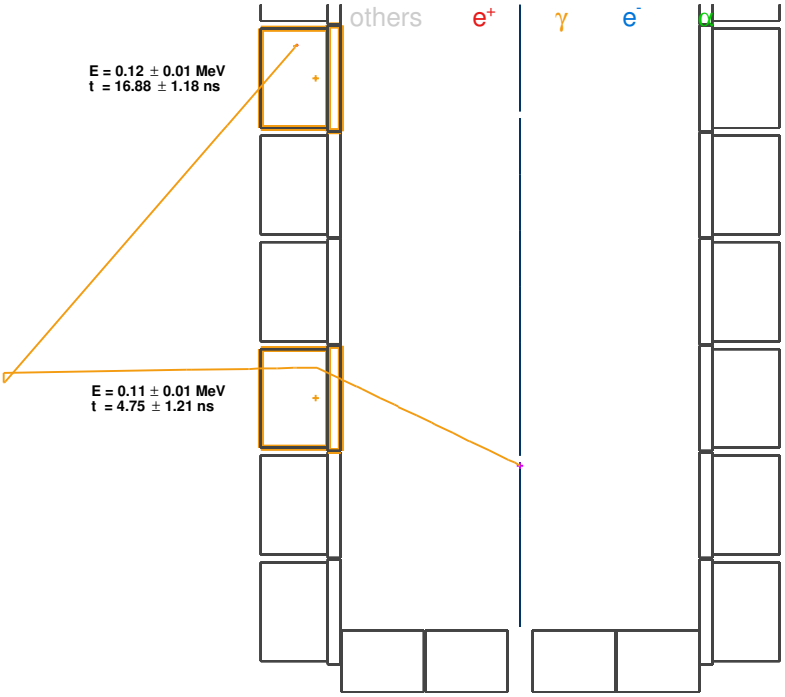

Figure 5.9 – Event display of γ leaving the detector and coming back without being detected.

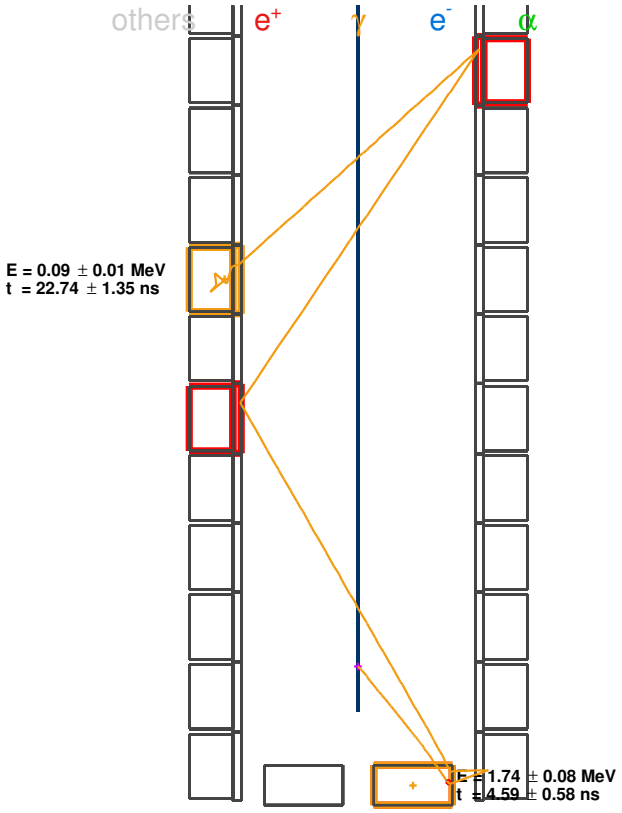

Figure 5.10 – Event display of a γ not depositing enough energy to trigger intermediate calorimeter blocks. The red blocks represent calorimeter blocks that have received some energy in the simulation but too little to pass the energy threshold.

5.4 Study of the γ-clustering and γ-tracking reconstruction efficiencies

The simulations were performed with the SuperNEMO software. As a reminder, the calorimeter time resolution is 400 ps at 1 MeV and the calorimeter low energy threshold is 50 keV. Indeed, the 150 keV high energy threshold is only relevant for charged particles since a minimum number of tracker cells must be triggered for the event to be recorded in the first place. The same conditions are therefore applied to the simulation.

5.4.1 Detection efficiency

Before looking at how both algorithms perform, it might be interesting to study the detector behavior regarding the γ-particles. Obviously, the next results were obtained using a simulation software trying to reproduce the physics processes occurring in SuperNEMO and, as such, these results do not pretend to perfectly describe the genuine detector behavior. Though caution must be exercised when dealing with absolute measurements based on simulations, this study still allows a qualitative comparison of different reconstruction methods before genuine data are available.

In the following, a calibrated hit is defined as a calorimeter block where at least one energy deposit was simulated and for which the energy after calibration is higher than the energy threshold specified beforehand. The γ detection efficiency is defined as the ratio of events where at least one calorimeter hit was calibrated, over the total amount of events simulated. This quantity is evaluated thanks to the simulations of single monokinetic γ's emitted randomly and isotropically from the source foil. The γ detection efficiency is presented in orange as a function of the γ energy in Figure 5.11.

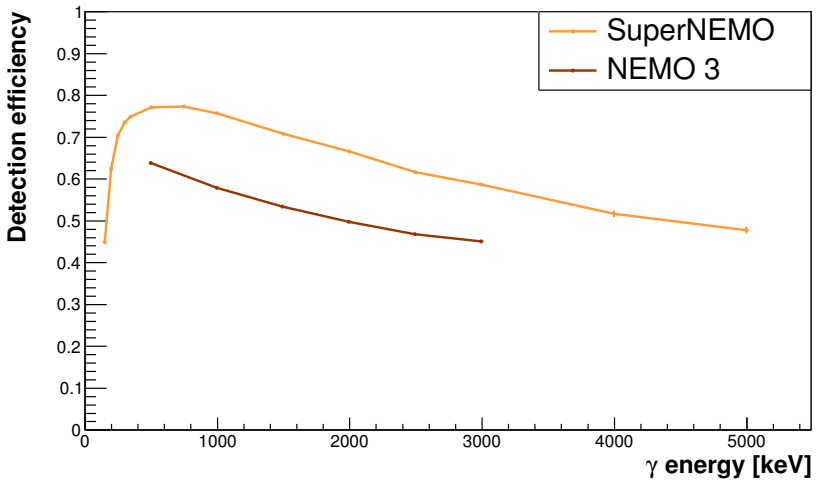

Figure 5.11 – In orange, the γ detection efficiency of the SuperNEMO calorimeter as a function of the simulated γ energy. In brown, the same parameter in NEMO-3 [94].

The NEMO 3 detection efficiency, in brown, is also represented for comparison. The curve presents a maximum detection efficiency of 78 % around 500 keV. Indeed, as the energy of the γ increases its total interaction cross section decreases, as shown previously in Figure 5.1. Yet, as the energy decreases, one should expect to see the detection efficiency increase for energies below 500 keV. But keeping in mind that a 50 keV energy threshold is required for the detection, combined with the Compton energy spectrum (Figure 5.3), actually fewer γ's are detected, hence the drop observed. The NEMO-3 γ detection efficiency [94] is consistently lower than SuperNEMO's, mainly because the scintillator blocks were thinner in NEMO-3.

5.4.2 Study of single γ events

The simplest physics process on which to test the algorithms is single monokinetic γ's emitted isotropically from the source foil. In this part and in the rest of this note, the performances of the algorithms are evaluated and compared *via* the reconstruction efficiency. The latter is defined as the ratio of events successfully reconstructed over the number of events eligible for reconstruction. These two categories of events must be defined:

- A successfully reconstructed event is an event where all the calorimeter hits are attributed to the proper particle, regardless of the sequence order. This last condition aims at including events where two neighboring calorimeter hits can easily be permuted due to the limited time resolution.
- The events eligible for reconstruction are the events where only the unassociated calorimeters remain to be treated. Typically, for single γ-particles simulations, this includes all the events with at least one unassociated calorimeter hit. For physics processes such as ^{208}Tl, the qualifying events will have to comprise at least one reconstructed electron and at least one unassociated calorimeter hit.

This allows us to define once and for all:

- the detection efficiency as the ratio of events eligible for reconstruction over the number of events simulated.
- the reconstruction efficiency as the ratio of events successfully reconstructed over the number of events eligible for reconstruction,
- the total reconstruction efficiency as the ratio of events successfully reconstructed over the number of simulated events (in other words, the product of the two previous efficiencies).

In the following parts, these quantities are compared and drawn as a function of various parameters such as the γ energy, the energy threshold, etc.

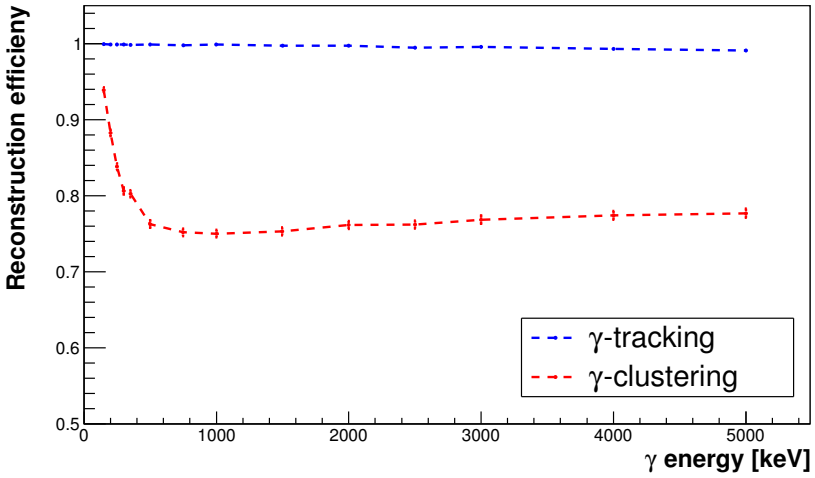

Figure 5.12 – γ reconstruction efficiency as a function of the γ energy, using the γ-clustering, in red, or the γ-tracking, in blue.

Energy of the simulated γ

The dependence of the γ reconstruction efficiency as a function of the single γ energy is presented in Figure 5.12, for both the γ-clustering and the γ-tracking algorithm.

The γ-tracking performs almost perfectly regardless of the γ energy. Since no mix up with another γ sequence is expected, the minimum probability required can be set very low (10^{-5}), letting a great liberty to the algorithm for making associations of calorimeter hits. The only few events the algorithm fails to reconstruct correctly are the events where the γ spent a significant amount of time between two hits without being detected *e.g.* Figure 5.9 or 5.10. Obviously, when reconstructing genuine data, the number of γ's involved in the event is unknown and it is impossible to know which minimum probability to set without biasing the analysis. That is why a preliminary optimization based on simulations will be required for each channel studied.

For γ's with a 300 keV energy and more, the γ-clustering reconstruction efficiency ranges between 75 % and 80 %. This shows that approximately[b] one-fourth of the γ's bounce back in the detector since the γ-clustering cannot track these events. For lower γ energies however, the reconstruction efficiency rises back up: either the γ's deposit all their energy in a single cluster or, if they scatter back in the detector, they do so with a high scattering angle, thus depositing a high fraction of their energy which does not leave them enough energy to trigger a second calorimeter module. The slight increase in the efficiency with the energy corresponds to the γ's tendency to scatter forward at higher energies (Figure 5.2) which makes backscatterings and thus misconstructions less

[b] Events where a γ triggers a calorimeter module, travels across a neighboring scintillator block without interacting and triggers a second calorimeter module also fail the γ-clustering reconstruction. Such events are however very rare.

likely. As shown previously in Figure 5.11, the γ's are not systematically detected, so it might be interesting to look at the total γ reconstruction efficiency which is the product of the detection and the reconstruction efficiency curves. As a matter of fact, more than the reconstruction efficiency, it is the total reconstruction efficiency which is the relevant quantity for the physics analysis since it will be used to measure the activities from the decay rate observed and, more generally, make the Monte-Carlo simulations match the data. This particular total reconstruction efficiency for single monokinetic γ's with a variety of energies is presented in Figure 5.13. Given the quasi-perfect reconstruction efficiency of the γ-tracking, the corresponding total reconstruction efficiency is simply limited by the detection efficiency of the detector. For the γ-clustering, the resulting total reconstruction efficiency is basically a decreasing linear function of the γ's energy, systematically lower than the γ-tracking reconstruction efficiency.

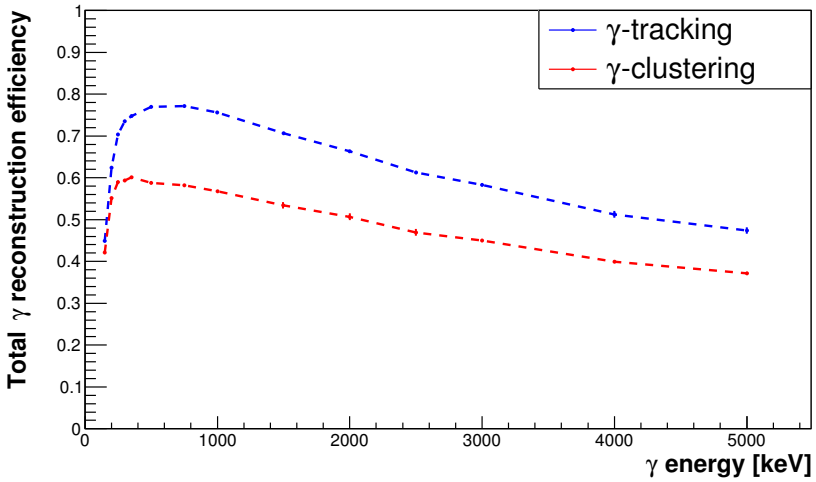

Figure 5.13 – Total γ reconstruction efficiency as a function of the γ energy.

Calorimeter low energy threshold

The calorimeter energy thresholds, namely 150 keV and 50 keV for the high and low energy thresholds respectively, need to be as low as possible to keep the maximum number of events. At the same time, the calorimeter self-triggering rate limits the range of possibilities. Below 50 keV, the PMTs noise might systematically induce fake γ detections, thus polluting the content of the analysis channels. In this study, low energy thresholds as low as 5 keV were considered even if this choice seems unlikely for the SuperNEMO demonstrator. The impact of the calorimeter low energy threshold on the detection efficiency for 1 MeV γ's is illustrated in Figure 5.14 (top).

As expected, fewer events are detected as the energy threshold increases. Figure 5.14 also shows the reconstruction efficiency (middle plot) and the total reconstruction efficiency (bottom plot) for both algorithms. It is understandable that the average complexity of the events increases when the threshold decreases since more calorimeter modules

will be triggered. This increasing complexity does not seem to impact the γ-tracking reconstruction efficiency, unlike the γ-clustering. Indeed, the γ-tracking, with a low minimum probability required, can efficiently reconstruct the γ path, whichever the number of calorimeter blocks involved in the event. If anything, it should be improved because it reduces the number of events where a calorimeter hit is missed due to an energy threshold too high. On the contrary, the γ-clustering efficiency seems to highly depend on the energy threshold: if one requires the energy deposits to be higher than 400 keV, both algorithm perform ideally, while if this constraint is loosened, the γ-clustering efficiency drops. By lowering the energy threshold, the hits occurring after a first rebound are more likely to be detected, thus increasing the amount of failed events. Once again, the total reconstruction efficiency for the γ-tracking is simply dominated by the detection efficiency whereas the γ-clustering curves exhibits a maximum in the 150-200 keV region. Above 350 keV, the two algorithms perform equally.

Calorimeter time resolution

It can be interesting to study the impact of the calorimeter time resolution on the γ reconstruction performances. These results are presented in Figure 5.15, for a 1 MeV γ and a calorimeter energy threshold set back to 50 keV.

It appears the γ-tracking depends less on the time resolution than the γ-clustering does. As explained in the γ-clustering section, it was required that two neighboring hits should not be separated by more than 2.5 ns to be part of the same cluster. If the energy resolution is worsened, two neighboring calorimeter hits might become separated by more than 2.5 ns and thus not be considered as being triggered by the same γ. By loosening this constraint or even removing it, the observed dependence should disappear and the γ-clustering efficiency should be constant around 77 %, the maximum efficiency assuming a perfect calorimeter time resolution. The slight slope observed for the γ-tracking efficiency is mathematically explained: if the uncertainty on the time measurement decreases, the χ^2 values increase and the associated probabilities decrease, at which point more pairs will not pass the minimum probability requirement and the sequence will be split into two γ's. The requirement on the minimum pair probability being very permissive, this efficiency decrease is not very significant.

5.4.3 Study of two-γ events

Similarly to the single γ study, this section exposes the results of the study with two monokinetic γ's of same energy, emitted simultaneously from the source foil, without any kind of correlation. Unless mentioned otherwise, the calorimeter time resolution is still 400 ps at 1 MeV, with a 50 keV energy threshold.

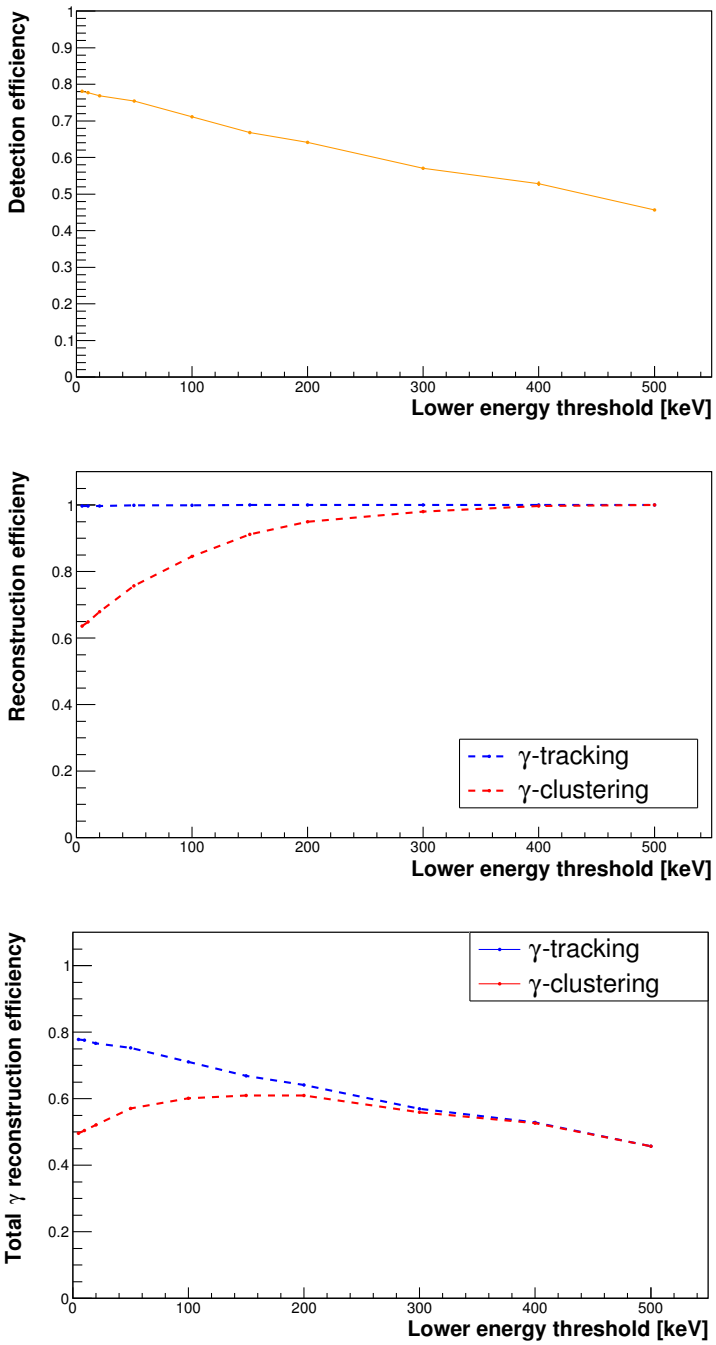

Figure 5.14 – Impact of the low energy threshold for 1 MeV γ's on: *(top)* the detection efficiency, *(middle)* the reconstruction efficiency and *(bottom)* the total reconstruction efficiency.

Energy of the simulated γ's

The reconstruction efficiency of the γ-tracking as a function of the γ's energies is displayed in Figure 5.16, for different minimum pair probabilities (the probability between two calorimeter hits). Unlike with single γ events, the γ-tracking is now struggling to properly reconstruct the correct sequences, particularly when the minimum pair probability is kept to its default value.

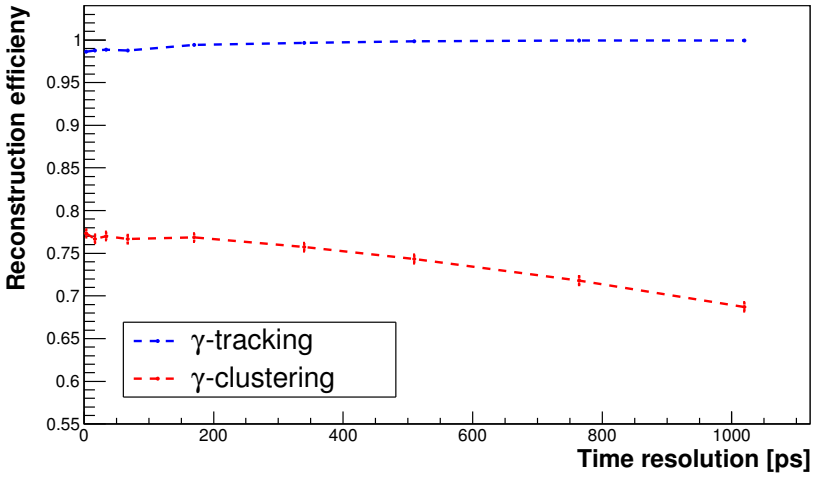

Figure 5.15 – γ reconstruction efficiency as a function of the calorimeter time resolution.

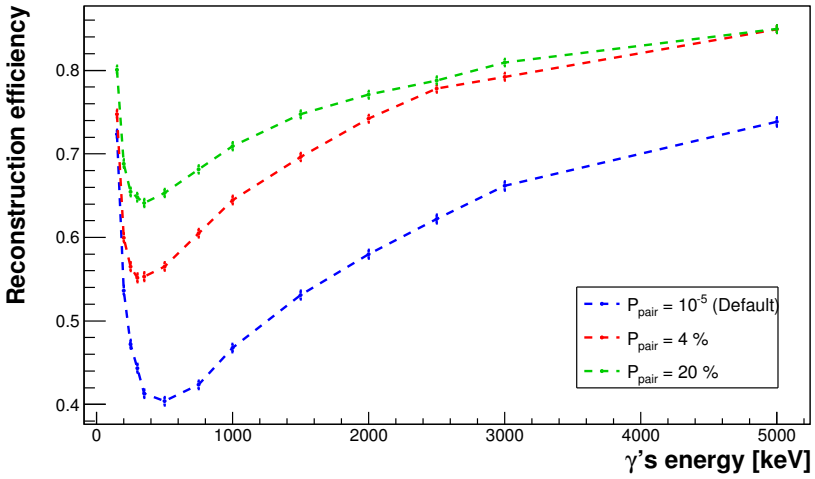

Figure 5.16 – γ-tracking reconstruction efficiency as a function of the γ energy for different minimum pair probabilities.

If kept at the previous permissive value, the minimum pair probability will favor mix up of γ sequences, thus decreasing the γ-tracking reconstruction efficiency. This efficiency can be improved by increasing the minimum pair probability requirement, the optimal value being P_{pair}=20 % (above, the reconstruction efficiency decreases again). The efficiency for the usual cut value for an internal hypothesis, namely P_{pair}=4 %, is also represented. Even with an optimized minimum pair probability, the reconstruction efficiency is overall worse than for single γ events because the algorithm fails to distinguish which calorimeter hit belongs to which γ. In other words, it can happen that a pairing of two calorimeter hits triggered by two different γ is favored because it has a better probability or that an extra calorimeter hit is included in the wrong sequence because it does not lower the overall probability below the minimum requirement (the track length prevails

over a shorter sequence with a better probability). Above P_{pair} = 20 %, the requirement is too stringent and the sequences are split into more γ's.

Keeping the optimum pair probability P_{pair} = 20 % for the γ-tracking algorithm, the reconstruction efficiency is compared with that of the γ-clustering algorithm, as a function of the γ energies in Figure 5.17.

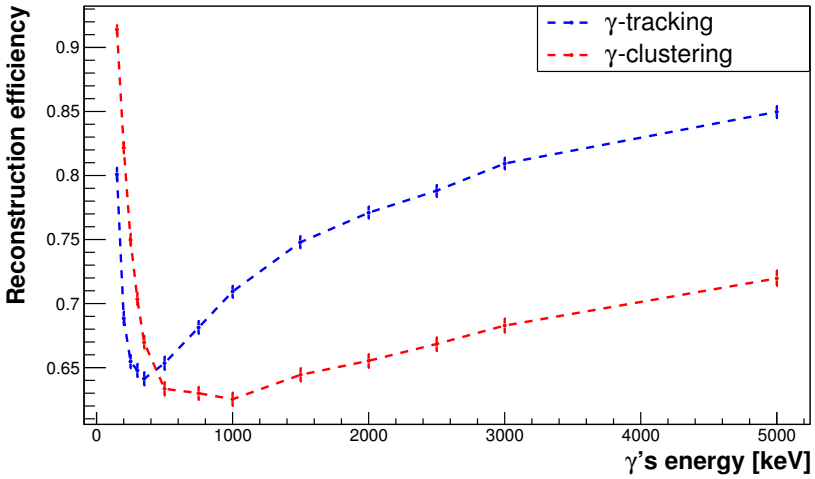

Figure 5.17 – γ reconstruction efficiency as a function of the 2 γ's energies.

Both algorithms perform the worst in the low energy region, namely from 200 keV up to 1 MeV. In light of Figure 5.11, γ's with these energies are more likely to be detected, thus generating complex events more frequently than at higher energies, where γ's are more likely to escape the detection. At lower energies, the γ-tracking performs worse than the γ-clustering because, with low energy deposits come high time uncertainties and thus higher probabilities, making the unjustified pairs more frequent. On the contrary, the γ-clustering reconstruction efficiency improves at lower energies because the γ's are more likely to be confined to a couple of neighboring calorimeter blocks, as explained earlier for single γ events.

For both algorithms, the efficiency is limited by the amount of events where two γ's interact in the same calorimeter block or only in two neighboring blocks, as illustrated in Figure 5.18

Indeed, considering the calorimeter energy resolution and the uncertainty on the track length due to the unknown interaction points in the blocks, it is impossible to discriminate between a single γ or a multiple γ event. If the two γ's are uncorrelated and isotropically emitted from the source, this should represent less than a 3 % chance for the γ to interact in the same block and less than 15 %, including the neighboring calorimeter blocks (these numbers represent the less favorable scenario where the γ's are emitted perpendicularly to the foil).

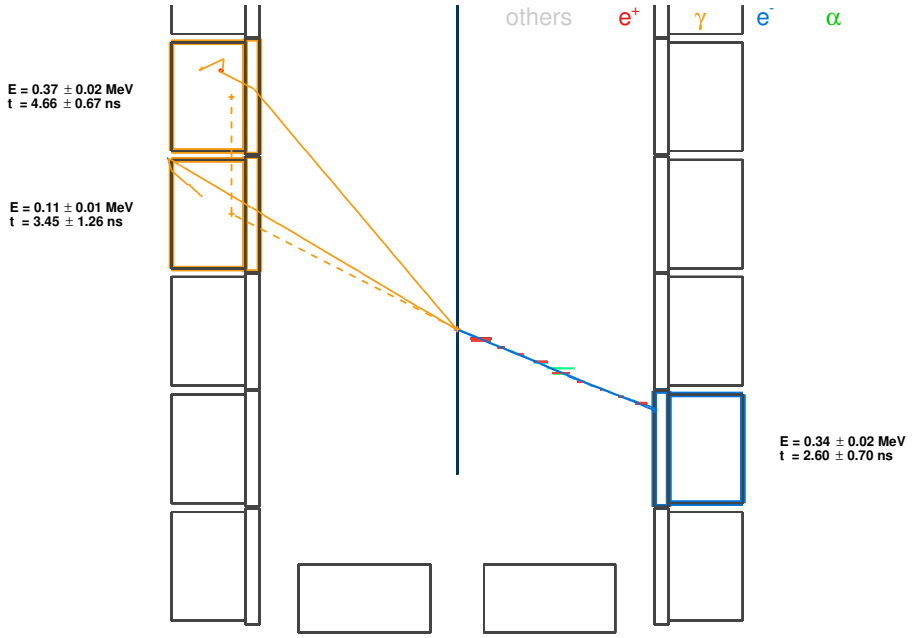

Figure 5.18 – Event display of a failed reconstruction where two colinear γ's interact in two neighboring blocks.

The detection efficiency for two γ's events is the same as for single γ events, only one calorimeter hit is required. Its dependence as a function of the energy is not represented here but follows basically the same behavior as for single γ's, though logically higher in absolute value. The resulting total γ reconstruction efficiency is shown in Figure 5.19.

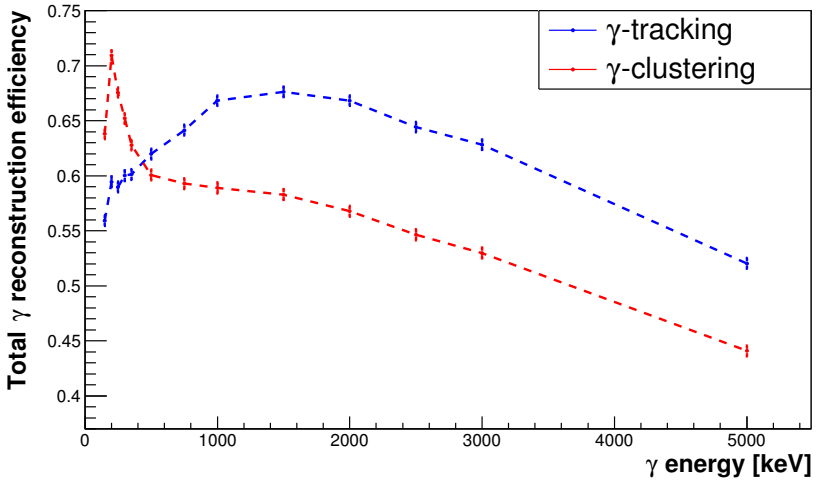

Figure 5.19 – Total γ reconstruction efficiency as a function of the 2 γ's energies.

The γ-tracking performs better than the γ-clustering, except for very low energies where events are mostly made of a simple clusters. For the γ-tracking, the wrongful associations of two hits with low energies and thus high time uncertainties are more frequent.

The γ-tracking performs best for 1.5 MeV γ's, then the two total efficiencies decrease with the energy, dominated by the drop of the detection efficiency. It is also worth noticing that the efficiency difference is reduced compared to the single γ efficiencies plotted previously.

Calorimeter lower energy threshold

The Figure 5.20 is a good illustration of the strengths and weaknesses of both algorithms. By purposefully oversimplifying, one could say that below a 150 keV threshold, the events are more complex and the γ rebounds more frequently detected, which tends to favor the γ-tracking over the γ-clustering. However, above 150 keV, as the events become simpler, the γ-tracking is still vulnerable to its bad habit of diligently creating pairs, even uncalled-for. This is when the simplicity of the γ-clustering overcomes the γ-tracking. The desire to get the best of each algorithm motivated the developement of a new algorithm, exposed later in this chapter.

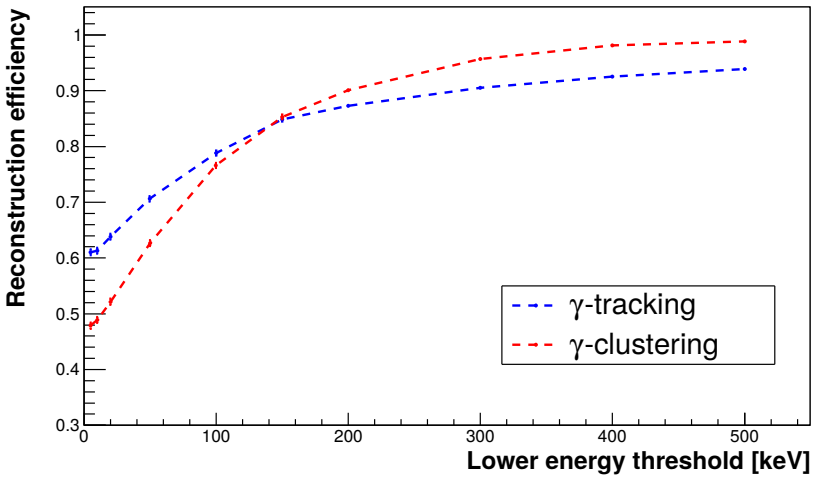

Figure 5.20 – γ reconstruction efficiency as a function of the lower energy threshold.

The detection efficiency presented in Figure 5.21, although mechanically higher, follows basically the same behavior as the single γ detection efficiency.

Eventually, below a 150 keV lower energy threshold, the total γ reconstruction efficiency is higher using the γ-tracking, while higher using the γ-clustering above this value, as shown in Figure 5.22.

The best total reconstruction efficiency is obtained using the γ-clustering, combined with an energy threshold close to 300 keV. The γ-tracking efficiency is maximum for a 150 keV energy threshold, where the γ-clustering performs equally. The better total reconstruction efficiency (for 2-γ events) obtained with an energy threshold higher than planned does not single-handedly justify an increase of the experiment's lower energy

threshold, especially considering the little gain it would provide compared to the number of $\beta\beta$-like events that would be missed. However, a higher energy threshold can be considered to be applied at the software level, only for the unassociated calorimeter hits.

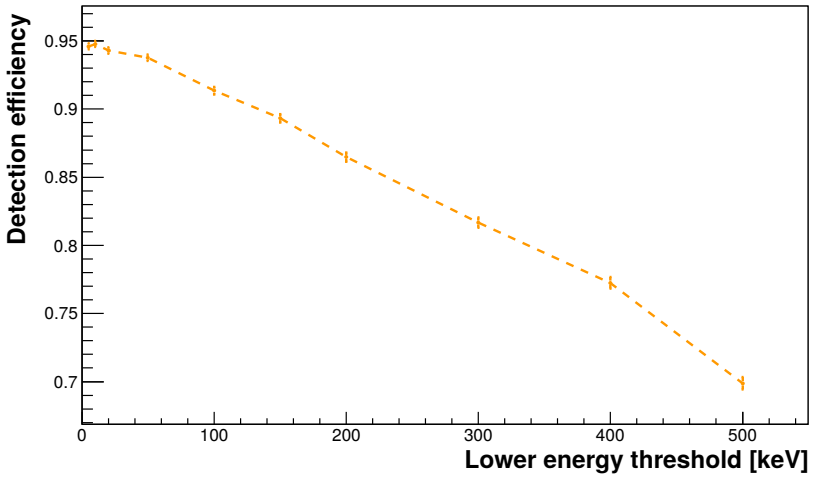

Figure 5.21 – γ detection efficiency as a function of the lower energy threshold

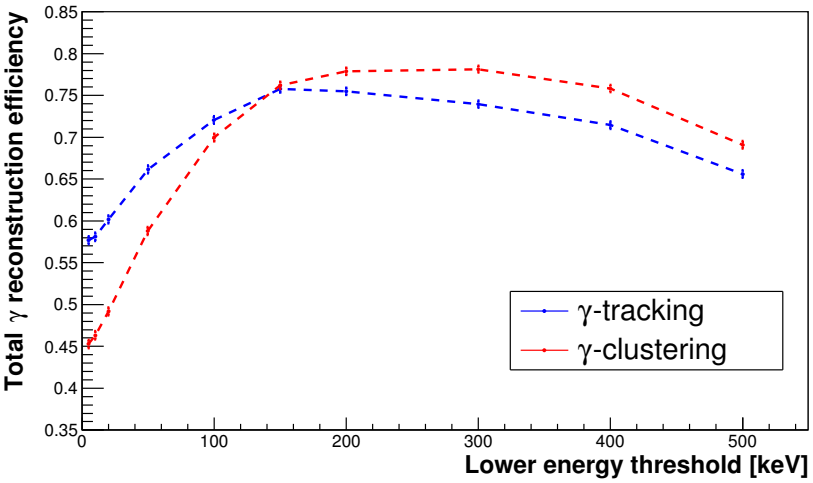

Figure 5.22 – Total γ reconstruction efficiency as a function of the lower energy threshold

Calorimeter time resolution

The γ-tracking reconstruction efficiency drops as the calorimeter time resolution worsens (*cf.* Figure 5.23). Indeed, with a higher time uncertainty, the measured calorimeter times are more smeared, which will blur the line even more between the two γ sequences

and increase the possibility of creating a wrongful pair of calorimeter blocks (as explained previously). For the same reasons as in the single γ study, the γ-clustering is also sensitive to the calorimeter time resolution. If no time difference between the neighboring calorimeter block is required, this dependence would disappear and the γ-clustering would become more efficient than the γ-tracking above a 600 ps time resolution.

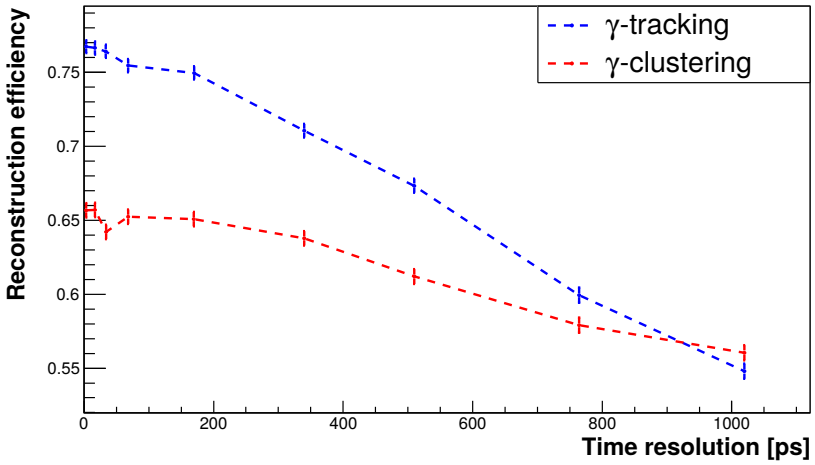

Figure 5.23 – γ reconstruction efficiency as a function of the calorimeter time resolution

Time delay between the γ's

In some processes, the γ-particles are not emitted simultaneously. By construction, the γ-tracking is sensitive to this phenomenon while the time measurements less affect the γ-clustering. The impact of a delay between the two γ emissions is presented in Figure 5.24. It appears that a 3 ns delay is more harmful to the γ-tracking algorithm than two simultaneous γ's. It might be counter-intuitive at first but a delay seems to increase the number of calorimeters blocks compatible for association with the "prompt" calorimeter hit. In particular, 3 ns is approximately the time it would take for a γ to go from one calorimeter wall to the other. However, above 20 ns the two γ's become uncorrelated, as if they were two independent γ's. For such events, one may notice that the reconstruction efficiency is 90 % at its best, in apparent disagreement with the previous, almost perfect, reconstruction efficiency for single γ events. However, this optimal efficiency was obtained with the standard and very low minimum pair probability. This was possible because no extra hits, other than from the single γ, were expected. For two γ events, it was shown that the value optimizing the γ-tracking reconstruction efficiency was significantly higher, namely P_{pair} = 20 %. Hence, the 90 % reconstruction efficiency for independent γ's.

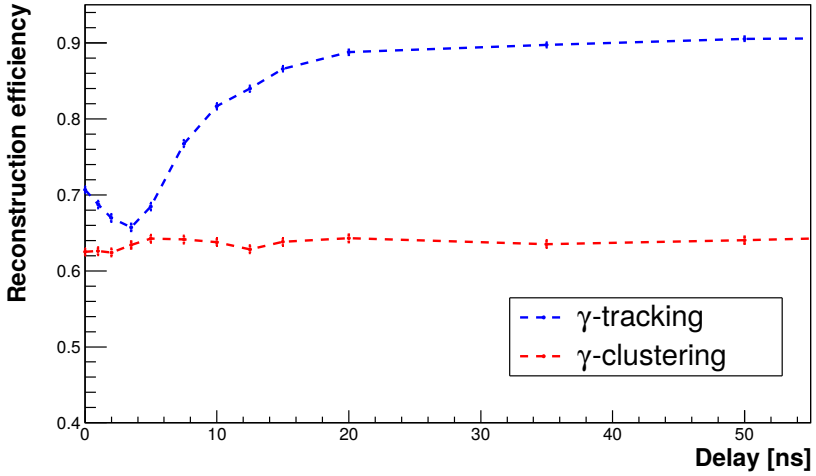

Figure 5.24 – γ reconstruction efficiency as a function of the time delay between the emissions of the two γ's.

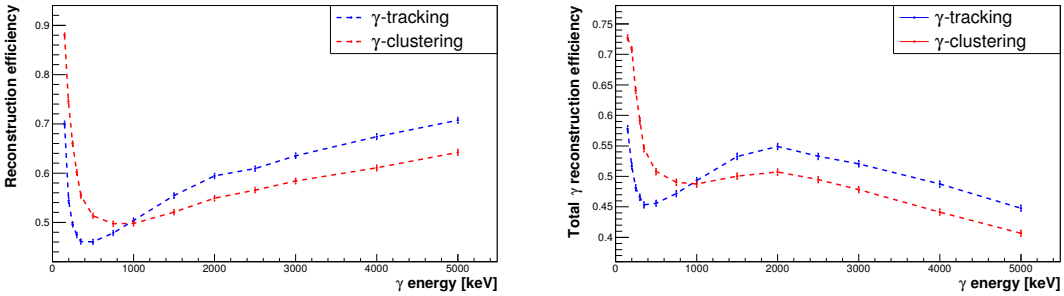

Figure 5.25 – Reconstruction efficiency *(left)* and total γ reconstruction efficiency *(right)* as a function of the 3 γ's energies.

5.4.4 Study of three-γ (and more) events

Once again, the reconstruction efficiency is the percentage of events correctly reconstructed, *i.e.* all the calorimeter hits are associated with the γ responsible for their triggering, among all the events eligible for reconstruction, *i.e.* with at least one calorimeter hit. What is called the total reconstruction efficiency is the percentage of events correctly reconstructed among the total number of events simulated. The higher these efficiencies, the better, even if the total reconstruction efficiency will systematically be lower than the reconstruction efficiency, due to the detector imperfect detection efficiency. From the single γ and the two γ studies, it is clear that the reconstruction efficiency is going to decrease, the more γ's are involved. The results for three, four and five monokinetic γ's are presented in Figures 5.25, 5.26 and 5.27.

The minimum pair probability in the γ-tracking was optimized for each number of γ's emitted and need to be increased as the γ content becomes higher. The two algorithms reconstruction efficiencies behave similarly for 3 γ, 4 γ and 5 γ events, as a function of the γ's energies. Low energy γ's (a few hundreds of keV), as explained before, only interact with one or two neighboring calorimeter blocks. According the Compton spectrum,

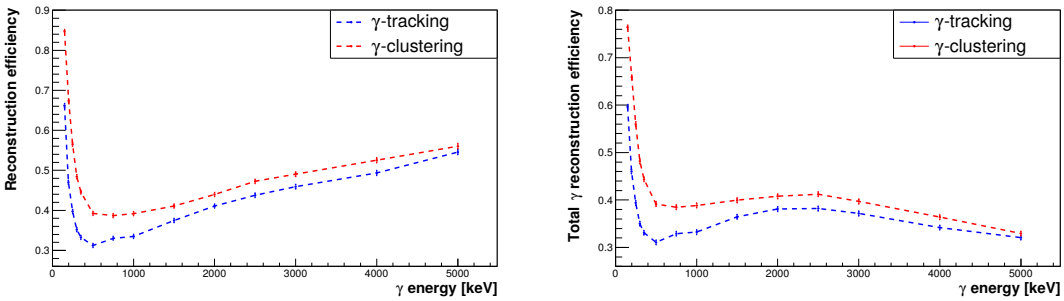

Figure 5.26 – Reconstruction efficiency *(left)* and total γ reconstruction efficiency *(right)* as a function of the 4 γ's energies.

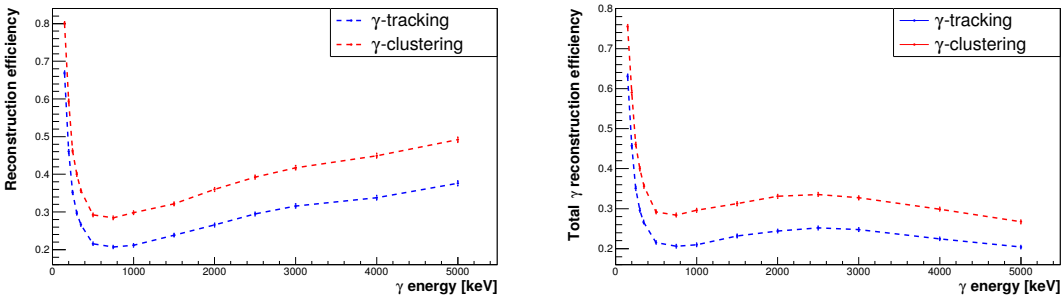

Figure 5.27 – Reconstruction efficiency *(left)* and total γ reconstruction efficiency *(right)* as a function of the 5 γ's energies.

the energy deposits might not even be enough to pass the trigger threshold. The events generated by low energy γ's are thus very simple and easily reconstructed with both algorithms. The γ-clustering consistently better reconstruct these events however, since there is still a chance for the γ-tracking to wrongfully link two distant clusters, and even more so when the number of γ's increases. As the energy of the particles increases, the events become more complex and the reconstruction efficiencies quickly plummet. With more γ's involved, the chances for at least one of them to backscatter and trigger two distant calorimeter blocks increase, which explains the drop in efficiency for the γ-clustering algorithm. Concerning the γ-tracking, the more calorimeter hits there are, the higher the chances for a mix up between the sequences, hence the same drop observed. The reconstruction efficiencies of both algorithms increases with the energy for the same reason the detection efficiency decreases: higher energy γ's have lower cross sections and mainly scatter forward *i.e.* out of the detector. The events are therefore simpler. In addition, higher energy deposits mean lower time uncertainties, thus yielding more accurate TOF measurements and improving the γ-tracking performance. The total reconstruction efficiencies are simply the product of the reconstruction efficiency by a detection efficiency decreasing with the energy. The γ-tracking performance appear to drop faster than that of the γ-clustering when the number of γ's grows. Eventually, the γ-clustering outperforms the γ-tracking for the events with more than 3 γ's.

5.4.5 Summary of pure γ events

To sum up the main results until this point:

- It was shown that the SuperNEMO bigger scintillator blocks compared to NEMO-3 improves the γ detection efficiency (*cf* Figure 5.11).
- For simple single γ events, the γ-tracking performs perfectly while the γ-clustering is mistaken in about one-fourth of the events (*cf* Figure 5.12). The total γ reconstruction efficiency for the γ-tracking is best for 500 keV γ's, with almost 80 % of the simulated γ's correctly reconstructed, while the γ-clustering tops at 60 % for γ's of lower energies (*cf* Figure 5.13).
- Regarding the influence of the energy threshold on single γ events (*cf* Figure 5.14): if the threshold is chosen to be high (either at the trigger level or during the analysis), say 350 keV, both algorithm perform equally (*cf* Figure 5.13). However, lowering the energy threshold provides a higher detection efficiency and while the γ-clustering reconstruction efficiency decreases at lower energy threshold, that of the γ-tracking remains steady, thus conferring an advantage to this algorithm.
- For 2 or 3 γ's events, the γ-tracking still performs better than the γ-clustering. It is only by increasing the energy threshold above 150 keV that the γ-clustering can prove more efficient than the γ-tracking and performs best with a 300 keV threshold.
- With more than 3 γ's in the event, the reconstruction efficiency is severely impacted, regardless of the algorithm employed. Thankfully, events with such γ contents are not expected in SuperNEMO and no analysis channels are dedicated to their study. As will be shown later, events with 3 γ's are already expected to represent few statistics in the analysis.

5.4.6 Study of ^{208}Tl events

Pure γ events are useful to characterize the behavior of both the detector and the reconstruction algorithms. However, such events will not constitute an analysis channel, not only because of trigger constraints, but also because all relevant physics processes involve at least one charged particle. The topologies expected from the ^{208}Tl background are $1e1\gamma$, $1e2\gamma$ and $1e3\gamma$ as reminded in Figure 5.62.

A 2.615 MeV γ is always expected while a 583 keV and a 511 keV γ are expected in 86 % and 22 % of the decays, respectively. These are only the most common γ-rays emitted and the number of γ-particles expected ranges between 1[c] and 3, with a variety of energies. The events of interest contain (at least) one reconstructed electron and at least one unassociated calorimeter hit. The reconstruction efficiency echoes the previous definition, namely all the calorimeter hits need to be attributed to the proper γ regardless of the strict chronological ordering of the calorimeter hits. Before looking at the overall reconstruction efficiency, it might be interesting to look at how both the γ-tracking and

[c] Actually, single-γ ^{208}Tl decays only occur in about 0.03 % of the decays.

the γ-clustering perform, depending on the topology of the events. Figure 5.28 shows the distribution of the number of γ clusters per event. The clusters are reconstructed with the γ-clustering algorithm and can contain only one calorimeter hit.

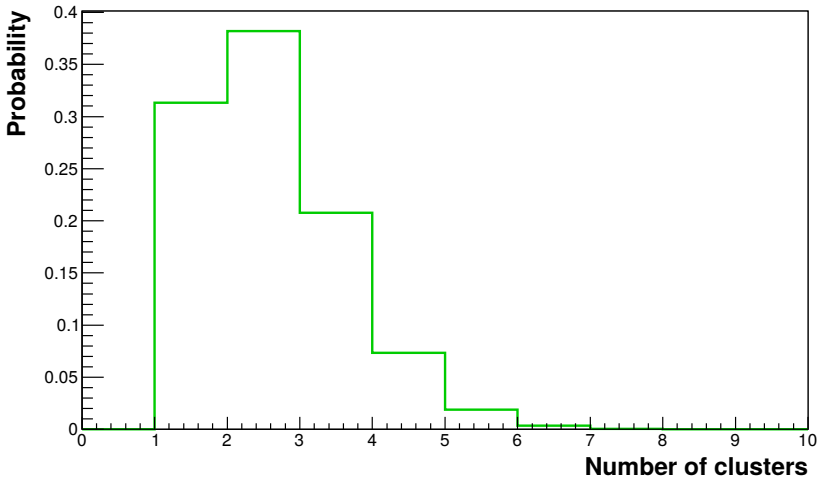

Figure 5.28 – ^{208}Tl number of clusters distribution

This distribution is the result of the convolution of the number of γ's emitted and the detection efficiency at their respective energies[d]. The most frequent events contain 2 clusters but up to 7 distinct clusters can be triggered. As mentioned before, the minimum pair probability allowed in the γ-tracking algorithm needs to be optimized depending on the complexity of the event. Figures 5.29, 5.31, 5.32, 5.33 and 5.34 show the two algorithms reconstruction efficiencies as a function of the γ-tracking minimum pair probability for events with 1 to 5 clusters. As a reminder, the γ-tracking minimum pair probability is the probability value above which the algorithm considers that two calorimeter hits have been triggered by the same γ-particle. No dependence of this parameter on the γ-clustering is expected. It is represented on the whole range to help as a reference.

For single cluster events (*cf.* Figure 5.29), the 12 % of failed reconstructions (for both clustering and tracking) consist mainly of events where a γ interacted in the same scintillator block as the electron (Figure 5.30) or in events where two γ's were emitted almost collinearly, consequently generating a single cluster (similarly to Figure 5.18).

Such events are, by design, impossible to reconstruct correctly. Coming back to Figure 5.29, increasing the minimum pair probability, up to the point where a sequence of neighboring calorimeter is split into two clusters, will induce the observed decrease in efficiency.

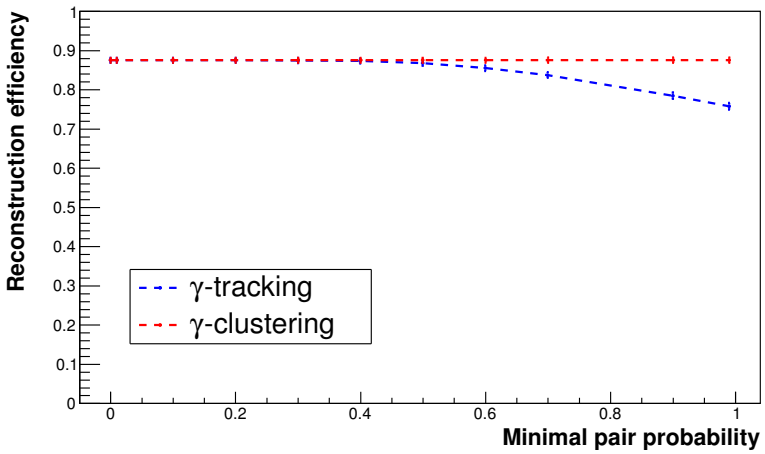

Figure 5.29 – Comparison of the two algorithms reconstruction efficiencies for ^{208}Tl events with 1 cluster, depending on the γ-tracking minimum pair probability.

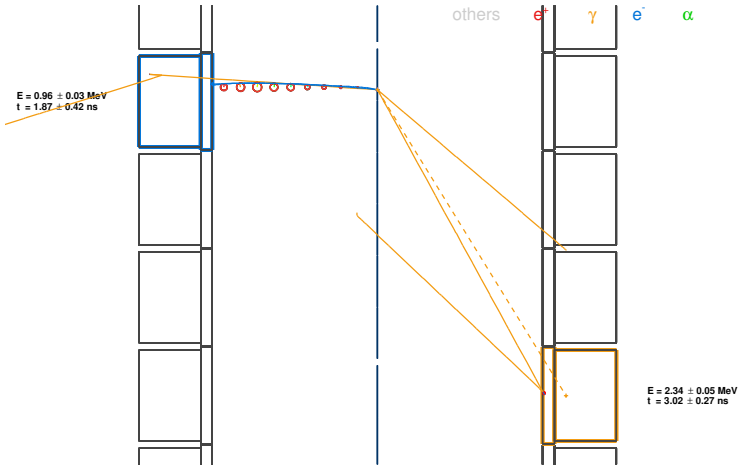

Figure 5.30 – Example of failed reconstruction where a γ interacts in the same block as the electron.

For 2-cluster events (*cf.* Figure 5.31), the optimization of the γ-tracking minimum pair probability enables a reconstruction efficiency comparable to that of the γ-clustering to be reached. The decrease of the γ-tracking reconstruction efficiency for higher minimum pair probabilities shares the same explanation as for single cluster events *.i.e.* if the condition is too stringent, clusters with multiple hits might be split up into two clusters or more. However, if the probability is too low, the two clusters might be considered as belonging to the same γ.

As the events become more complex (*cf.* Figure 5.32), the γ-tracking becomes more efficient than the γ-clustering. The more γ's there are, the more likely it is for a backscattering to occur. For 4-cluster events, since 4-γ events are not expected from the ^{208}Tl decay, the γ-clustering efficiency logically drops to zero (*cf.* Figure 5.33). The same goes for 5-cluster events (*cf.* Figure 5.34). The behavior of the γ-tracking reconstruction efficiency

[d]The γ-clustering efficiency to associate two neighbouring calorimeter hits in a cluster, based on the 2.5 ns maximum time difference required between them, plays a negligible role here.

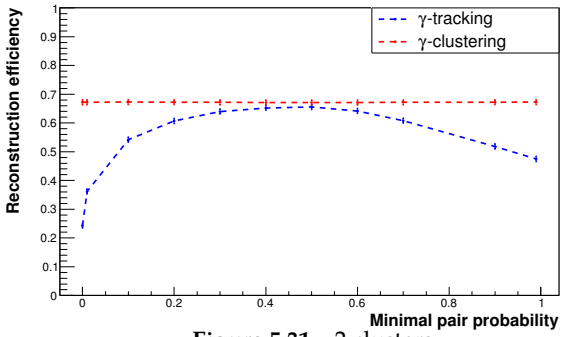

Figure 5.31 – 2 clusters

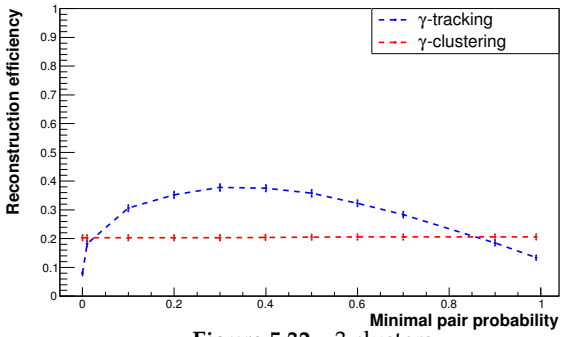

Figure 5.32 – 3 clusters

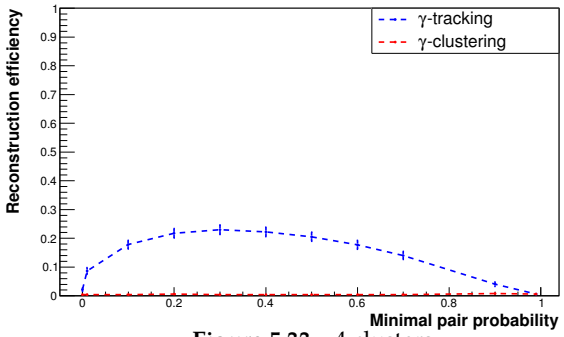

Figure 5.33 – 4 clusters

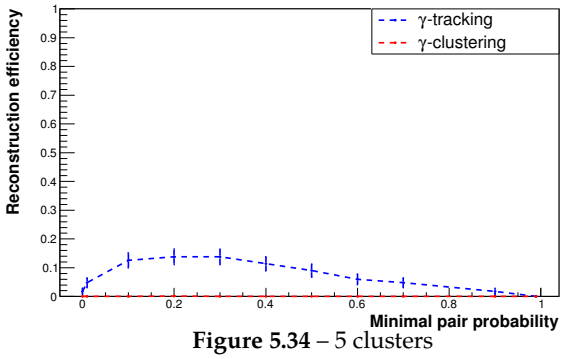

Figure 5.34 – 5 clusters

Figures 5.31, 5.32, 5.33, 5.34: Comparison of the two algorithms reconstruction efficiencies for ^{208}Tl events with 2, 3, 4 and 5 clusters respectively, depending on the γ-tracking minimum pair probability.

as a function of its minimum pair probability is roughly the same for 2-cluster events and more. It even manages to keep a decent reconstruction efficiency for 4- and 5-cluster events, albeit low. Figure 5.35 sums up these results, where the optimum minimum pair probability is considered. Both algorithms perform equally for single or double clusters events but the γ-tracking is more efficient for higher number of events. In particular, the γ-clustering cannot reconstruct correctly 4- and 5-cluster events since a maximum of 3 γ's can be emitted in ^{208}Tl decays. However, such events are not very frequent, as shown in Figure 5.28.

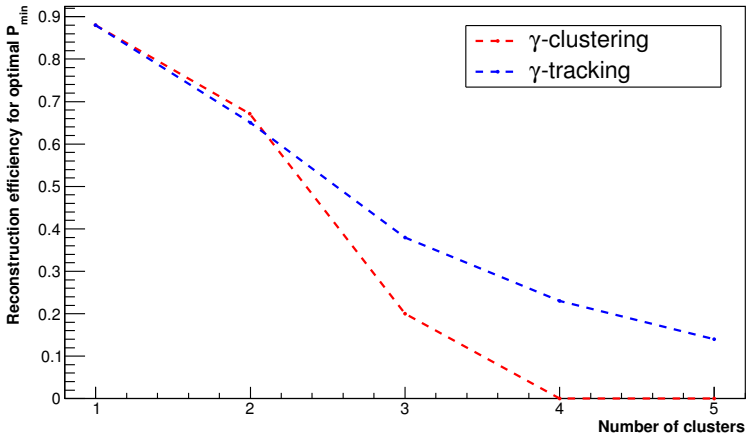

Figure 5.35 – Comparison of the two algorithms reconstruction efficiencies for ^{208}Tl events, depending on the number of clusters reconstructed.

To help better understand in which situation either algorithm is beneficial, the data from Figures 5.28 and 5.35 are superimposed in the upper part of Figure 5.36.

Indeed, by multiplying these two distributions, the overall improvement of the γ-tracking over the γ-clustering for ^{208}Tl events can be quantified. The most frequent events contain two clusters, which is a topology where the γ-clustering performs better than the γ-tracking. Yet, both algorithms perform almost as well for this category of events, with a slight advantage for the γ-clustering. On the contrary, even if 3 clusters (or more) events are less frequent, the γ-tracking is so much better for these topologies that it outweighs the gain of the γ-clustering for the 2-cluster events. Ultimately, the γ-tracking improves the overall reconstruction efficiency of ^{208}Tl events by 5 %.

By merging all the ^{208}Tl events topologies, the γ-tracking minimum pair probability can be optimized, as shown in Figure 5.37. It turns out the γ-tracking reconstruction efficiency can reach 63 % while the final γ-clustering reconstruction efficiency is 58 %.

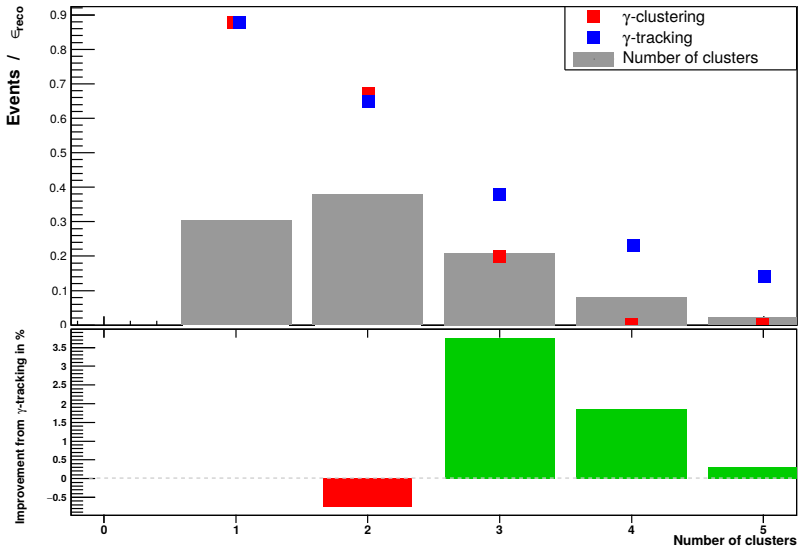

Figure 5.36 – Evaluation of the improvement from γ-tracking on the populations of events defined by their number of clusters.

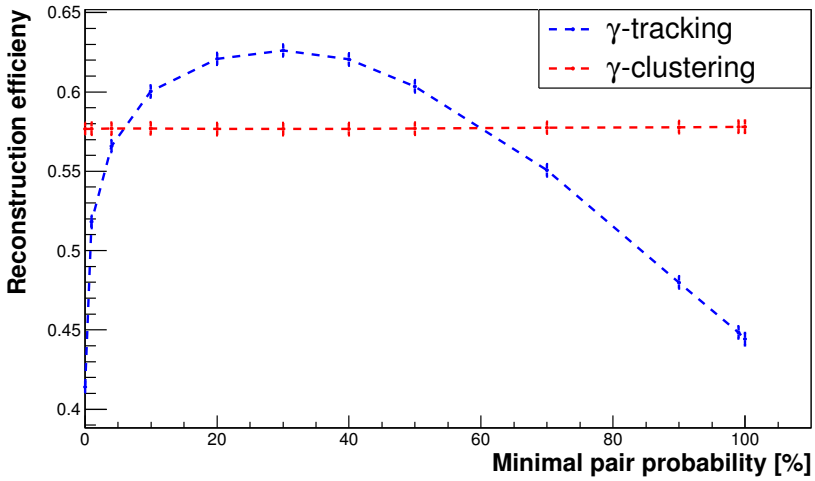

Figure 5.37 – ^{208}Tl reconstruction efficiency as a function of the γ-tracking minimum pair probability.

It might be interesting to study the influence of the lower energy threshold on the algorithms performances. On the hardware side, this value is driven by the PMTs single rate, etc., but the threshold is often chosen higher in physics analyses. By increasing the threshold, less hits are detected and the events become topologically simpler, which will ease the reconstruction process. This evolution is displayed in Figure 5.38.

In agreement with the previous results, the γ-tracking performs better than the γ-clustering at lower energy thresholds, where the γ's rebounds are more likely to be detected. On the contrary, increasing the energy threshold *i.e.* reducing the number of calorimeter hits, plays in the γ-clustering's advantage. Above a 200 keV threshold, the increase in the reconstruction efficiency is limited because the events are already simplified such that only pathological events, impossible to reconstruct, are remaining. Finally,

since, unlike the reconstruction efficiency, the detection efficiency (Figure 5.39) decreases with the energy threshold, an optimum is expected to be observed for the total reconstruction efficiency. The latter is drawn in Figure 5.40.

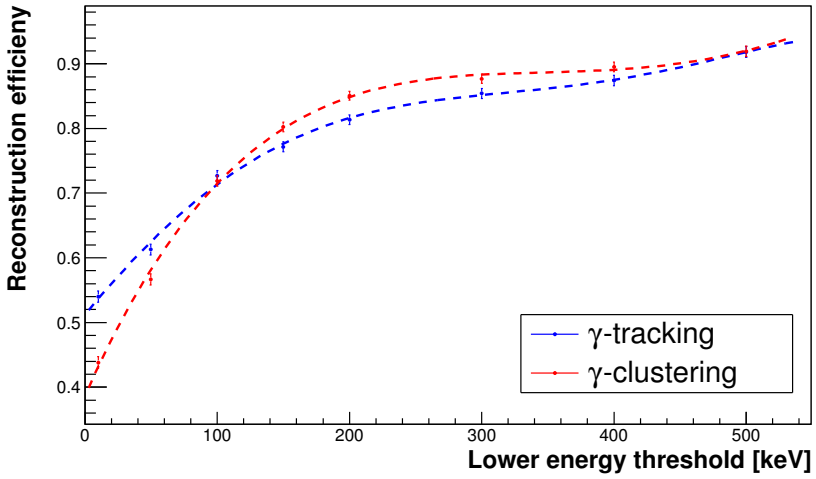

Figure 5.38 – ^{208}Tl reconstruction efficiency as a function of the lower energy threshold.

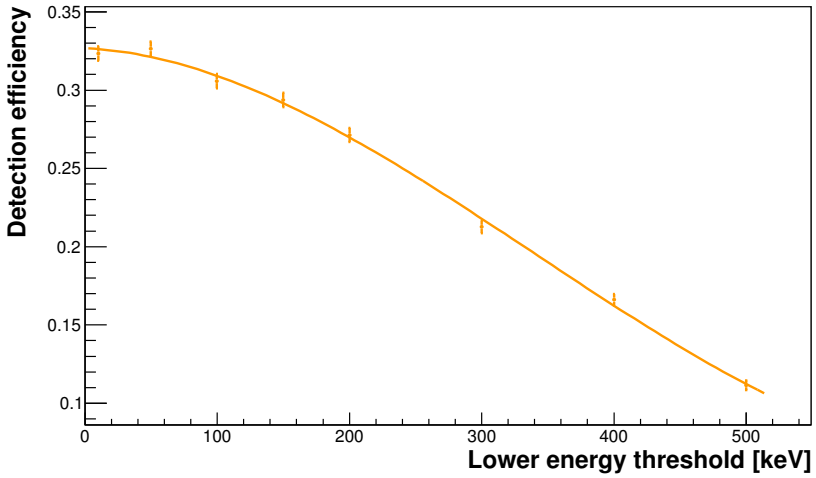

Figure 5.39 – ^{208}Tl detection efficiency as a function of the lower energy threshold.

Both algorithms perform optimally with a 150 keV lower energy threshold. This information can prove useful when the time comes to study the demonstrator data.

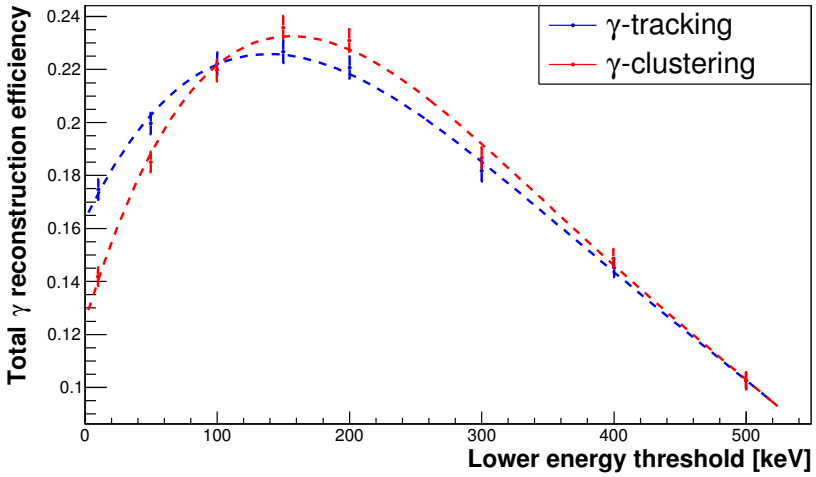

Figure 5.40 – ^{208}Tl total reconstruction efficiency as a function of the lower energy threshold.

5.4.7 Study of ^{214}Bi events

The exact same study has been performed for ^{214}Bi events. The observations and conclusions are very similar so this part will be stripped down to the results. The intermediate de-excitation levels of ^{214}Po from the ^{214}Bi decays are presented in Figure 5.70.

The most frequent γ is emitted in 46 % of the decays with a 609 keV energy and follows, in most cases (15 %), the emission of a 1.12 MeV γ. However, neither γ's can be emitted along with the 1.764 MeV de-excitation γ, occurring in almost 16 % of the decays. For ^{214}Bi, a decay to the ground state of ^{214}Po is possible, in which case no γ's are emitted. Eventually, the expected number of γ's emitted ranges from zero to two, with a variety of energies. The distribution of the reconstructed number of clusters is superimposed to the reconstruction efficiency for each topology in the upper part of Figure 5.41.

Unsurprisingly, less clusters are created and reconstructed in ^{214}Bi events than in ^{208}Tl events. Almost half of the events contain a single cluster while less than 5 % contain 4 or more. For each number of clusters, an optimum minimum pair probability yielding the best γ-tracking reconstruction efficiency was found. This time, the γ-tracking appears to systematically outperform the γ-clustering, regardless of the number of clusters involved in the event. The lower part of Figure 5.41 shows the improvement brought by the γ-tracking over the γ-clustering for each topology of events. The highest improvement is obtain for 3-cluster events. Since ^{214}Bi decays involving 3 γ's are very rare, these events are mostly made up of 2-γ events where one of them bounced around and triggered two distant calorimeter clusters. The γ-tracking is able to aptly reconstruct such events while the γ-clustering performs poorly. This way, about 9 % percents of the ^{214}Bi events are better reconstructed thanks to the γ-tracking compared to the γ-clustering.

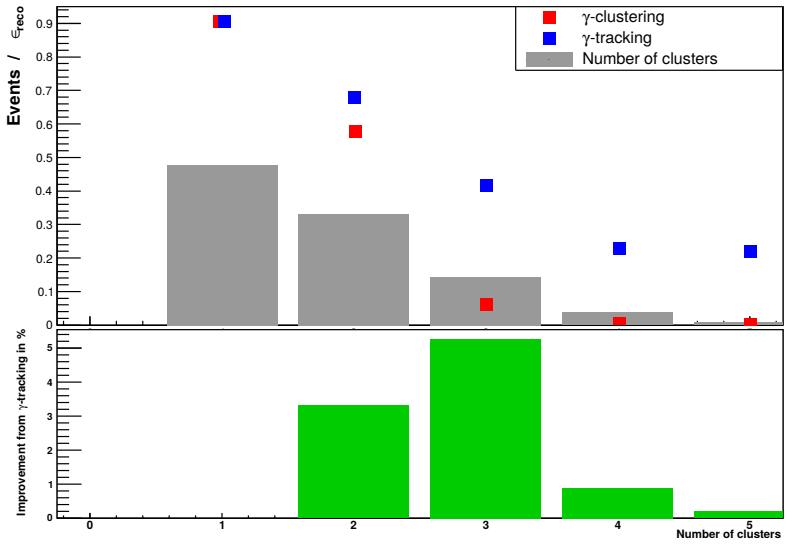

Figure 5.41 – Evaluation of the improvement from the γ-tracking on the populations of events defined by their number of clusters.

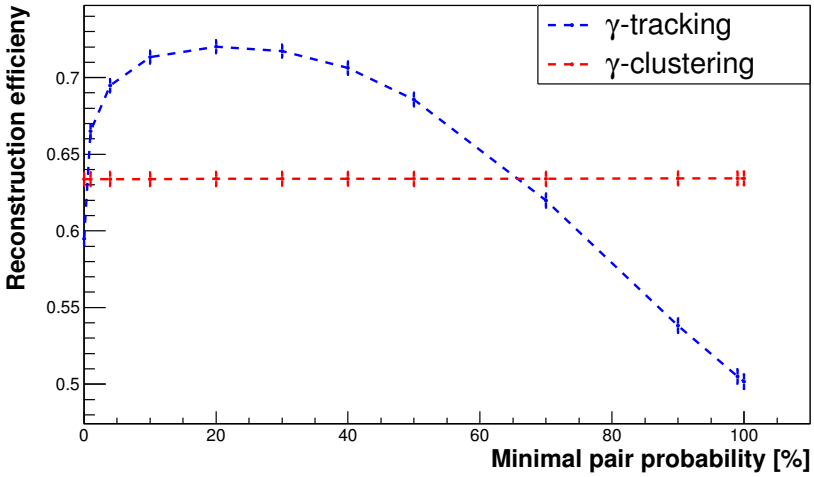

Figure 5.42 – ^{214}Bi reconstruction efficiency as a function of the γ-tracking minimum pair probability.

The optimization of the minimum pair probability (Figure 5.42) finally yields a 72 % reconstruction efficiency for the γ-tracking with P_{pair} = 20 %, while the γ-clustering correctly reconstruct 63 % of the events.

Like for ^{208}Tl decays, the γ-tracking performs better compared to the γ-clustering at lower energy thresholds, though the inversion occurs at a higher value, as illustrated in Figure 5.43.

The detection efficiency is not presented here but it also logically decreases with the energy threshold. However, since the average number of γ's emitted in a ^{214}Bi decay is lower than in a ^{208}Tl decay, the detection efficiency is overall lower.

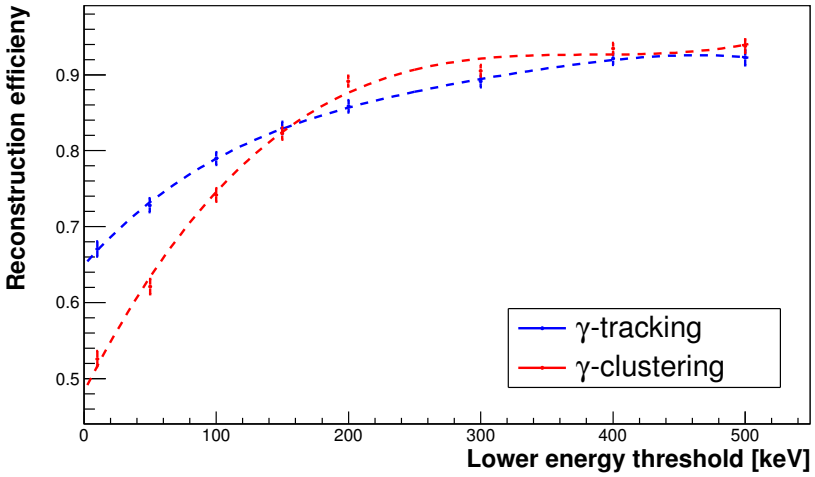

Figure 5.43 – ^{214}Bi reconstruction efficiency as a function of the lower energy threshold.

Looking at the total reconstruction efficiency in Figure 5.44, both algorithms perform equally with an energy threshold higher than 200 keV. The γ-clustering performs best with a 150 keV threshold while the γ-tracking performs even better with a 100 keV threshold.

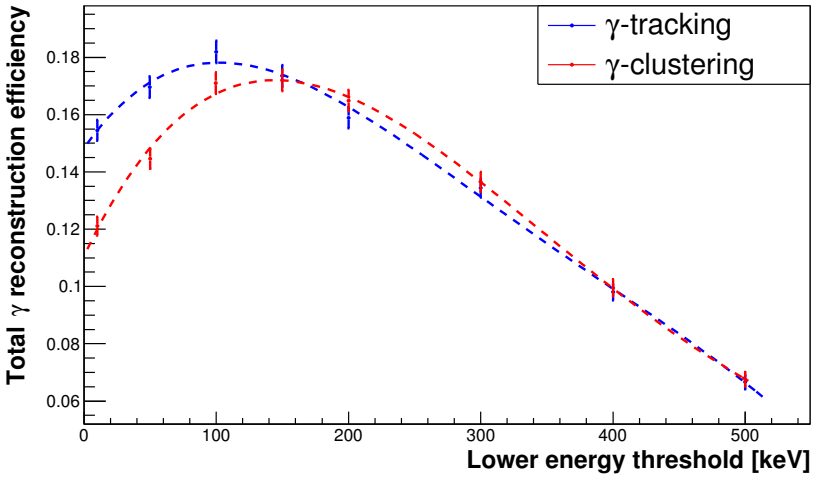

Figure 5.44 – ^{214}Bi total reconstruction efficiency as a function of the lower energy threshold.

Another interesting information, for both isotopes, is the distribution of the clusters size, presented in Figure 5.45. This shows that, independently of the isotope, the clusters size are the same and that the vast majority of these clusters are actually made up of a single calorimeter hit. The γ-clustering is thus only useful in about 10 % of events, while the γ-tracking, in addition to these events, also intervenes in back-scattering events, which can occur for about one-fourth of the γ's.

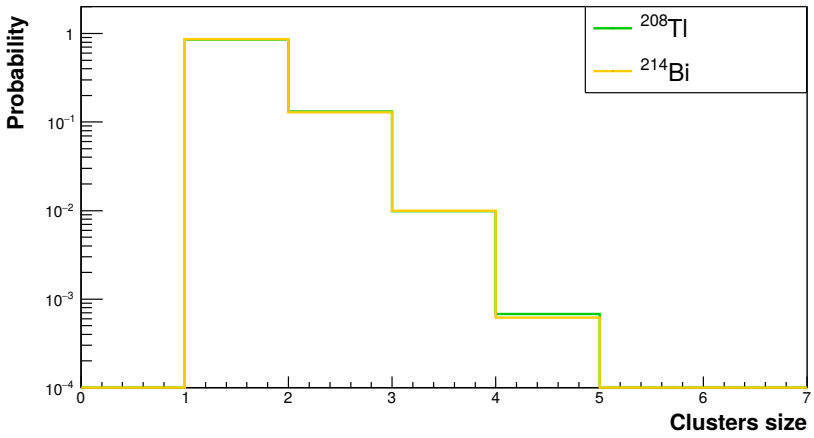

Figure 5.45 – Distributions of the reconstructed cluster sizes for ^{208}Tl and ^{214}Bi events.

5.4.8 Summary

Figure 5.46 summarizes the performances of both the γ-tracking and the γ-clustering algorithms for different physics processes. The γ-tracking appears to be more efficient for the physics processes relevant in SuperNEMO. The Table 5.4.8 sums up the performances of both the γ-clustering and the γ-tracking algorithms for the two main background sources for the $0\nu\beta\beta$ search in NEMO-3, and probably in SuperNEMO as well. These efficiencies are presented with the standard 150 keV and 50 keV energy thresholds. The γ-tracking offers a 11-21 % relative increase in the proportion of faithfully reconstructed events in the$1eN\gamma$ channel, compared to the γ-clustering:

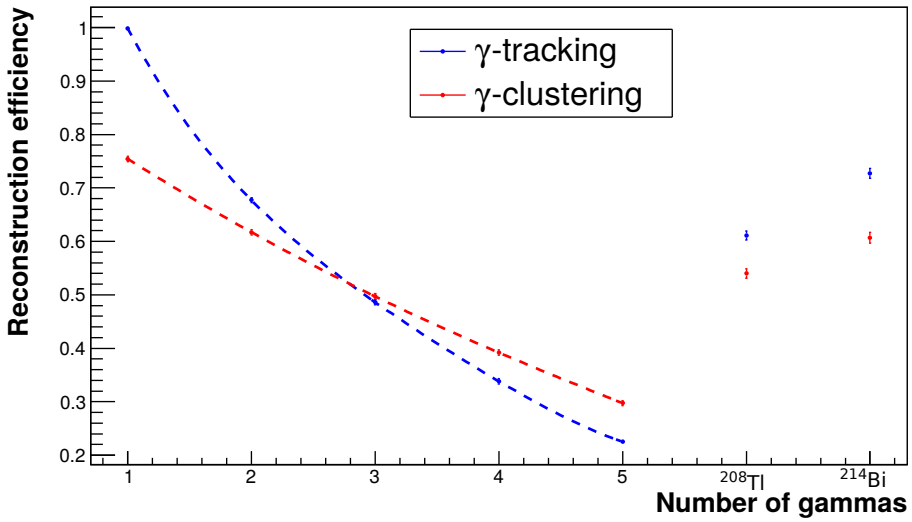

Figure 5.46 – Reconstruction efficiency of the γ-tracking and the γ-clustering algorithms for several physics processes.

	γ-clustering	γ-tracking
	ϵ_{rec} / ϵ_{tot}	ϵ_{rec} / ϵ_{tot}
^{208}Tl	58 % / 18 %	63 % / 20 %
^{214}Bi	65 % / 14 %	72 % / 17 %

Despite the higher reconstruction efficiencies for ^{214}Bi events compared to ^{208}Tl events, one can notice that the total reconstruction efficiencies are better for the ^{208}Tl than for the ^{214}Bi. This comes from the lower detection efficiency in ^{214}Bi events because the average number of γ's emitted is lower than in ^{208}Tl events. It should also be noted that the minimum pair probability and the lower energy thresholds were studied independently. There might actually exist a better combination of these parameters which would provide better reconstruction efficiencies. However, the 50 keV lower energy threshold in the demonstrator is a sensible choice, considering that higher thresholds can be used later, at the analysis stage. The analysis of the calibration runs should also shed light on the optimum parameters for the γ-reconstruction algorithms.

5.4.9 Motivation for a new algorithm

The studies presented until this point might have provided a sense of the strengths and weaknesses of both algorithms, but also given rise to the feeling that these approaches might actually be complementary. Indeed, the two populations of successfully reconstructed events do not fully overlap: this means that some events are only aptly reconstructed with the γ-tracking, but not *via* the γ-clustering, and vice-versa. Figure 5.47 shows the distribution of these events for the ^{208}Tl isotope.

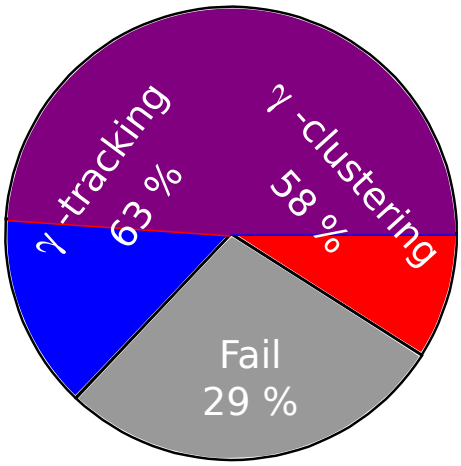

Figure 5.47 – Distribution of the ^{208}Tl events according to whether they are successfully reconstructed using the γ-tracking, the γ-clustering, both or neither. 63 % of the events are successfully reconstructed using the γ-tracking (blue) and 58 % using the γ-clustering (red). The violet part represents the events successfully reconstructed by both the algorithms and the gray part by neither of them.

Ideally, if one was able to benefit from both algorithms, up to 71 % of the ^{208}Tl events could be correctly reconstructed, hence the motivation to create a new algorithm, called γ-tracko-clustering.

The idea behind the γ-tracko-clustering algorithm is to take advantage of what each algorithm does best, namely cluster building with the γ-clustering and pair recognition thanks to the γ-tracking.

5.5 The γ-tracko-clustering

5.5.1 Principle

This new algorithm, along with the two others, was implemented in Falaise and made available to the collaboration. Its principle is exposed in the following lines and illustrated in Figure 5.48.

First, a standard clustering on the unassociated calorimeter hits is performed. The required time difference between two calorimeter hits within the same cluster below which they are considered as belonging to the same γ is left free for the user to choose (by default it is set to Δ t_{intra} = 2.5 ns). The next step is to figure out if the clusters can be linked together using the same TOF probability calculations as in the γ-tracking. When dealing with clusters, the simplest and most logical times to be used in TOF calculations are those of the last calorimeter hit from the first cluster and the first calorimeter hit from the second cluster. However, a 50 keV energy deposit, considering the calorimeter energy and time resolution, will induce a 1.8 ns time uncertainty on the measurement. Yet, the time scale separating two neighboring calorimeter blocks is typically of the order of 1 ns. In clusters with low energy deposits, the chronological sequence is not accurate: the first calorimeter hit could actually be the second, or the penultimate or even the last. An example of a chronological inversion of hits within a cluster is displayed in Figure 5.49.

Consequently, a criterion on the calorimeter hit "quality" is simply the value of the associated time uncertainty. This criterion is a free parameter of the algorithm and can be optimized. Finally, the TOF probability between the last "good" hit of a cluster and the first "good" hit of another cluster is computed. This computation is performed for all possible combinations of clusters. Like in the γ-tracking, the probability threshold above which the association is considered righteous is configurable. Assuming a cluster exhibits good probabilities with several other clusters, the pair with the highest probability is chosen[e]. If the second cluster is already involved in a γ sequence, the choice is made to skip it, regardless of its probability. In addition, this tracko-clustering algorithm forbids the association of two clusters from the same wall. Indeed, the probability for a γ to cross a scintillator laterally, and *a fortiori* several scintillators, without interacting is quite low. Eventually, the sequences of hits are built, pairs of clusters after pairs of clusters.

[e]This choice might be questionable since, assuming a Gaussian distribution of the experimental and theoretical TOF differences, the resulting probability distribution will be flat. This means there are as many pairs in the 50-55 % probability range as there are in the 90-95 % probability range. However, since random coincidences will more likely populate the lower pair probabilities region, the choice was made to arbitrarily select the pair with the highest probability.

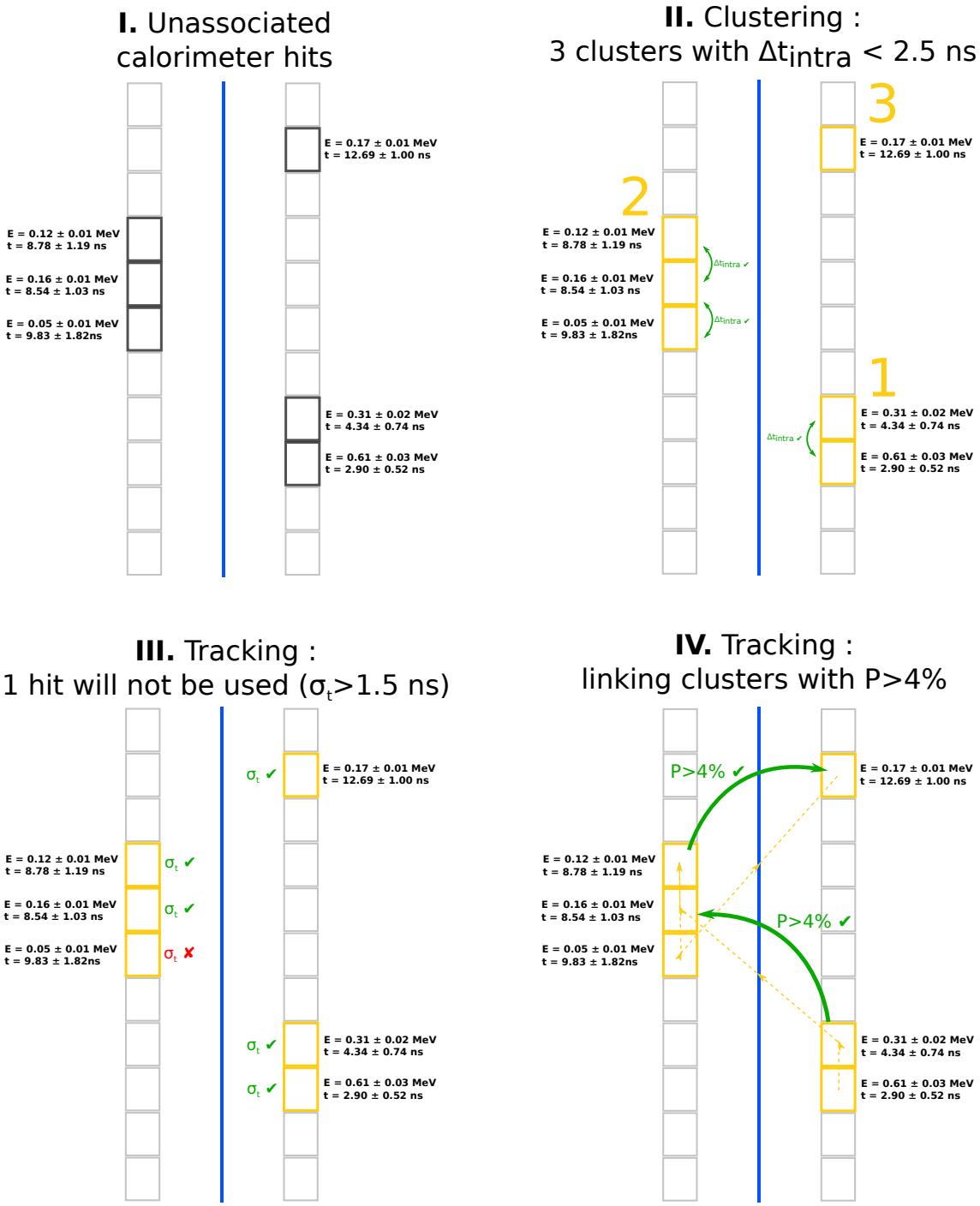

Figure 5.48 – **I.** Unassociated calorimeter hits to be reconstructed. **II.** Standard clustering with a customizable condition on the time difference between two calorimeter hits within the same cluster. **III.** Selection of the ”good” calorimeter hits for the TOF calculations. **IV.** Computation of the TOF probability between the last and first ”good” hits of two clusters. The reconstructed path follows the chronological order.

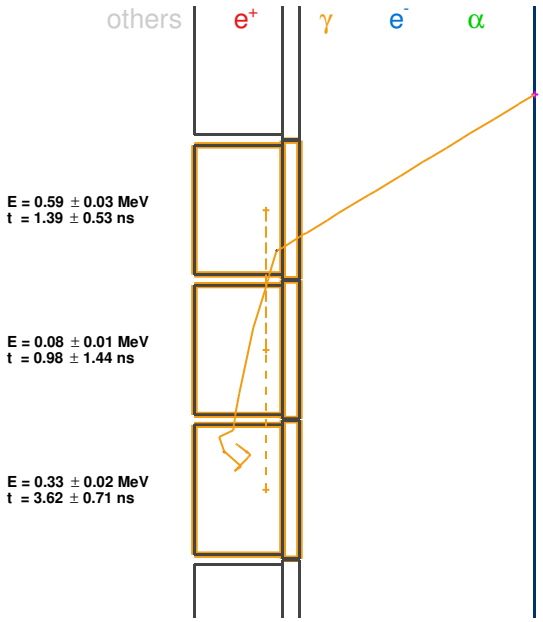

Figure 5.49 – Display of a cluster where the chronological sequence is different from the simulated sequence, due to the limited energy resolution in low energy deposits.

5.5.2 Example of parameters optimization on ^{208}Tl events

The minimum pair probability is the first parameter one can be tempted to optimize. Figure 5.50 shows the γ-tracko-clustering reconstruction efficiency as a function of the minimum pair probability. The γ-clustering reconstruction efficiency serves as a reference. The algorithm operates best around P_{pair} = 30 %: below that, more unfortunate associations are allowed while above, some are missed. This behavior is naturally not dissimilar to that of the γ-tracking.

The influence of the internal time difference within a cluster on the reconstruction efficiency is shown in Figure 5.51. It appears that completely releasing this constraint improves the reconstruction efficiency. The default value still provides a quasi-optimum reconstruction efficiency.

The optimization of the "good" calorimeter hit criterion, namely the time uncertainty, does not seem to bring any improvement in the reconstruction efficiency.

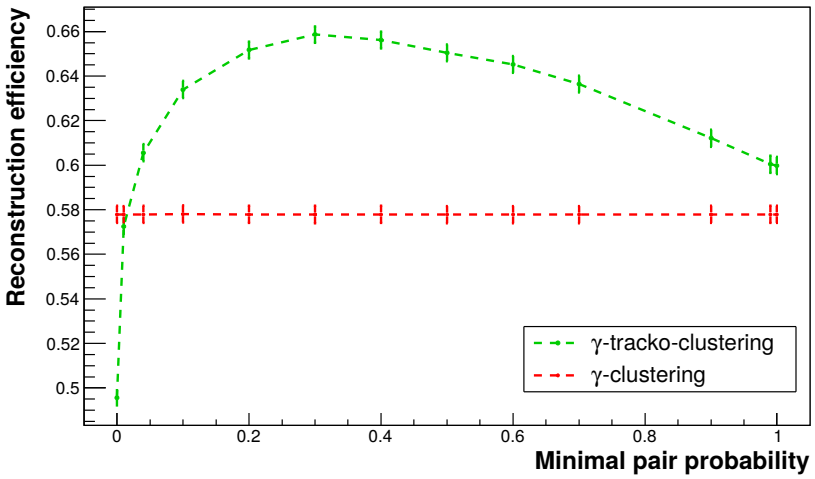

Figure 5.50 – ^{208}Tl reconstruction efficiency as a function of the minimum pair probability.

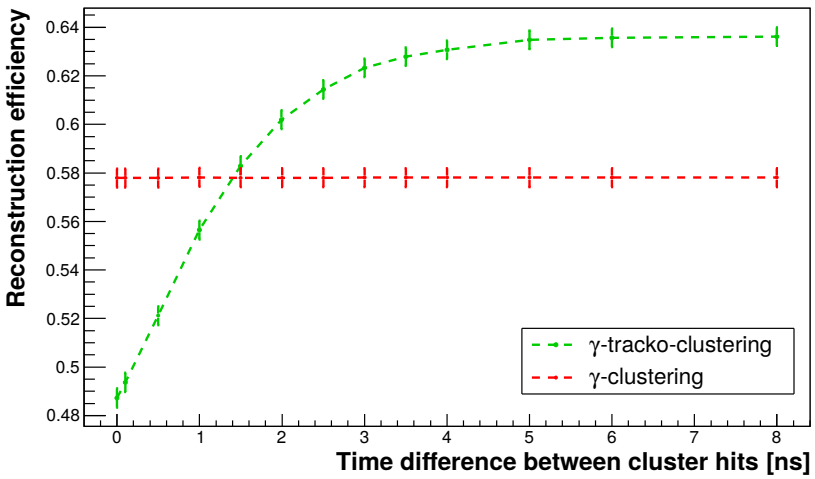

Figure 5.51 – ^{208}Tl reconstruction efficiency as a function of the cluster internal time difference $\Delta_{t_{\text{intra-cluster}}}$

5.5.3 Comparison of the performances

Now that an optimum configuration of the γ-tracko-clustering algorithm has also been established, the reconstruction efficiency of each algorithm is presented in Figure 5.52, as a function of the lower energy threshold. For lower energy thresholds, where the γ-tracking used to perform the best, the γ-tracko-clustering now performs even better. Above 150 keV, the γ-tracko-clustering and the γ-clustering performs almost equally with a slight advantage for the latter. With a very high threshold, it is possible to reach almost a 90 % reconstruction efficiency. Yet, taking into account the detection efficiency, the total reconstruction efficiency, displayed in Figure 5.53, is optimum with the γ-tracko-clustering algorithm with a 150 keV threshold and amounts to 24 %. Using the γ-tracko-clustering reconstruction would ensure the best reconstruction efficiency regardless of the energy threshold. The results are essentialy the same with ^{214}Bi events, as shown in Figure 5.54 and Figure 5.55.

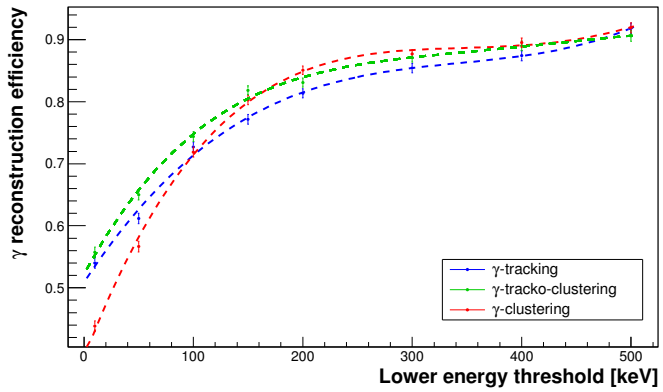

Figure 5.52 – ^{208}Tl reconstruction efficiency as a function of the lower energy threshold.

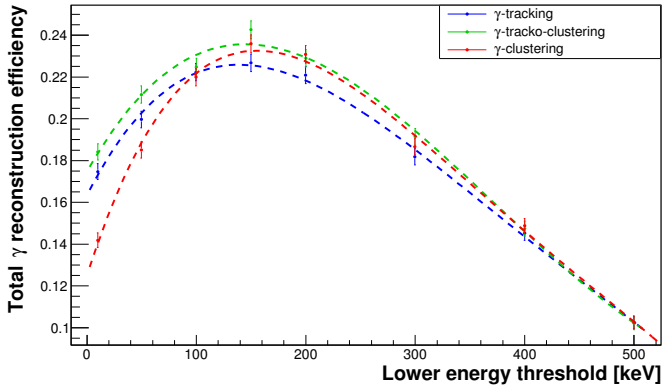

Figure 5.53 – ^{208}Tl total reconstruction efficiency as a function of the lower energy threshold.

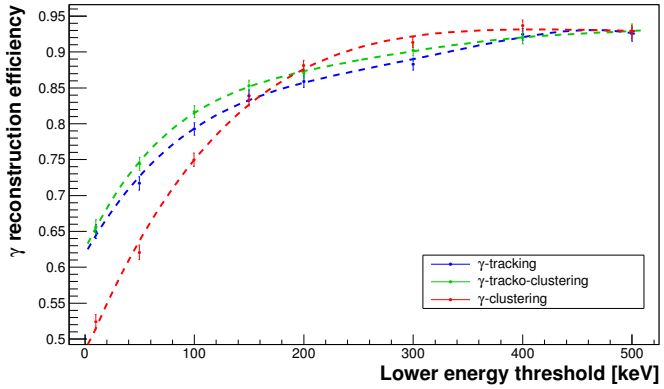

Figure 5.54 – ^{214}Bi reconstruction efficiency as a function of the lower energy threshold

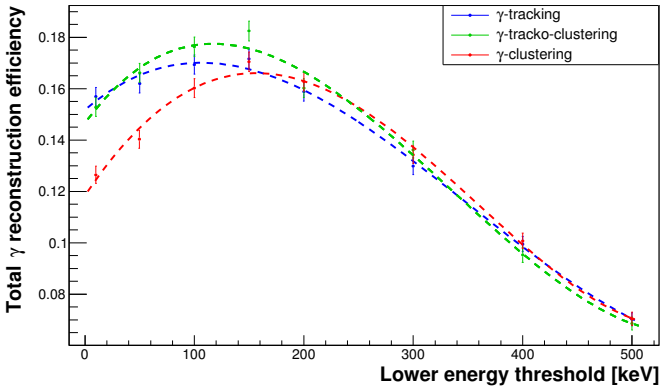

Figure 5.55 – ^{214}Bi total reconstruction efficiency as a function of the lower energy threshold

The improvements for both ^{208}Tl and ^{214}Bi events are gathered in the Table 5.1 [f].

Eventually, the γ-tracko-clustering provides a 17-24 % relative increase in the total reconstruction efficiency compared to the simpler γ-clustering. This means that this new algorithm managed to successfully reconstruct events that were previously only correctly reconstructed by either the γ-clustering or the γ-tracking. The improvement is not however as high as expected. The γ-tracko-clustering can operate on a spectrum of regimes, depending on its configuration, that will make it behave more like the γ-clustering or, on the other end of the spectrum, more like the γ-tracking. However, the optimum set of parameters does not appear to allow the complete merge of both populations of successfully reconstructed events. Based solely on an increase in statistics, there seems to be little incentive to use a more intricate reconstruction algorithm. However, the possible biases

[f] The efficiencies presented are only accurate to within 1 %. In addition, these efficiencies have been evaluated on a different simulation sample. These two factors explain the slight variations in efficiencies, compared to the previous ones.

	ϵ_{rec} / ϵ_{tot}		
	γ-clustering	γ-tracking	γ-tracko-clustering
^{208}Tl	56 % / 18 %	61 % / 20 %	65 % / 21 %
^{214}Bi	63 % / 14 %	72 % / 16 %	75 % / 17 %

Table 5.1 – Comparison of the three algorithms performances for ^{208}Tl and ^{214}Bi events: the reconstruction efficiency ϵ_{rec} represents the ability of the algorithm to reconstruct faithfully enough an event provided it has all the required calorimeter's information, while the total γ reconstruction efficiency ϵ_{tot} takes into account the γ detection efficiency (undetected γ's make the event misconstructed)

induced by simpler algorithms on the reconstructed energy spectra are crucial. As will be shown in the next part, the interest of the γ-tracko-clustering does not only resides in a better reconstruction efficiency.

5.6 Study of the γ energy reconstruction

The individual energies of the γ's are pivotal, since they provide information that will allow the identification of the process at the origin of the event. More than an efficient algorithm, a faithful γ-reconstruction algorithm is essential to SuperNEMO. This part is dedicated to the characterization and comparison of the energy reconstruction capabilities of the three available algorithms.

5.6.1 Single monokinetic γ spectrum

To understand the response of the detector and the shape of the reconstructed γ energy spectra, it might be useful to focus on a simple case first: a single 2 MeV- γ. The 2 MeV energy choice was motivated by the wish to bring out all the different spectrum features. To simplify, only one reconstruction algorithm is first considered, say the γ-tracking.

If an energy deposit occurs with a single Compton scattering, one would expect a flat energy distribution, with a Compton edge below the original simulated energy, similar to that of Figure 5.3. Instead, the reconstructed energy spectrum, presented in Figure 5.56, exhibits a peak right below its genuine energy and a flat distribution for lower energies.

Indeed, given the size of the scintillator, once a γ interacts through Compton effect, its energy decreases, making following Compton interactions more likely (Figure 5.1). If the γ particle is contained in a single block through multiple Compton scattering, close to all its energy can be measured, hence the peak observed close to the total γ energy. Before comparing the spectra obtained using the different reconstruction algorithms, we focus on the unexpected "peak" observed in the low-energy region. Increasing the detection threshold above this peak allows its removal without inducing a similar effect, it is thus not a threshold effect. In order to explain this peak and to validate our model of γ interaction in the detector, the impact of the number of energy deposits in the event is studied. To simplify, only the events with one calorimeter block triggered are selected. Figure 5.57 provides the distribution of the number of interactions and, *a fortiori*, of energy deposits

for a single 2 MeV-γ in one scintillator block.

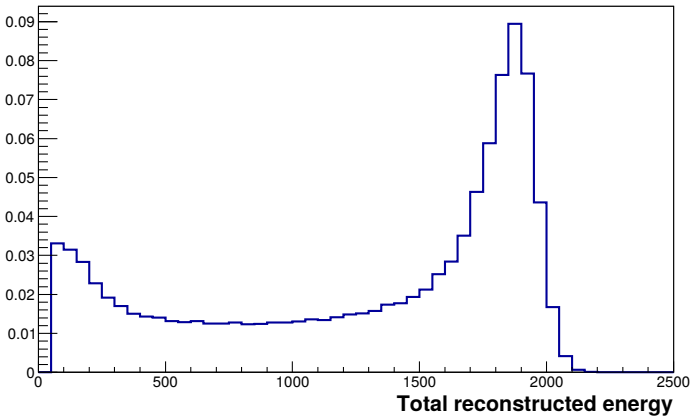

Figure 5.56 – Reconstructed energy spectrum for a single monokinetic 2 MeV-γ in a single calorimeter block.

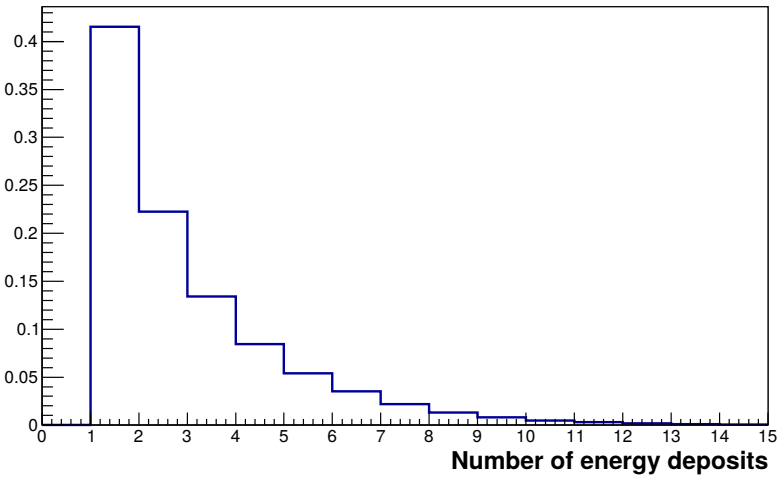

Figure 5.57 – Distribution of the number of energy deposits in one scintillator block.

Most of the events interact once and leave the scintillator, while some γ's interact more than 10 times in a single calorimeter block. It might then be relevant to look at the energy reconstructed for each of these populations of γ's. The spectra of γ's interacting once, twice and five times in the detector are presented in Figure 5.58.

Unexpectedly, the spectrum obtained with single energy deposits does not resemble that of the theoretical Compton energy spectrum. Though the spectrum is arguably flat for energies higher than 400 keV, the low energy peak is also present. For two energy

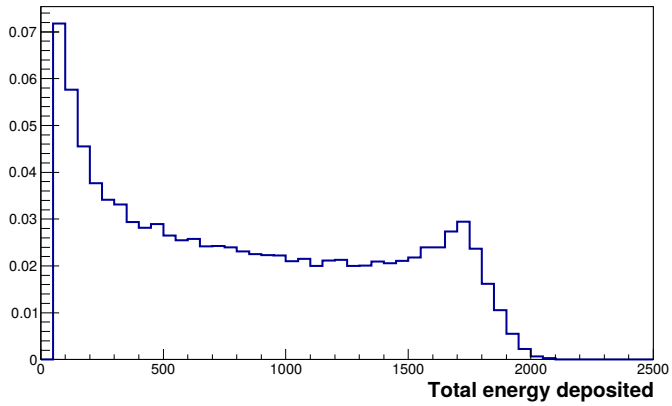

(a) 1 energy deposit

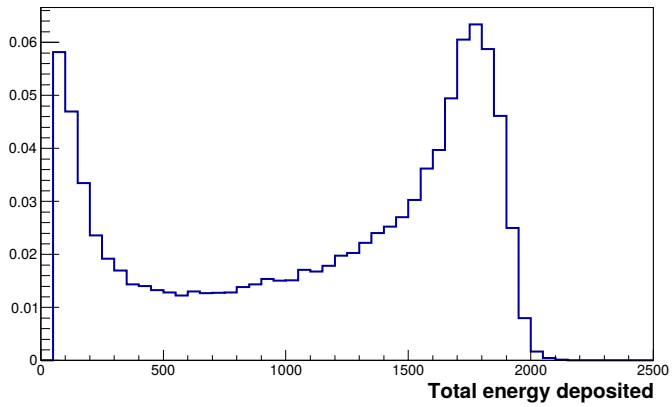

(b) 2 energy deposits

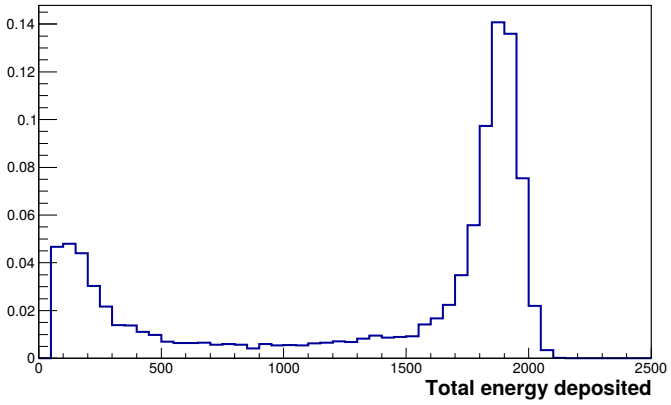

(c) 5 energy deposits

Figure 5.58 – Energy spectra for events with 1 (5.58a), 2 (5.58b) or 5 (5.58c) energy deposits in a single calorimeter block.

deposits and, *a fortiori*, for five, the energy distribution is located below the genuine energy, which is somewhat expected. However, in both cases, the lower energy peak is once again present. In theory, it might be possible for a γ to undergo several low angle Compton scattering, thus depositing only a few hundreds of keV. But given the geometry of the detector, it more likely means that the γ has lost most of its energy, before dying in the calorimeter. Actually, looking at the events interacting several times in the calorimeter, while deposing little energy, corroborates this explanation. Two examples are shown in Figure 5.59 and 5.60: the γ interacts with a non-sensitive part of the detector before depositing the remaining of its energy in the calorimeter.

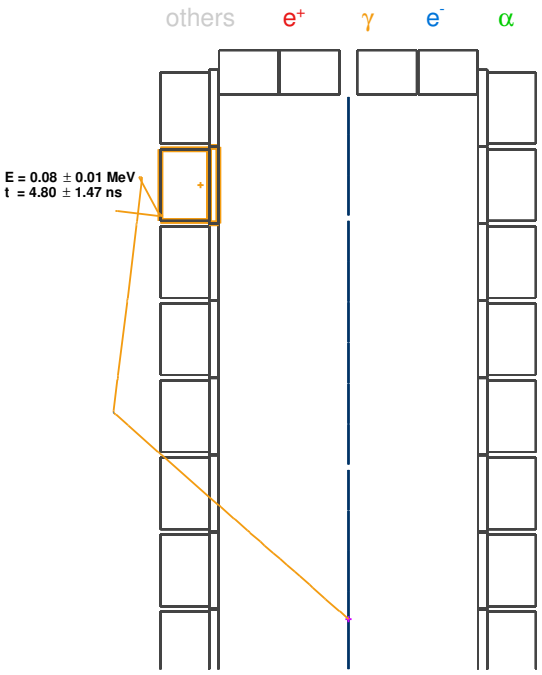

Figure 5.59 – Display of an event where the γ interacted outside the detector before being detected.

Obviously, the γ's leaving the detector and coming back are the γ's which either backscattered or scattered multiple times: these γ's consequently come back with little energy remaining. The non-sensitive parts of the detector can either be the tracker upper and lower parts, the magnetic shieldings or even any material outside the calorimeter, if the γ went through the scintillator without interacting. Of course, events with small energy deposits due to small angle Compton interactions, such as the one presented in Figure 5.61, also populate this peak, with the same frequency they do the flat region of the spectra.

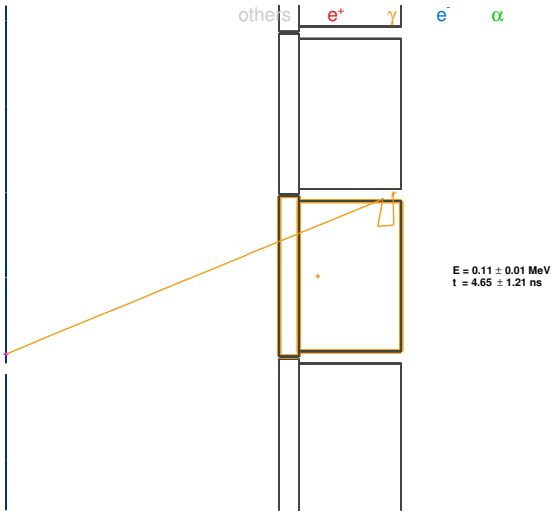

Figure 5.60 – Display of an event where the γ interacted in the magnetic shielding before being detected.

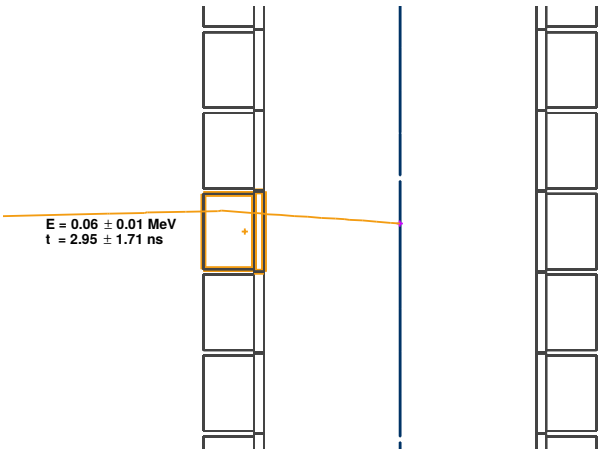

Figure 5.61 – Small angle Compton interaction leading to a small energy deposit.

Eventually, this effect accounts for less than 10 % of the γ's[g] (about 8.5 % in this simple example). The conclusion is that this effect is specific to the SuperNEMO detector and this spectrum distortion should be kept in mind in future analyses. Now that the energy spectrum of single γ events in SuperNEMO is understood, let's compare the performances of the different γ reconstruction algorithms on ^{208}Tl and ^{214}Bi events.

5.6.2 ^{208}Tl spectra

The ^{208}Tl decay scheme is reminded in Figure 5.62 for convenience.

The algorithms mechanics are different so, for the same event, the number of γ's each algorithm will reconstruct might be different. The distribution of the reconstructed number of γ's is shown in Figure 5.63: the γ-clustering expectedly tends to reconstruct more

[g] Actually, a fraction of these events could easily be rejected by requiring a good internal probability of the γ with a charged particle from the source for instance. Indeed, it takes some time for these γ to scatter before being detected. This delay will then cause lower internal probabilities.

γ's (a bouncing γ is seen as multiple γ's) while the TOF-based algorithms strive to make pairs of clusters, thus decreasing the average number of γ's reconstructed.

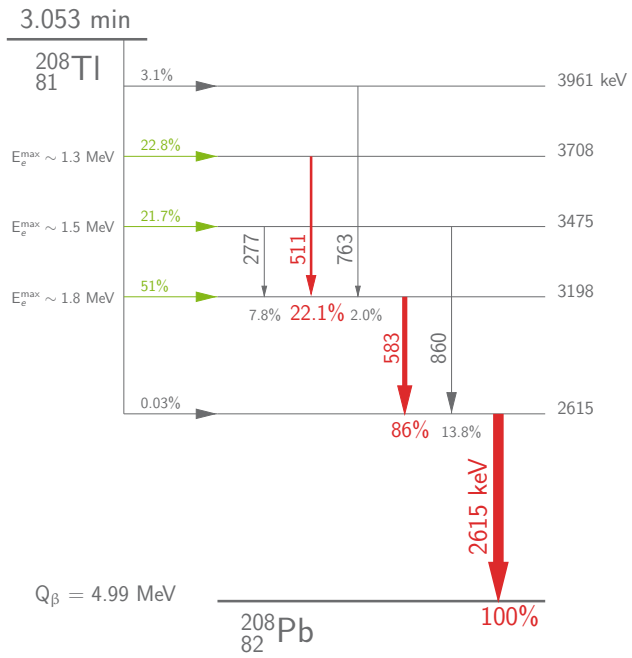

Figure 5.62 – ^{208}Tl decay scheme: The red arrows represent the most frequent γ-rays emitted where the percentage is the fraction of decay events in which they appear.

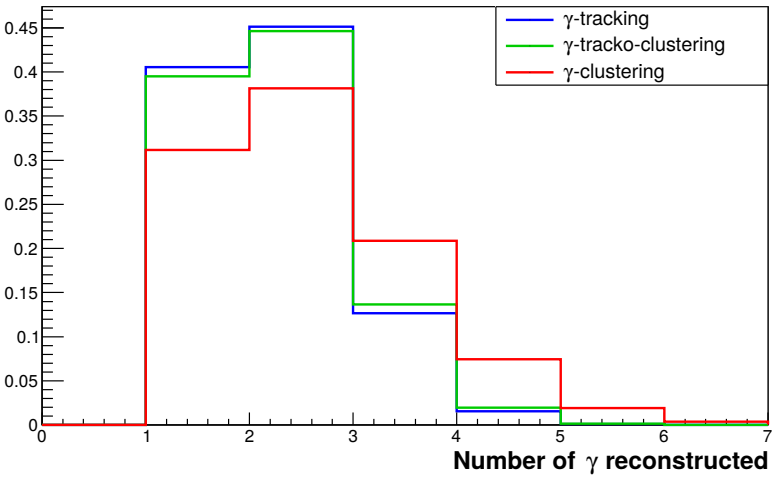

Figure 5.63 – Distributions of the number of γ's reconstructed in ^{208}Tl events

Each of these algorithms allows us to consider specific channels, namely the $1e1\gamma$, $1e2\gamma$ and $1e3\gamma$ channels and gives us access to the energy of every single particle. The statistical differences in each of these channels depend on the reconstruction algorithm employed. Thus, by normalizing the spectra, the different algorithms can be compared and the biases inherent to each of them can be brought out.

First, the energy spectrum of the γ in the $1e1\gamma$ channel from ^{208}Tl events is displayed in Figure 5.64.

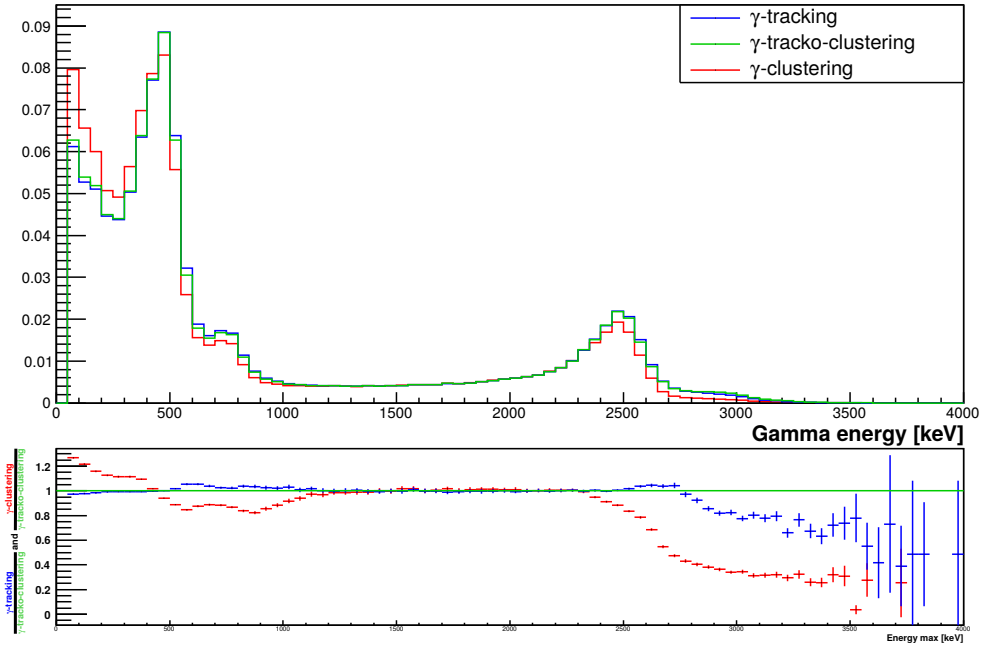

Figure 5.64 – Energy distribution of the γ in the $1e1\gamma$ channel of ^{208}Tl. All spectra are normalized to 1. The lower plot shows the ratio of the γ-tracking spectrum with the γ-tracko-clustering spectrum (in blue) and the ratio of the γ-clustering spectra with the γ-tracko-clustering spectra (in red).

In this Figure 5.64, and in the following similar ones, the lower part of the Figures represent the ratio of the γ-tracking spectra with the γ-tracko-clustering spectra (in blue) and the ratio of the γ-clustering spectra with the γ-tracko-clustering spectra (in red). The most noticeable features of this spectrum are the expected 2.615 MeV peak and the undistinguishable 511-583 keV peaks. These peaks are not located at their genuine transition energies due to: the energy losses, the Compton edge (even in multiple Compton scattering deposit) and of course the calorimeter energy threshold. The 700-800 keV bump is attributed to both the 860 keV γ, and to pile-ups of a 511/583 keV γ with another low energy deposit. Indeed, low energy deposits induce high time uncertainties which makes the hit more susceptible to be paired with another deposit, hence the higher bump amplitude for TOF-based algorithms. The divergence of the TOF-based spectra at higher energies compared to the γ-clustering is explained by the very same reasons. Also, because the sequence of hits attributed to a single γ using γ-clustering will always be shorter

(whenever the latter builds clusters, the γ-tracking and γ-tracko-clustering will also build them), the high energy events will be relatively less frequent than the low energy events.

The pile-up makes the two TOF-based algorithms reconstruct γ's with energies higher than 3 MeV. The γ-clustering is less prone to pile-up, though it is up to the user to require more stringent minimum pair probability. Here, the choice was statistics-driven, in order to optimize the reconstruction efficiency. By requiring higher minimum probabilities, the high-energy tail can be reduced in TOF-based algorithms. The choice belongs to the user, whether to favor higher statistics or better energy reconstruction *i.e.* more faithful spectra.

The$1e2\gamma$ channel holds more events because it is more likely for a 2.615 MeV γ to be detected than to be missed (*cf.* Figure 5.11) and that up to two other γ's can be emitted. Thanks to SuperNEMO's segmented calorimeter, it is possible to distinguish the two γ's. If one considers the three most frequent γ's, the γ of higher energy should either be the 2.615 MeV γ or the 583 keV γ. This also means that the two 511 keV and 583 keV peaks should not appear in the same spectrum. Indeed, looking at the energy spectrum of the γ of higher energy in Figure 5.65, the low energy peak is narrower than in the $1e1\gamma$ channel.

However, depending on the reconstruction algorithm employed the peak is not located at exactly the same energy. The γ-clustering seems to shift the peak towards the lower energies. Indeed, lower energies γ's are more likely to back-scatter, so such γ's, with little energy remaining, are either simply missed, because it does not pass the energy threshold or are reconstructed as a second γ and populate the lower end of the other γ spectrum.

The 750 keV bump, coming from the 763 keV and 860 keV transitions, is also more pronounced with the tracking algorithms, due to their better reconstruction efficiencies. Indeed, with more frequent and faithful reconstructions, peaks are more easily discernable because less γ's have their energies only partially reconstructed. This not only increases the amplitude of the transition peaks but also decreases the pollution induced by partially reconstructed γ's as they are randomly distributed across the spectra.

The energy spectrum of the γ of lower energy is presented in Figure 5.66. The γ-tracko-clustering and γ-tracking are undeniably more efficient at discriminating the 400 keV peak from the very low energy tail. The γ-clustering reconstructs significantly more γ's with an energy just above the energy threshold than the two other algorithms. Some of these events probably come from bouncing γ's, generating two clusters and being split into 2 particles. On the other hand, it can also be interpreted as the tendency that TOF-based algorithms have to easily link clusters when one of them is made of a low energy deposit *i.e.* a high time uncertainty. Single low energy calorimeter hits will thus be more often integrated into a sequence than with a simple clustering.

$1e3\gamma$ events are less frequently detected since it implies detecting all three γ's. The reconstruction efficiency for such processes is significantly lower with all methods, and especially with the γ-clustering. And yet, this method produces almost twice as many events with this topology than the other two approaches. A significant fraction of these events probably comes from $1e2\gamma$ events, where one the γ's triggered two distant clusters. It is therefore interesting to see how each algorithm performed in this topology. The

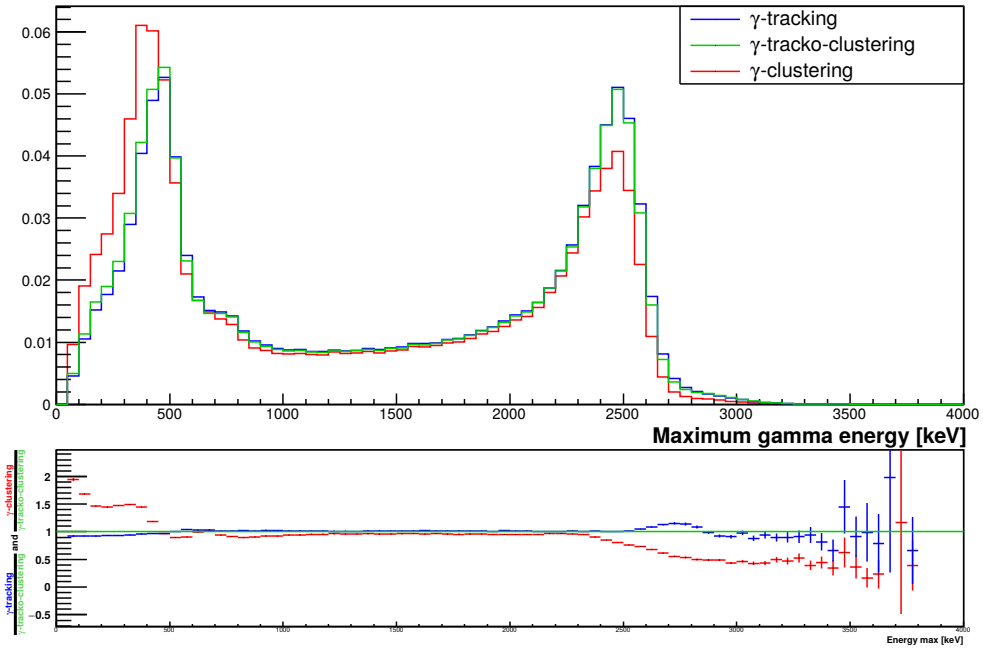

Figure 5.65 – Energy distribution of the γ of maximum energy in the $1e2\gamma$ channel of ^{208}Tl. All spectra are normalized to 1. The lower plot shows the ratio of the γ-tracking spectrum with the γ-tracko-clustering spectrum (in blue) and the ratio of the γ-clustering spectra with the γ-tracko-clustering spectra (in red).

spectrum of the γ of highest energy is presented in Figure 5.67.

Ideally, in light of Figure 5.62, these spectra would only contain 2.615 MeV γ's. All three spectra exhibit the same features, but, not mentioning the expected difference in the relative amplitude of the two peaks, the γ-clustering-generated spectrum seems overall shifted by 150 keV towards the lower energies compared to the two others distributions. The opposite, yet barely noticeable effect, could be argued for the γ-tracking curve, which seems to systematically reconstruct higher energy events compared to the γ-tracko-clustering. This illustrates the flaws of both algorithms: the γ-tracking strives to find the hits belonging to the same γ and sometimes more, while the γ-clustering cannot follow γ's triggering two distant clusters, thus underestimating their energies.

For the γ of intermediate energy, the expected γ's are mainly the 583 keV γ, but also, to a lesser extent, the 763 keV γ. Once again, as shown in Figure 5.68, the γ-clustering appears to be reconstructing lower energy γ's, while the γ-tracko-clustering is here arguably the most efficient algorithm.

The 763 keV peak cannot be identified by any of the algorithms. All three algorithms generate a tail extending up to 1 MeV. These events are pile-up events. Though statistically not significant, they are more frequent with the γ-tracking, for which the pile-up is not only geometrical but also temporal in a way.

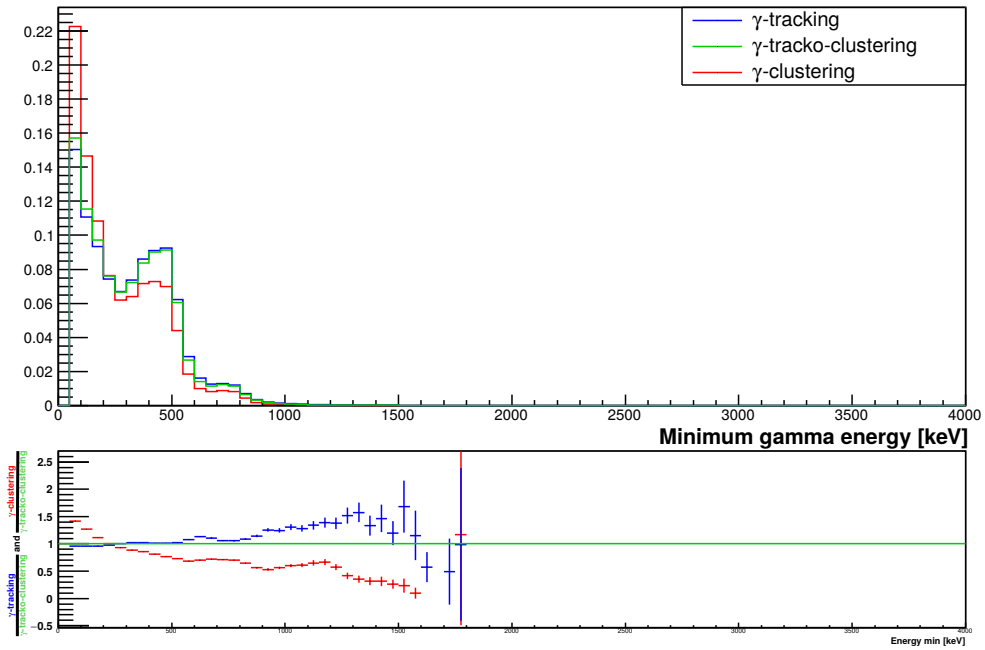

Figure 5.66 – Energy distribution of the γ of minimum energy in the $1e2\gamma$ channel of ^{208}Tl. All spectra are normalized to 1. The lower plot shows the ratio of the γ-tracking spectrum with the γ-tracko-clustering spectrum (in blue) and the ratio of the γ-clustering spectra with the γ-tracko-clustering spectra (in red).

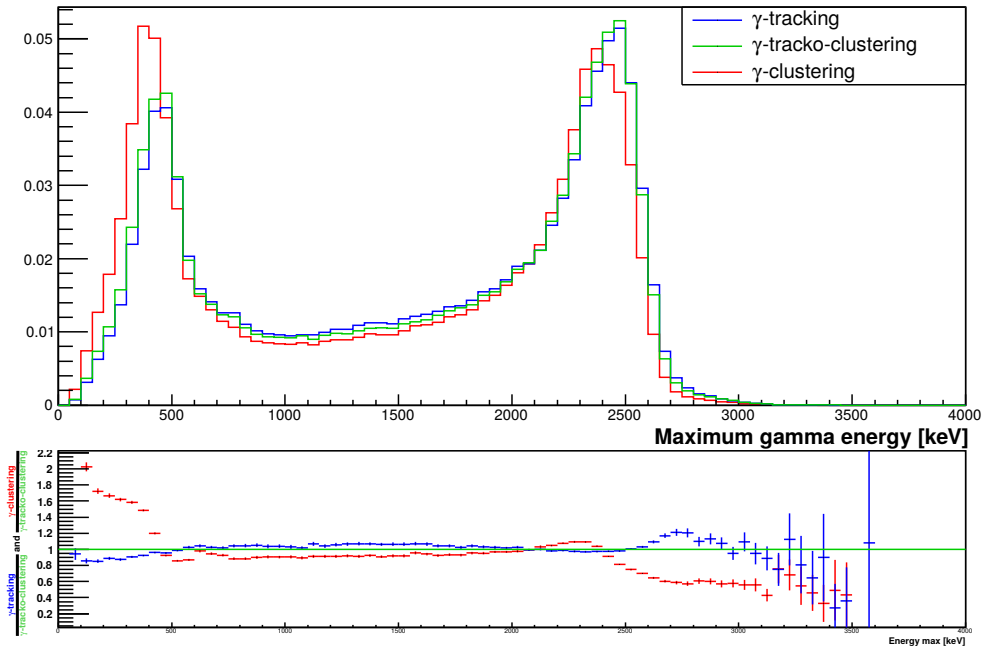

Figure 5.67 – Energy distribution of the γ of maximum energy in the $1e3\gamma$ channel of ^{208}Tl. All spectra are normalized to 1. The lower plot shows the ratio of the γ-tracking spectrum with the γ-tracko-clustering spectrum (in blue) and the ratio of the γ-clustering spectra with the γ-tracko-clustering spectra (in red).

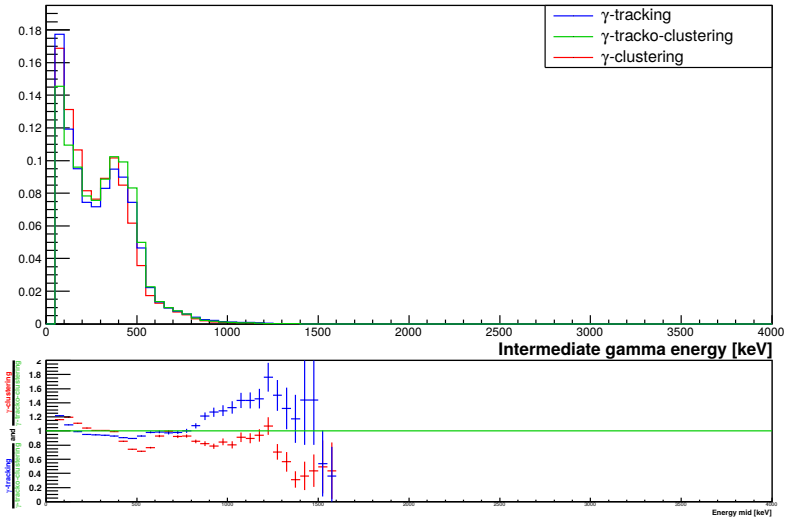

Figure 5.68 – Energy distribution of the γ of medium energy in the $1e3\gamma$ channel of ^{208}Tl. All spectra are normalized to 1. The lower plot shows the ratio of the γ-tracking spectrum with the γ-tracko-clustering spectrum (in blue) and the ratio of the γ-clustering spectra with the γ-tracko-clustering spectra (in red).

Actually, the same behavior concerning the γ-clustering is observed for the γ of lowest energy, as can be seen in Figure5.69. Nevertheless, no peak can here be identified. The interest of this variable in an analysis is thus very limited.

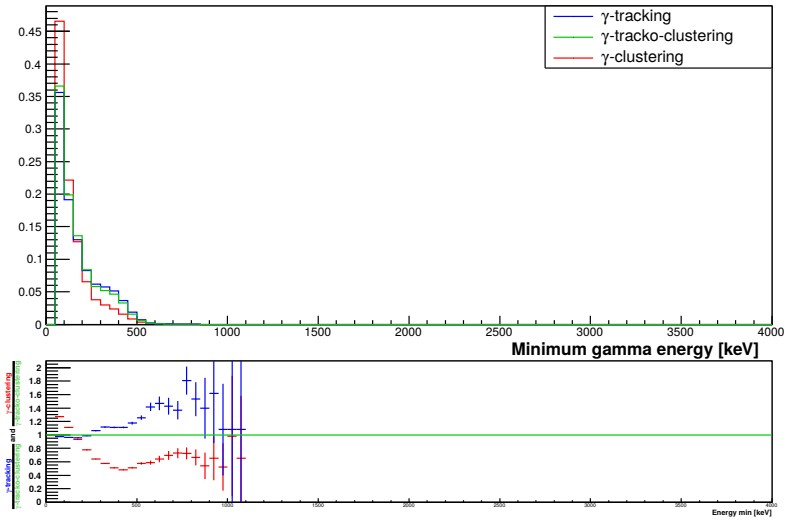

Figure 5.69 – Energy distribution of the γ of minimum energy in the $1e3\gamma$ channel of ^{208}Tl. All spectra are normalized to 1. The lower plot shows the ratio of the γ-tracking spectrum with the γ-tracko-clustering spectrum (in blue) and the ratio of the γ-clustering spectra with the γ-tracko-clustering spectra (in red).

5.6.3 ^{214}Bi spectra

As explained previously, one expects less γ's emitted in ^{214}Bi decays than in ^{208}Tl decays, as reminded in Figure 5.70. The probability for 3 γ's to be emitted is very low so the relatively high number of 3-γ's events reconstructed, as shown in Figure 5.71, are known to be mostly bad reconstructions. This is especially true for the γ-clustering algorithm.

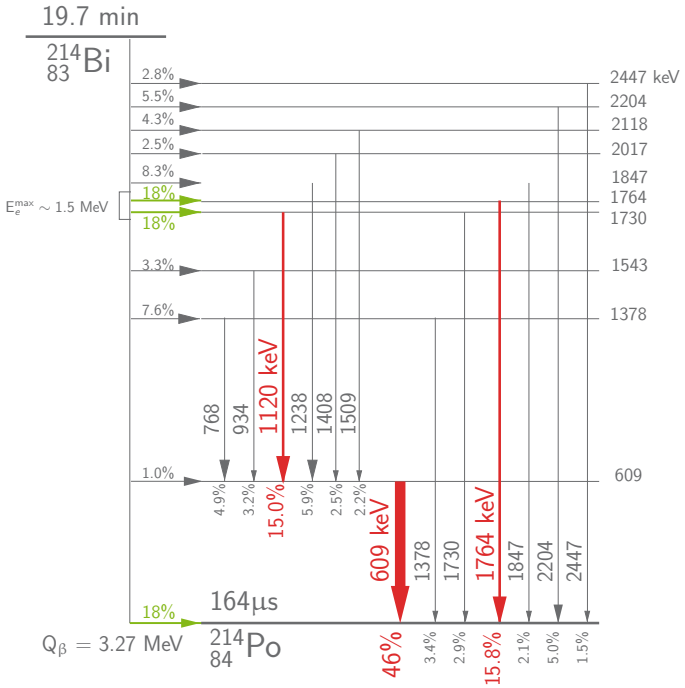

Figure 5.70 – ^{214}Bi decay scheme: The red arrows represent the most frequent γ-rays emitted, where the percentage is the fraction of events in which they appear.

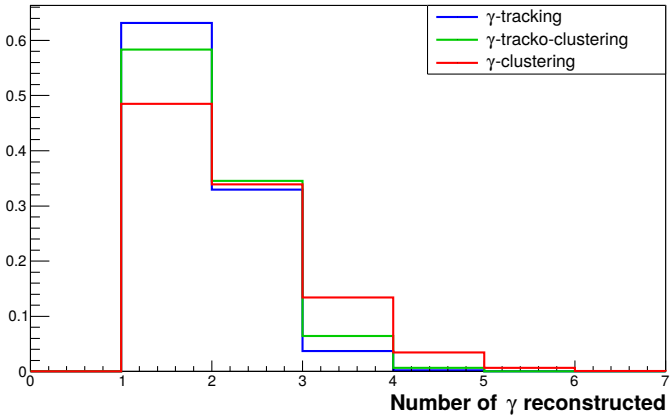

Figure 5.71 – Distributions of the number of γ's reconstructed for ^{214}Bi.

This, solely, advocates for the use of tracking in γ reconstruction. The energy spectra of these events, known to be bad, will be presented later. Like in ^{208}Tl events, the γ-tracking tends to reconstruct more single-γ events while the γ-clustering offers a broader variety of topologies. The γ-tracko-clustering performs, once again, in between.

Looking at the γ energy spectrum in the $1e1\gamma$ channel, presented in Figure 5.72, one can recognize several peaks: the 609 keV and 1730-1764 keV peaks, shifted to slightly lower energies, as well as a bump in the 2-2.1 MeV region attributed to the 2.204 MeV γ.

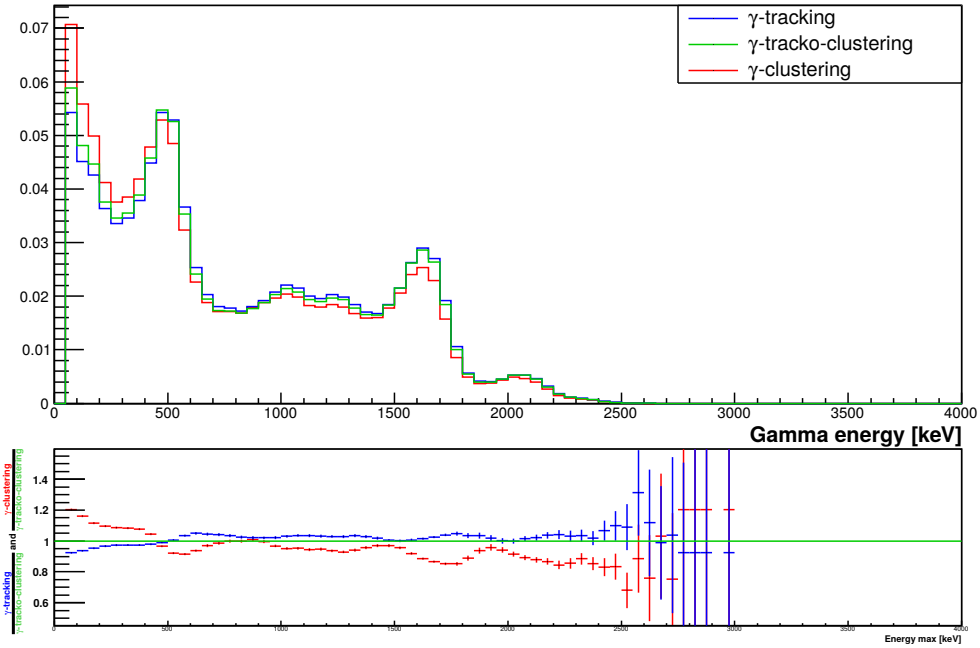

Figure 5.72 – Energy distribution of the γ in the $1e1\gamma$ channel with ^{214}Bi events. All spectra are normalized to 1. The lower plot shows the ratio of the γ-tracking spectrum with the γ-tracko-clustering spectrum (in blue) and the ratio of the γ-clustering spectra with the γ-tracko-clustering spectra (in red).

The 1.12 MeV γ is also discernible but its frequency (15 %) is not enough compared to the 934 keV (3.2 %), 1238 keV (5.9 %) and 1408 keV (2.5 %) γ's, to make it stand out more significantly. Invariably, the γ-clustering algorithm appears to systematically reconstruct the events with a lower energy than with the other algorithms. Furthermore, though the 609 keV γ is three times more frequent than the 1764 keV γ and despite the higher detection efficiency in favor of the former, its amplitude is only twice as high. Indeed, for the 609 keV γ to appear in the $1e1\gamma$ channel, also means a second γ must escape the detection, which consequently reduces its occurrence in this channel. On the contrary, the $1e2\gamma$ channel should not contain any 1730 or 1764 keV γ and be mostly sensitive to the two steps de-excitation γ's, such as the 609/1120 keV pair of γ's. The reconstructed energy spectra for both these γ's are presented in Figure 5.73 and 5.74.

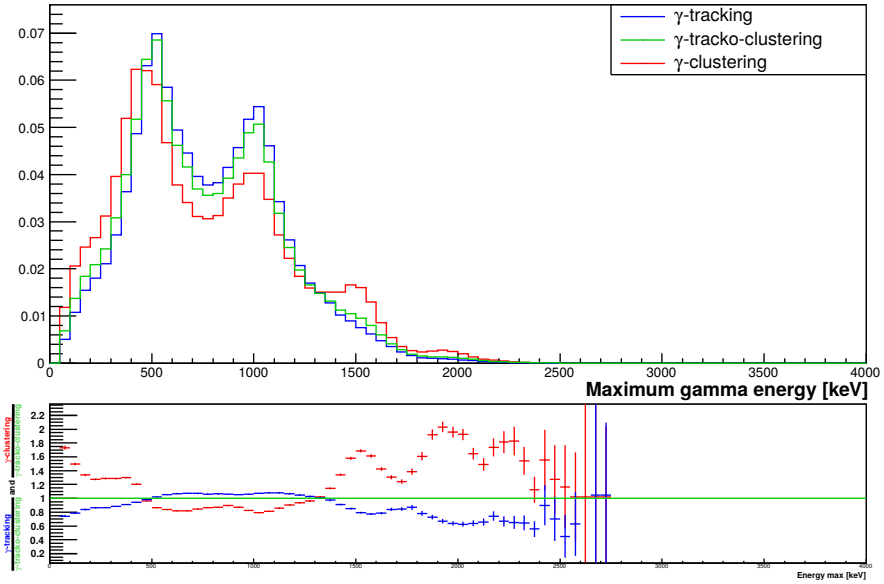

Figure 5.73 – Energy distribution of the γ of maximum energy in the $1e2\gamma$ channel of ^{214}Bi. All spectra are normalized to 1. The lower plot shows the ratio of the γ-tracking spectrum with the γ-tracko-clustering spectrum (in blue) and the ratio of the γ-clustering spectra with the γ-tracko-clustering spectra (in red).

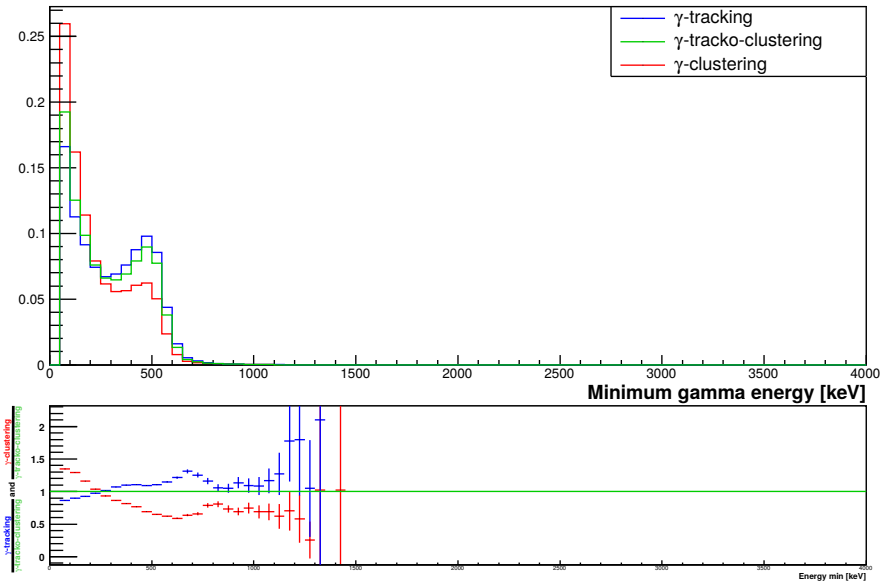

Figure 5.74 – Energy distribution of the γ of minimum energy in the $1e2\gamma$ channel of ^{214}Bi. All spectra are normalized to 1. The lower plot shows the ratio of the γ-tracking spectrum with the γ-tracko-clustering spectrum (in blue) and the ratio of the γ-clustering spectra with the γ-tracko-clustering spectra (in red).

The 1120 MeV and 609 keV peaks are indeed present in the $E_{\gamma_{max}}$ and $E_{\gamma_{min}}$ spectra, respectively. Ideally, if the γ's were always contained and their energy fully measured, the 609 keV peak in the $E_{\gamma_{max}}$ spectrum should not appear. If this γ appears to be the γ of

higher energy means the second γ only deposited a fraction of its energy. The γ-clustering and, to a lesser extent, the γ-tracko-clustering, induce pseudo-peaks in the 1.5 and 1.9 MeV regions, which can be attributed to the 1.764 MeV and 2.204 MeV γ-rays, respectively. Yet, these γ's are emitted alone, so a second lower energy deposit from a second γ is impossible. These events are actually due to single γ's, scattering and triggering two distant clusters, which are reconstructed are two γ's. The extended high energy tail can be attributed to rare γ rays. The information brought by the low energy γ spectrum is already very limited.

The $1e3\gamma$ channel is not expected in ^{214}Bi events: only poorly reconstructed events can populate this topology (two γ's emitted, one of which bounces but fails to be tracked, for instance). The most relevant information comes from the spectrum of the highest energy γ, presented in Figure 5.75.

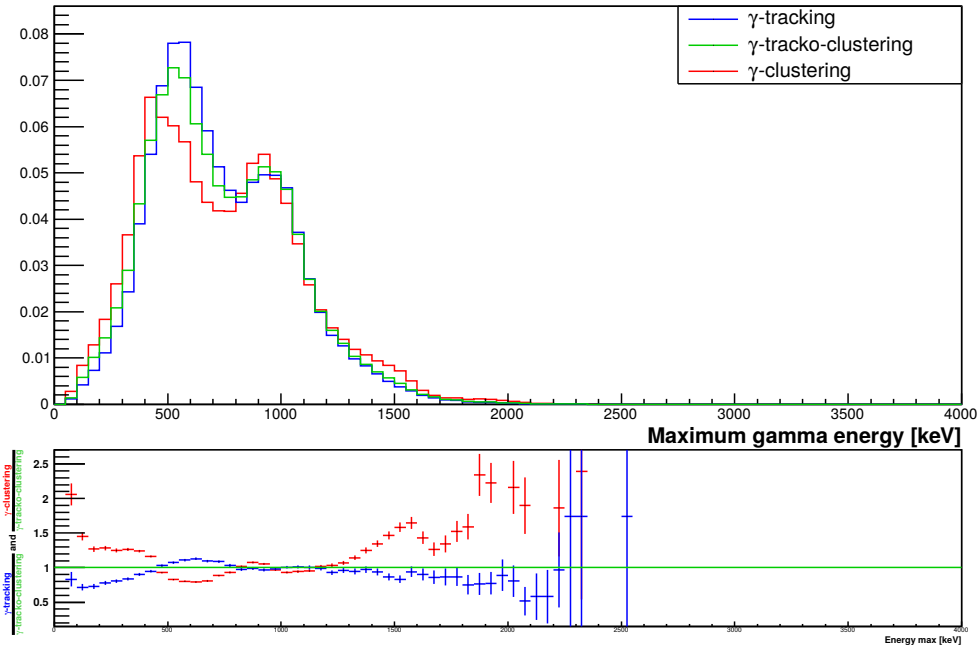

Figure 5.75 – Energy distribution of the γ of maximum energy in the $1e3\gamma$ channel of ^{214}Bi. All spectra are normalized to 1. The lower plot shows the ratio of the γ-tracking spectrum with the γ-tracko-clustering spectrum (in blue) and the ratio of the γ-clustering spectra with the γ-tracko-clustering spectra (in red).

The same peaks as in the $1e2\gamma$ channels are observed, albeit shifted towards lower energies. This "missing" energy is probably deposited in another distant cluster which was unsuccessfully related to this γ and was recognized as a third γ. The 1.5 and 1.9 MeV bumps from the γ-clustering are less pronounced since it requires three distant clusters to be generated to fall in the $1e3\gamma$ channel.

The 400 keV peak is still visible in the intermediate energy spectrum in Figure 5.76 while the lowest energy spectrum, in Figure 5.77, holds only partial deposits from a variety of γ's. No truly useful information can be extracted from either of these spectra.

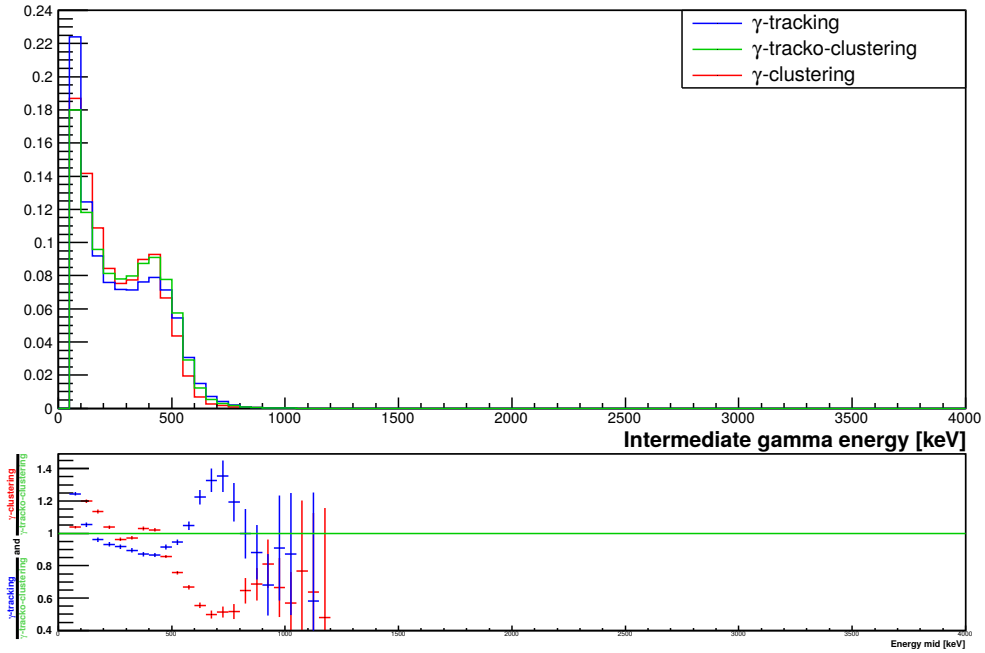

Figure 5.76 – Energy distribution of the γ of medium energy in the $1e3\gamma$ channel of ^{214}Bi. All spectra are normalized to 1. The lower plot shows the ratio of the γ-tracking spectrum with the γ-tracko-clustering spectrum (in blue) and the ratio of the γ-clustering spectra with the γ-tracko-clustering spectra (in red).

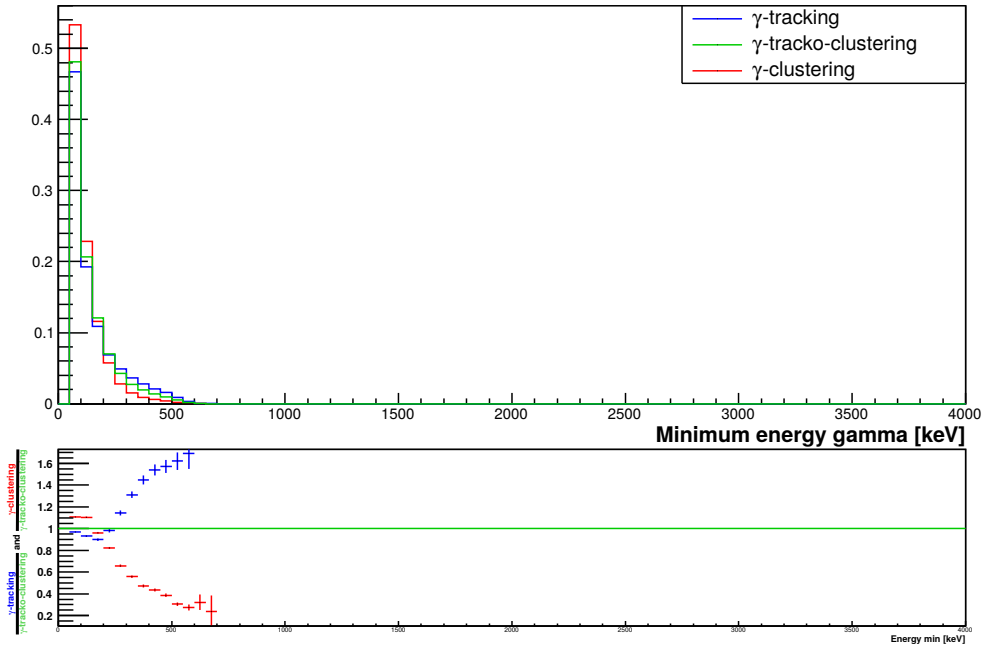

Figure 5.77 – Energy distribution of the γ of minimum energy in the $1e3\gamma$ channel of ^{214}Bi. All spectra are normalized to 1. The lower plot shows the ratio of the γ-tracking spectrum with the γ-tracko-clustering spectrum (in blue) and the ratio of the γ-clustering spectra with the γ-tracko-clustering spectra (in red).

5.7 Conclusion

Three γ-reconstruction algorithms have been developed and implemented in the SuperNEMO software. Studies performed on simple pure γ events helped better understand the γ detection in the SuperNEMO demonstrator and characterize the performances of each algorithm, regarding their efficiencies and energy reconstructions. The three algorithms were also put to the test with ^{208}Tl and ^{214}Bi events, which are the main γ-emitting source backgrounds expected in the SuperNEMO demonstrator.

The new γ-tracko-clustering algorithm, combining the perks of the γ-clustering and γ-tracking algorithms, provides the better reconstruction efficiencies. This represents a relative increase of about 15-20 % of ^{208}Tl and ^{214}Bi events being correctly reconstructed, compared to the γ-clustering. This study helped determine the optimum configurations for each algorithm. It also emerges that a 150 keV lower energy threshold could increase the γ reconstruction efficiency. Dedicated studies should be performed to evaluate the impact this could have on the search for the neutrinoless double beta decay (a higher energy threshold means the $0\nu\beta\beta$ reconstruction efficiency would be decreased). However, one could contemplate using different energy thresholds at the software level, depending on the event topology. The calibration runs (^{207}Bi and ^{232}U sources) will provide a deeper characterization of the algorithms, in particular regarding their configurations.

The differences in the number ofγ's reconstructed, depending on the algorithm, are significant. For both isotopes, the γ-clustering tends to overestimate the number of γ's involved in an event. By construction, the γ-tracking tries, on the contrary, to minimize the number of γ's. The γ-tracko-clustering exhibits an intermediate behavior, albeit closer to that of the γ-tracking.

Concerning the energy reconstruction, all algorithms possess their own biases, which transpire on the energy spectra of the individual γ's. Generally, the γ-clustering tends to underestimate the energies collected which translates into a shift of the spectra towards the lower energies as well as a more significant escape peak compared to the other algorithms. The γ-tracking and γ-tracko-clustering algorithms are, however, more prone to pile-ups, especially in the $1e1\gamma$ channel. They provide sharper peaks, closer to the genuine γ energy.

To conclude, none of the algorithms presented above are perfect. Yet, the γ-tracko-clustering provides the highest reconstruction efficiency while inducing the lowest biases in the energy reconstruction. Only a comparison with real data, and especially from calibration runs, will tell which algorithm should be preferred. The better performance of an algorithm might be overbalanced by the biases and systematical uncertainties they induce in the analysis. Indeed, an accurate reconstruction of the event topologies and the individual γ energy spectra is paramount to the physics analysis.

At this stage, very few improvements come to mind that could further improve the γ reconstruction. The only solution which could bring significant enhancements is the introduction of a machine learning algorithm, like neural networks, which could take

into account more subtle patterns and correlations (high energy deposits sometimes come from a high-angle Compton scattering, so a hit in the opposite direction of the incident γ is more likely, etc.). However, SuperNEMO is not dedicated to the precise reconstruction of γ particles. This means that, regardless of the effort invested in improving the reconstruction algorithm, a fair share of events will always remain too intricate and impossible to reconstruct, simply because of the detector limitations.

Chapter 6

Sensitivity of the SuperNEMO demonstrator to the backgrounds

The simulation and reconstruction software was presented in Chapter 3. In particular, an improved γ-reconstruction algorithm, presented in Chapter 5, as well as a Particle Identification module, were developed during this thesis. These tools provide a better event reconstruction and allow the identification of event topologies. In this Chapter, we will see how SuperNEMO is able to accurately characterize its own background model, thanks to these dedicated analysis channels. The topologies and variables best suited to the measurement of the main backgrounds are presented. These variables are used to fit the background contributions in a large number of pseudo-experiments in order to estimate the statistical and systematic uncertainties inherent to the background measurements. In particular, the evolution of these uncertainties with time is presented.

6.1 Conditions of the simulation

At the time of the simulation, the implemented detector geometry was already very close to that of the SuperNEMO demonstrator. The main difference with the final design is the use of a uniform 25 G magnetic field. However, as explained in more details in Chapter 4, using a non-uniform magnetic field does not significantly impact the charge identification, such that our confidence in the results obtained in this Chapter is unshaken. Of course, one must still keep in mind that the detector design implemented in the simulation is optimum and does not take into account the flaws and breakdowns which might be revealed during its commissioning.

The reconstruction process was explained extensively earlier. In almost all topologies, the electrons and positrons are required to have a vertex reconstructed on the source and an associated calorimeter hit. The α particles are delayed straight tracks, with a vertex extrapolated on the source as well. The only exception is for the $1e1\alpha$ topology from the tracker which aims at selecting Radon events. In that case, the electron and the α particle are required to have a vertex reconstructed in the tracker volume. The new γ-tracko-clustering algorithm is employed for the reconstruction of γ particles: the default configuration is chosen, except for the minimal pair probability which is set to 25 %. This

choice appeared to provide the best reconstruction efficiencies for both ^{208}Tl and ^{214}Bi events (Sections 5.4.6 and 5.4.7).

The energy thresholds are set to the lowest values planned in SuperNEMO, namely a 150 keV high energy threshold and a 50 keV low energy threshold. The energy resolution of the calorimeter is 8 % at 1 MeV (FHWM) and its time resolution 400 ps at 1 MeV.

Due to the time it would take to simulate every expected background contribution, the choice of a simplified background model, containing only the most harmful backgrounds to the $0\nu\beta\beta$ decay search, was adopted. These backgrounds are the $2\nu\beta\beta$ decay, a contamination of the source in ^{208}Tl and ^{214}Bi, and a contamination of the tracker gas with Radon. The backgrounds vertices are simulated randomly in the source bulk, with the exception of Radon events, which are simulated randomly on the surface of the field shaping wires (where the positively charged Radon daughter nuclei will deposit).

The target background activities (also called nominal activities in the following) are reminded in Table 6.1. Assuming the demonstrator runs for 2.5 years with 7 kg, the number of decays expected, as well as the number of simulated decays for each background, are also presented in Table 6.1.

	Half-life or activity	Expected decays	Simulated decays
$2\nu\beta\beta$	9 10^{19} years	10^6	10^8
^{208}Tl	2 μBq/kg	1.1 10^3	10^8
^{214}Bi	10 μBq/kg	5.5 10^3	10^8
Radon	150 μBq/m^3	1.8 10^5	10^8

Table 6.1 – Backgrounds half-life or target activities, translated into their expected number of decays in the SuperNEMO demonstrator (17.5 kg.y). The size of the Monte-Carlo simulations for each isotope is also presented.

With 100 times more $2\nu\beta\beta$ events simulated than expected in the demonstrator (and far more for the other backgrounds), the efficiencies and Monte-Carlo templates obtained with the simulation should be accurate.

In addition, 1000 pseudo-experiments were simulated. In practice, it consists in choosing a set of processes, with each their own activities or half-lives, and simulating a number of decays corresponding to a given duration. In our case, the background model is composed of the four processes presented in Table 6.1. The activities or half-life attributed to each process are translated to an expected number of decays, also shown in Table 6.1, corresponding to a 2.5 years measurement. These numbers of decays are then simulated for each contribution. The events kinematics are randomly generated such that no two pseudo-experiments can be the same. The different contributions go through the same reconstruction process, before being merged to make up a pseudo-experiment *i.e.* a dataset similar to what could be measured with a genuine detector.

6.2 Distribution of the event topologies

Each contamination generates a variety of event topologies. In addition to the different types of decays possible, some events might not be fully detected or correctly reconstructed. For instance, even the $2\nu\beta\beta$ decay, which always emits two electrons, is not always reconstructed in the two electrons ($2e$) topology. If one of the electrons does not leave the source, the event will be recognized as belonging to the one electron ($1e$) topology. If an electron exits the source but does not trigger any calorimeter block, the event is rejected because the energy sum of the event, which is ultimately the parameter of interest, can not be fully reconstructed. The distribution of the reconstruction efficiencies for the different event topologies and for each background origin is presented in Figure 6.1.

The first observation that can be made is that a large majority of the events do not fall in any of the categories of interest in SuperNEMO. The main selection criterion is that at least one charged particle must be fully reconstructed *i.e.* a track with an associated calorimeter hit is required. This requirement is consistent with the trigger system since an event where a particle leaves a track in the wire chamber without triggering a calorimeter block would not be recorded anyway[a]. In addition, any events holding tracks to which no calorimeter hit is associated is rejected because an energy measurement solely based on the track curvature is not accurate. If more than 3 γ's are reconstructed, the event is not considered either. Eventually, an event needs to be somewhat clean, such that useful information can be extracted from it. It follows that the reconstruction efficiency for $2\nu\beta\beta$ events in the $2e$ topology is just below 10 %. As will be shown later, the reconstruction efficiency of the $0\nu\beta\beta$ process in the $2e$ topology is more favorable since electrons carry a higher energy. The most efficient topology for the $2\nu\beta\beta$ process is the $1e$ topology (23 %). However, considering the high reconstruction efficiency for the backgrounds in this same category, this topology is less pure than the $2e$ topology (where the other backgrounds are expected to contribute with less than 2 events in a 1000 decays).

One can also notice that only ^{214}Bi and Radon events contribute to the $1e1\alpha$ topologies. The $1e1\alpha$ topology contains only events where both the electron and alpha vertices are reconstructed on the source foil. Yet, the Radon efficiency in this topology is higher than that of the ^{214}Bi. This illustrates the fact that the probability for α's from ^{214}Bi decays to exit the source and be detected in the tracker is quite low. It is much easier for α's from ^{214}Bi decays occurring on the surface of the tracker wires to be detected. Considering that Radon events where the tracks are close to the source are more likely to be extrapolated on the latter, this makes up for the unexpected efficiency difference observed in this topology. On the contrary, very few ^{214}Bi events are reconstructed in the $1e1\alpha$ topology from the tracker and Radon is expected to be the only contributor to this topology.

About 1 % of the $2\nu\beta\beta$ decays are identified as a $1e1p$ event (1 electron plus 1 positron). This happens when the charge of one of the electrons is mistaken due to the scattering of

[a] Actually, the minimum trigger conditions are a calorimeter hit (passing the energy threshold) with some patterns of tracker cells triggered in the direct vicinity.

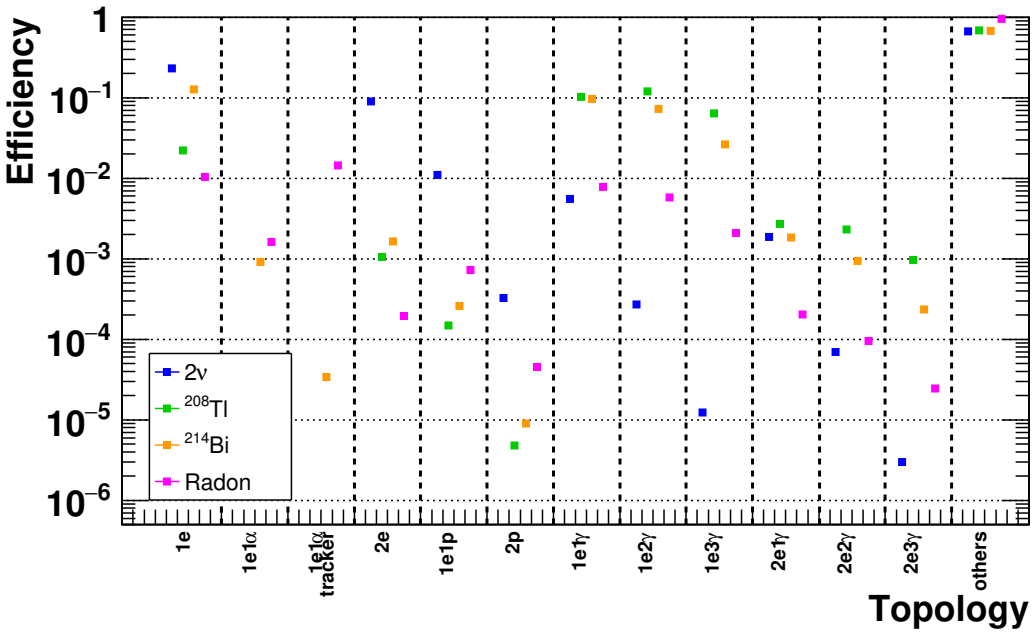

Figure 6.1 – Distribution of the reconstructed topologies for the main backgrounds. All the charged particles are required to have a vertex on the source foil, except for the $1e1\alpha$ topology from the tracker. No topological cuts (vertices separation, internal probability, etc.) are applied here.

the electron in the tracker or when a high energy electron generates an almost straight track for which the best fit solution is degenerated and the track of positive curvature is preferred. As expected, the most efficient contributors to the $1e\mathrm{N}\gamma$'s topologies are ^{208}Tl and ^{214}Bi events.

In order to better understand how the ability to reconstruct several different topologies can help build an accurate background model, let's normalize the Figure 6.1 to the expected number of decays coming from each contribution. This results in the Figure 6.2.

Looking first at the $2e$ topology, considering the very stringent background levels required and their efficiencies presented in Figure 6.1, this topology is almost purely composed of $2\nu\beta\beta$ events: only thirty Radon events, ten ^{214}Bi events and one ^{208}Tl event, are expected. These numbers do not even take into account the topological cuts (vertices separation, internal probability, etc.) which might be applied later.

The $1e$ topology also looks promising[b] for the study of the $2\nu\beta\beta$ process, even if the other backgrounds contribution is less negligible than in the $2e$ topology. However, only a simplified background model, containing only the most harmful isotopes for the search of the $0\nu\beta\beta$ decay, is considered here. Any other contaminants, which are mostly lower energy β/γ emitters, would also contribute to this topology, making it less interesting from an analysis point of view. As expected, only ^{214}Bi and Radon events contribute to the $1e1\alpha$ topology. However, significantly more events from Radon are expected in this

[b] Our background model does not include other possible contributions from β emitters in the source, like ^{40}K, ^{210}Bi or ^{234m}Pa, which could also mimick $\beta\beta$ events [95].

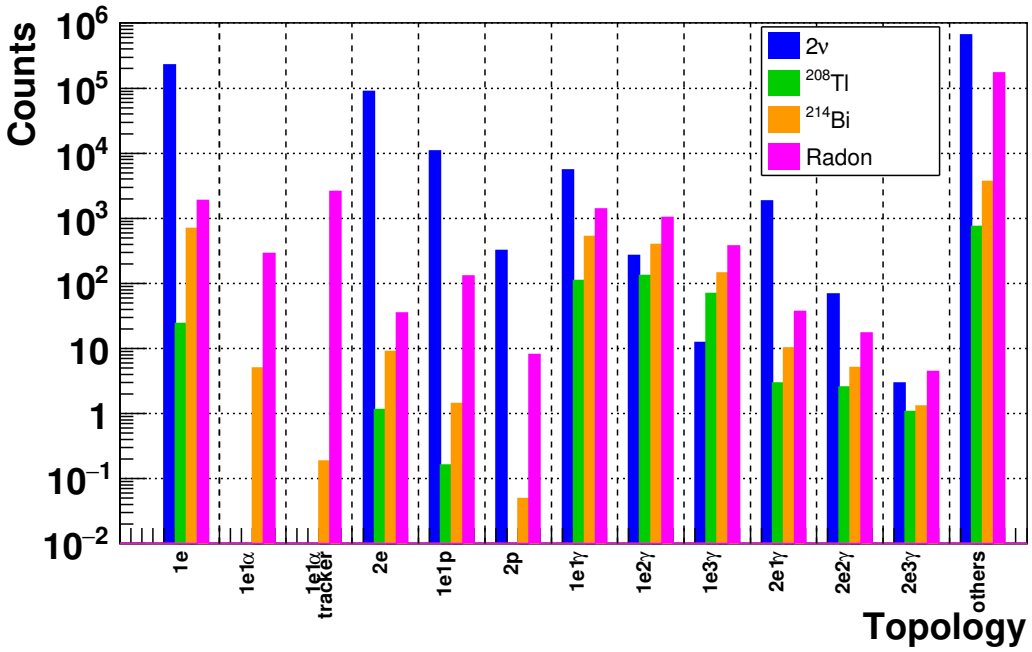

Figure 6.2 – Distribution of the expected number of events in the different topologies for the main backgrounds, in the demonstrator conditions, namely a 17.5 kg.y exposure and A(^{208}Tl) = 2 μBq/kg, A(^{214}Bi) = 10 μBq/kg and A(Radon) = 150 μBq/m^3.

topology because of its higher efficiency and higher activity. The $1e1\alpha$ topology from the tracker is only composed of Radon events which makes it a pure and reliable means of measuring the Radon activity.

Concerning the $1e1\gamma$ topology: even if the most efficient contributors to this topology are the ^{208}Tl and ^{214}Bi isotopes, the majority of the events actually comes from the $2\nu\beta\beta$ decay (where one electron is not detected and a Bremsstrahlung is emitted for instance), which simply stems from the much higher number of decays expected. The $1e2\gamma$ and $1e3\gamma$ topologies, intended to study mostly ^{208}Tl and ^{214}Bi events, are not dominated by the $2\nu\beta\beta$ contribution, but by the Radon events.

The $2e$Nγ 's topologies can be dedicated to the study of the double beta decays (with or without neutrino emission) to the excited states of the daughter nucleus.

Knowing the expected contributions of the different backgrounds to all these topologies will guide our analysis strategy. Before looking for the neutrinoless double beta decay, it is important to understand how SuperNEMO can accurately characterize its own background.

6.3 Estimation of the statistical and systematic uncertainties

The pseudo-experiments aforementioned are used to estimate how well an activity or a half-life can be measured by the detector. The principle is illustrated in Figure 6.3.

For a given contribution and a given duration, we start with a fixed activity A_0, which can be translated into a fixed expected number of decays N_0. A large number of pseudo-experiments is then generated, starting with the same number of decays N_0. The kine-

matics of the events are randomly generated and are unique to the pseudo-experiment. Each pseudo-experiment goes through the same simulation and reconstruction processes. However, given the randomness of the starting kinematics and the stochastic nature of the simulation and reconstruction procedures, the number of reconstructed events N_{reco} in the topologies of interest will vary from one pseudo-experiment to the other. This process is repeated for every contributions simulated. The different contributions are then merged to make up a pseudo-experiment. The final variables distributions built from these topologies are different, both in numbers and in shapes. The reconstruction efficiencies specific to each topologies are known from the simulation. The variables distributions can, therefore, be fitted with the Monte-Carlo templates (obtained from independent large Monte-Carlo simulations), as explained in Section 3.3.1. The fit result gives an estimation of the original number of decays and thus of the original activity. The distribution of the activities measured with each pseudo-experiment provides an estimation of the systematic uncertainty induced by the reconstruction and fit processes. This approach assumes an ideal detector, so dedicated studies should be performed in order to estimate the impact of a degraded detector (dead calorimeter modules or tracker cells for instance) on the systematic uncertainty.

In addition, for a given activity or a given half-life, the expected number of decays is actually Poisson distributed. This statistical uncertainty propagates to the reconstructed number of events N_{reco}, which is the quantity measured by the detector. For a large number of events, this distribution follows the normal distribution. Consequently, the standard deviation from the mean expected number of reconstructed events provides a good estimation of the statistical uncertainty.

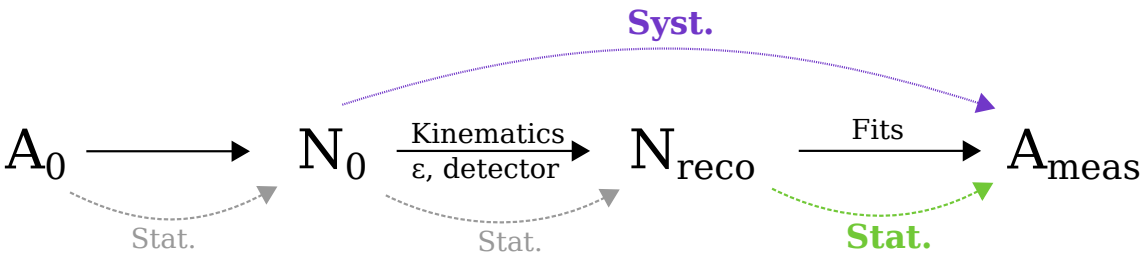

Figure 6.3 – Illustration of the origin of the uncertainties on an activity measurement. This principle is also valid for a half-life measurement. The goal is to measure a fixed activity A_0. This translates into a fixed expected number of decays N_0. Pseudo-experiments are generated with N_0 decays. The random kinematics of the events, the reconstruction efficiency and the detector effects, means the reconstructed number of events N_{reco} fluctuates. The final variable distributions are fitted with Monte-Carlo templates in order to measure a number of events, which is translated back into an activity A_{meas}. The distribution of the activities measured with each pseudo-experiment gives an estimate of the systematic uncertainty. The statistical uncertainty comes from the random nature of radioactive decays. These fluctuations propagate to the reconstructed number of events.

6.4 Measurement of the background contributions

When building a background model, starting with supposedly unknown contributions, it might be relevant to lead off the analysis by studying a pure topology, providing a large number of events. Doing so will provide an accurate measurement of at least one of the contributions.

6.4.1 Radon measurement : discriminating variables

In the conditions of the SuperNEMO demonstrator, looking first at the $1e1\alpha$ events from the tracker volume allows an accurate determination of the Radon contamination in the tracker gas. The events of interest here are decays of ^{214}Bi nuclei deposited on the surface of the field wires. These events are called "Radon events" in the following, in order to distinguish them from ^{214}Bi events originating from the source. The $1e1\alpha$ events from the tracker are selected by requiring an electron track with an associated calorimeter but no vertex extrapolated on the source. An alpha must also be present in the event and at least one of its Geiger cell composing its track must be a direct neighbor to the reconstructed vertex of the electron. Given the proximity of the first tracker layers to the source, a contribution from ^{214}Bi events from the source is expected but strongly reduced by the selection criteria. However, no events are expected from ^{208}Tl and $2\nu\beta\beta$ decays and, indeed, none have been reconstructed in this topology in the Monte-Carlo simulations. The Table 6.2 summarizes the selection efficiencies and number of events expected from Radon and ^{214}Bi in the demonstrator running for 2.5 years.

	$\epsilon_{1e1\alpha,\text{tracker}}$	1e1α tracker events expected
A(Radon) = 150 μBq/m^3	1.42 10^{-2}	2600
A(^{214}Bi) = 10 μBq/kg	3.5 10^{-5}	$\sim$ 0.2

Table 6.2 – Reconstruction efficiency of $1e1\alpha$ events in the tracker and their expected number of decays after 2.5 years from Radon and ^{214}Bi.

This topology provides an effectively pure sample of Radon events. Since, as explained earlier, Radon and ^{214}Bi tend to share the same kinematics, finding discriminating variables will help raise the possible degeneracy in the multi-variable fit. This will prove especially useful when measuring the background levels in the demonstrator since it should be able to measure its own background levels, without prior information from external measurements.

The first discriminating variable chosen, shown in Figure 6.4, is the position of the reconstructed vertex in the tracker along the X axis *i.e.* perpendicularly to the source. The exact vertex of origin cannot be pinpointed accurately, so it is, by construction, located at the end of the fitted electron track. The reconstructed tracks stop at the point closest to center of the cell located at the extremity of the cluster, as illustrated in Figure 6.5. The vertices consequently tend to be reconstructed closest to the center of the cells, hence the peaks observed in Figure 6.4. It also shows that the Radon events are expectedly homogeneously distributed across the tracking volume while the few ^{214}Bi events reconstructed

in this topology are localized closer to the source foil.

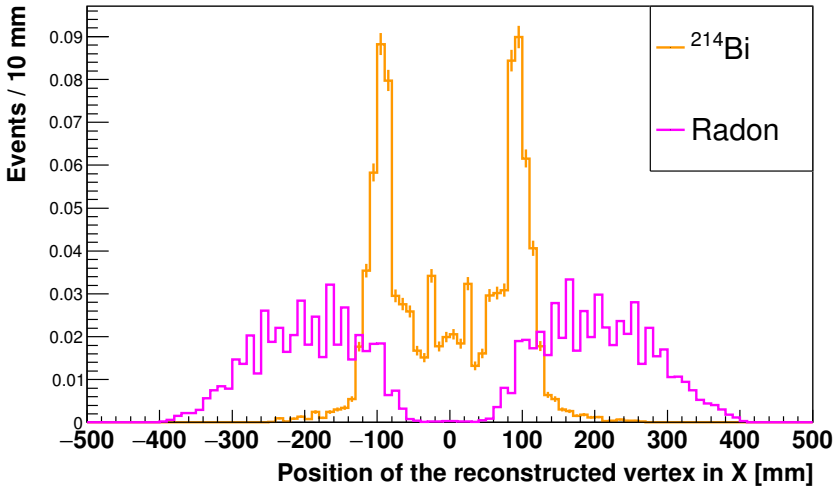

Figure 6.4 – Distributions of the position of the reconstructed vertices of the $1e1\alpha$ events in the tracker along the X axis *i.e.* perpendicular to the source.

A second discriminating variable is the electron energy, displayed in Figure 6.6. As a matter of fact, electrons emitted in Radon induced events do not have to go through the dense source, in contrast to electrons from ^{214}Bi events. Electrons from Radon events will, therefore, have higher energies.

Another discriminating variable is the length of the α track, shown in Figure 6.7. Similarly to electrons, α's emitted in the source will lose some energy as they go through the source material, before being detected by the tracker. Their tracks will consequently be shorter than that of α's emitted in the tracker. This variable can also be useful to measure the marginal deposit of ^{214}Bi nuclei from Radon decays on the surface of the source foil, which was not considered here. The irregular shapes of the α track length distributions are also explained by the granularity of the tracker.

These three variables are sufficient to provide a reliable measurement of the Radon activity.

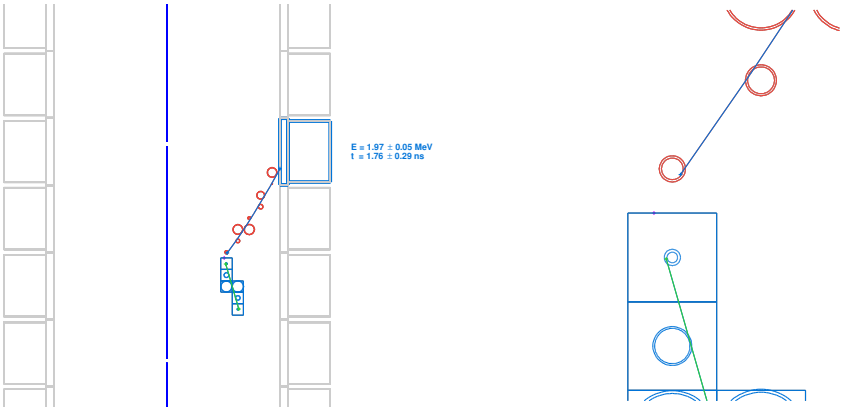

Figure 6.5 – *(left)* Display of a Radon event reconstructed in the $1e1\alpha$ topology in the tracker. The cells at the extremities of the two tracks are direct neighbors. *(right)* Zoom on the two reconstructed vertices of origin. The tracks stop where the tracks are closest to the center of the cell at the extremity of the cell clusters.

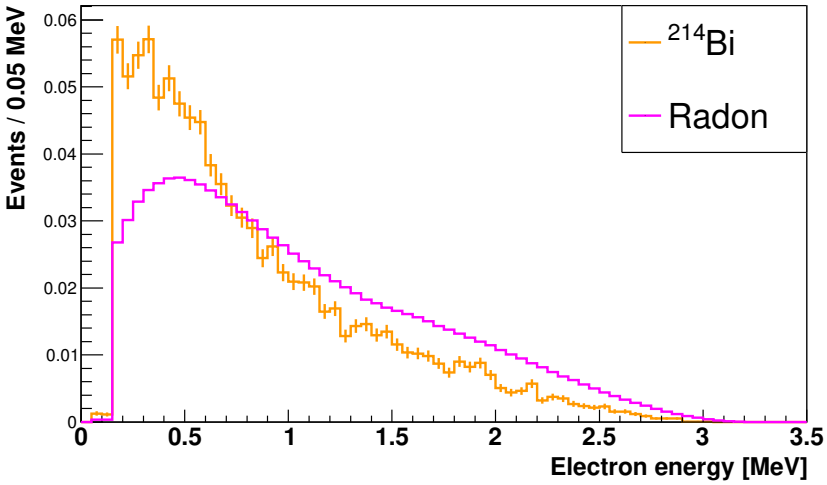

Figure 6.6 – Reconstructed electron energy spectra of the $1e1\alpha$ events in the tracker. The electrons emitted from ^{214}Bi decays in the source lose more energy as they go through the dense source material than electrons emitted in the tracker by Radon daughter nuclei.

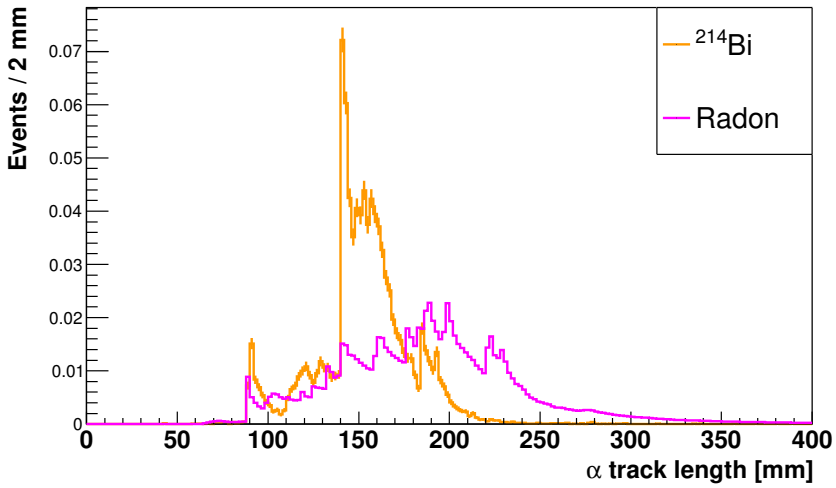

Figure 6.7 – Distributions of the reconstructed α track lengths of the $1e1\alpha$ events in the tracker. Like electrons, α's emitted in the source and detected by the tracker lose more energy than those emitted in the tracker. Their tracks are consequently shorter on average.

6.4.2 Radon measurement : pseudo-experiments

In order to estimate the accuracy of this measurement, some pseudo-experiments are generated. The pseudo-experiments provide datasets similar to what will be measured with the demonstrator after 2.5 years.

An example of pseudo-experiment with the best fit (using a binned log-likelihood minimization, as explained in Chapter 3.3.1) of the Radon and ^{214}Bi contributions is shown in Figures 6.8, 6.9 and 6.10.

The fit is performed simultaneously on all three variables and Radon is recognized as being almost the only contributor.

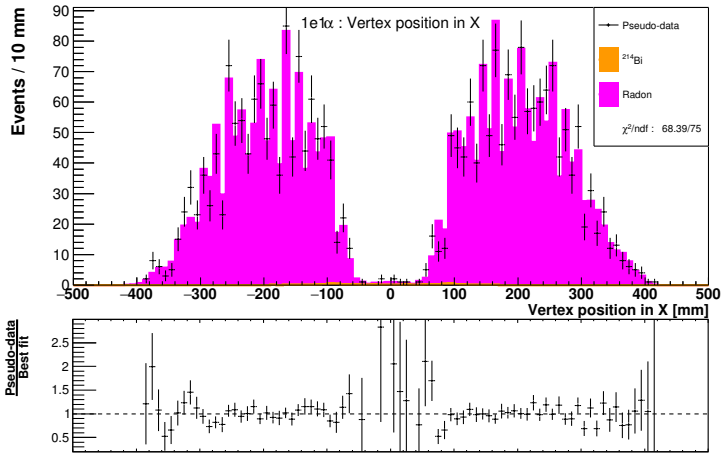

Figure 6.8 – Fit of a pseudo-experiment on the distribution of the position of the reconstructed vertex (along the X axis, *i.e.* perpendicularly to the source) for $1e1\alpha$ events in the tracker.

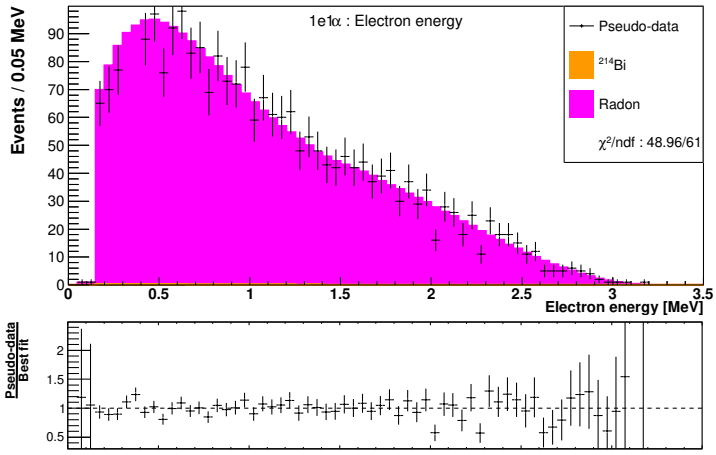

Figure 6.9 – Fit of pseudo-experiment on the electron energy spectrum for $1e1\alpha$ events in the tracker.

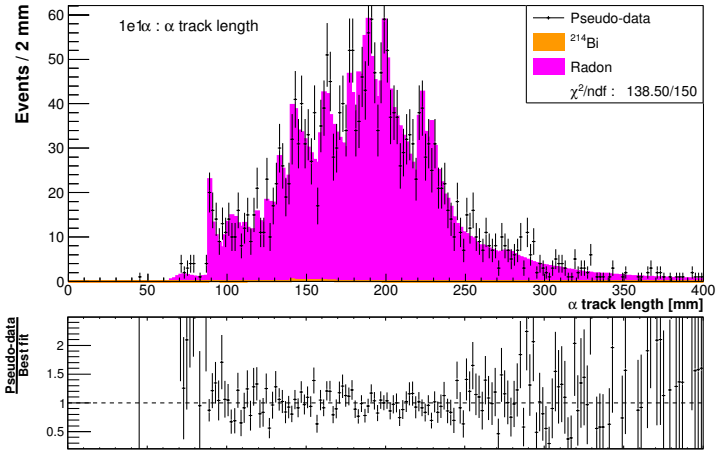

Figure 6.10 – Fit of a pseudo-experiment on the distribution of the α track length for $1e1\alpha$ events in the tracker.

The distribution of the Radon activities measured for a thousand pseudo-experiments is displayed in Figure 6.11. The measured activities are normally distributed around the expected Radon activity. The mean value is about 1 % higher than the nominal activity. This is imputed to the rounding of the reconstruction efficiency and to the rounding of the number of decays simulated in the pseudo-experiment. This shows that the simulated activity can be measured with a 1.9 % systematic uncertainty in the conditions of the demonstrator. The expected number of radon events reconstructed in the tracker in the 1e1α topology after 2.5 years at the nominal activity is about 2600. The statistical uncertainty is then also around 2 %.

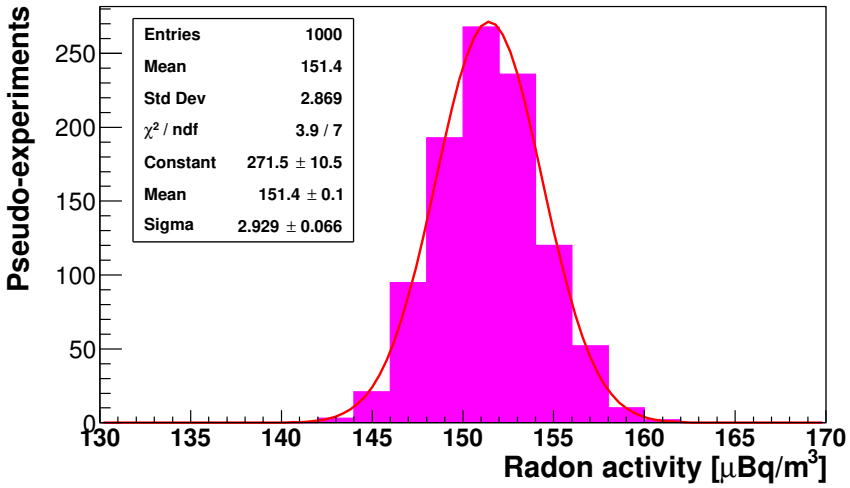

Figure 6.11 – Distribution of the Radon activities measured from the pseudo-experiments (17.5 kg.y).

The same procedure can be repeated for different measurement durations : this gives the evolution of the statistical and systematic uncertainties on the Radon measurement with time, shown in Figure 6.12. After 2.5 years, the statistical uncertainty becomes comparable to the systematic uncertainty.

Knowing accurately the Radon contamination means its contribution can be constrained in the topologies used for other background measurements.

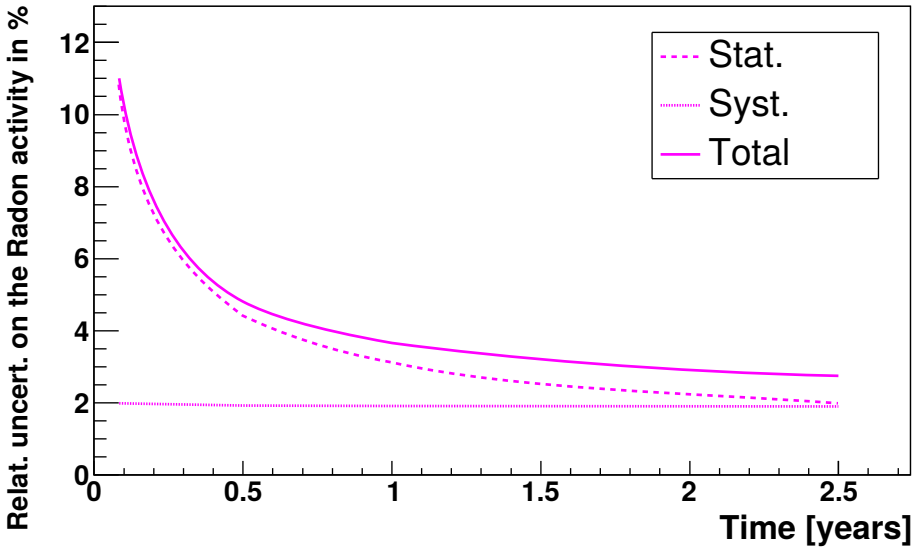

Figure 6.12 – Relative statistical, systematic and total uncertainties on the Radon activity measurement, as a function of the duration of the measurement.

6.4.3 ^{208}Tl and ^{214}Bi measurements: discriminating variables

One could consider measuring the ^{214}Bi activity in the $1e1\alpha$ topology from the source since the only other contributor, namely the Radon (Figure 6.2), was measured independently. However, in addition to the systematic uncertainty introduced by the extrapolation from one topology to the other, less than ten ^{214}Bi events are expected over the lifetime of the experiment, which is far below the fluctuations from the 300 expected Radon events. This topology consequently does not allow an accurate determination of the ^{214}Bi source contamination.

According to Figure 6.2, the topologies providing the most ^{214}Bi events are the $1e\mathrm{N}\gamma$ topologies. The latter are also interesting for the measurement of the ^{208}Tl in the source. As explained earlier, the $1e$ topology would prove useful if it was not also contaminated with a multitude of other β (and/or γ) emitters not considered here.

Since several contributions are expected in the $1e\mathrm{N}\gamma$ topologies, some discriminating variables need to be identified and used to raise the degeneracy of the fit. The main contributor to these topologies is Radon but the expected number of events can be inferred from the measurement performed in the tracker beforehand. The selected discriminating variables are displayed in Figures 6.13, 6.14, 6.15, 6.16 and 6.17. These distributions are normalized, which explains why ^{214}Bi and Radon share almost exactly the same distributions.

The $2\nu\beta\beta$ events reconstructed in the $1e1\gamma$ topology are the events where a Bremsstrahlung is produced while one of the electrons is not detected (because it did not leave the source or it triggered less than 3 tracker cells for instance). The resulting energy sum spectrum is a continuous spectrum, such as presented in Figure 6.13, while the exponentially decreasing γ energy spectrum is characteristic of Bremsstrahlung radiation (Figure 6.14). Another contribution to this topology from $2\nu\beta\beta$ events could come from events where the vertex of emission is close to the calorimeter X-walls, such that one of the electrons triggers less than 3 tracker cells. This would not be enough to reconstruct an electron track. The calorimeter hit would then be reconstructed as having no track associated with it *i.e.* as being triggered by a γ. However, such events are rejected by requiring the unassociated calorimeter hit to have no triggered tracker cells in its direct vicinity (*i.e.* the cells from the first layer in front of it).

The $1e1\gamma$ total energy spectrum (Figure 6.13) generated by ^{208}Tl events and extending to the 5 MeV region clearly shows why it is a harmful background for the $0\nu\beta\beta$ decay search. A simple Compton scattering could be enough to fake new physics. The Figure 6.14 shows the expected peaks associated with the ^{208}Tl and ^{214}Bi decays. Apart from the ^{214}Bi/Radon degeneracy, this $1e1\gamma$ topology provides two discriminating variables allowing a disambiguation between the different backgrounds.

Adding more discriminating variables from different topologies will not only provide a better background discrimination but also decrease the statistical uncertainties inherent

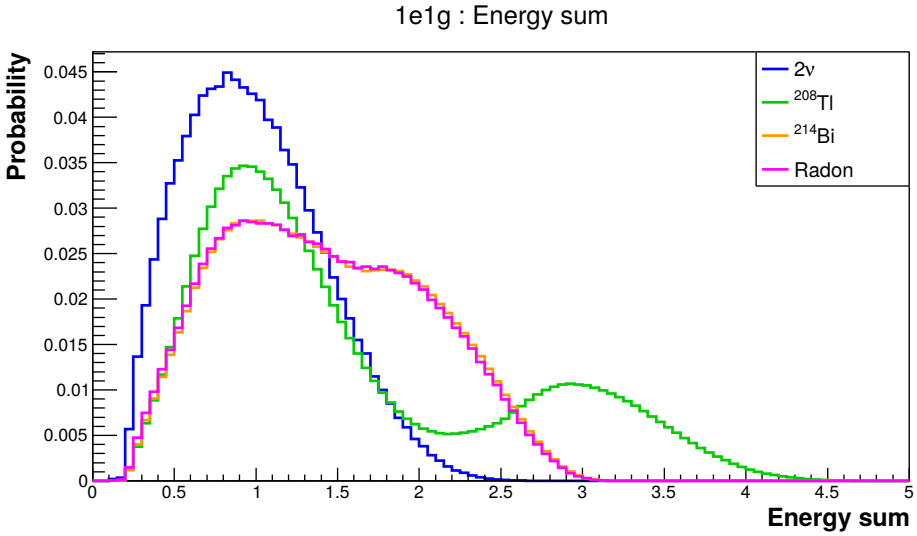

Figure 6.13 – Normalized total energy spectrum from the $1e1\gamma$ topology.

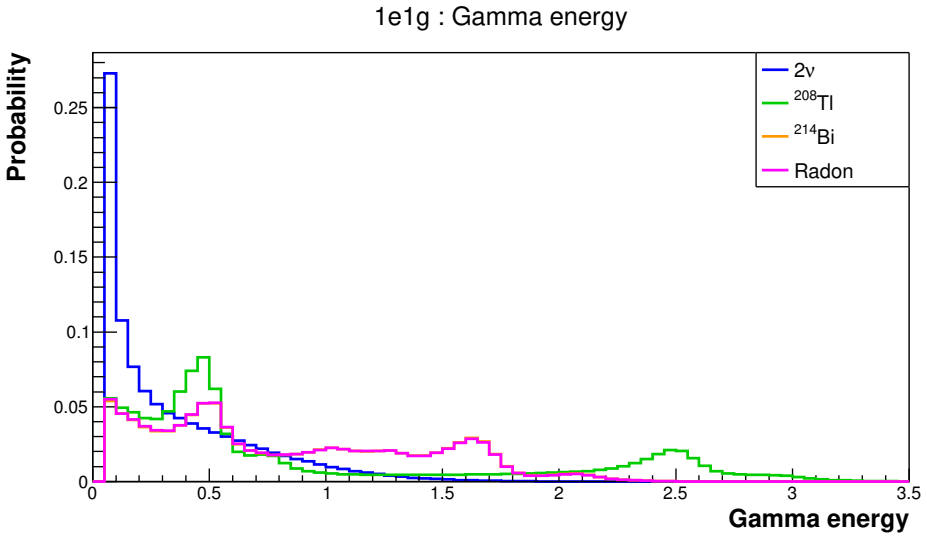

Figure 6.14 – Normalized energy spectrum of the γ from the $1e1\gamma$ topology. Even more so than for the electron energy spectra in Figure 6.13, the ^{214}Bi and the Radon γ energy spectra exactly overlap. The γ energy is indeed barely impacted whether it is emitted from the source or from the tracker.

in the measurement.

The two same variables, namely the electron and γ's energy sum and the energy of the γ of higher energy, are chosen for the $1e2\gamma$ topology. The $2\nu\beta\beta$ contribution is here strongly reduced, while this is a natural topology for the ^{208}Tl and ^{214}Bi backgrounds. The total energy spectra peak at different energies for the three isotopes, as shown in Figure 6.15. The γ content, unique to each isotope, is visible in Figure 6.16. This variable allows us to clearly distinguish the different background contributions.

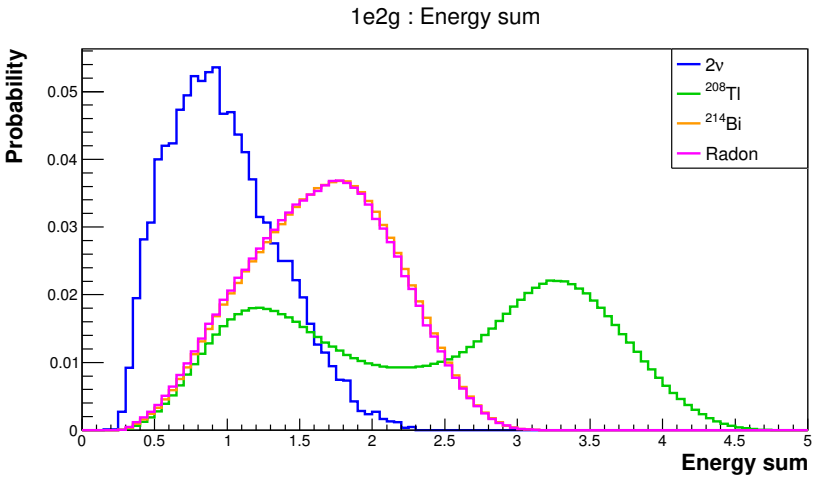

Figure 6.15 – Normalized total energy spectrum from the $1e2\gamma$ topology.

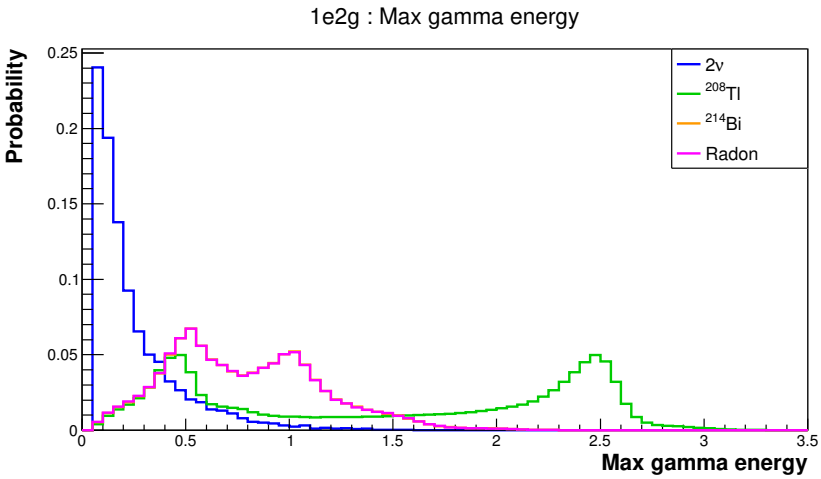

Figure 6.16 – Normalized energy spectrum of the γ of highest energy from the $1e1\gamma$ topology.

One last topology can improve the measurement accuracy: the $1e3\gamma$ topology. Theoretically, in light of Figure 5.62, only ^{208}Tl is expected to contribute to this topology, but a significant amount of $1e2\gamma$ or even $1e1\gamma$ events, coming from all the isotopes, will be mistakenly reconstructed as $1e3\gamma$ events. Faking this topology is very inefficient for $2\nu\beta\beta$ decays, which translates into the ill-defined $2\nu\beta\beta$ spectrum in Figure 6.17, despite a large amount of simulated events. This time, only the total energy is considered since most of the reconstructed γ's will have only partially deposited their energy.

Other variables could have been considered, but increasing the number of constraints makes it harder for the final fit to converge.

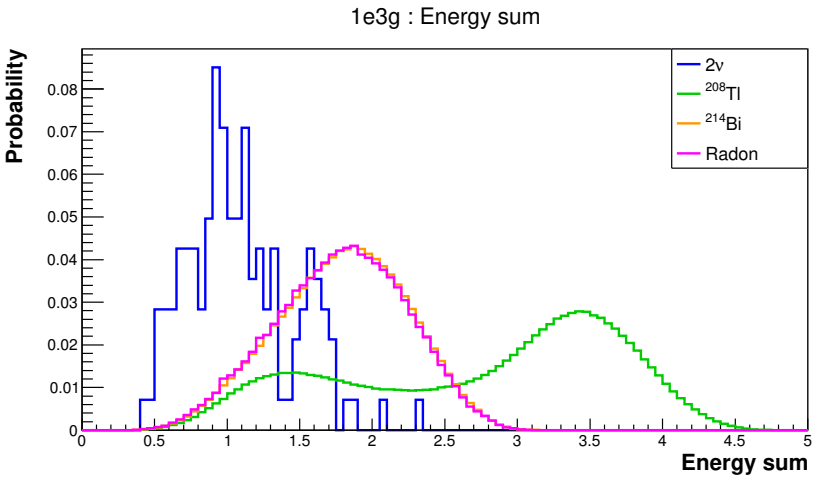

Figure 6.17 – Normalized total energy spectrum from the $1e3\gamma$ topology.

6.4.4 ^{208}Tl and ^{214}Bi measurements: pseudo-experiments

The pseudo-experiments generated to emulate a SuperNEMO demonstrator data taking campaign are once again used to estimate the uncertainty on the ^{208}Tl and ^{214}Bi measurements. A binned log-likelihood is minimized to fit the ^{208}Tl and ^{214}Bi contributions onto several distributions, across several topologies at the same time. The choice was made to fix the Radon contribution to its nominal activity instead of the activity measured previously with the $1e1\alpha$ tracker events. This might induce an overestimation of the systematic uncertainty but this way the ^{208}Tl and ^{214}Bi measurements are not correlated to that of the Radon. The $2\nu\beta\beta$ contribution was let free to vary within 10 % of its nominal half-life since the $2\nu\beta\beta$ half-life of ^{82}Se has already been measured by NEMO-3 [96].

While performing the fit on a large number of variables should provide more accurate measurements, the five distributions provided appeared to be too much for the minimization tools to handle. Instead, only the most discriminating variable per topology was chosen: the γ energy in the $1e1\gamma$ topology, the higher γ energy in the $1e2\gamma$ topology and the energy sum in the $1e3\gamma$ topology. If the number of constraints is limited, it is indeed preferable to include the most topologies possible in an effort to reduce the statistical uncertainty, rather than using several distributions per topology.

The result of the fit to a pseudo-experiment is shown in Figures 6.18, 6.19 and 6.20. In Figure 6.18, $2\nu\beta\beta$ events constitute the main contribution, albeit concentrated at lower energies. On the contrary, ^{208}Tl events have the lowest contribution but reach higher energies. Since ^{214}Bi and Radon share the same distributions, it was essential to determine the Radon contribution independently.

Figures 6.19 illustrate even more the need to measure the Radon level beforehand, since it is here the main contributor.

The Figure 6.20 shows arguably the less reliable measurement but, used conjointly with the $1e3\gamma$ topology, it still helps improve the accuracy of the fit.

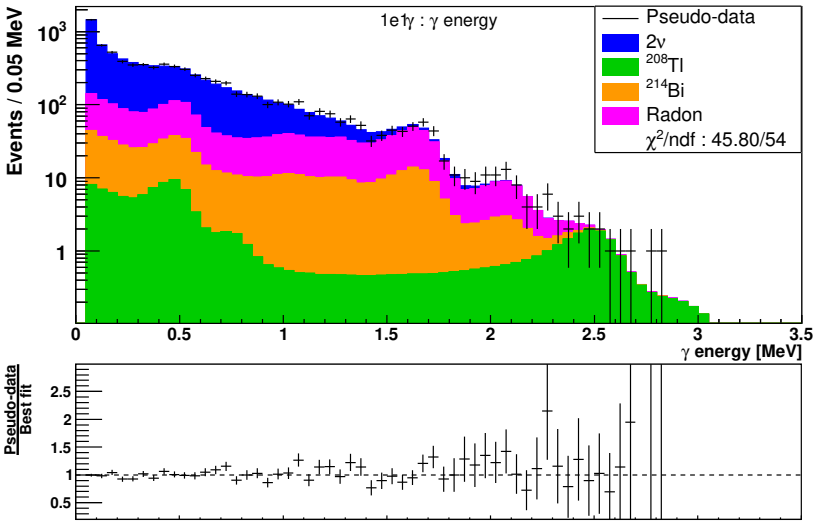

Figure 6.18 – Fit of a pseudo-experiment on the γ energy spectrum in the $1e1\gamma$ topology.

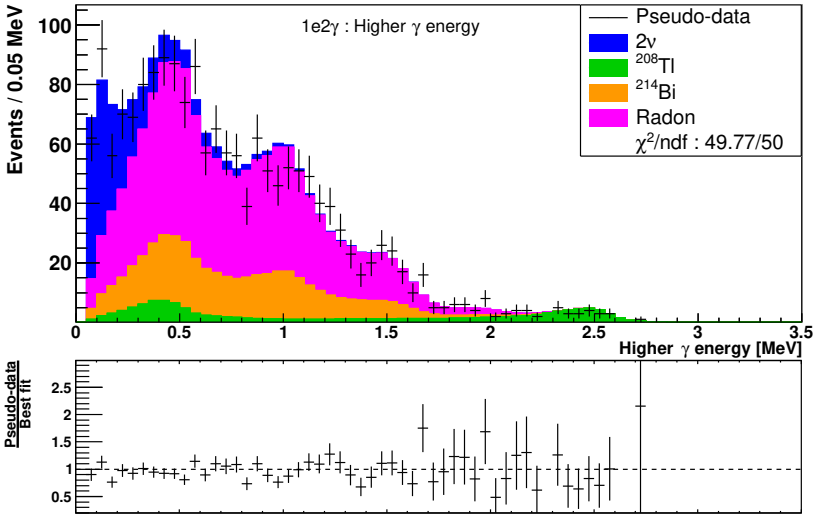

Figure 6.19 – Fit of a pseudo-experiment on the energy spectrum of the γ of highest energy in the $1e2\gamma$ topology.

For these distributions, the fit expectedly agrees with the pseudo-data, within statistical fluctuations. The same process is repeated for a large number of experiments in order to evaluate the stability of the approach and determine the systematic uncertainty expected for these measurements. The distribution of the activities measured with each pseudo-experiment, running for 2.5 years, are presented in Figure 6.21 for the ^{208}Tl and ^{214}Bi contaminations.

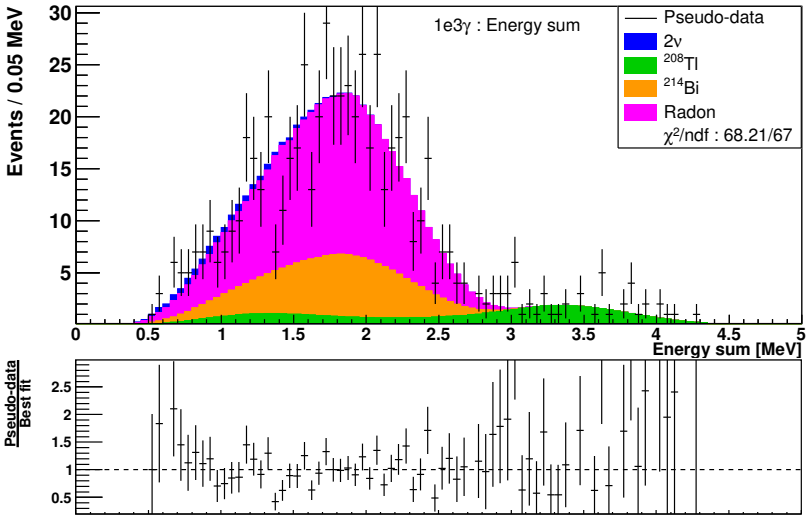

Figure 6.20 – Fit of a pseudo-experiment on the total energy spectrum in the $1e3\gamma$ topology.

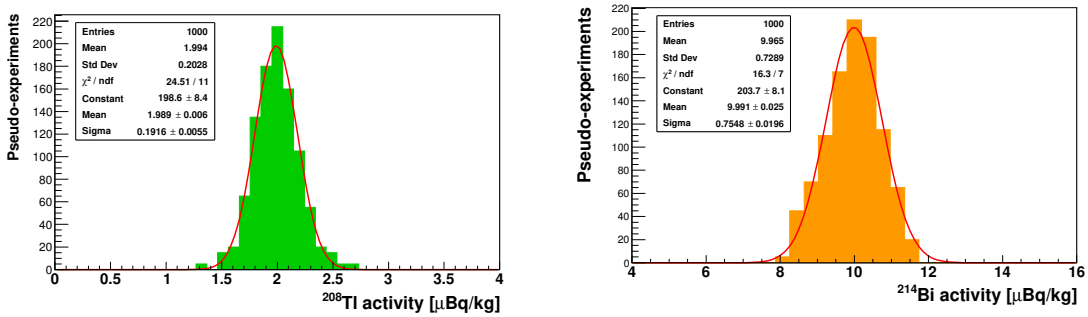

Figure 6.21 – *(left)* Distribution of the ^{208}Tl activities measured from the pseudo-experiments. *(right)* Distribution of the ^{214}Bi activities measured from the pseudo-experiments. The pseudo-experiments are generated assuming a 17.5 kg.y exposure.

The two distributions are fitted with Gaussian functions and one standard deviation is taken as the uncertainty on the measurement. Since these distributions are not exactly normally distributed, the root mean square could also have been chosen but it would yield similar results. The mean ^{208}Tl and ^{214}Bi activities are well within 1 % of their expected values. This shows that after 2.5 years, the systematic uncertainty on the ^{208}Tl activity would be just below 10 % while the systematic uncertainty on the ^{214}Bi would be around 7.5 %.

These systematic uncertainties are much larger than for Radon since the $1e\mathrm{N}\gamma$ topologies are not as pure as the $1e1\alpha$ topology from the tracker. They are indeed dominated by $2\nu\beta\beta$ and/or Radon events which means that a slight statistical fluctuation from any of these contributors can reverberate on the normalizations of the ^{208}Tl and ^{214}Bi templates in order to better accommodate the pseudo-data.

Once again, pseudo-experiments can also be generated with a lower number of events in order to simulate shorter measurement durations. This yields the time evolution of the uncertainties associated with the measurement of a 2 μBq/kg ^{208}Tl contamination and a 10 μBq/kg ^{214}Bi contamination, presented in Figure 6.22 and Figure 6.23, respectively.

The statistical uncertainties are computed by summing the events from the three $1e\mathrm{N}\gamma$ topologies.

For lower exposures, the distributions of the activities measured with a thousand pseudo-experiments depart even more from a Gaussian distribution. The root mean square of the distribution is thus preferred when the fit does not agree with the latter. In both cases, the dominating source of uncertainty over the course of the experiment remains the systematic uncertainty. Little improvement on the uncertainty is to be expected after the planned 2.5 years.

Assuming the effective ^{208}Tl activity is actually closer to the latest BiPo-3 measurements, *i.e.* a 50 μBq/kg weighted average (with activities ranging from $\sim$20 μBq/kg to $\sim$140 μBq/kg depending on the source strip) the ^{208}Tl contamination would be known more accurately, simply because of the larger number of events expected. Thanks to the vertex reconstruction, the systematic uncertainties could also be reduced by comparing the ^{208}Tl activities (and ^{214}Bi activities) measured for individual source strips to the measurements provided by the BiPo-3 detector.

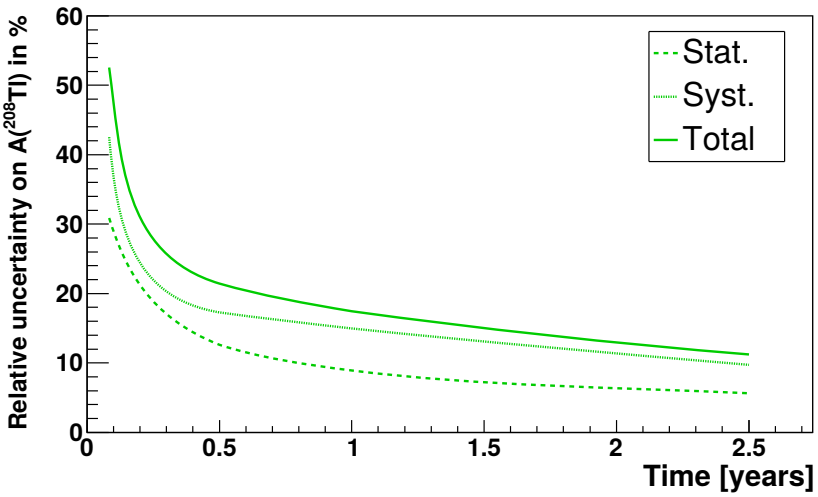

Figure 6.22 – Relative statistical, systematic and total uncertainties on the ^{208}Tl activity measurement, as a function of the duration of the measurement.

6.4.5 $2\nu\beta\beta$ half-life measurement: discriminating variables

Knowing accurately the background model is essential for the neutrinoless double beta decay search but it is also important for the precise measurement of the $2\nu\beta\beta$ decay half-life, which is a useful input to the nuclear models, in particular for the determination of the nuclear matrix elements.

Though a significant amount of $2\nu\beta\beta$ events are expected to populate the $1e$ topology, the latter cannot provide a reliable constraint on the $2\nu\beta\beta$ half-life measurement since

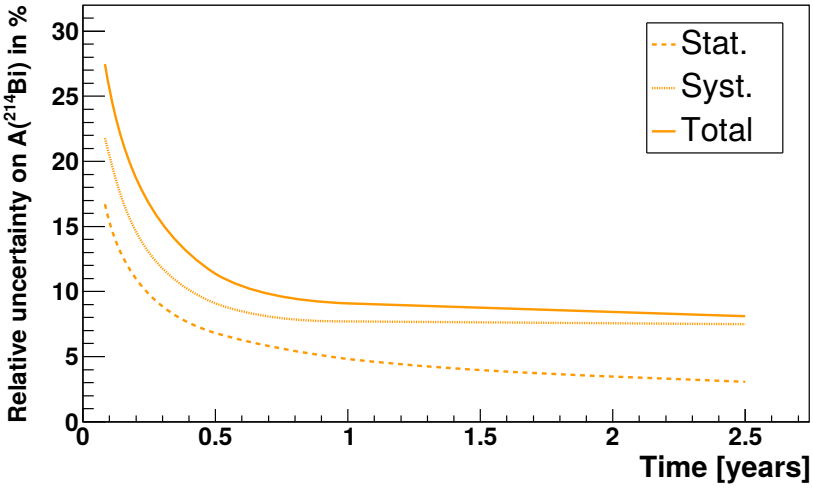

Figure 6.23 – Relative statistical, systematic and total uncertainties on the ^{214}Bi activity measurement, as a function of the duration of the measurement.

other important contributions are expected, which are not considered in this simplified background model. Only the $2\nu\beta\beta$ natural topology, namely the $2e$ topology, will be used to estimate its half-life. The most discriminating variables selected are the electrons energy sum, the energy of the higher energy electron and the cosine of the angle between the two particles.

Figure 6.24 shows the normalized total energy distribution for the main backgrounds.

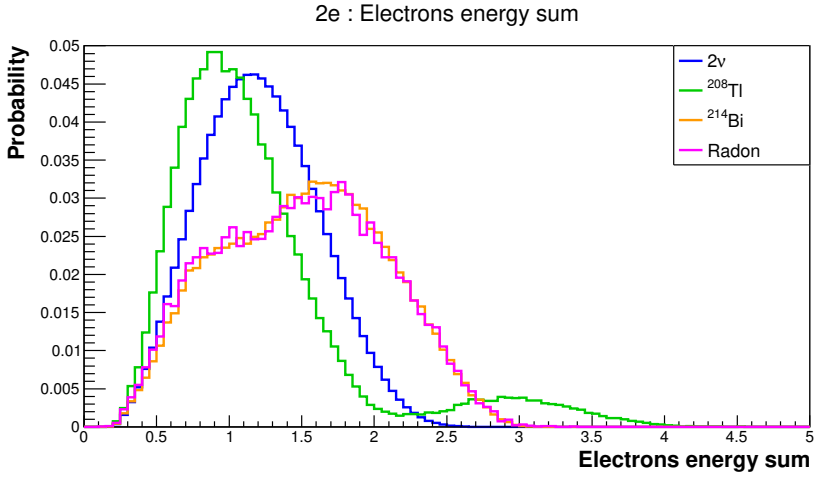

Figure 6.24 – Electrons total energy spectrum in the $2e$ topology.

The characteristic electron conversion peaks from the γ emitters (the 2.615 MeV conversion electron from ^{208}Tl or the 1.764 MeV conversion electron from ^{214}Bi for instance) should also help better isolate the $2\nu\beta\beta$ contribution if needs be (Figure 6.25).

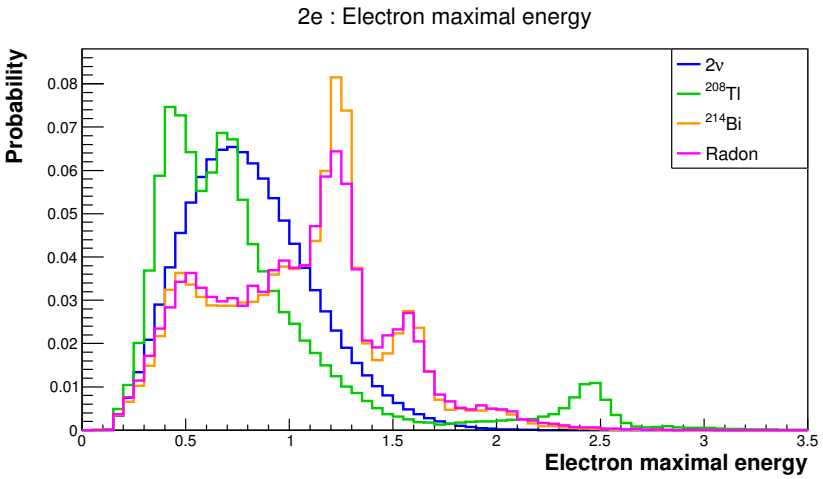

Figure 6.25 – Energy spectrum of the highest energy electron in the $2e$ topology.

The cosine of the angle (Figure 6.26) does not provide a good separation but it can help raise the ambiguity between the ^{214}Bi and the Radon contributions if need be. Indeed, the two electrons generated from ^{214}Bi decays are emitted isotropically inside the source, since the two electrons emission processes are not correlated. In Radon decays, the two electrons are also emitted isotropically but the events originate from the tracker. One of the most effective ways for Radon events to fake two electrons coming from the source is thus for one of the electron to cross the source. The reconstructed angle is therefore close to π and the angle distribution is consequently more peaked at low values of the cosine of the angle.

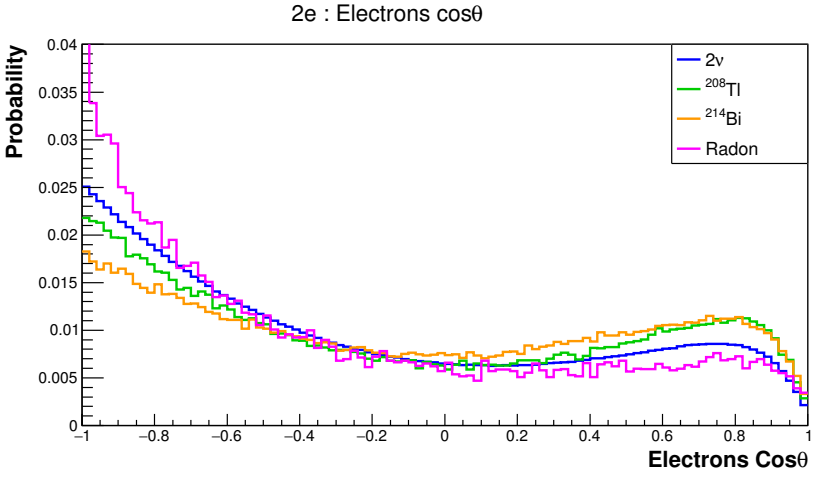

Figure 6.26 – Distribution of the cosine of the angle between the two electrons in the $2e$ topology.

6.4.6 $2\nu\beta\beta$ half-life measurement: pseudo-experiments

The number of events from the 2ν contribution is estimated by fitting these three distributions obtained from pseudo-experiments. The half-life of the $2\nu\beta\beta$ process is then

deduced from this event rate, as explained in Section 3.3.2. For the same reason as before, the other background contributions, determined independently from this topology, are fixed to their nominal activities and not to the activities measured for the same pseudo-experiment.

Figures 6.27, 6.28 and 6.29 illustrate the vast domination of the $2\nu\beta\beta$ events in this topology, such that knowledge of the other contributions is almost useless (they are negligible compared to the $2\nu\beta\beta$ statistical fluctuations).

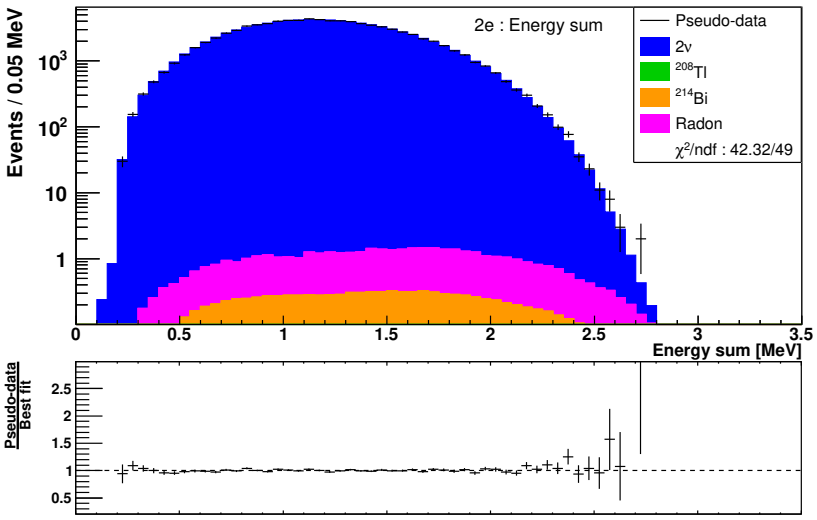

Figure 6.27 – Fit of a pseudo-experiment on the electrons total energy spectrum in the $2e$ topology.

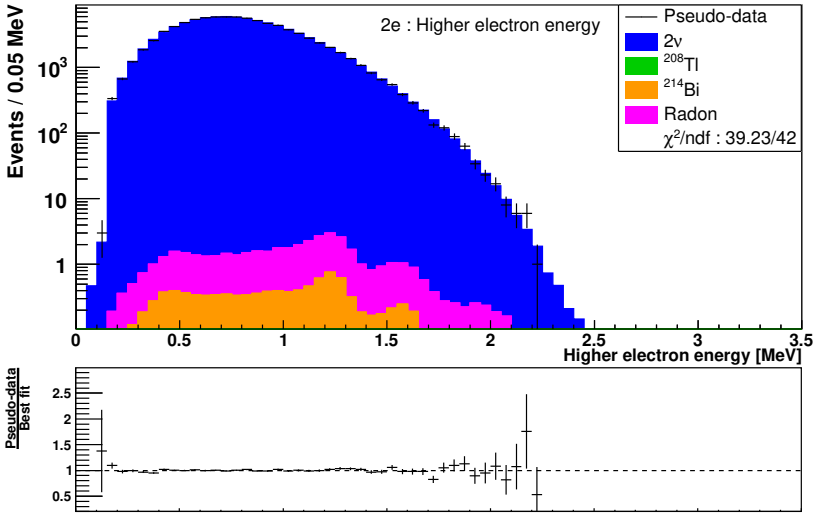

Figure 6.28 – Fit of a pseudo-experiment on the energy spectrum of the highest energy electron in the $2e$ topology.

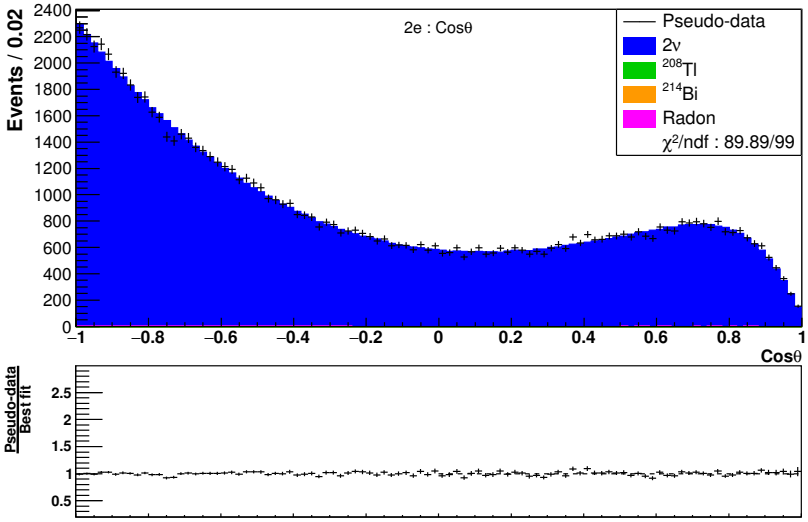

Figure 6.29 – Fit of a pseudo-experiment on the distribution of the cosine of the angle between the two electrons in the $2e$ topology.

This very pure topology means that the systematic uncertainty is expected to be much lower than for the ^{208}Tl and ^{214}Bi measurements. Indeed, looking at the distributions of the half-lives measured with each pseudo-experiment, presented in Figure 6.30, the systematic uncertainty is estimated at around 0.3 % after 2.5 years. The mean half-life deviates by 1 % from the expected half-life. This deviation is significative compared to the systematic uncertainty. This is once again due to the rounding of the expected number of 2ν events. The pseudo-experiments were generated with 10^6 2ν events, instead of the theoretical 989801 decays expected considering a 9 10^{19} years. Correcting for this effect, one finds back exactly the 8.908 10^{19} y mean half-life.

The evolution with time of the statistical and systematic uncertainties of the 2ν half-life measurement are presented in Figure 6.31. Despite its very high half-life, a large amount of $2\nu\beta\beta$ events is expected compared to the other backgrounds. The relative statistical uncertainty consequently quickly decreases, such that the systematic uncertainty becomes the dominating and limiting uncertainty on the half-life measurement after a few months only. After 2.5 years, the total uncertainty should be lower than 0.4 %. This would represent an improvement on the precision of the ^{82}Se $2\nu\beta\beta$ half-life by more than a factor 3 over the measurement performed by NEMO-3 with an exposure to ^{82}Se of 4.90 kg.y [96].

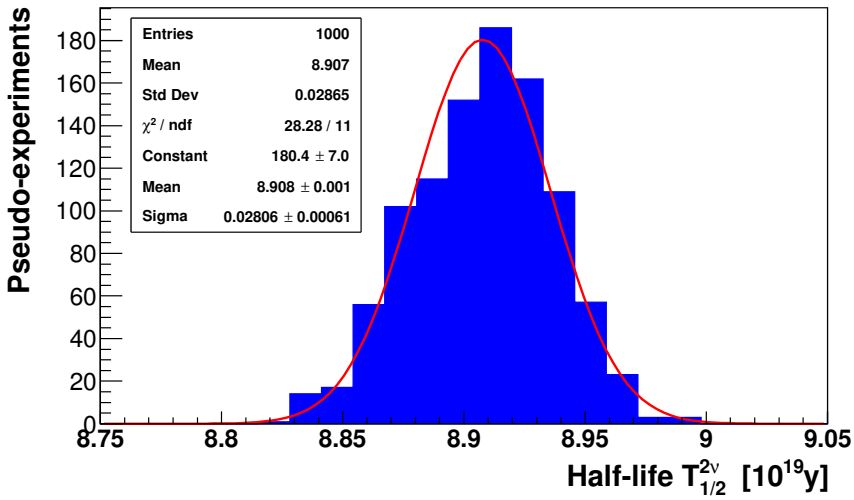

Figure 6.30 – Distribution of the $2\nu\beta\beta$ half-lives measured from the pseudo-experiments.

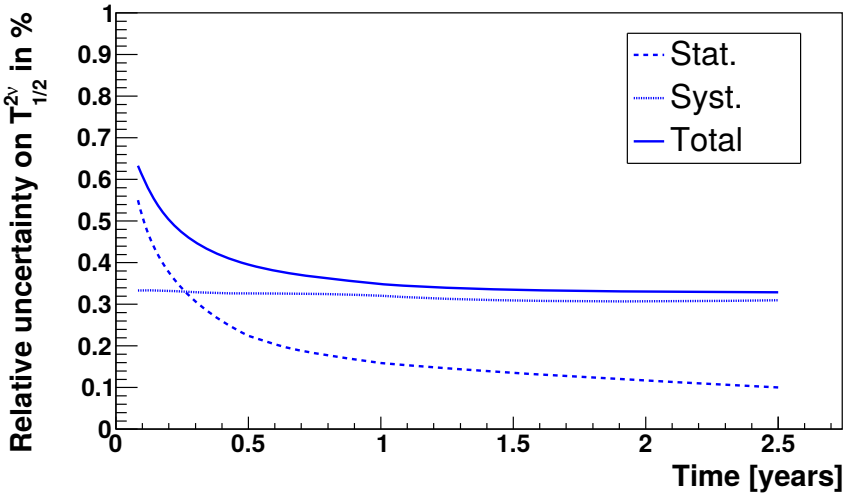

Figure 6.31 – Relative statistical, systematic and total uncertainties on the ^{214}Bi activity measurement, as a function of the duration of the measurement.

6.5 Conclusion

This Chapter shows how the SuperNEMO demonstrator, thanks to its ability to reconstruct different event topologies, and despite very stringent radiopurity constraints, will be able to accurately and independently characterize its own background model.

This study provides the first estimation of the systematic and statistical uncertainties expected for the measurements of the main backgrounds, performed by and for the SuperNEMO demonstrator. The Radon activity and the $2\nu\beta\beta$ half-life, because of their pure

dedicated topologies and high number of events, will be the most accurately measured backgrounds.

Ideally, all the contributions would be fitted simultaneously, across all topologies, using the most discriminating variables possible. However, this approach was not successful with only three topologies and five distributions. The measurements of the ^{208}Tl and ^{214}Bi activities could probably benefit from including more constraints to the final fit.

Regarding the four main backgrounds, the dominating source of uncertainty after 2.5 years of measurement appears to be the systematic uncertainty. Since this uncertainty does not decrease with time (*i.e.* with more events), little improvement on the knowledge of the background model is expected after 2.5 years.

Actually, a better estimation of the systematic uncertainties induced by the detector and the analysis technique could be performed with the calibration sources. The approach would essentially stay the same, namely using the different topologies available to measure the activity of the calibration sources. Comparing the activities obtained with the different topologies could shed light on possible biases. The measured activities could also be compared to independent external measurements of the calibration sources activities.

Chapter 7

Sensitivity to the $0\nu\beta\beta$ decay with SuperNEMO

In this Chapter, the principle of the search for the neutrinoless double beta decay is presented. The topology of interest is the $2e$ topology. The two electrons energy sum is used in every double beta decay experiments to discriminate the signal from the background events. This single variable is sufficient to look for the neutrinoless double beta decay. However, we will see how SuperNEMO, thanks to its tracking capabilities and segmented calorimeter, can take advantage of some extra topological information in a multivariate analysis to improve its sensitivity. The impact of the level of contamination of the main backgrounds on the sensitivity is also presented. Finally, different limit setting solutions are compared.

7.1 Conditions of the simulation

The same background model, as described in the previous chapter, is also considered here for the evaluation of the sensitivity of the search for neutrinoless double beta decay. The hypothetical signal would be detected on a variable distribution as an excess of events, with respect to what is predicted by the background-only model. The sensitivity to this excess is obviously better when the expected number of background events is low. Such variable is, for instance, the electrons energy sum in the $2e$ topology: the $0\nu\beta\beta$ signal would be located close to the transition energy $Q_{\beta\beta}$, where most background spectra end. The size of the Monte-Carlo simulations was consequently increased, in order to better describe the background templates in the less favorable regions of the parameter space since (internal backgrounds have very low efficiencies in the $2e$ topology). The size of the Monte-Carlo simulations for each isotope is presented in Table 7.1 and compared to the expected number of decays in the SuperNEMO demonstrator conditions (17.5 kg.y exposure). These simulations were performed under the same experimental conditions as before but with an updated version of the SuperNEMO software, which did not introduce any changes on the physics.

The assumed underlying mechanism for the $0\nu\beta\beta$ decay is the mass mechanism. As mentioned in Section 1.2.4, this mechanism is the most natural and widespread mecha-

	Expected decays	Simulated decays
$0\nu\beta\beta$ ($T^{0\nu}_{1/2} = 610^{24}$y)	3.9	10^7
$2\nu\beta\beta$	10^6	$1.2\ 10^9$
^{208}Tl	$1.1\ 10^3$	$4\ 10^8$
^{214}Bi	$5.5\ 10^3$	$4\ 10^8$
Radon	$1.8\ 10^5$	$7\ 10^8$

Table 7.1 – Size of the Monte-Carlo simulations, compared to the expected number of decays in the SuperNEMO demonstrator (17.5 kg.y).

nism. The kinematics being different from one mechanism to the other, the results quoted in this chapter are only valid for the mass mechanism, unless specified otherwise.

We select only events matching the $2e$ topology. As a reminder, an electron is defined as a negatively curved track with a vertex on the source and an associated calorimeter hit. These are the minimum criteria to select $\beta\beta$-like events. Other criteria, based on topological information, can be required afterward.

7.2 Single variable approach

Most double beta decay experiments are only sensitive to the 2 electrons energy sum. Fortunately, this variable turns out to be the most discriminating variable for the search of the $0\nu\beta\beta$ decay. The electrons energy sum, as reconstructed by SuperNEMO, is displayed in Figure 7.1, where the different spectra are arbitrarily normalized.

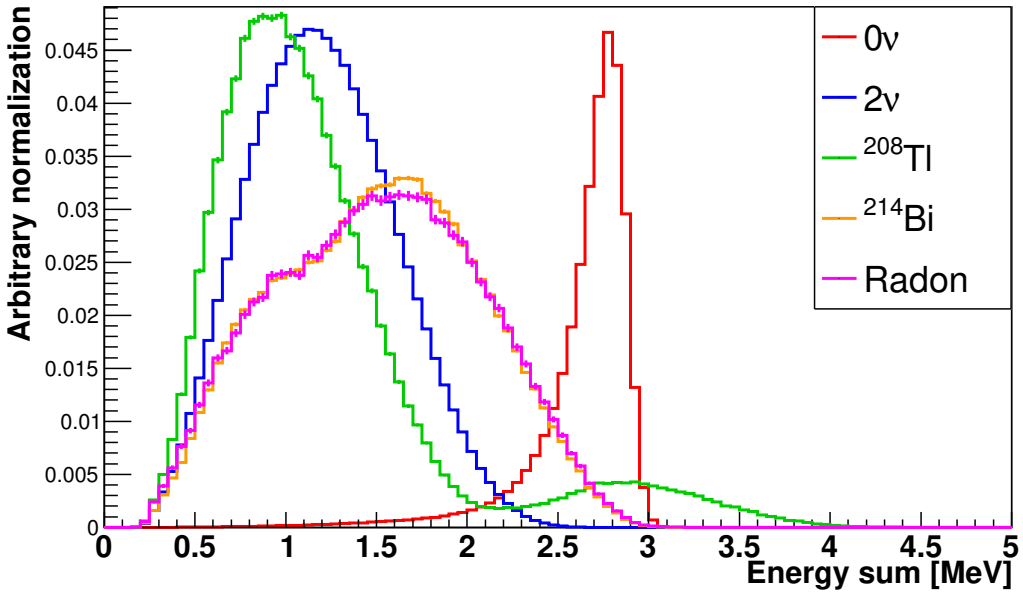

Figure 7.1 – Two electrons energy sum spectra for the $0\nu\beta\beta$ process (in red) and the main backgrounds.

The $0\nu\beta\beta$ spectrum is peaked close to the maximum available energy $Q_{\beta\beta} = 2.995$ MeV. It is however slightly shifted towards lower energies because of the energy losses, mainly occurring when the electrons go through the dense source material. The electrons can also lose some energy via multiple scattering in the tracker gas, as well as when they go through the calorimeter wrapping. Harder scatterings can also happen on the tracker wires, in which case an electron can lose a significant part of its energy. These energy losses explain the $0\nu\beta\beta$ asymmetric distribution, differing from the expected Gaussian distribution, which width comes from the calorimeter energy resolution. The background distributions were already commented in the previous chapter, but, superimposing the expected signal distribution helps realize why ^{208}Tl, ^{214}Bi and Radon constitute backgrounds for the $0\nu\beta\beta$ search, in addition to the $2\nu\beta\beta$ natural and irreducible background.

In order to understand the impact of each of the backgrounds on the $0\nu\beta\beta$ decay search, each template is normalized by the number of events expected in the $2e$ topology in Figure 7.2a. Once again, a 17.5 kg.y exposure is considered and the target activities presented in Table 6.1 are assumed to be reached. The spectra are presented in the logarithmic scale because the $2\nu\beta\beta$ events largely dominate this topology. The $2\nu\beta\beta$ decays might appear as if they were the only background source, but focusing on the region of interest (Figure 7.2b) shows that the other backgrounds count for a significant part of the background in the $0\nu\beta\beta$ search, even with such low expected number of events.

	$2\nu\beta\beta$	^{208}Tl	^{214}Bi	Radon	$0\nu\beta\beta$ efficiency
Full energy range	88 750	1.16	9.0	35.2	100 %
[2.65;3.2] MeV	1.50	0.05	0.10	0.46	63.75 %
[2.7;3.2] MeV	0.43	0.05	0.07	0.31	54.00 %
[2.75;3.2] MeV	0.11	0.04	0.04	0.20	41.68 %
[2.8;3.2] MeV	0.02	0.04	0.03	0.12	27.54 %

Table 7.2 – Expected number of events in the $2e$ topology for the SuperNEMO demonstrator (17.5 kg.y). The fraction of the $0\nu\beta\beta$ spectrum contained in the different energy windows is presented in the "$0\nu\beta\beta$ efficiency" column and does not take into account the detection/reconstruction efficiency.

Table 7.2 sums up the number of events expected in the $2e$ topology from the main backgrounds on the full energy range and in several energy windows. The $2\nu\beta\beta$ spectrum and the ^{214}Bi/Radon spectra quickly decay with the energy but the end points of the latter are located at a higher energy, such that the probability for a ^{214}Bi or a Radon event to fall in the region of interest is much higher. This is all the more true for the ^{208}Tl spectrum, which high-energy peak sits right into the region of interest, hence the much more stringent constraint on the ^{208}Tl activity. The target background activities were defined so that each background has a similar contribution to that of the $2\nu\beta\beta$ in the region of interest [97]. The Radon contribution is here clearly higher than that of the backgrounds originating from the source because no topological cuts are applied. Indeed, requiring a minimum internal probability or a maximum source vertices separation between the two electrons can reject most of the Radon events, at the expense of a small signal efficiency loss. The pros and cons of these cuts will be addressed later.

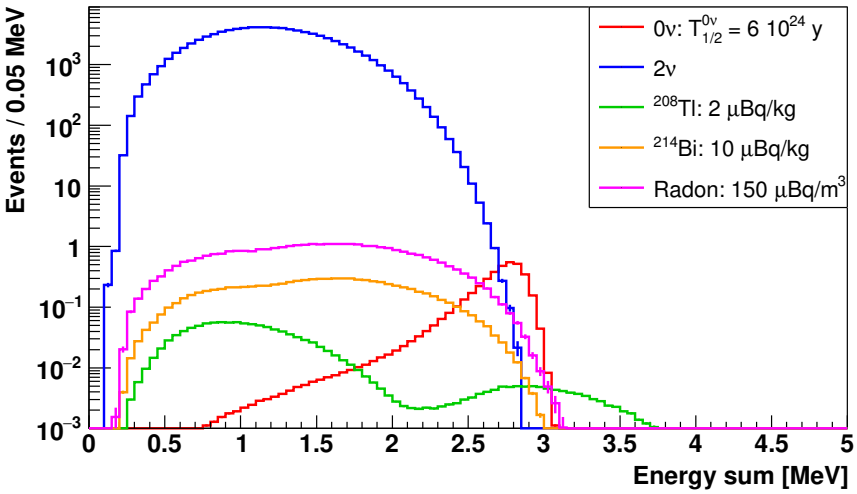

(a)

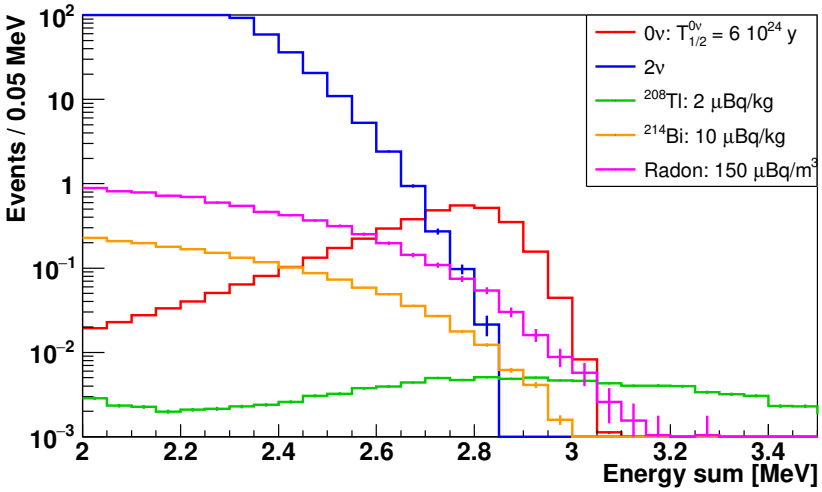

(b)

Figure 7.2 – Two electrons energy sum spectra for the $0\nu\beta\beta$ process (in red) and the main backgrounds, 7.2a on the full energy range and 7.2b focused on the region of interest. The backgrounds are normalized to the expected number of events in the $2e$ topology. The $0\nu\beta\beta$ signal is normalized to 1.

At this stage of the analysis, we've only taken advantage of the SuperNEMO tracking capabilities to focus on the $2e$ events but no topological cuts have been performed and only a single variable, the electrons energy sum, is used, similarly to most double beta experiments. The background index is a useful quantity to compare the different experiments performances. Without topological cuts, depending on the energy window, the SuperNEMO expected background index varies from 3 10^{-5} cts.kev^{-1}.kg^{-1}.y^{-1} in the [2.8;3.2] MeV energy window to 2 10^{-4} cts.kev^{-1}.kg^{-1}.y^{-1} in the wider [2.65;3.2] MeV energy window. This also means that in a energy window as wide as [2.7;3.2] MeV, less than one background event is expected in the region of interest for the demonstrator.

Using the semi-frequentist approach with the COLLIE software, as described in Section 3.3.3, the SuperNEMO demonstrator could set a limit on the $0\nu\beta\beta$ process:

$$T_{1/2}^{0\nu} > 5.35\ 10^{24}\ \text{y} \tag{7.1}$$

The use of topological information to perform an event selection could improve this sensitivity. The idea is to reject the most background events while keeping as many signal events as possible. Obviously, rejecting background events may also lead to the loss of some signal events; a balance must be found if one wants to improve the sensitivity of the experiment.

Let's consider for instance the following cuts:

- $P_{int} > 4$ %: the two internal electrons must have an internal probability (based on the TOF computation) higher than 4 %. This is a standard value in NEMO-3 analyses and its effectiveness in rejecting non internal background in SuperNEMO was confirmed [98].

- $\Delta_y < 60$ mm and $\Delta_z < 70$ mm: the two electrons vertices extrapolated on the source must not be separated by more than 60 mm horizontally (perpendicularly to the wires) and 70 mm vertically (in parallel with the wires). These values allow 95 % of the signal events to be kept [98].

These cuts are designed to reject events where the two electrons are not emitted simultaneously or from the same location in the source. Consequently, these cuts will mainly impact the Radon contribution, as shown in Figure 7.3 and Table 7.3.

The application of topological cuts decreases the number of expected events for all the backgrounds but especially for Radon. As explained before, the Radon events are not emitted from the source[a] but mainly from the tracker wires. The internal probability and vertices separation can therefore help discriminate such events from signal events. This table also shows that the $2\nu\beta\beta$ process remains the main background contributor. However, its contribution becomes similar to that of the other backgrounds in the narrowest energy windows. The signal selection efficiency is naturally reduced by these cuts. On

[a] A small fraction of the Radon daughter nuclei may deposit on the surface of the source foils.

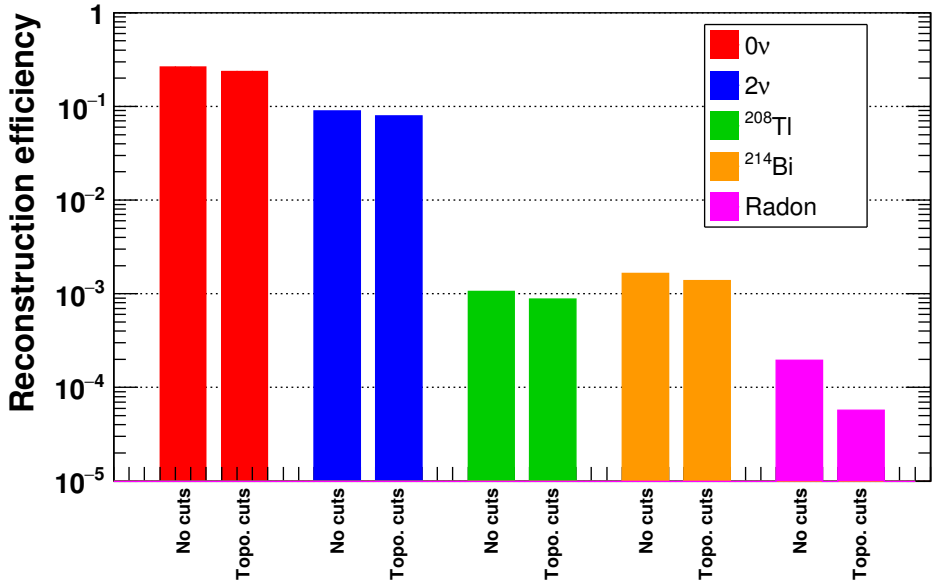

Figure 7.3 – Reconstruction efficiencies before and after the application of topological cuts. These cuts aim at rejecting events where the two electrons were not emitted simultaneously from the same region of the source. The Radon contribution can be reduced by a factor 4.

	$2\nu\beta\beta$	^{208}Tl	^{214}Bi	Radon	$0\nu\beta\beta$ efficiency
Full energy range					
No cuts	88 750	1.16	9.0	35.2	100 %
With topological cuts	78 010	0.96	7.6	10.4	90.31 %
[2.65;3.2] MeV					
No cuts	1.50	0.05	0.10	0.46	63.75 %
With topological cuts	1.26	0.04	0.09	0.12	59.24 %
[2.7;3.2] MeV					
No cuts	0.43	0.05	0.07	0.31	54.00 %
With topological cuts	0.38	0.04	0.06	0.08	50.42 %
[2.75;3.2] MeV					
No cuts	0.11	0.04	0.04	0.20	41.68 %
With topological cuts	0.11	0.03	0.04	0.05	39.11 %
[2.8;3.2] MeV					
No cuts	0.02	0.04	0.03	0.12	27.54 %
With topological cuts	0.02	0.03	0.02	0.03	25.94 %

Table 7.3 – Comparison of the expected number of events in the $2e$ topology for the SuperNEMO demonstrator (17.5 kg.y) with and without topological cuts. The fraction of the $0\nu\beta\beta$ spectrum contained in the different energy windows is presented in the "$0\nu\beta\beta$ efficiency" column and does not take into account the detection/reconstruction efficiency.

the full energy range, this translates into a loss of about 10 % of the signal events. Yet, the most relevant signal efficiency is the one in the region of interest. In the [2.8;3.2] MeV energy window for instance, the relative decrease in signal efficiency is only 6 % while the Radon level is reduced by a factor 4. The signal rejection is lower at higher energies

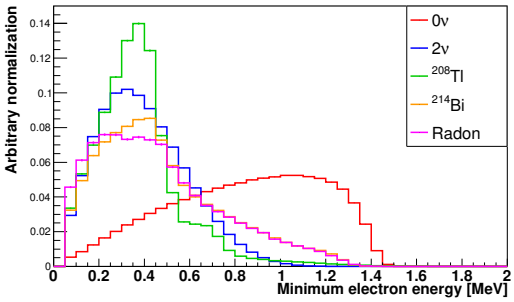

Figure 7.4 – Energy spectra of the lower energy electron for the $0\nu\beta\beta$ process (in red) and the main backgrounds.

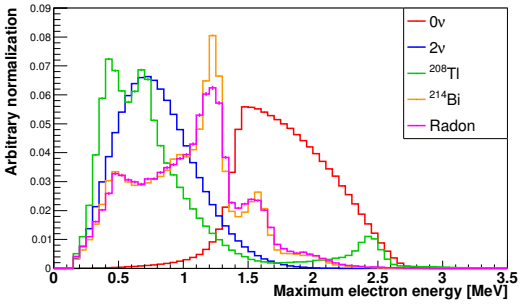

Figure 7.5 – Energy spectra of the higher energy electron for the $0\nu\beta\beta$ process (in red) and the main backgrounds.

because electrons did not lose energy by scattering in the tracker, for example. On the contrary, events where one of the electron lost some energy because of a scattering will also have a larger source vertices separation since the reconstruction of the tracks is likely to be impaired by the scattering.

These standard cuts, even without optimization, might already seem beneficial but, considering the gain on the already very low background constraints compared to the loss of signal efficiency, the sensitivity is actually decreased, with a 90 % C.L. limit on the half-life:

$$T_{1/2}^{0\nu} > 5.31\ 10^{24}\ \text{y} \tag{7.2}$$

The use of topological cuts will be revisited later but with background constraints so low, it does not appear to be worth it. This is of course an overstatement, but if the only way to improve the sensitivity of the analysis is to apply very loose cuts, the improvement is also bound to be marginal. That's why, instead of performing a tedious optimization of the cuts on a limited number of topological variables, the choice was made to take advantage of some multivariate analysis tools, already widespread in the particle physics community. This approach has the advantage of taking all the events topological information into account without sacrificing the signal efficiency.

7.3 Multivariate approach : the discriminating variables

SuperNEMO is able to record the full kinematics of an event. This gives access to several topological variables which can be taken advantage of thanks to a multivariate analysis. The choice of TMVA's Boosted Decision Trees was introduced and motivated in Section 3.3.4.

The most relevant variables which might help us discriminate signal from background events are displayed in Figures 7.4, 7.5, 7.6, 7.7, 7.8, 7.9, 7.10, 7.11, 7.12 and 7.13. The two electrons energy sum was already presented earlier.

SuperNEMO is able to distinguish the two electrons in a $0\nu\beta\beta$ event. The normalized spectra of the lower energy electron is presented in Figure 7.4 and that of the higher energy

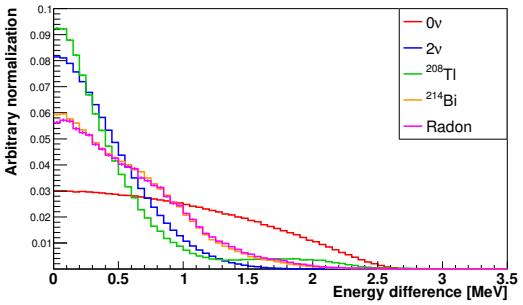

Figure 7.6 – Energy difference spectra for the $0\nu\beta\beta$ process (in red) and the main backgrounds.

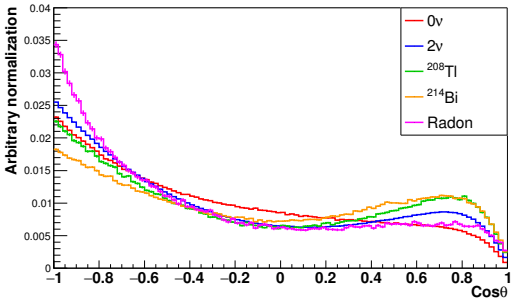

Figure 7.7 – Distribution of the cosine of the angle between the two electrons for the $0\nu\beta\beta$ process (in red) and the main backgrounds.

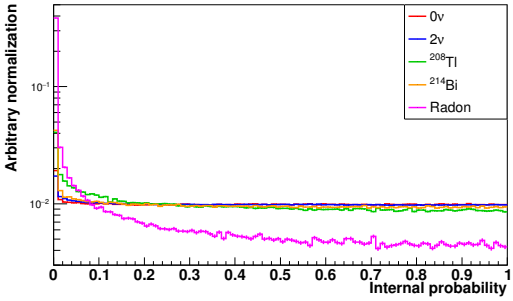

Figure 7.8 – Internal probability distributions for the $0\nu\beta\beta$ process (in red) and the main backgrounds.

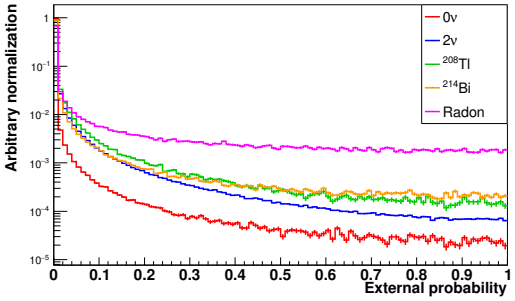

Figure 7.9 – External probability distributions for the $0\nu\beta\beta$ process (in red) and the main backgrounds.

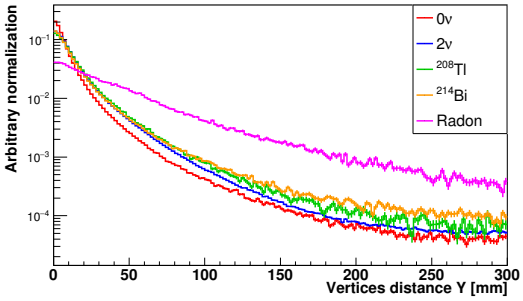

Figure 7.10 – Horizontal (Y) source vertices separation distributions for the $0\nu\beta\beta$ process (in red) and the main backgrounds.

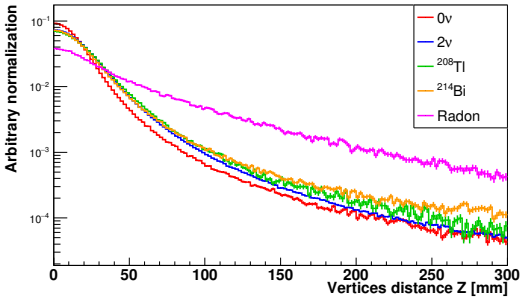

Figure 7.11 – Vertical (Z) source vertices separation distributions for the $0\nu\beta\beta$ process (in red) and the main backgrounds.

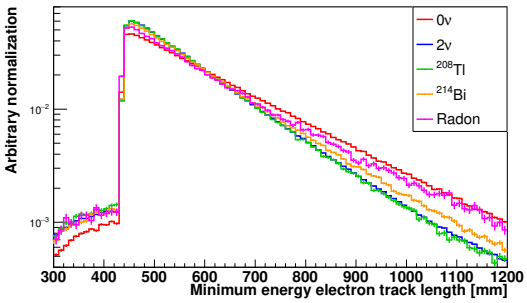

Figure 7.12 – Distribution of the track length of the electron of lower energy for the $0\nu\beta\beta$ process (in red) and the main backgrounds. The minimum track length is the distance between the source and the calorimeter main wall *i.e.* 440 mm. Electrons with a track length lower than this value trigger the side or top/bottom calorimeter modules.

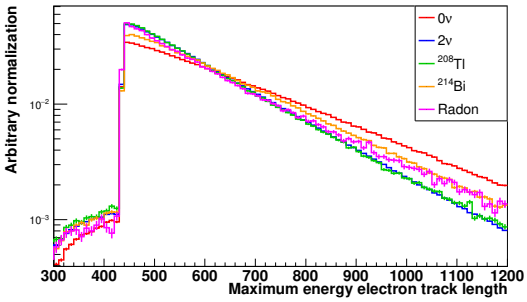

Figure 7.13 – Distribution of the track length of the electron of higher energy for the $0\nu\beta\beta$ process (in red) and the main backgrounds. The minimum track length is the distance between the source and the calorimeter main wall *i.e.* 440 mm. Electrons with a track length lower than this value trigger the side or top/bottom calorimeter modules.

electron is shown in Figure 7.5. In both spectra, the $2\nu\beta\beta$ distribution is the expected continuous spectrum. While in both cases, the 0ν spectra are clearly distinguishable from the background spectra, their separation is lower. This means that for a given number of signal and background events, the signal would be harder to identify with the individual energy spectra than with the energy sum spectrum. This makes the individual energies less sensitive variables than the energy sum. In the higher energy electron spectrum, one can notice some peaks at various energies for the ^{208}Tl, ^{214}Bi and Radon spectra, which are characteristic of the internal conversion electrons.

The energy difference between the two electrons, displayed in Figure 7.6, also shows a $0\nu\beta\beta$ distribution which is different, not only, from the 2ν spectrum, but also from the other backgrounds. Though different, it is not separated. This means that, even more than for the individual energies, a relatively large number of signal events is required to make its distribution stand out significantly above the combined background spectra. It is worth mentioning that this variable is not only interesting for discriminating against the backgrounds but also to discriminate between the different $0\nu\beta\beta$ underlying mechanisms. The different mechanisms induce different kinematics distributions. For instance, the mass mechanism, considered in this study, has a different energy partitioning than that of the Right Handed Current $\langle\lambda\rangle$ mechanism[b].

These four energy-related variables available are obviously highly correlated. This is not an issue for the BDT algorithm but this naturally mitigates the role of correlated discriminating variables. Indeed, the algorithm tends to favor the most discriminating variable and a node splitting operated with this variable will most likely separate the same population of events as would a selection with the other correlated variables.

The reconstructed angular distributions for the different processes are displayed in

[b]The Right Handed Current $\langle\lambda\rangle$ mechanism refers to the mechanism where a W_L couples to a $\overline{\nu_R}$ at one vertex and is absorbed at a V+A vertex without helicity flip required.

Figure 7.7. Similarly to the energy difference, the angular distribution is a variable which might allow the identification of the $0\nu\beta\beta$ underlying mechanism (assuming a signal observation and sufficient statistics). However, the reconstructed angular distributions do not reflect exactly the theoretical distributions. First, the angles are smeared by the diffusion of the electrons inside the source. In addition, as can be hinted by Figure 7.7, the reconstruction is less efficient for orthogonal directions of emission. The best electron reconstruction efficiency is indeed obtained when both electrons are emitted perpendicularly to the source foil. This configuration minimizes the track length and thus the probability for the electrons to scatter or miss the calorimeter due to the curvature induced by the magnetic field. On the contrary, the more the electrons are emitted in parallel with the source the less likely they are to reach the calorimeter. Thus, when electrons are emitted with a 90° angle, both electrons cannot be optimally directed to reach the calorimeter. The best case scenario being where both electrons have 45° angle with respect to foil. That's why, the detector introduces a reconstruction bias, distorts the angular distributions and makes them look more similar to each other than their primary distributions. Nevertheless, this variable can still be taken advantage of, when related to other variables in a multivariate analysis.

The internal and external probabilities are displayed in Figure 7.8 and 7.9 respectively.

The internal probability distributions for the $0\nu\beta\beta$ and $2\nu\beta\beta$ processes follow the expected flat distribution for electrons emitted simultaneously from the source. As explained earlier, the probability distribution is obtained from a transformation of the χ^2 distribution. If the errors involved in the computation of the latter are aptly estimated, the χ^2 should follow a Gaussian distribution, simply generated by the limited time and energy resolution of the detector. This Gaussian distribution is then reshaped into the flat distributions seen in Figure 7.8 for the $0\nu\beta\beta$ and $2\nu\beta\beta$ processes. The ^{208}Tl and ^{214}Bi distributions are also arguably flat. The former distribution is however distorted at low internal probabilities. This might be imputed to a metastable excited state ($T_{1/2} = 294$ ps [99]) of the daughter nuclei, which would slightly delay the second electron emitted via internal conversion. The Radon, *qua* non-internal background, exhibits an internal probability distribution peaked at very low probabilities (almost half of the events have an internal probability lower than 1 %).

The external probability distributions logically show the opposite behaviours. Almost no signal event is reconstructed with an external probability greater than 1 %. The $2\nu\beta\beta$ events are more prone than $0\nu\beta\beta$ events to generate high external probability events. This is due to the fact that the electrons carry less energy, which makes the time measurement less accurate. The external probability distributions are very similar for the two internal contaminations, while a third of the radon events are reconstructed with an external probability greater than 1 %. The internal and external probabilities are expected to be anticorrelated since an event with a good internal probability (greater than a few percents) is unlikely to also have a good external probability.

The separation between the two source vertices is an interesting variable to identify the events where the vertex of origin is not located in the source. Given the geometry of the tracking chamber, it is more relevant to look at the horizontal (Figure 7.10) and

vertical separations (Figure 7.11) instead of the absolute distance between the two vertices. In addition, the horizontal resolution is expected to be better than the vertical one (see Section 3.1.2).

The better resolution in the horizontal plane transpires in Figure 7.10, where the distributions are narrower than in the vertical plane (Figure 7.11). In both cases, the $0\nu\beta\beta$ events appear to be the better reconstructed events. Since electrons carry, on average, a higher energy, they are less affected by the magnetic field, which helps the track reconstruction. The three internal backgrounds follow almost the same distributions. Radon events, however, are expectedly the worst reconstructed events since they do not actually originate from the source. These Figures show that the previous 60 mm-horizontal and 70 mm-vertical cuts are already somewhat loose cuts (keeping 95 % of the signal). In addition, these two variables are also correlated because a high separation in one direction is symptomatic of a scattering inside the tracker so it will also reverberate on the separation in the other direction.

The relevance of the use of the individual track lengths to discriminate between signal and background events is not obvious but since a BDT will ignore variables with little to no discriminating power, we can afford to include these distributions into the analysis (Figure 7.12 and 7.13). The shape of the distributions is explained by the type of calorimeter block the electrons triggered. Indeed, an electron need to travel at least 440 mm to reach the main calorimeter wall but it can also trigger a side (X-wall) or a top/bottom wall (γ veto), which requires a lower track length if the vertex of emission is located at the periphery of the source foil. In both distributions, one can notice that since the $0\nu\beta\beta$ electrons carry more energy, they are less affected by the magnetic field, which translates into a better reconstruction efficiency for longer tracks. Eventually, regardless of the process, the reconstruction efficiency decreases with the track length, hence the distributions observed.

These Monte-Carlo templates can be normalized to the expected number of events in the $2e$ topology. However, since these normalized distributions would mainly contain $2\nu\beta\beta$ events, they would bring little additional information and are consequently not displayed here. These 11 variables are then fed to the BDT as input variables.

7.4 Multivariate approach : the BDT configuration

Machine learning algorithms, such as BDTs, require at least two datasets:

- a training dataset, composed of a large number of signal and background events.
- an application dataset, on which the result of the training will be applied. It can contain few or many events but can not contain the same events used during the training.

In addition to the tools provided by TMVA, the datasets were split evenly in four smaller datasets (that we will call A, B, C and D) in order to check for overtraining. The size of these samples, obtained from the simulations already described above, is enough

to ensure that each background samples still possesses enough statistics in the regions of the variables where the $0\nu\beta\beta$ and the background distributions overlap. Doing this separation will allow us to further test the overtraining and evaluate the stability of our classifications with different samples. In practice, this consists in training and applying the classification using different combination of datasets. For instance, we can use both the A and B samples to train our BDT and then apply the resulting classification on either the sample C or the sample D. Conversely, we can use the C and D samples for the training and apply the result on the samples A or B. This way, unlike TMVA, which only checks that for a given training result all the samples on which the classification is applied should produce the same BDT score distributions, this approach also makes sure that, regardless of the training sample used, the final results (in our case a limit on the $0\nu\beta\beta$ half-life) are equivalent. Indeed, two trainings performed on different samples may yield different BDT score distributions when applied on the same sample. This does not mean that some degree of overtraining is in play. The opposite, however, which would be to obtain two different BDT distributions for two different application samples while using the same classification, built from a single training sample, is not true and is symptomatic of an overtraining.

Since no $0\nu\beta\beta$ events with a total energy lower than 2 MeV is expected to be identifiable among the vast majority of background events at these energies, a preselection cut is performed on the datasets. This speeds up the training and classification processes and reduces the computing resources necessary. Since the total energy is the most discriminating variable, a similar cut at a higher energy is likely to be the first choice for the early node splitting anyway. The effect of this 2 MeV energy cut on the variable distributions can be seen in Figure 7.14. Apart from the energy sum, shown in Figure 7.1, the signal distributions are barely separated from the background distributions when the background events are required to have sufficient energies to start mimicking $0\nu\beta\beta$ events. This augurs to be a challenging task for the multivariate analysis to improve the sensitivity.

Though BDTs require less tuning than neural networks, a sensible configuration is still required in order to avoid underfitting or overfitting (*a.k.a.* overtraining). The different tunable parameters, described in Section 3.3.4 were scanned individually in an effort to find the best configuration but also the most stable. Indeed, a configuration yielding a worse average half-life limit, but where the limits are similar regardless of the training and application samples used, is preferred to a configuration providing a better average half-life limit but which limits vary significantly with the training and classification samples combinations.

The first choice performed was that of the boosting algorithm employed. The several algorithms available in TMVA have been tested, the other parameters being set to their default values. Since no significant improvement is achieved by using different algorithms, the choice was made to keep the standard and simpler boosting algorithm AdaBoost.

Even our most discriminating variables are far from resembling an ideal binary cut. Furthermore, some of the best discriminating variables are correlated with each other. It is thus more advantageous to favor weak classifiers *i.e.* trees with little discrimination power, and increase the number of boost steps. This can be achieved by decreasing

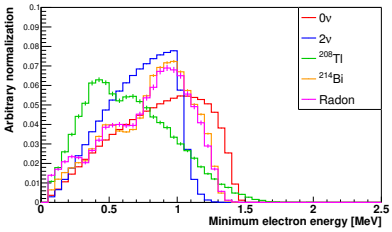

(a) Minimum electron energy

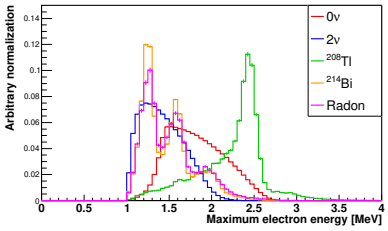

(b) Maximum electron energy

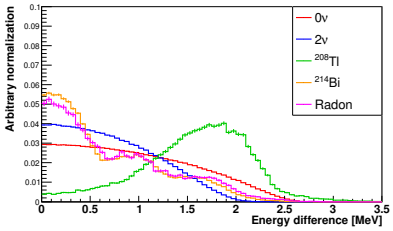

(c) Electrons energy difference

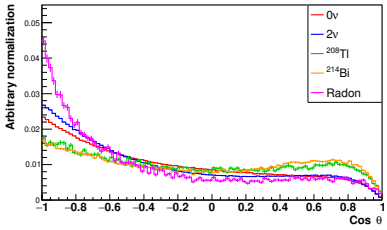

(d) Cosine of the angle between the electrons

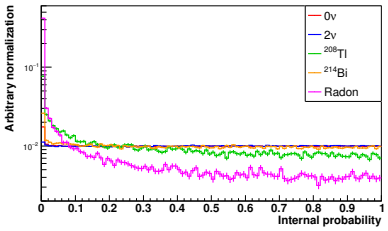

(e) Internal probability

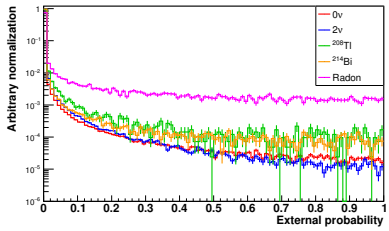

(f) External probability

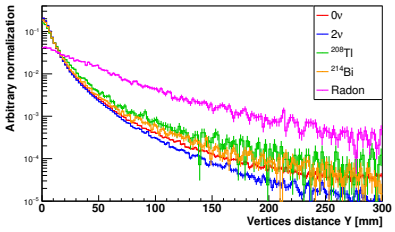

(g) Vertices separation in Y

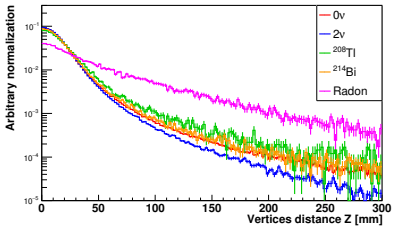

(h) Vertices separation in Z

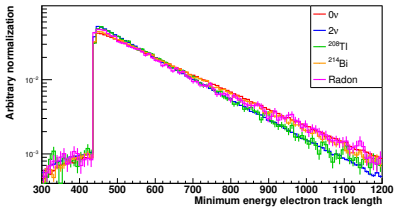

(i) Track length of the minimum energy electron

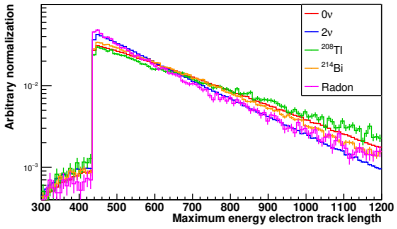

(j) Track length of the maximum energy electron

Figure 7.14 – Discriminating variables in the $2e$ topology after an energy cut requiring the events to have an energy sum greater than 2 MeV.

the learning rate β. A good compromise between performance and computing time was found to be $\beta = 0.2$. In return, the number of trees was increased to 1200 in order to make sure no improvement can be gained anymore, as illustrated in Figure 7.15. In the last few hundreds trees, the separation error fraction reaches close to the maximum theoretical value of 0.5, where the selection is no better than a simple random arbitrary selection (the final leaves being composed of half signal events and half background events).

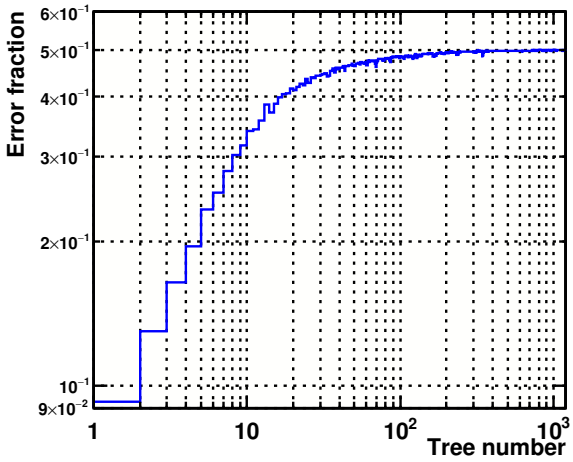

Figure 7.15 – Tree error fraction as a function of the tree generation.

The different separation criteria available were also tested, but none of them appeared to significantly overperform the others. We settled for the Gini Index which is the default separation criteria.

The granularity of the search for the optimal value of the cut on a variable was set to 400. This means that the gain of the separation will be tested for 400 different points on the full variable range. TMVA provides an algorithm to search for the optimal cut value but, while it significantly increases the training time, it did not appear to enhance the performance obtained with 400 points. The last two parameters are the most tricky parameters to tune since they have to do with the complexity of the trees: these are the maximum tree depth and the minimum node size. They are the two tree development stopping criteria and are responsible for the overtraining if they are poorly determined. The minimum node size was chosen to be equivalent to 100 events. This means that below this number, no separation between signal and background events can be operated. This prevents the algorithm from training on statistical fluctuations.

With this minimum node size, the best compromise for the maximum tree depth was set to 4. Below this value, the final half-life limits are worse. Right above this value, at say 5 or 6, slightly better limits can be achieved, but the range of limits obtained depending on the training and application samples becomes wider. This phenomenon can be imputed to a slight overtraining. Eventually, the performances drop for even deeper trees, which is a clear manifestation of overtraining.

The Table 7.4 sums up the parameters used for the configuration of the BDT algorithm. The configuration process is a pivotal part in a multivariate analysis. The parameters choice, only briefly overviewed here, sprouted some in-depth studies, the details of which are spared to the reader.

BDT Parameter	Choice
Boosting algorithm	AdaBoost
Learning rate β	0.2
Number of trees	1200
Separation criterion	Gini index
Optimum cut search	400 points
Minimum node size	100 events
Maximum tree depth	3

Table 7.4 – Summary of the BDT parameters chosen for this analysis.

7.5 Multivariate approach : estimation of the sensitivity to the $0\nu\beta\beta$ decay

The background model used for the training is a compound of the different backgrounds, weighted by their contribution in the signal region of the energy sum spectrum. Indeed, considering once again the target activities are reached, if the background weights are set proportionally to the expected number of events in the $2e$ topology, the algorithm will only be trained to recognize $2\nu\beta\beta$ events. Instead, we'd rather the algorithm to be able to also discriminate against the ^{208}Tl events for instance, since they have a non-negligible contribution in regions where we are sensitive to the $0\nu\beta\beta$ signal. Having several background contributions instead of one consequently impairs the performance of the classification. This drawback can be mitigated by adapting the background weights to match the different expected background levels. The compound background model was defined using the contributions in a wide energy window ([2.65;3.2] MeV), such that $2\nu\beta\beta$ events remain the most important background.

The correlation matrices for the signal and this compound background model are presented in Figure 7.16.

As mentioned earlier, the 4 energy-related variables are strongly correlated/anti-correlated with each other, both for signal and background events. The energy sum, however, is the variable the less correlated with the others. This makes it a potentially more useful variable. The other striking correlation is that of the two vertices separation variables. This was also anticipated since a scattering will most of the time induce a larger vertices separation in both directions. Some other smaller correlations and anticorrelations are noticeable. In particular, one can notice that the higher the vertices separation is, the higher the external probability tends to be. Indeed, if, because of a scattering, the reconstruction is less faithful to the real scenario, the wrong hypothesis is also more likely to be true. Concerning the signal events, the energy sum appears to be anticorrelated with most of

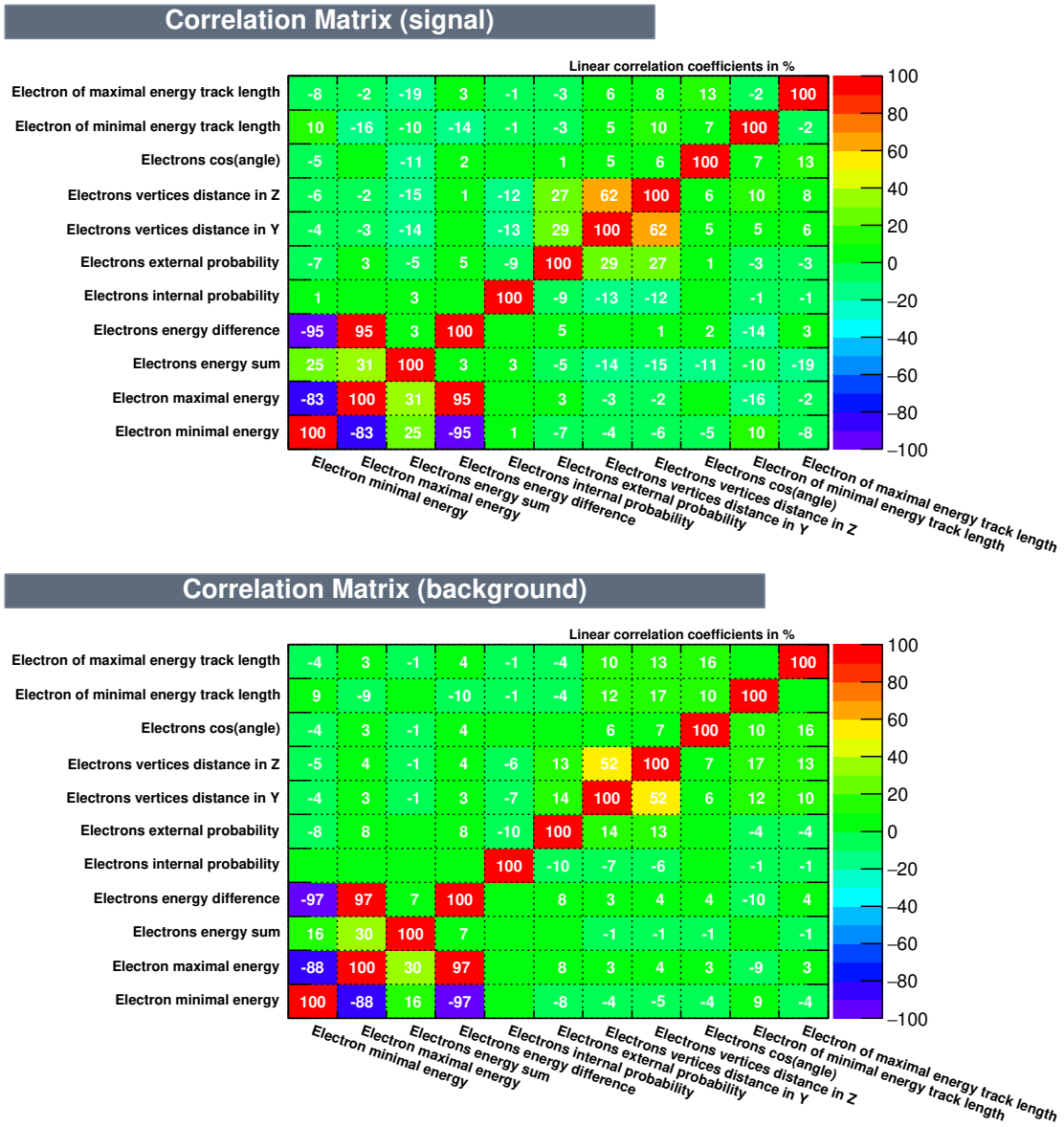

Figure 7.16 – Correlation matrices between the BDT input variables for the signal *(top)* and the background *(bottom)*.

the topological variables. This shows that the events reconstructed with an energy lower than the maximum theoretical one, are due to a scattering in the tracker.

Once the input variables have been identified, two quantities are relevant to evaluate their usefulness: the separation and the importance. The separation helps quantify how much the signal and the background distributions are separated. For a variable x, it is defined as:

$$\langle S^2 \rangle = \frac{1}{2} \int \frac{(f_S(x) - f_B(x))^2}{f_S(x) + f_B(x)} dx \tag{7.3}$$

where f_S and f_B are the signal and background PDF respectively. For a variable with no overlap between the signal and the background distributions, the separation will be

maximum and equal to 1, while if the signal and background distributions for a variable are identical, the separation will be minimum and equal to 0. In a way, this quantifies how different two distributions are.

The separation provided by each of our variable is presented in Table 7.5.

Variable	Separation
Electrons energy sum	$8.063\ 10^{-1}$
Electron maximum energy	$3.250\ 10^{-1}$
Electron minimum energy	$1.488\ 10^{-1}$
Electrons energy difference	$5.990\ 10^{-2}$
Electron of maximal energy track length	$1.679\ 10^{-2}$
Electron of minimal energy track length	$8.507\ 10^{-3}$
Electrons cosθ	$2.856\ 10^{-3}$
Electrons vertices distance in Z	$1.453\ 10^{-3}$
Electrons vertices distance in Y	$1.337\ 10^{-3}$
Electrons external probability	$8.251\ 10^{-4}$
Electrons internal probability	$2.383\ 10^{-4}$

Table 7.5 – Input variables ranked by the separation they provide.

This confirms that the energy sum is by far the most discriminating variable. It is followed by the other energy-related variables. As illustrated in Figure 7.14, the remaining topological variables are not well separated.

The variable importance, shown in Table 7.6 quantifies how useful a variable was in the trees construction. It takes into account how often the variable was used in a node splitting, weighted by the separation gain squared it has achieved and the number of events in the node. As expected, the electrons energy sum is the most important variable to discriminate between signal and background events. It is followed by the individual electrons energies but with a lesser importance than their separation could have suggested since they are correlated with the main variable. The remaining variables appear to contribute equally to the classification process, at the exception of the external probability, which, in addition to its poor separation, is designed to identify external background events.

An example of BDT score, where each distribution is normalized to 1, is shown in Figure 7.17. The closer to +1 the signal distribution is, the better, while a perfect classification would see the background distributions accumulate towards -1. Since the $2\nu\beta\beta$ background was given the greatest weight during the training process, it appears to be the background the better separated from the signal. On the contrary, ^{208}Tl was given the lowest weight. In addition, some cuts applied during the tree generation on the energy sum (Figure 7.1) and the maximum energy (Figure 7.14c) also favor the selection of ^{208}Tl events. These two facts explain why the ^{208}Tl BDT score distribution is more signal-like than the other backgrounds. The ^{214}Bi and Radon distributions also share the same BDT score distribution. The Figure 7.18 shows the same distributions but normalized to the expected number of events above 2 MeV. Because of the 2 μBq/kg stringent constraint on

Variable	Importance
Electrons energy sum	$4.893\ 10^{-1}$
Electron minimum energy	$9.564\ 10^{-2}$
Electron maximum energy	$7.090\ 10^{-2}$
Electrons internal probability	$6.399\ 10^{-2}$
Electrons $\cos\theta$	$5.987\ 10^{-2}$
Electrons energy difference	$5.308\ 10^{-2}$
Electrons vertices distance in Y	$4.731\ 10^{-2}$
Electrons vertices distance in Z	$4.094\ 10^{-2}$
Electron minimal energy track length	$3.782\ 10^{-2}$
Electron maximal energy track length	$3.249\ 10^{-2}$
Electrons external probability	$8.664\ 10^{-3}$

Table 7.6 – Input variables ranked by their importance.

the ^{208}Tl contamination only $\sim$0.1 event is expected from this background in the demonstrator. It consequently barely contributes in the signal region. The ^{214}Bi and Radon produce similar contributions in the region of the BDT score where the signal amplitude is expected to be the strongest. Actually, despite its weight being emphasized in the training, the irreducible $2\nu\beta\beta$ decay is still the main background, due to the sheer number of events expected. However, the overlap between the signal and the background distributions with the BDT scores is lower than with energy sum spectra. This shows that the objective of a background free experiment is within reach.

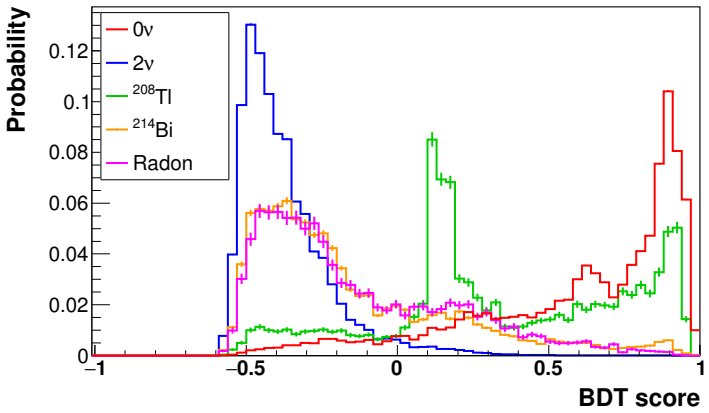

Figure 7.17 – An example of normalized BDT score distributions for the signal and background contributions.

Eventually, the sensitivity on the half-life reached thanks to the BDT is:

$$T_{1/2}^{0\nu} > 5.85\ 10^{24}\ \text{y} \tag{7.4}$$

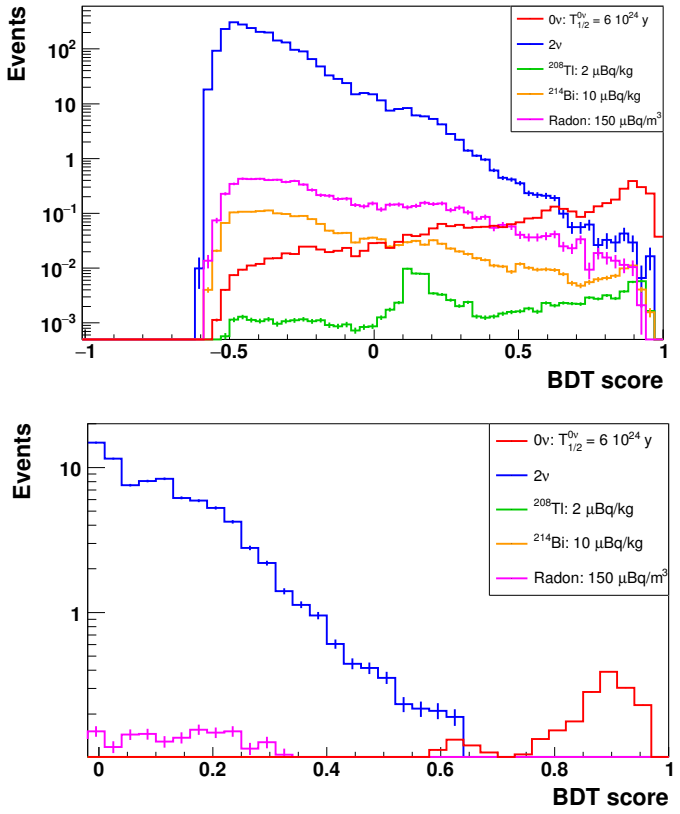

Figure 7.18 – An example of BDT score distributions for the signal and background contributions, normalized to their expected number of events with an energy sum greater than 2 MeV. The top plot shows the whole BDT score range while the bottom plot focuses on the signal region.

This represents a 9 % increase of the sensitivity compared to a single variable approach. The improvement might appear somewhat underwhelming. This is because, similarly to the use of topological cuts, the goal is to decrease a background level which is already very low. The improvement might be greater for the full scale SuperNEMO experiment (500 kg.y), where a few background events are expected in the ROI. It might also be interesting to look at the evolution of the sensitivity obtained with different approaches as a function of the background contamination levels.

7.6 Impact of the background levels on the $0\nu\beta\beta$ sensitivity

The contaminations levels considered until then were the target activities *i.e.* A(^{208}Tl)= 2 μBq/kg, A(^{214}Bi) = 10 μBq/kg and A(Radon) = 150 μBq/m^3. It can be interesting to see how the sensitivity might be impacted if these targets are not reached.

Concerning the single variable approach, it simply consists in increasing the normalization of the energy sum spectrum to the number of expected events for a particular background. The same procedure is applied to all the variables for the multivariate approach. In addition, the background input weights fed to the BDT algorithm are adapted to match the new levels of contamination. New BDTs are trained to take into account the

relative background contributions.

In this part, we also consider the use of topological cuts, applied in an effort to reject background events from the energy sum region of interest. The cuts applied are the same as before, namely an internal probability better than 4 % and a source vertices separation lower than 60 mm in the horizontal direction and lower than 70 mm in the vertical direction. They are not optimized for each new background contamination.

Figure 7.19 shows the evolution of the sensitivity with the ^{208}Tl contamination for different approaches as well as the improvement brought by the multivariate analysis over a single variable approach without topological cuts. The other contaminations are kept at their nominal activities. Figure 7.20 shows the same evolution but with the ^{214}Bi contamination.

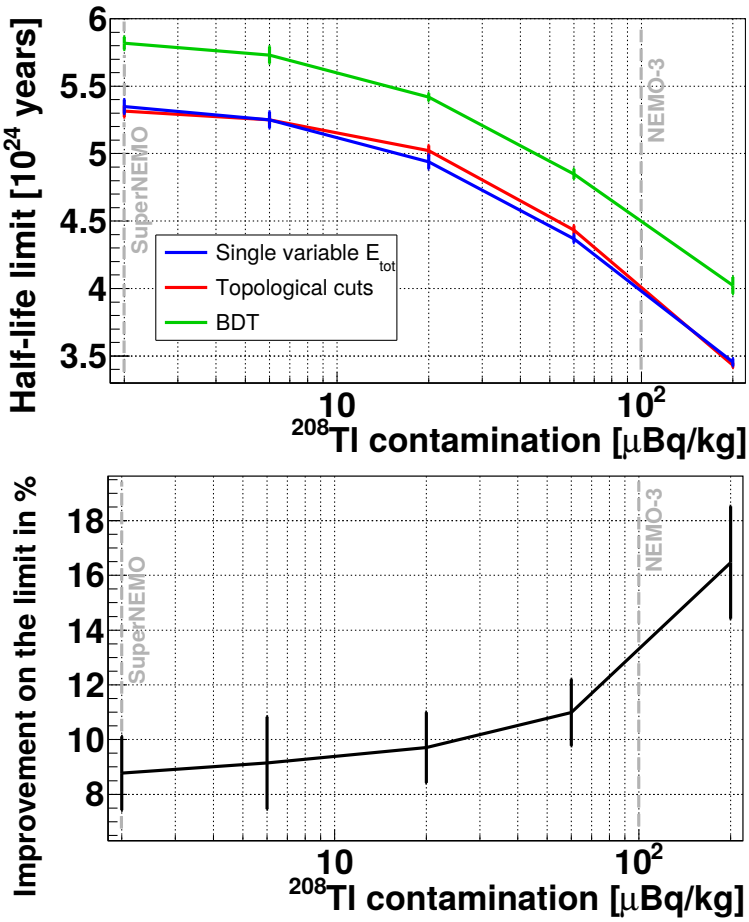

Figure 7.19 – *(top)* Sensitivity as a function of the ^{208}Tl contamination for the different approaches. *(bottom)* Sensitivity improvement brought by the multivariate analysis as a function of the ^{208}Tl contamination.

These Figures show that, regarding the internal backgrounds, the topological cuts do not appear to bring any significant sensitivity improvement. However, the use of a multivariate analysis helps enhance the sensitivity of the demonstrator, starting with a 9 % improvement for the nominal activities and reaching around 20 % for contaminations two orders of magnitudes larger that the target ones.

Figure 7.21 shows the impact of the Radon contamination on the sensitivity for differ-

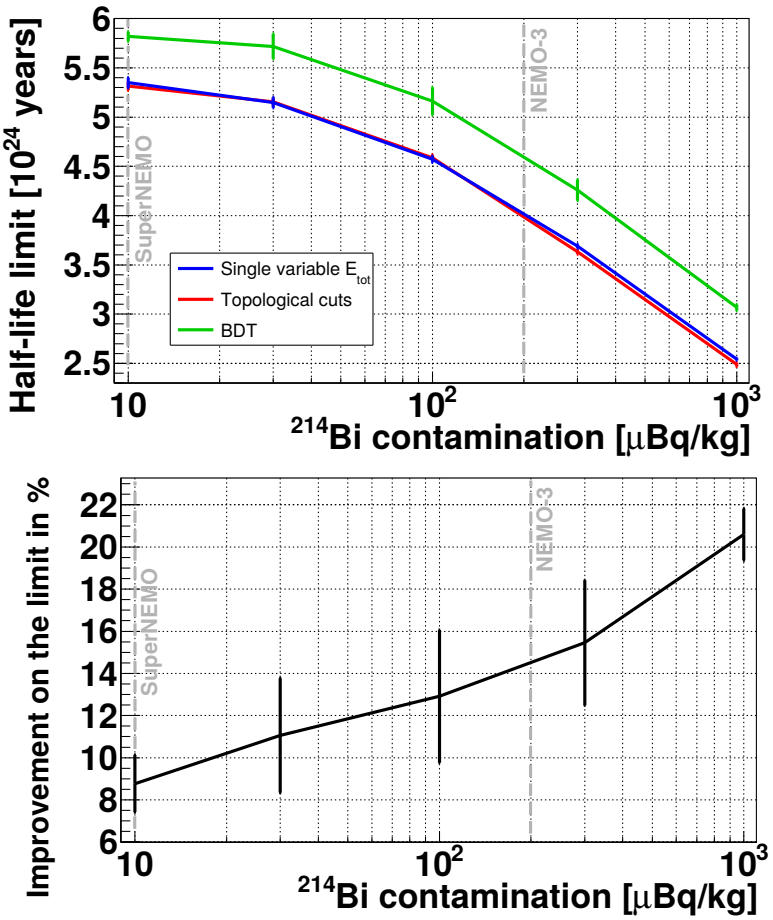

Figure 7.20 – *(top)* Sensitivity as a function of the ^{214}Bi contamination for the different approaches. *(bottom)* Sensitivity improvement brought by the multivariate analysis as a function of the ^{214}Bi contamination.

ent approaches.This time, topological cuts appear to be useful in rejecting Radon events. The sensitivity is thus improved for larger contaminations than the nominal level. The multivariate approach is even more efficient and manages to maintain almost the same sensitivity for a contamination ten times larger than the target one. With another order of magnitude on the radon contamination, this sensitivity improvement is larger than 200 % compared to the single variable approach without topological cuts.

The errors displayed in these Figures come from the statistical variations in the toy experiments used in COLLIE. For the multivariate approach, we also take into account the variations coming from the different input samples, which each yield slightly different limits.

These results show that the more background there is, the more relevant the multivariate analysis becomes. Actually, assuming the same background levels as NEMO-3, *i.e.* A(^{208}Tl) $\approx$ 100μBq/kg, A(^{214}Bi) $\approx$ 200μBq/kg and A(radon) $\approx$ 5 mBq/m^3, in the SuperNEMO demonstrator (with an improved energy resolution, a better 0ν efficiency, etc.), a multivariate analysis would improve the sensitivity by 90 %.

Assuming the ^{214}Bi and Radon target activities are reached, with an effective ^{208}Tl activity of 50 μBq/kg, the multivariate analysis almost makes up for the loss in sensitivity.

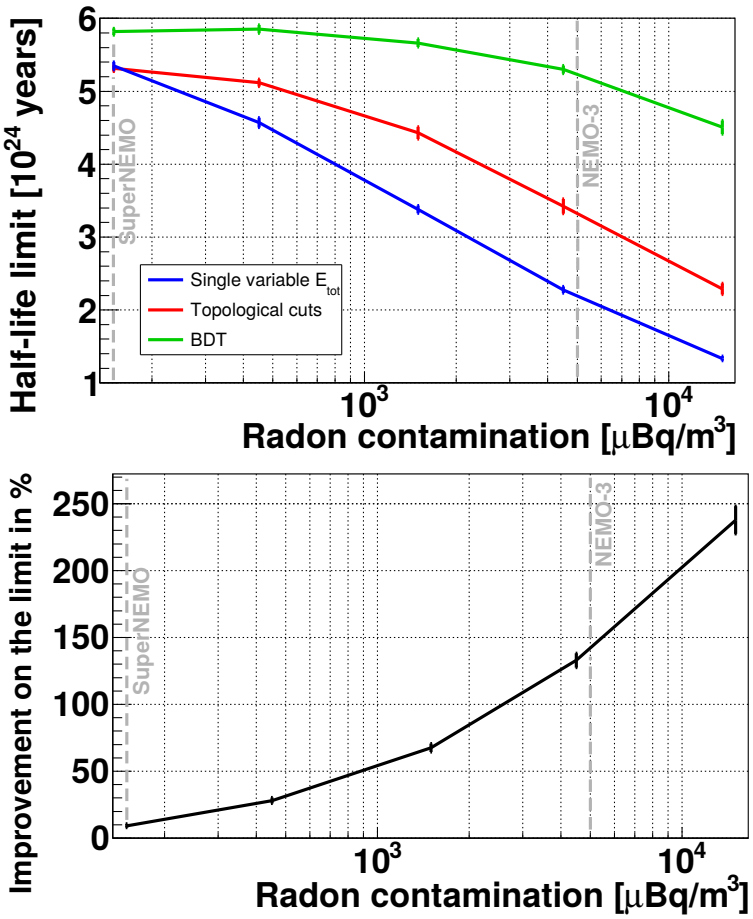

Figure 7.21 – *(top)* Sensitivity as a function of the radon contamination for the different approaches. *(bottom)* Sensitivity improvement brought by the multivariate analysis as a function of the radon contamination.

Regardless of the approach, the higher than expected ^{208}Tl contamination causes a 17 % decrease in sensitivity, while the use of BDTs over a single variable approach increases the sensitivity by 11 %

7.7 Comparison of the different limit setting approaches

This section aims at comparing the different limit setting approaches. The limits presented until now were obtained with the COLLIE software package, based on a semi-frequentist approach. This is a reference tool used by the collaboration since the analysis of the NEMO-3 data. Other approaches are available in the RooStats package, as described in Section 3.3.3. Similarly to COLLIE, the Profile Likelihood Calculator (PLC) takes advantage of Wilk's theorem [c] to determine decision regions for a particular hypothesis. This algorithm computes the distribution of a test statistic which will be asymptotically chi-squared distributed. This correspondence can be used to assign a statistical significance to the test statistic of the data. A standard Bayesian approach, described in Section 3.3.3,

[c] Wilk's theorem, stating that -2log(Q) follows a χ^2 distribution, is assumed to be valid.

is considered as well. A similar Bayesian approach uses Monte-Carlo Markov Chains (MCMC), which makes the numerical integrations faster. The limits obtained with these four solutions are compared in Table 7.7 for the single variable analysis (the electrons energy sum) and in Table 7.8 for the multivariate analysis.

Single variable E_{tot}	Median half-life (10^{24}y)	Average half-life (10^{24}y)
COLLIE	5.31	
PLC	6.12	5.18
Bayesian	4.63	4.33
Bayesian MCMC	4.67	4.32

Table 7.7 – Comparison of the $0\nu\beta\beta$ half-life limits obtained with four limit setting approaches. The limit is extracted from the energy sum spectrum. The different algorithms were applied to a large number of pseudo-experiments. The median and average half-life limits are displayed.

Multivariable	Median half-life (10^{24}y)	Average half-life (10^{24}y)
COLLIE	5.85	
PLC	7.30	5.91
Bayesian	4.98	4.59
Bayesian MCMC	5.06	4.64

Table 7.8 – Comparison of the $0\nu\beta\beta$ half-life limits obtained with four limit setting approaches. The limit is extracted from the final BDT score. The different algorithms were applied to a large number of pseudo-experiments. The median and average half-life limits are displayed.

Apart from COLLIE, where we assumed a 5 % systematic uncertainty, no systematic uncertainties are considered here. These limits (in particular that of PLC) are thus expected to be deteriorated when the systematic uncertainties will be evaluated and taken into account. The frequentist approach (PLC) and semi-frequentist approach (COLLIE) appear to provide better exclusion limits than Bayesian approaches. In addition, the improvement brought by the multivariate analysis is larger when evaluated with frequentist approaches. The two Bayesian approaches are consistent with each other. Some differences are expected between the frequentist and Bayesian approaches because they do not derive limits the same way. To simplify, in the frequentist approach, the limit is set by evaluating how often the experiment would observe better results than the limit if it was repeated a large number of times. With the Bayesian approach, however, the limit is set by estimating the probability for our experiment to observe a better result than our limit. The Bayesian approach is consequently more conservative and this is especially true for experiments with low number of events, where it usually yields worse limits.

7.8 Conclusion

Assuming the target background levels are reached, the SuperNEMO demonstrator, running for two and half years with 7 kg of ^{82}Se would be able to a set a limit on the $0\nu\beta\beta$ process $T^{0\nu}_{1/2} > 5.85\ 10^{24}$ y, translating into a limit on the neutrino effective mass $\langle m_{\beta\beta}\rangle < 0.2 - 0.55$ eV (depending on the Nuclear Matrix Elements [100]). This limit was obtained thanks to a multivariate analysis which represents almost a 10 % increase in sensitivity compared to the use of a single variable, the electrons energy sum, similarly to what is done in other double beta decay experiments. The goal of the demonstrator (17.5 kg.y) is to show that such a tracko-calo experiment can be a background-free experiment and that it can reach competitive sensitivities. Extrapolating to the full scale SuperNEMO experiment with a 500 kg.y exposure, the limit would be raised to $T^{0\nu}_{1/2} > 10^{26}$ y or $\langle m_{\beta\beta}\rangle < 40 - 110$ meV.

Conclusion

The nature of the neutrino is one of the most investigated questions in neutrino physics. A Majorana neutrino would not only help explain the matter-antimatter asymmetry observed in the Universe but it is also required by some models, like the See-Saw mechanism, in order to explain the very small neutrino masses. To this day, the only way to determine the neutrino nature is to look for the neutrinoless double beta decay $0\nu\beta\beta$.

Several experiments, such as NEMO-3, have already carried searches for this process, albeit unsuccessfully. SuperNEMO should overcome the limitations faced by its predecessor NEMO-3 thanks to an increased isotope mass but also some crucial improvements on the energy resolution, the source and detector radiopurity as well as the background rejection. Part of this thesis was devoted to the construction, integration and commissioning of the first SuperNEMO module, called the demonstrator. This detector is not only able to measure the individual electrons energies thanks to a segmented calorimeter but it can also reconstruct the tracks of charged particles thanks to a wire chamber. These tracking capabilities, coupled with the presence a magnetic field, means that SuperNEMO is capable of identifying the type of particles involved in an event: electron, positron, α particle or γ particle.

The value of this magnetic field was optimized thanks to Monte-Carlo simulations performed with the SuperNEMO simulation and reconstruction software. In addition, some measurements performed with a reduced number of shieldings in a small scale magnetic coil and in a magnetic coil prototype have raised two serious issues. First, the magnetic field inside the shieldings was found to be higher than expected, at values which would be detrimental to the energy resolution. However, it was shown that taking advantage of the ferromagnetic properties of the pure iron shieldings can cancel the magnetic field seen by the photomultipliers. Furthermore, it was revealed that the shieldings presence lowers the value of the magnetic field at distance from them, making the magnetic field in the tracking volume no longer uniform. This triggered dedicated magnetic simulations which confirmed this effect. Nonetheless, taking into account this non-uniform magnetic field in the simulation proved it should not significantly impact the neutrinoless double beta decay reconstruction efficiency. Further simulations including the main background sources should be performed in order to check the impact of a non-uniform magnetic field on the demonstrator sensitivity to the $0\nu\beta\beta$ search.

These studies, based on simulations, are made possible by the SuperNEMO simulation software and the variety of reconstruction algorithms developed over the years. The reconstruction of γ particles in the detector is challenging since they are detected by the

calorimeter, sometimes multiple times, but do not leave tracks in the tracking chamber. Two main reconstruction approaches were first considered: the γ-clustering, which gathers the calorimeter hits based on geometrical criteria, and the γ-tracking, which uses the Time-Of-Flight information to reconstruct the γ trajectories. Actually, a new algorithm combining both approaches was developed and allowed an optimization of the γ reconstruction efficiency and an improvement of the γ energy reconstruction. The reconstruction software was then completed by the development of a module aimed at identifying the particles, according to the user's definitions. An event topology can therefore be defined and the topological measurements relevant to the event are then computed in order to be used later in the analysis (vertices distance, angle, Time-Of-Flight, etc.).

Some of these event topologies are dedicated to the measurement of the main background contributions. The backgrounds for the $0\nu\beta\beta$ search are the $2\nu\beta\beta$ decay but also β/γ decays from natural radioactive contaminants, which can mimic a $\beta\beta$ event. Apart from the $2\nu\beta\beta$ decay, the most harmful backgrounds are a contamination of the source foil in ^{208}Tl and ^{214}Bi, which are high energy β/γ emitters. Radon gas can also migrate inside the tracking volume and close to the source foil, which makes it very harmful since it then decays to ^{214}Bi. Focusing on the $1e1\alpha$ events from the tracker, the target Radon contamination A(Radon) = 150 μBq/m^3 could be determined within 10 % after 5 weeks and with a total uncertainty lower than 3 % after 2.5 years. Using the $1e$Nγ topologies, the ^{208}Tl and ^{214}Bi source contamination can be measured independently from external measurements. After 2.5 years, the total uncertainty on the target ^{208}Tl activity A(^{208}Tl) = 2 μBq/kg should be better than 11 %, while the target ^{214}Bi activity A(^{214}Bi) = 10 μBq/kg should be measured with an 8 % total uncertainty. An accurate measurement of the $2\nu\beta\beta$ half-life is very useful to better constrain the different nuclear models and thus improve their precision. The ^{82}Se $2\nu\beta\beta$ half-life $T_{1/2}^{2\nu\beta\beta} = 9{\cdot}10^{19}$ y should be known with a 0.33 % total uncertainty after 2.5 years and be dominated by the systematic uncertainty after 4 months.

Actually, the $2e$ topology is employed to look for $0\nu\beta\beta$ events. The most discriminating variable is the two electrons energy sum which should exhibit a peak located at the transition energy since, in the absence of neutrino emission, all the energy is carried by the electrons. However, the analysis can benefit from other topological variables made available by the SuperNEMO's full kinematics reconstruction capabilities. The use of a multivariate analysis (Boosted Decision Trees) provides at least a 10 % improvement of the demonstrator sensitivity compared to a single variable approach. If no excess of $0\nu\beta\beta$ events is observed, the SuperNEMO demonstrator should be able to set a limit on the $0\nu\beta\beta$ half-life of $T_{1/2}^{0\nu} > 5.85\ 10^{24}$ y, translating into a limit on the effective Majorana neutrino mass $\langle m_{\beta\beta}\rangle < 0.2 - 0.55$ eV. Extrapolating this result to the full-scale SuperNEMO experiment, *i.e.* 500 kg.y, the sensitivity would be raised to $T_{1/2}^{0\nu} > 10^{26}$ y or $\langle m_{\beta\beta}\rangle < 40 - 110$ meV.

Chapter 8

Résumé

8.1 La Physique du neutrino

L'existence d'une nouvelle particule, aujourd'hui appelée neutrino, fut postulée en 1930 par W. Pauli afin d'expliquer l'observation du spectre en énergie continu de la désintégration beta. Le neutrino électronique fut détecté pour la première en fois en 1956 par C.L. Cowan et F. Reines auprès de réacteurs nucléaires. À ce jour, trois saveurs de neutrinos ont été observées: le neutrino électronique, le neutrino muonique et le neutrino tauique. L'observation de l'oscillation des neutrinos entre ces trois saveurs a par ailleurs permis de prouver que les neutrinos avaient bien une masse, contrairement à la prédiction faite par le Modèle Standard de la Physique des particules. Leurs masses sont en revanche très faibles et ni la valeur de leurs états propres de masse, ni même leur hiérarchie n'ont pu encore être déterminées. Ceci s'explique prinicipalement par le fait que les neutrinos n'intéragissent que très peu avec la matière et uniquement via l'interaction faible. Outre leurs masses, la nature du neutrino demeure encore inconnue. En tant que fermion neutre, le neutrino pourrait être une particule de Dirac ou de Majorana. Si le neutrino est une particule de Dirac, cela siginifie que le neutrino et son antiparticule, l'anti-neutrino, seraient deux particules distinctes. En revanche, si le neutrino s'avère être une particule de Majorana, alors neutrino et anti-neutrino ne seraient qu'une seule et même particule. La seule approche expérimentale trouvée à ce jour permettant de déterminer la nature du neutrino est la recherche de la désintégration double beta sans émission de neutrinos.

La désintégration double beta, tout d'abord, est un type de radioactivité naturelle pouvant se produire au sein d'un noyau pour lequel une simple désintégration beta est énergétiquement impossible, tel qu'illustré par la Figure 8.1. Pour le ^{82}Se, ainsi que pour une trentaine d'autres isotopes, une désintégration double beta reste cependant possible.

La désintégration double beta avec émission de neutrinos $2\nu\beta\beta$, bien que très rare, a déjà été observée chez de nombreux isotopes. Cette désintégration, illustrée par la Figure 8.2, s'apparente à deux simples désintégrations beta se produisant simultanément au sein d'un même noyau.

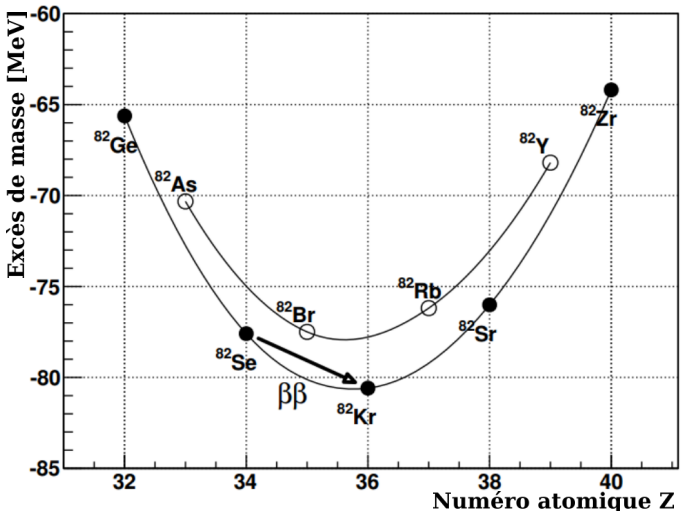

Figure 8.1 – Excès de masse chez l'isotope ^{82}Se.

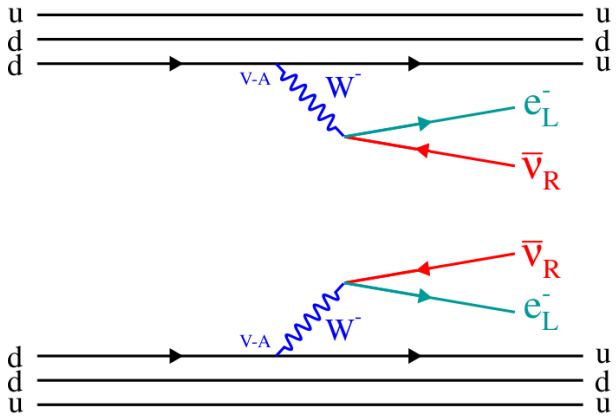

Figure 8.2 – Diagramme de Feynman illustrant le processus de désintégration double beta avec émission de neutrinos.

Un deuxième type de désintégration, baptisée désintégration double beta sans émission de neutrinos $0\nu\beta\beta$, pourrait aussi être possible si, et seulement si, le neutrino est une particule de Majorana. Ainsi, observer ce processus reviendrait à prouver que le neutrino est une particule de Majorana, tel que formulé par le théorème de Schechter-Valle. Plusieurs hypothèses ont été émises quant au mécanisme qui pourrait être responsable d'une telle désintégration. Le mécanisme de masse, illustré par la Figure 8.3, consiste en l'échange d'un neutrino de Majorana léger au vertex d'interaction et est souvent considéré comme le mécanisme le plus naturel.

Ces deux types de désintégration double beta se distinguent expérimentalement au travers de leurs spectres en énergie. En effet, lors d'une désintégration double beta standard $2\nu\beta\beta$, l'énergie de transition $Q_{\beta\beta}$ est partagée entre les deux électrons et les deux neutrinos. Or, les neutrinos échappant à la détection, seule l'énergie portée par les deux électrons peut être mesurée. Il en résulte un spectre en énergie continue, similaire à celui

de la simple désintégration beta. En revanche, lors d'une désintégration double beta sans émission de neutrinos, l'énergie de transition serait entièrement portée par les deux électrons, puisqu'aucun neutrino n'est émis. Dans ce cas, le spectre en énergie attendu serait donc un pic situé à l'énergie de transition. La signature énergétique serait ainsi un moyen efficace de distinguer les deux processus.

C'est donc sur ce principe que reposent les expériences de recherche de la désintégration double beta sans émission de neutrinos, dont fait partie SuperNEMO.

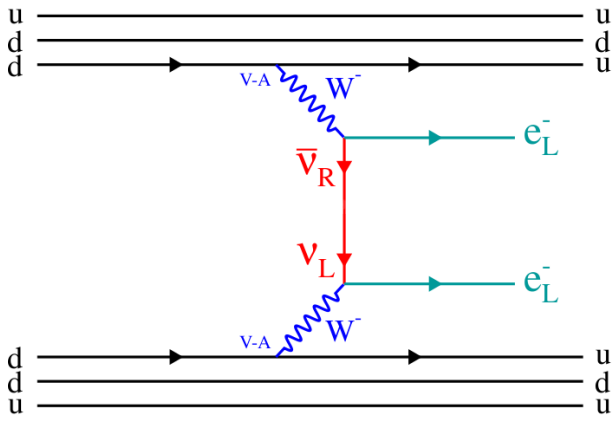

Figure 8.3 – Diagramme de Feynman illustrant le processus de désintégration double beta sans émission de neutrinos dans le cas du mécanisme de masse.

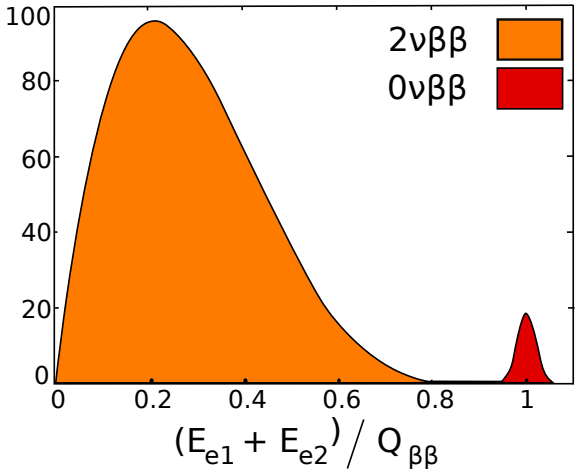

Figure 8.4 – Spectres en énergie de la désintégration $2\nu\beta\beta$ en orange et de la désintégration $0\nu\beta\beta$ en rouge. Le pic du spectre $0\nu\beta\beta$ est élargi par une résolution en énergie ici choisie arbitrairement.

8.2 L'expérience SuperNEMO

L'expérience SuperNEMO repose sur un principe unique combinant à la fois un trajectographe et un calorimètre. Ce principe est illustré par la Figure 8.5. La source se présente sous forme de fines feuilles source enrichies en isotopes émetteurs double-β. Le trajectographe se situe de part et d'autre de la feuille source et permet la détection et la reconstruction des traces de particules chargées. Un faible champ magnétique est en outre appliqué afin de courber la trajectoire des particules chargées et ainsi permettre d'identifier leurs charges. Enfin, un calorimère segmenté entoure le tout et rend possible la mesure individuelle de l'énergie et du temps d'arrivée des particules.

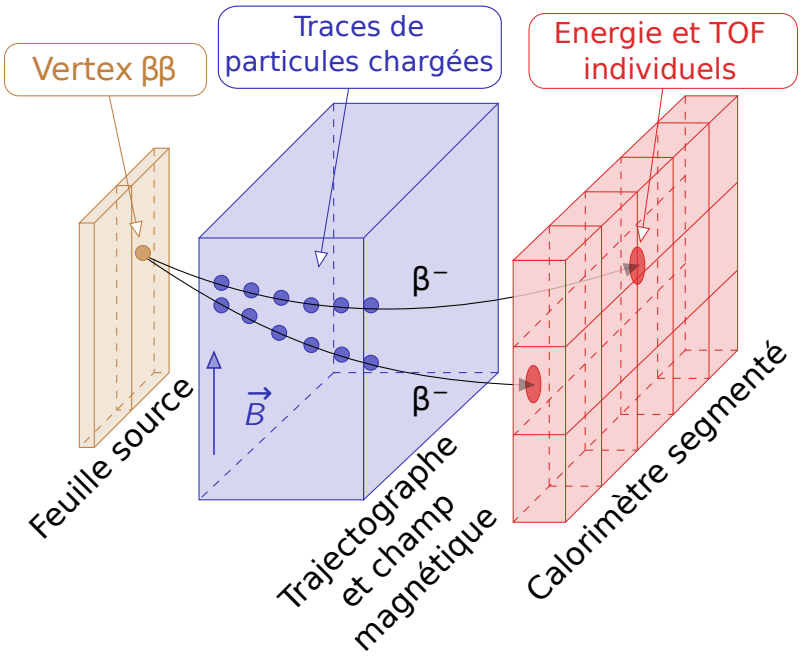

Figure 8.5 – Principe expérimental des expériences NEMO.

En pratique, l'expérience SuperNEMO se divise en plusieurs modules (20 au total) similaires au premier module déjà construit, aussi appelé démonstrateur, et présenté en Figure 8.6.

La source est décomposée en 36 bandes, pour un total de 7 kg de ^{82}Se. Cet isotope présente l'avantage de posséder une énergie de transition élevée ($Q_{\beta\beta} = 2.998$ MeV), ce qui rend la recherche de la désintégration $0\nu\beta\beta$ beaucoup moins susceptible aux processus de radioactivité naturelle. Le trajectographe est une chambre à fils, comptant 2034 cellules Geiger (4.4 cm de diamètre) répartis en 9 plans, de part et d'autre de la feuille source. Les murs du calorimètre sont composés de photomultiplicateurs couplés à des scintillateurs plastiques. Les deux murs principaux comptent 440 photomultiplicateurs 8". Le reste du calorimètre est composé de 272 photomultiplicateurs 5" qui assurent une couverture à 4π sr du détecteur. Le calorimètre principal offre ainsi une résolution en énergie $\sigma = 1.7$ % à l'énergie de transition $Q_{\beta\beta}$ et une résolution temporelle $\sigma = 400$ ps à 1 MeV. La bobine

magnétique, fournissant le champ mangétique, entoure ces différents sous-modules. En outre, le démonstrateur est protégé de l'atmosphère extérieure, riche en Radon, grâce à une tente anti-radon, ainsi que des rayonnements externes grâce à un blindage d'eau et de fer pur.

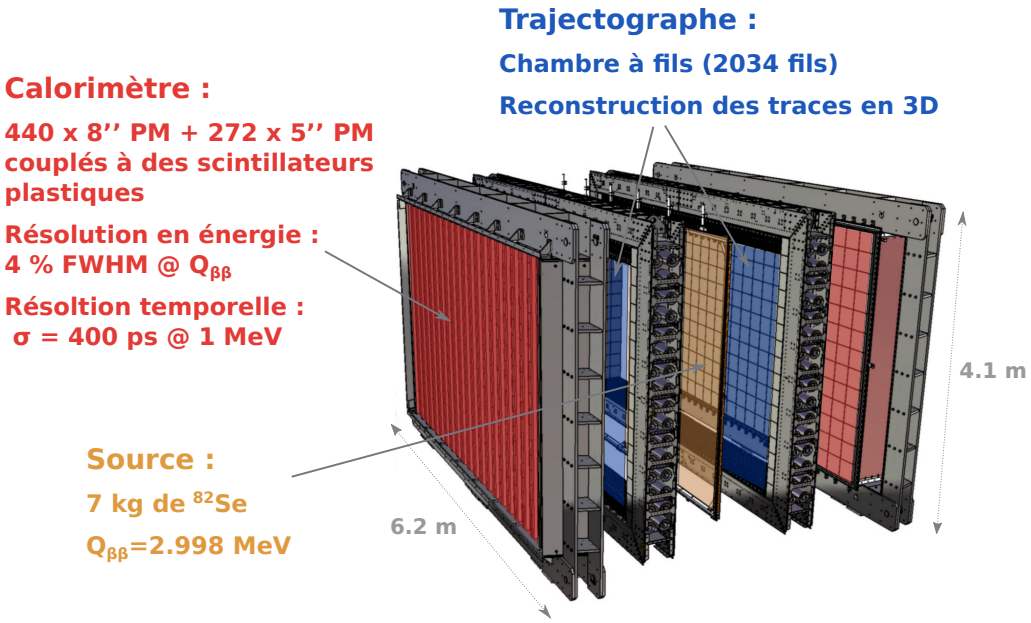

Figure 8.6 – Dessin du démonstrateur SuperNEMO. Les couleurs font ici écho aux couleurs utilisées dans la Figure 8.5.

Une fois le démonstrateur complètement assemblé, ce dernier doit acquérir des données durant 2.5 ans avec 7 kg de ^{82}Se. Il est par ailleurs envisagé d'étudier du ^{150}Nd lors d'une seconde phase (un effort de R&D pourrait permettre d'enrichir efficacement cet isotope $\beta\beta$). Le but du démonstrateur SuperNEMO est de prouver que cette technique "tracko-calo" permet une recherche de la désintégration $0\nu\beta\beta$ sans bruit de fond dans la région d'intérêt (*i.e.* autour du $Q_{\beta\beta}$). En effet, en l'absence de bruit de fond, la sensibilité d'une expérience augmente linéairement avec l'exposition :

$$T_{1/2}^{0\nu,\mathrm{lim}} \propto \epsilon \cdot m \cdot t \tag{8.1}$$

où ϵ est l'efficacité de reconstruction du signal, m est la masse d'isotope $\beta\beta$ étudiée, t est le temps d'acquisition,

En revanche, en présence d'évènements de bruit de fond, la sensibilité d'une expérience n'augmente plus que selon la racine de carrée de l'exposition :

$$T_{1/2}^{0\nu,\mathrm{lim}} \propto \epsilon \cdot \sqrt{\frac{m \cdot t}{b \cdot \Delta E}} \tag{8.2}$$

où b est le taux de d'évènements de bruit de fond en coups.keV^{-1}.kg^{-1}.an^{-1} et ΔE représente la largeur de la région d'intérêt en keV (proportionnelle à la résolution en énergie).

Les nombreuses améliorations apportées par rapport à NEMO-3, prédecesseur de SuperNEMO, afin d'atteindre cet objectif, sont recensées dans le Tableau 8.1.

	NEMO-3	Démonstrateur SuperNEMO
Masse	7 kg	7 kg
Isotopes	^{100}Mo	^{82}Se
	parmi 7 isotopes	(^{150}Nd)
Rés. énergie calo. @ $Q_{\beta\beta}$		
FWHM - σ	8 % - 3.4 %	4 % - 1.7 %
Bruits de fond :		
$T_{1/2}^{2\nu\beta\beta}$	7 10^{18} ans	9 10^{19} ans
A(^{208}Tl)	$\sim$ 100 μBq/kg	$\leq$ 2 μBq/kg
A(^{214}Bi)	$\sim$ 300 μBq/kg	$\leq$ 10 μBq/kg
A(Radon) in tracker	$\sim$ 5 mBq/m^3	$\leq$ 0.15 mBq/m^3
Efficacité 0ν	18 %	30 %
Exposition	35 kg·an	17.5 kg·an
Sensibilité		
$T_{1/2}^{0\nu2\beta}$ (90% C.L.)	> 1.1 10^{24} ans	> 6 10^{24} ans
$\langle m_{\beta\beta} \rangle$	< 0.33 - 0.87 eV	< 0.2 - 0.55 eV

Table 8.1 – Comparaison des spécifications techniques et sensibilité des expériences NEMO-3 et SuperNEMO

Alors que NEMO-3 étudia principalement du ^{100}Mo, entre autres isotopes, SuperNEMO se concentrera principalement sur le ^{82}Se. Ce dernier possède une énergie de transition similaire à celle du ^{100}Mo, mais sa demi-vie pour le processus $2\nu\beta\beta$ est beaucoup plus grande, ce qui diminue d'autant le nombre d'évènements de bruit de fond attendu de ce processus. Des contraintes beaucoup plus fortes ont par ailleurs été établies sur la radiopureté de la source en ^{208}Tl et ^{214}Bi ainsi que sur la radiopureté du gaz du trajectographe en Radon. Nous verrons plus tard pourquoi ces isotopes sont particulièrement problématiques. Une campagne de R&D a aussi permis d'améliorer la résolution du calorimètre par un facteur 2. L'efficacité de reconstruction des évènements de signal devrait aussi être améliorée grâce à une nouvelle géométrie. Ainsi, avec une exposition deux fois moindre, le démonstrateur SuperNEMO devrait être plus sensible que NEMO-3 et devrait, en l'absence d'observation d'évènements de signal, offrir des limites compétitives sur la demi-vie de ce processus.

Les avantages de la technique dite "tracko-calo" sont nombreux. Tout d'abord, la source est passive, c'est à dire qu'elle ne sert qu'à fournir les évènements et ne participe pas activement à la détection. Cela signifie que de nombreux isotopes différents peuvent être étudiés pourvu qu'ils puissent être fabriqués sous forme de feuilles source. La capacité de SuperNEMO à identifier la nature des particules impliquées dans un évènement lui apporte une très forte capacité de rejection du bruit de fond. De plus, la variété des topologies d'évènements reconstructibles rend SuperNEMO capable de mesurer lui même son propre bruit de fond. En outre, si un signal était observé, SuperNEMO, grâce

à la reconstruction complète de la cinématique des évènements, serait la seule expérience capable d'identifier le mécanisme responsable de la désintégration $0\nu\beta\beta$, parmi les nombreux modèles théoriques proposés. Enfin, l'approche expérimentale adoptée par SuperNEMO le rend sensible à d'autres types de processus rares, voire même jamais observés auparavant, tels que la désintégration double beta (avec ou sans émission de neutrinos) vers les états excités du noyaux fils. Ces nombreux avantages ont le potentiel de faire de SuperNEMO une expérience dépourvue de bruit de fond. Toutefois, cette technique n'est pas sans inconvénients. En effet, il s'avère difficile d'atteindre des masses élevées d'isotopes puisque cela ne peut uniquement être réalisé qu'en multipliant le nombre de modules. Enfin, la résolution en énergie apportée par ce design n'est pas aussi bonne que celle des expériences basées sur des détecteurs Germanium ou sur des bolomètres, même si elle reste néanmoins meilleure que celle des expériences utilisant des liquides scintillants.

Après avoir introduit la physique du neutrino, la désintégration double beta sans émission de neutrinos, ainsi que l'expérience SuperNEMO, les parties suivantes sont dédiées aux travaux effectués durant cette thèse.

8.3 Caractérisation des blindages magnétiques

Comme mentionné précédemment, un champ magnétique est appliqué afin d'identifier la charge des particules laissant une trace dans le trajectographe. Les photomultiplicateurs étant très sensibles à la présence d'un champ magnétique, des blindages magnétiques en fer pur entourent ces derniers, tel qu'illustré par la Figure 8.7. Ces blindages magnétiques assurent aussi un rôle mécanique puisque les modules calorimètriques peuvent ainsi être empilés plus facilement.

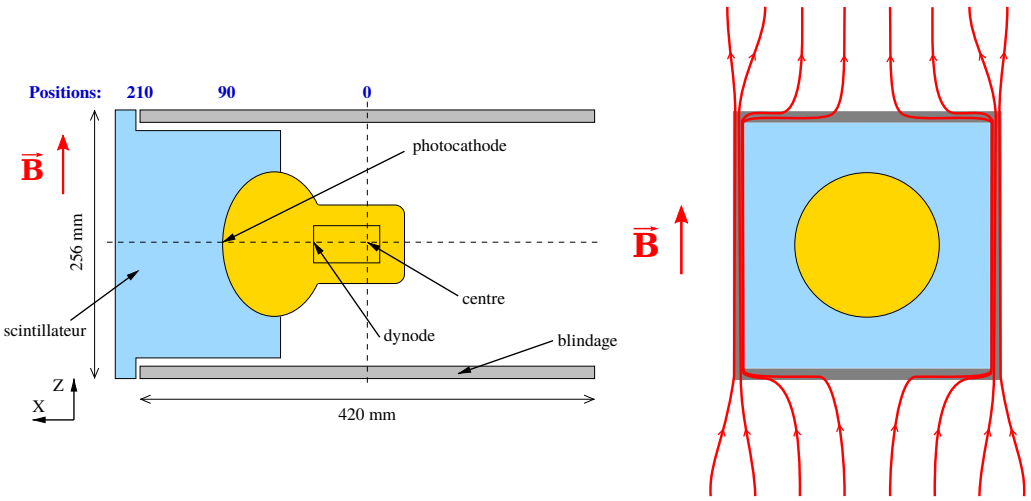

Figure 8.7 – *(gauche)* Schéma d'un module calorimètrique. *(droite)* Illustration du principe de protection contre le champ magnétique. Le champ magnétique est redirigé au travers du blindage grâce à sa plus grande susceptibilité magnétique.

Afin de tester leur pouvoir de protection contre le champ magnétique, les blindages ont été soumis à un champ magnétique généré par une bobine fabriquée au Laboratoire de l'Accélérateur Linéaire. Les blindages ont testés individuellement et soumis à des champs pouvant aller jusqu'à 40 G. Le champ magnétique à l'intérieur du blindage est mesuré par un magnétomètre et il a été montré que ce champ pouvait atteindre 1 G. Cela peut paraître faible de prime abord mais il a aussi été démontré que c'est assez pour détériorer la résolution en énergie de 8 % à 8.4 % FWHM à 1 MeV. Cependant, en observant l'évolution du champ magnétique mesuré à l'intérieur du blindage en fonction du champ magnétique appliqué (*cf.* Figure 8.8), il semble possible d'annuler complètement le champ magnétique à l'intérieur du blindage.

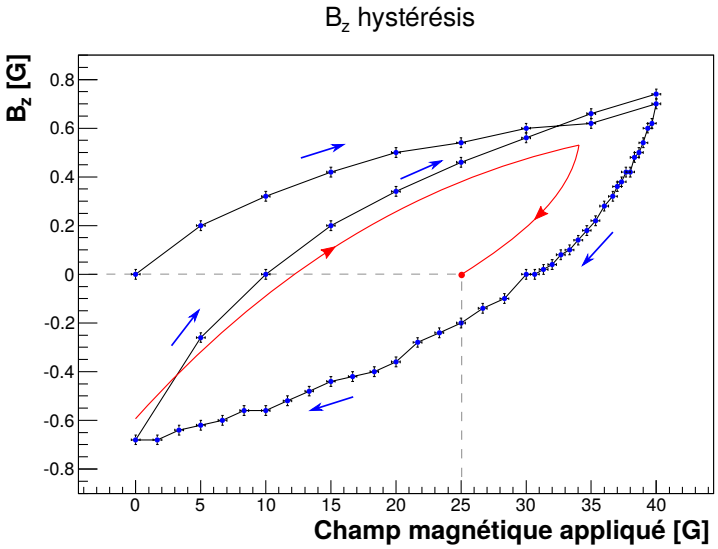

Figure 8.8 – Évolution du champ magnétique à l'intérieur d'un blindage lorsque le champ magnétique extérieur est augmenté puis diminué. Les propriétés ferromagnétiques du fer pur participent à l'amélioration du pouvoir de protection des blindages. Ainsi, il est possible de tirer profit du cycle d'hystérésis afin d'annuler complètement le champ magnétique à l'intérieur du blindage, tout en ayant un champ magnétique extérieur de 25 G, tel qu'illustré par la courbe rouge.

En effet, lors de la montée du champ magnétique extérieur, le champ magnétique à l'intérieur du blindage augmente lui aussi. Toutefois, contrairement à ce que l'on pourrait attendre, lors de la descente du champ magnétique extérieur, la valeur du champ magnétique ne suit pas la même évolution que lors de la montée. Par la suite, lorsque le champ magnétique est augmenté ou diminué, la valeur du champ magnétique à l'intérieur du blindage suit la même "boucle". Ce comportement est imputé au caractère ferromagnétique du blindage et la boucle observée est aussi connue sous le nom de cycle d'hystérésis. Ainsi, la courbe rouge illustre l'approche à suivre si l'on désire un champ magnétique extérieur de 25 G tout en mesurant un champ mangétique nul à l'intérieur du blindage: il suffit de monter le champ magnétique extérieur à une valeur plus importante que celle désirée (autour de 35 G dans notre exemple) afin d'induire une magnétisation du blindage, avant de redescendre à la valeur du champ magnétique désiré. La magnétisation induite

dans le blindage sert ainsi à annuler le champ magnétique à l'intérieur de ce dernier. Un prototype de bobine magnétique construit au Laboratoire de Physique Corpusculaire a aussi été utilisé afin d'estimer l'impact des blindages magnétiques sur le champ magnétique à l'intérieur du trajectographe. Cette bobine est en effet assez grande pour mesurer le champ magnétique à la fois à l'intérieur et à l'extérieur du blindage. La Figure 8.9 montre l'évolution du champ magnétique en fonction de la distance au blindage.

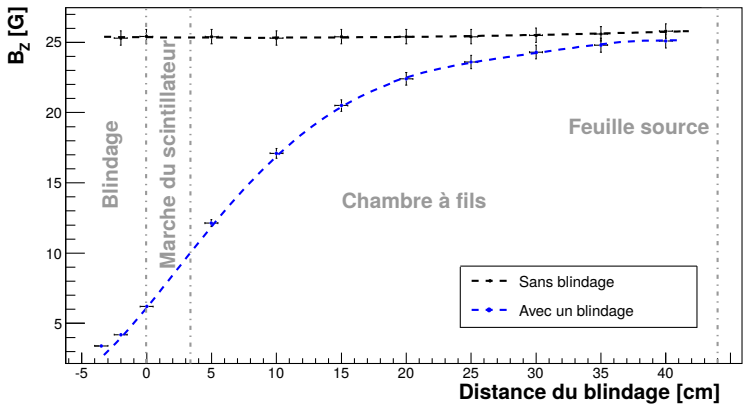

Figure 8.9 – Évolution du champ magnétique en fonction de la distance au blindage.

En l'absence de blindage magnétique, le champ est mesuré uniforme à 25 G. En revanche, lorsqu'un blindage est introduit dans la bobine, le champ magnétique à l'extérieur du blindage n'est plus du tout uniforme et décroît rapidement lorsque l'on se rapproche de ce dernier. Cet effet est d'autant plus important lorsque davantage de blindages sont rajoutés. Des simulations du champ magnétique dans le démonstrateur ont permis d'estimer qu'en appliquant un champ magnétique extérieur de 25 G, le champ magnétique au niveau de la source ne serait plus que de 10 G et décroîtrait fortement en se rapprochant des murs du calorimètre. Cependant, des simulations Monte-Carlo prenant en compte la non-uniformité du champ magnétique ont montrées que mis à part une légère réduction de la résolution spatiale (les trajectoires fittées étant des hélices), l'efficacité de reconstruction des évènements $0\nu\beta\beta$ demeurait très similaire. Une étude plus approfondie prenant en compte les différents bruits de fond reste nécessaire afin de déterminer si l'impact des blindages magnétique sur le champ magnétique dans le trajectographe peut aussi impacter la sensibilité du démonstrateur.

8.4 Développement d'outils de reconstruction

La collaboration SuperNEMO a developpé son propre logiciel de simulation (basé sur GEANT4) et de reconstruction. La reconstruction de la cinématique complète et l'identification de la topologie d'un évènement reposent sur une variété d'algorithmes de reconstruction.

Le design du démonstrateur SuperNEMO le rend capable d'identifier la nature des particules impliquées dans un évènement. La Figure 8.10 illustre les différentes signatures attendues, propres à chaque type de particule.

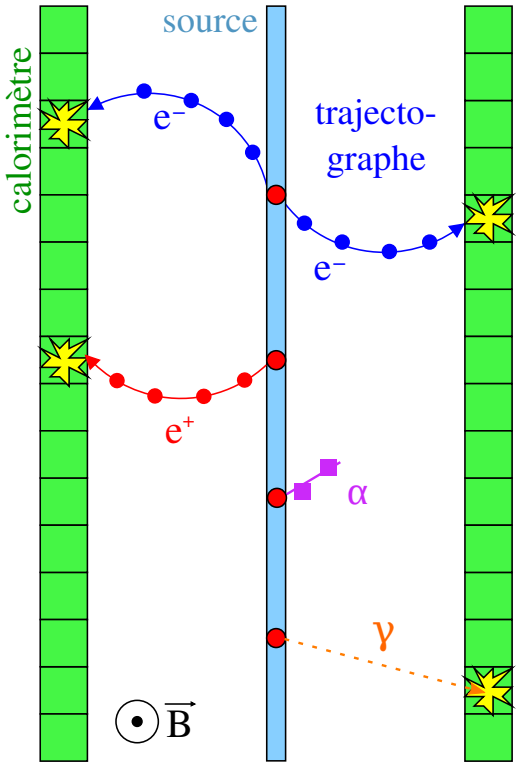

Figure 8.10 – Illustration des signatures laissées par les différents types de particules dans SuperNEMO.

Un électron sera reconstruit comme une longue trace de courbure négative avec un module calorimètrique déclenché associé. Un positron générera une signature très similaire mais de courbure opposée. Une particule α sera reconnue comme une particule chargée laissant une trace très courte dans le trajectographe. Enfin, une particule γ ne laissera pas de traces dans le trajectographe et sera seulement détectée par le calorimètre, parfois même plusieurs fois. Sa signature sera donc un ou plusieurs modules calorimétriques déclenchés, sans traces associées.

8.4.1 Reconstruction des particules γ

L'un des travaux de cette thèse fut la reconstruction de ces particules γ. Pour ce faire, trois algorithmes furent développés:

- le γ-clustering : un simple automate cellulaire cherchant à associer des modules calorimétriques déclenchés et géométriquement voisins en "clusters".
- le γ-tracking : une implémentation dans le logiciel SuperNEMO d'un algorithme développé pour NEMO-3. Cet algorithme utilise l'information du temps de vol afin

de déterminer la probabilité que deux modules calorimètriques aient été déclenchés par la même particule γ.

- le γ-tracko-clustering : cet algorithme cherche à tirer profit des avantages des deux algorithmes précédents.

Le principe du γ-tracko-clustering est expliqué en Figure 8.11.

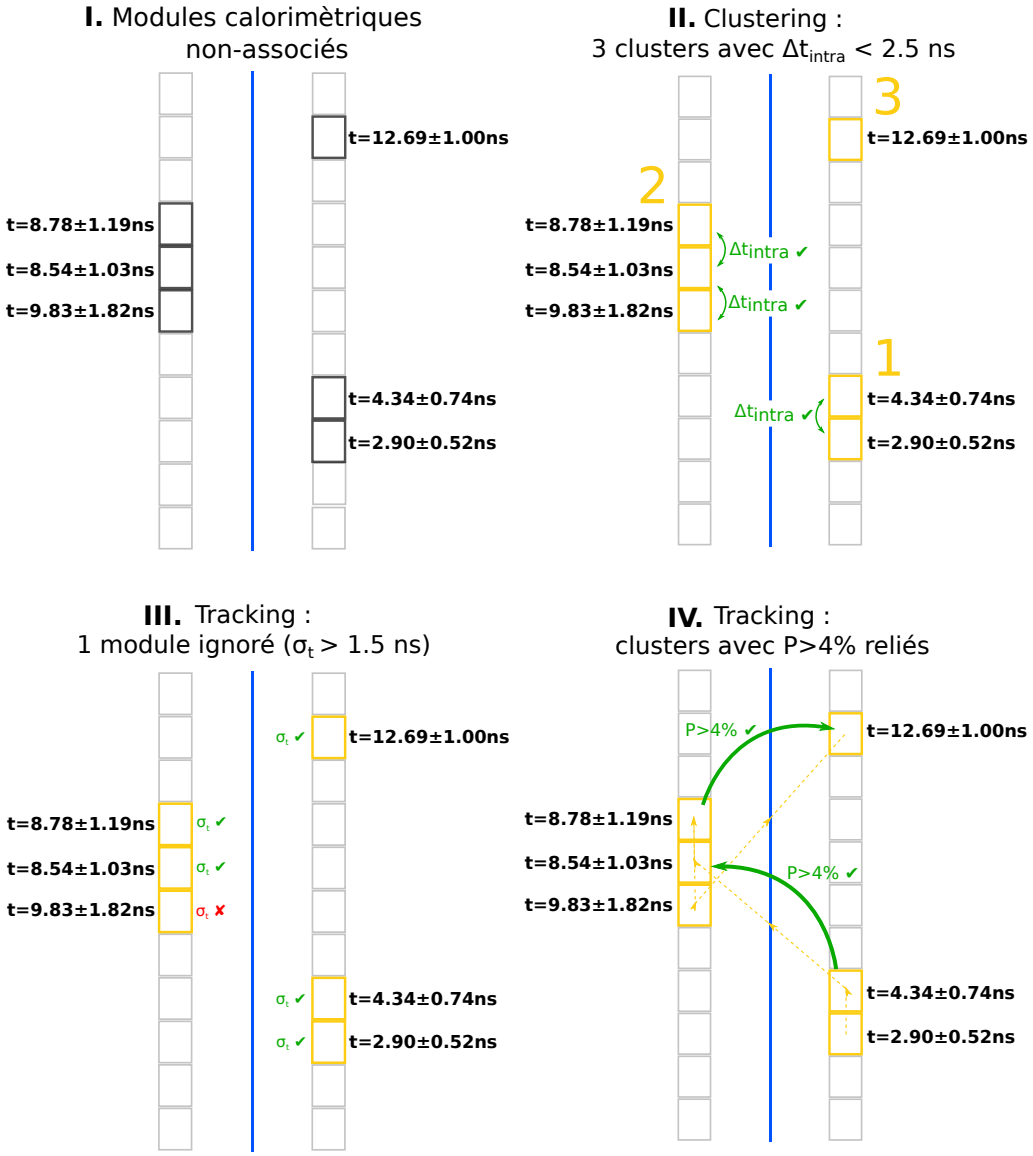

Figure 8.11 – Principe du fonctionnement de l'algorithme de γ-tracko-clustering.

Le point de départ de la reconstruction est illustré dans le point I. Plusieurs modules calorimètriques sont déclenchés, auxquels aucune trace n'est associée. Le calorimètre donne accès à l'énergie déposée mais surtout au temps du dêpot. La première étape de la reconstruction consiste en un simple *clustering*. Les modules voisins sont réunis en

clusters, pourvu qu'ils ne soient pas séparés par plus de 2.5 ns par exemple, afin de minimiser les chances de *pile-up* de particules γ. La probabilité de temps de vol entre clusters est ensuite calculée selon :

$$\chi^2_{\text{int}} = \frac{\left((t_2^{\text{exp}} - t_1^{\text{exp}}) - (\frac{\ell}{c})\right)^2}{\sigma^2_{t_1} + \sigma^2_{t_2} + \sigma^2_{\ell}/c^2}, \text{ puis } P(\chi_{\text{int}}) = \sqrt{\frac{2}{\pi}} \int_{\chi_{\text{int}}}^{+\infty} e^{-\frac{x^2}{2}} dx$$

où t_1^{exp} est le temps mesuré par le dernier module d'un premier cluster, t_2^{exp} celui du premier module d'un second cluster, ℓ la distance séparant ces deux modules, σ_{t_1} et σ_{t_2} les incertitudes sur les temps mesurés et σ_ℓ l'incertitude sur la longueur du trajet supposé du γ.

Cependant, avant de calculer les probabilités de temps de vol entre clusters, un critère de qualité est appliqué au sein des clusters. En effet, si l'énergie déposée dans un module calorimètrique est très faible, l'incertitude temporelle associée à ce dépôt sera très grande. Au regard de l'équation précédente, il est aisé de voir qu'une grande incertitude en temps diminuera le χ^2 et augmentera donc artificiellement la probabilité de temps de vol et avec elle, les chances de se tromper de séquence. Ainsi, dans notre exemple, un module sera ignoré pour le calcul de la probabilité de temps de vol du fait de sa trop grande incertitude temporelle. Lors de la dernière étape de la reconstruction, deux clusters sont considérés comme ayant été déclenchés par la même particule γ si la probabilité du temps de vol entre ces clusters est supérieure à une valeur prédéfinie, par exemple 4 %. Les performances et comportement de ces différents algorithmes ont été étudiés de manière extensive pour différents type d'évènements: 1γ, 2γ, 3γ, ^{214}Bi, ^{208}Tl, etc… Les efficacités de reconstruction obtenues avec ces trois algorithmes pour des évènements ^{208}Tl et ^{214}Bi (des émetteurs β/γ présents dans la source) sont présentées dans le Tableau 8.2.

	ϵ_{rec}		
	γ-clustering	γ-tracking	γ-tracko-clustering
^{208}Tl	56 %	61 %	65 %
^{214}Bi	63 %	72 %	75 %

Table 8.2 – Efficacité de reconstruction des différents algorithmes pour des évènements ^{208}Tl et ^{214}Bi.

Le γ-tracking offre une meilleure efficacité de reconstruction comparé au γ-clustering. L'emploi du γ-tracko-clustering permet d'améliorer davantage l'efficacité de reconstruction des évènements provenant des principaux émetteurs β/γ. Outre une meilleure efficacité de reconstruction, les deux algorithmes employant du tracking reconstruisent plus fidèlement le nombre de particules γ impliquées dans un évènement, ainsi que leurs énergies. Les performances et configurations optimales de ces algorithmes pourront être étudiées en profondeur lors des divers *runs* de calibration du démonstrateur (^{207}Bi et ^{232}U).

8.4.2 Identification des particules et mesures topologiques

Après la reconstruction des particules γ, les informations provenant du détecteur peuvent dorénavant être interprétées en terme d'évènement et non plus seulement en terme

de particules. Un programme fut développé afin de permettre aux utilisateurs d'attribuer automatiquement une étiquette à chaque particule, selon les définitions fournies au préalable par ces mêmes utilisateurs. Une fois toutes les particules d'un évènement identifiées, une topologie d'évènement peut être définie: $1e$, $2e$, $1e1\gamma$, $1e2\gamma$, $1e1\alpha$, etc. Toutes les quantités pertinentes à cette topologie sont ensuite automatiquement déterminées. Ces quantités seront par la suite utilisées lors de la phase d'analyse de données.

8.5 Sensibilité du démonstrateur SuperNEMO pour la mesure des bruits de fond

8.5.1 Origine des bruits de fond

Il convient tout d'abord de préciser l'origine des bruits de fond dans SuperNEMO. Outre la désintégration $2\nu\beta\beta$, dont les évènements de plus haute énergie peuvent être reconstruit dans la région d'intérêt du fait de la résolution en énergie limitée, la source peut être contaminée par des émetteurs β/γ, tels que le ^{208}Tl ou le ^{214}Bi, évoqués précédemment. La Figure 8.12 illustre les principaux mécanismes selon lesquels de simples émetteurs β/γ peuvent générer deux électrons provenant de la source et ainsi être considérés comme des évènements $0\nu\beta\beta$ si leur énergie est suffisante. Une désintégration β peut par exemple être accompagnée de l'émission d'un électron de conversion interne: dans ce cas, au lieu d'émettre un γ de désexcitation, l'atome se désexcite via l'émission d'un électron du cortège électronique. Une particule β peut aussi générer un second électron via diffusion Möller. Enfin, une désintégration β peut aussi être accompagnée de l'émission d'une particule γ, créant un deuxième électron par diffusion Compton et entraînant une fois de plus l'émission de deux électrons à partir de la source, similaire à un évènement $\beta\beta$.

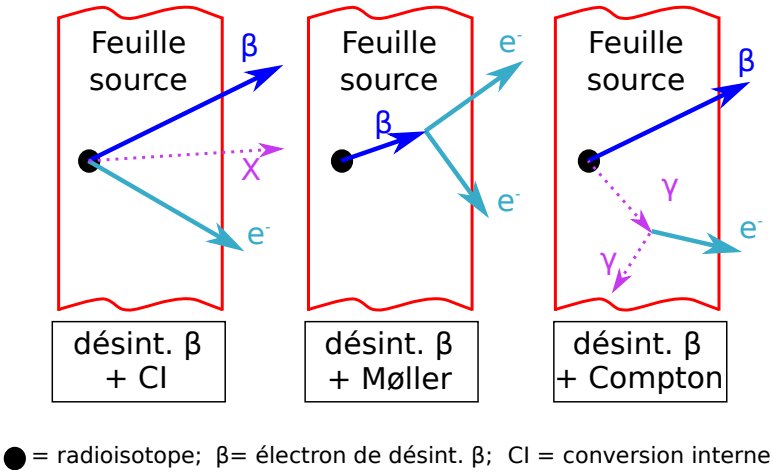

Figure 8.12 – Principaux mécanismes de production d'évènements de bruit de fond interne (*i.e.* provenant de la source).

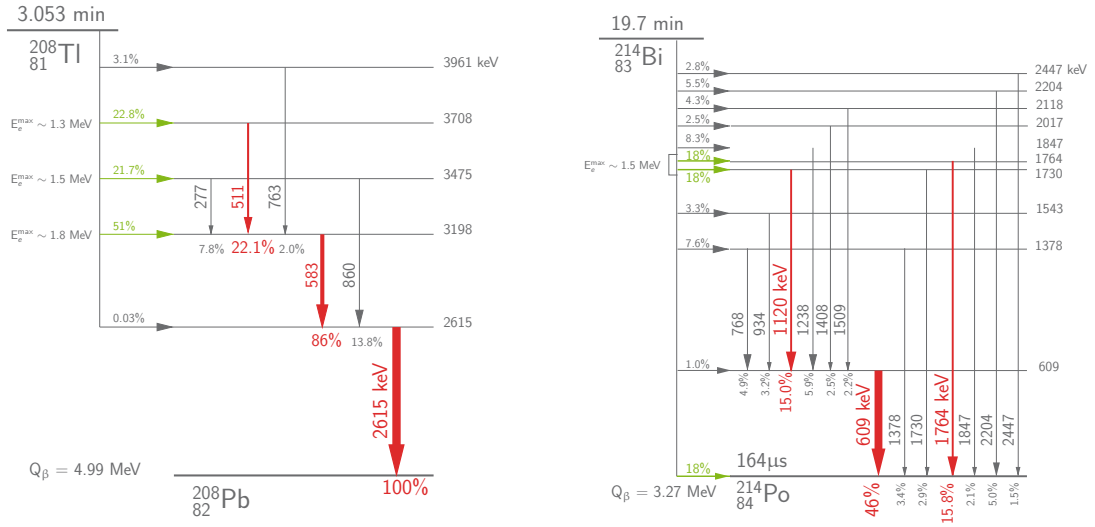

Figure 8.13 – Schéma de désintégration des noyaux de ^{208}Tl (gauche) et de ^{214}Bi (droite).

Pour qu'un de ces évènements puisse être considéré comme un évènement $0\nu\beta\beta$, il faut que les deux électrons aient une énergie totale suffisamment proche du $Q_{\beta\beta}$. C'est pourquoi, le ^{208}Tl et le ^{214}Bi, avec une énergie de transition respective de 4.99 MeV et 3.27 MeV, sont particulièrement problématiques. La Figure 8.13 recense les principaux modes de désintégration des noyaux de ^{208}Tl et de ^{214}Bi. Cette figure montre que le γ de 2.615 MeV du ^{208}Tl est particulièrement dangereux pour la recherche de la désintégration $0\nu\beta\beta$ puisque cette désexcitation peut aussi se produire par conversion interne, résultant en l'émission d'un électron de 2.615 MeV, en plus d'une particule β émise à chaque désintégration. On peut aussi remarquer qu'au moins 1 γ et jusque 3 γ sont attendus lors des désintégrations du ^{208}Tl et qu'entre 0 et 2 γ sont attendus lors des désintégrations du ^{214}Bi.

Le Radon est un gaz radioactif qui contribue aussi au bruit de fond. Ce radioisotope provient de la radioactivité naturelle (chaîne de désintégration de ^{238}U) et peut migrer de l'extérieur du détecteur jusque dans la chambre à fils ou bien émaner du détecteur lui-même, malgré les multiples protections (tente anti-radon, film nylon entre le calorimètre et le trajectographe, balayage et filtrage du gaz du tracker, etc…) et les précautions mises en place (sélection et mesures d'émanation des matériaux, etc…). Le Radon (^{222}Rn) n'est pas en lui-même problématique pour la recherche de la désintégration $0\nu\beta\beta$. En revanche cet isotope se désintègre jusqu'au ^{214}Bi, qui lui pose problème, pour les raisons exposées ci-dessus. Il est intéressant de noter que le ^{214}Bi se désintègre via désintégration β vers le ^{214}Po, qui lui-même se désintègre via désintégration α ($T_{1/2}$=164 μs) vers le ^{210}Pb. Cette signature "BiPo", constituée d'un électron prompt suivi d'un α retardé, est caractéristique de la désintégration de ce noyau.

SuperNEMO, grâce à ses capacités de reconstruction des traces et d'identification des particules, peut ainsi tirer profit des différentes signatures topologiques pour mesurer lui-même son bruit de fond *in-situ*. Un évènement $1e1\alpha$ provenant de la chambre à fils est ainsi caractéristique d'un évènement "Radon", tandis que les évènements $1eN\gamma$ provenant

de la source signent la présence de ^{208}Tl et de ^{214}Bi dans cette dernière.

La Figure 8.14 montre la distribution des topologies d'évènements attendus après 2.5 ans de prise de données avec le démonstrateur, en supposant les objectifs de radiopureté atteints : A(^{208}Tl) = 2μBq/kg, A(^{214}Bi) = 10μBq/kg et A(Radon) = 150μBq/m^3.

À partir de ces distributions, une stratégie de mesure des bruits de fond est établie. L'activité Radon peut être mesuré grâce aux évènements $1e1\alpha$ provenant de la chambre à fils. Cette topologie est à la fois très pure et fournit beaucoup d'évènements pour une mesure précise d'un premier bruit de fond. Une fois l'activité Radon contrainte, les activités ^{208}Tl et ^{214}Bi peuvent être mesurées grâces aux évènements $1eN\gamma$. Enfin, la demi-vie du processus $2\nu\beta\beta$ peut être mesurée grâce à la topologie $2e$. Afin d'estimer les incertitudes systématiques inhérentes à cette procédure, celle-ci est répétée sur de nombreuses pseudo-expériences. Ces pseudo-expériences sont générées en simulant un nombre d'évènements constant et égal aux nombres d'évènements attendus pour chaque bruit de fond et en supposant encore une fois les objectifs de radiopureté atteints. La génération des évènements étant aléatoire, le nombre d'évènements reconstruits dans chaque topologie varie d'une pseudo-expérience à l'autre.

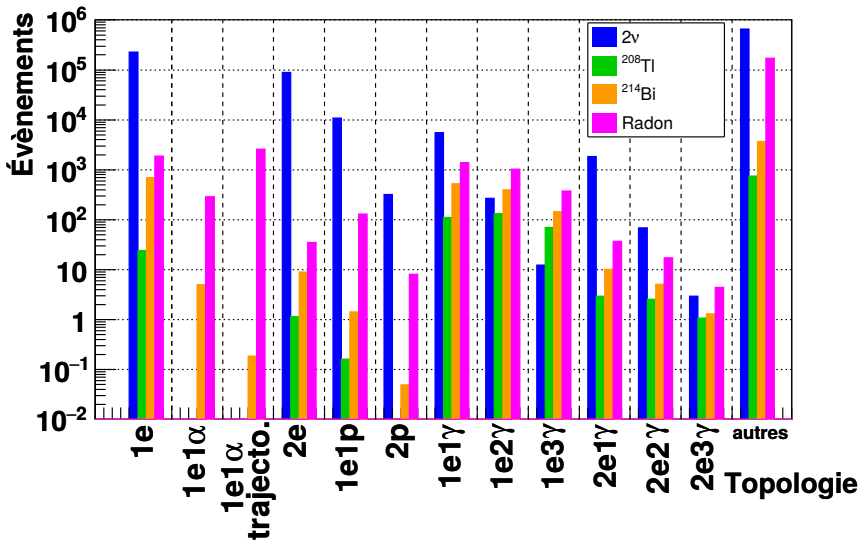

Figure 8.14 – Distribution des topologies d'évènements reconstruits après 2.5 ans, en supposant les objectifs de radiopureté atteints.

8.5.2 Mesure du Radon

La Figure 8.15 montre les distributions de l'énergie de l'électron et de la longueur de la trace α pour les évènements $1e1\alpha$, obtenus pour une pseudo-expérience.

Des modèles Monte-Carlo, obtenus à partir de simulations beaucoup plus importantes en terme de statistique, sont simultanément ajustés (minimisation d'un log-likelihood binné) aux distributions de trois des variables les plus discriminantes. Il en résulte une mesure du nombre d'évènements Radon qui peut être traduite en une mesure d'activité.

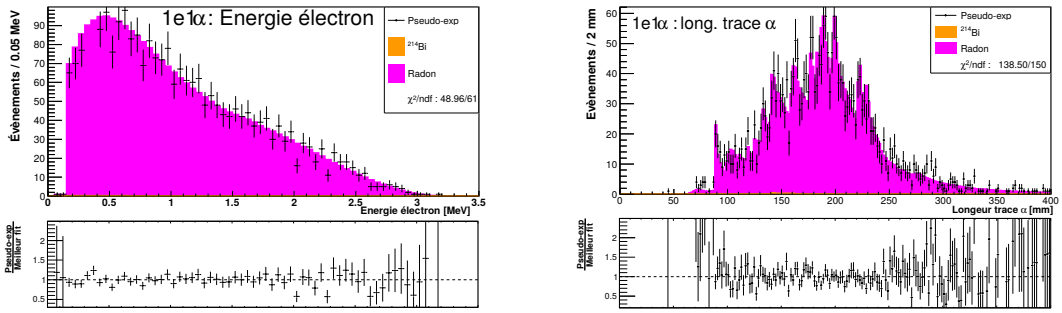

Figure 8.15 – Ajustement d'une pseudo-expérience dans le canal $1e1\alpha$ issu de la chambre à fils : *(gauche)* distribution de l'énergie de l'électron et *(droite)* distribution de la longueur de la trace α.

Cette procédure est répétée pour un grand nombre de pseudo-expériences. La distribution des activités Radon mesurées nous fournit ainsi une idée de la précision de la mesure : la largeur de cette distribution est une estimation de l'erreur systématique inhérente à cette procédure. L'incertitude statistique est simplement liée aux nombres d'évènements Radon disponibles pour la mesure. Cette procédure peut par ailleurs être répétée pour différents temps de mesure. Il en résulte la Figure 8.16, qui présente l'évolution relative des erreurs systématiques et statistiques sur la mesure de l'activité Radon, en fonction de la durée de la mesure. Cette figure montre qu'une mesure précise de l'activité Radon peut-être obtenue en quelques mois seulement. Il serait donc possible de se rendre compte assez rapidement si l'objectif de 150 μBq/m^3 est atteint, puis de suivre l'évolution de cette activité avec le temps.

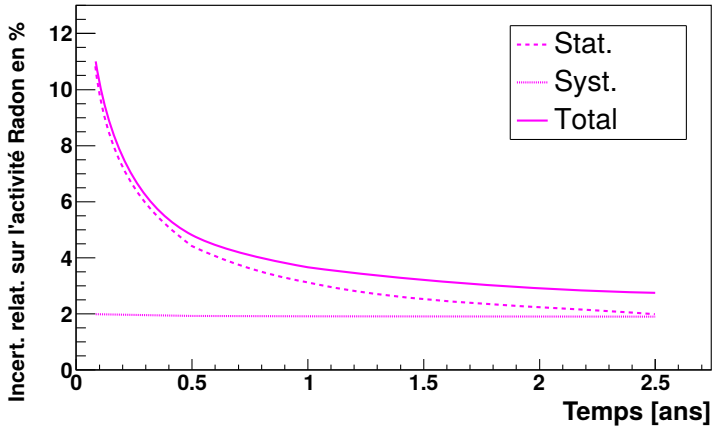

Figure 8.16 – Évolution des incertitudes sur la mesure de l'activité Radon en fonction du temps de mesure.

8.5.3 Mesure du ^{208}Tl et du ^{214}Bi

Le principe reste le même pour la mesure des activités ^{208}Tl et ^{214}Bi, en utilisant cependant les évènements $1eN\gamma$ et en ayant contraint la contribution du Radon. La Figure 8.17

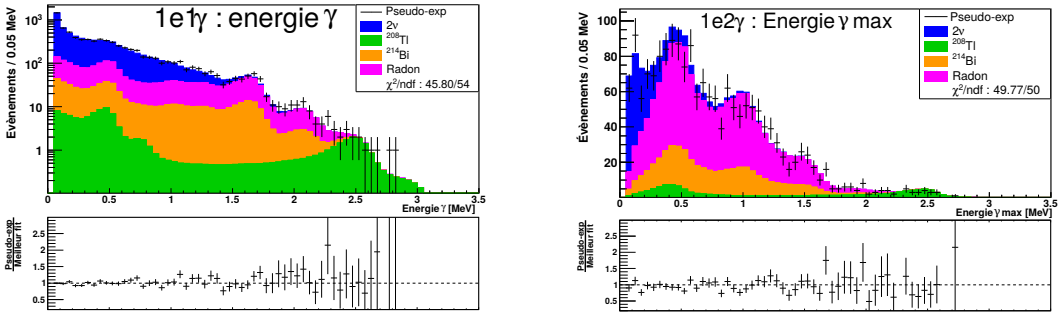

Figure 8.17 – Ajustement d'une pseudo-expérience : *(gauche)* distribution de l'énergie du γ dans la topologie $1e1\gamma$ et *(droite)* distribution de l'énergie du γ de plus haute énergie dans la topologie $1e2\gamma$.

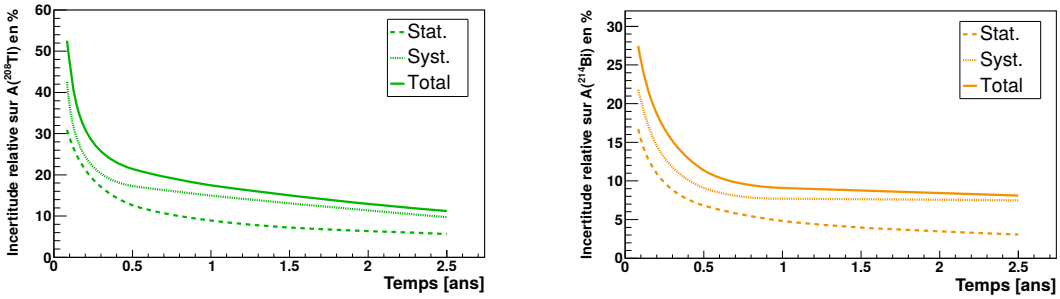

Figure 8.18 – Évolution des incertitudes sur la mesure de l'activité ^{208}Tl *(gauche)* et de l'activité ^{214}Bi *(droite)* en fonction du temps de mesure.

montre l'ajustement d'une pseudo-expérience sur deux des trois variables les plus discriminantes utilisées pour la mesure, à savoir l'énergie du γ dans la topologie $1e1\gamma$ (à gauche) et l'énergie du γ de plus haute énergie dans la topologie $1e2\gamma$.

L'évolution relative des incertitudes statistique et systématique sur la mesure des activités ^{208}Tl et ^{214}Bi en fonction du temps est présentée en Figure 8.18. Bien que l'erreur systématique reste dominante tout au long de la prise de données, une mesure précise de la contamination de la source peut être effectuée après quelques mois.

8.5.4 Mesure de la demi-vie du processus $2\nu\beta\beta$ du ^{82}Se

Dans cette étude, la topologie d'intérêt est naturellement la topologie deux électrons $2e$. Les distributions de l'énergie totale, de l'énergie de l'électron de plus haute énergie ainsi que de l'angle entre les deux électrons sont ici ajustées simultanément (*cf* Figure 8.19) pour un grand nombre de pseudo-expériences et pour des durées de mesure différentes. Comme l'illustre la Figure 8.20, l'incertitude systématique devrait devenir dominante après environ 5 mois de mesure et l'incertitude finale totale sur la mesure de la demi-vie $2\nu\beta\beta$ devrait être meilleure que le pourcent. Connaître aussi précisément la demi-vie de ce processus pour cet isotope apporterait une contrainte très importante sur les modèles théoriques qui possèdent aujourd'hui de grandes incertitudes.

Il est important de noter que les erreurs systématiques estimées ici supposent un détecteur idéal (pas de variations de la résolution en énergie, tous les modules optiques sont

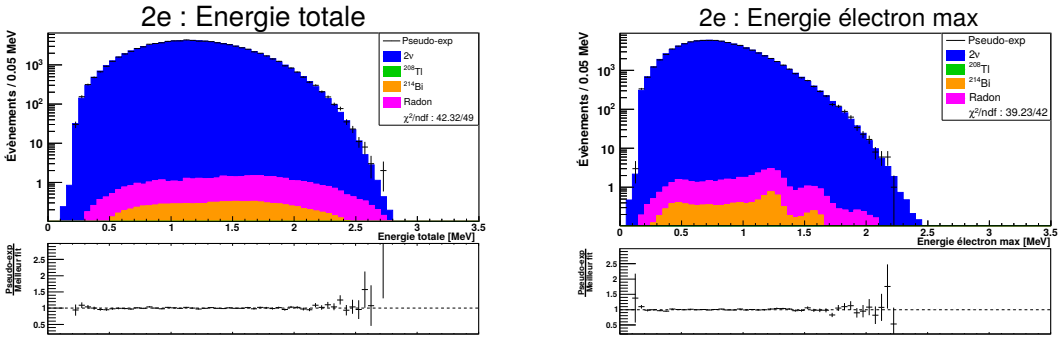

Figure 8.19 – Ajustement d'une pseudo-expérience dans la topologie $2e$: *(gauche)* distribution de la somme en énergie *(droite)* distribution de l'énergie de l'électron de plus haute énergie.

opérationels, etc…) et ne prennent donc uniquement en compte que les erreurs systémtiques inhérentes à notre approche, c'est à dire provenant de la simulation, de la reconstruction et de la procédure d'ajustement. De plus, le modèle de bruit de fond n'est ici pas complet et d'autres contributions seront amenées à polluer ces mesures. Enfin, les efficacités de reconstruction sont ici connues parfaitement (*i.e.* sans erreurs associées) et pourront être corrigées grâce à des *runs* de calibrations dédiés (^{207}Bi, ^{232}U et ^{90}Y). C'est pourquoi les erreurs systématiques finales seront sensiblement plus importantes que les estimations obtenues par ces travaux.

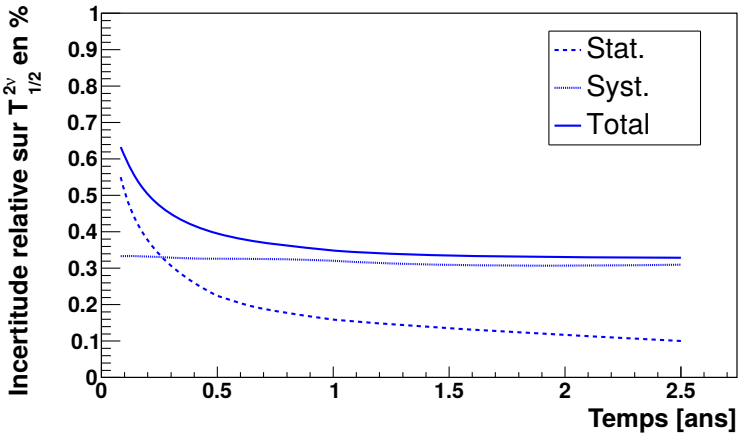

Figure 8.20 – Évolution des incertitudes sur la mesure de la demi-vie du processus $2\nu\beta\beta$ du ^{82}Se.

8.6 Sensibilité du démonstrateur SuperNEMO pour la recherche de la désintégration $0\nu\beta\beta$

La dernière partie des travaux exposés dans cette thèse consiste en l'estimation de la sensibilité du démonstrateur SuperNEMO pour la recherche de la désintégration $0\nu\beta\beta$. Pour ce faire, des évènements de signal $0\nu\beta\beta$ (supposant le mécanisme de masse) ont

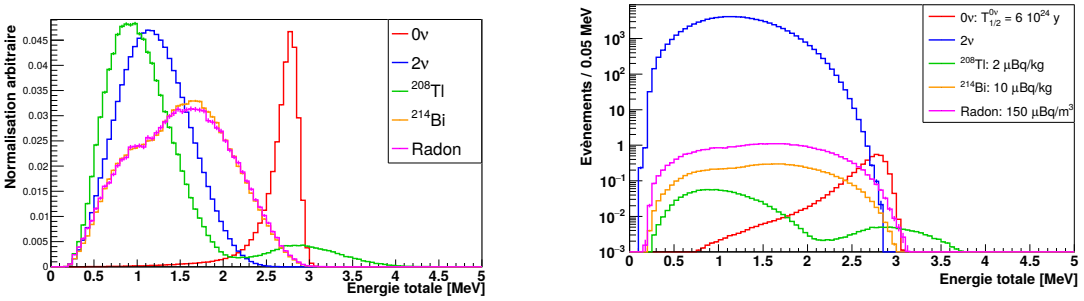

Figure 8.21 – Distribution de l'énergie totale dans le canal $2e$: *(gauche)* normalisations arbitraires et *(droite)* normalisations au nombre d'évènements attendus après 2.5 ans en supposant les objectifs de radiopureté atteints.

été simulés en plus des principaux bruits de fond présentés précédemment. Les évènements d'intérêt sont les évènements de la topologie $2e$. Les distributions, normalisées arbitrairement, Figure 8.21 à gauche, et normalisées au nombre d'évènements attendus après 2.5 ans, Figure 8.21 à droite, de la somme en énergie des deux électrons illustrent bien la difficulté d'observer un excès d'évènements $0\nu\beta\beta$ parmi les différentes sources de bruits de fond.

En utilisant uniquement cette variable et en supposant les objectifs de bruits de fond atteints mais qu'aucun évènement de signal n'est observé, le démonstrateur serait capable de mettre une limite inférieure sur la demi-vie du processus $0\nu\beta\beta$ de $T^{0\nu\beta\beta}_{1/2} > 5.35\,10^{24}$ ans (90 % C.L.). Cette limite est obtenue en utilisant la méthode CL_S, telle qu'implémentée dans le logiciel COLLIE. En supposant par ailleurs que le mécanisme de masse est bien responsable de la désintégration $0\nu\beta\beta$, il est possible de contraindre la masse effective du neutrino de Majorana, grâce à la relation suivante :

$$(T^{0\nu\beta\beta}_{1/2})^{-1} = G^{0\nu}(Q_{\beta\beta}, Z)|M_{0\nu}|^2|m_{\beta\beta}|^2 \tag{8.3}$$

où $G^{0\nu}(Q_{\beta\beta}, Z)$ est le facteur d'espace de phase nucléaire, $M_{0\nu}$ les éléments de matrice nucléaire et $m_{\beta\beta}$ la masse effective du neutrino de Majorana . Ainsi la limite sur la demi-vie du processus $0\nu\beta\beta$ peut être traduite en une limite sur la masse effective du neutrino de Majorana $\langle m_{\beta\beta}\rangle$ < 0.21 - 0.58 eV. Cette masse effective est en outre la seule quantité pertinente permettant de comparer entre elles les résultats d'expériences $\beta\beta$ étudiant des isotopes différents.

8.6.1 Analyse multivariée

Grâce à son design combinant un calorimètre et un trajectographe, SuperNEMO a accès à la cinématique complète des évènements et donc à de plus nombreuses variables, dont une analyse multivariée pourrait permettre d'améliorer la sensibilité du détecteur. La solution employée dans cette analyse repose sur des arbres de décision boostés (implémentés dans TMVA de ROOT). La discrimination entre évènements de signal et de bruit de fond peut ainsi être améliorée grâce à l'utilisation de 11 variables topologiques: les énergies individuelles des deux électrons, la différence et la somme de leurs énergies,

l'angle d'émission entre les deux électrons, les probabilités interne et externe (basées sur le temps de vol), les distances verticales et horizontales entre les deux vertex d'émission reconstruits sur la source ainsi que les longueurs de traces des deux électrons. Les jeux de données Monte-Carlo sont divisés en 4 échantillons afin de déterminer et de vérifier que la configuration de nos arbres de décision donne des résultats similaires, peu importe l'échantillon d'entraînement et d'application, c'est à dire de tester l'absence d'*overtraining*. Une fois l'entraînement de nos arbres de décisions boostés effectué, un score est attribué à chaque évènement, selon qu'il ressemble à un évènement de signal (scores proche de +1) ou au contraire à un évènement de bruit de fond (scores proche de -1). Les distributions normalisées aux activités ou demi-vie nominales de ce score sont présentées en Figure 8.22, pour le signal et les principaux bruits de fond.

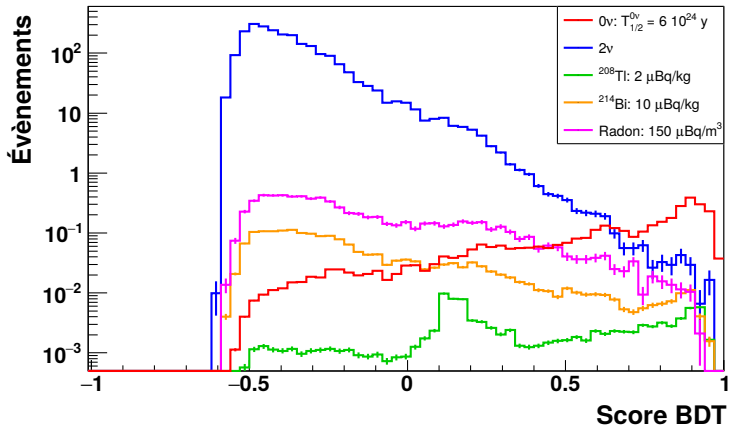

Figure 8.22 – Distributions des scores BDT pour chaque contribution, normalisées au nombre d'évènements attendus après 2.5 ans en supposant les objectifs de radiopureté atteints.

La limite extraite grâce à cette approche multivariée est améliorée à $T_{1/2}^{0\nu\beta\beta} > 5.85\,10^{24}$ ans (90 % C.L.). D'autres approches de détermination de limites (Profile Likelihood Calculator, approche bayésienne, approche bayésienne avec méthode de Monte-Carlo par chaînes de Markov) ont aussi été utilisées. Ainsi, en supposant les critères de radiopureté très sévères atteints, l'approche multivariée permettrait d'augmenter la sensibilité du démonstrateur SuperNEMO de 10 % par rapport à l'utilisation de l'énergie totale uniquement, à l'instar des autres expériences $\beta\beta$. L'apport de l'analyse multivariée est d'autant plus significatif si les niveaux de contaminations des bruits de fond sont plus importants que prévus. Les Figures 8.23, 8.24 et 8.25 montrent l'évolution de la sensibilité du démonstrateur en fonction de la contamination en ^{208}Tl, ^{214}Bi et Radon, respectivement.

L'utilisation de techniques d'apprentissage machine permet non seulement d'améliorer la sensibilité du détecteur mais aussi de rendre ce dernier moins sensible à la présence du bruit de fond et notamment à la contamination Radon. L'amélioration est plus importante pour cette contamination puisque, contrairement aux évènements ^{208}Tl et ^{214}Bi, les évènements Radon ne proviennent pas de la source, ce qui rend les variables topologiques beaucoup plus discriminantes (probabilité interne et distance entre les vertex notamment).

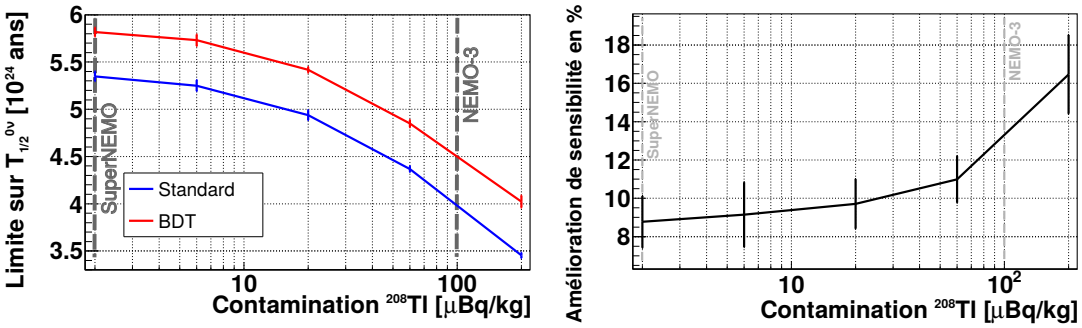

Figure 8.23 – *(gauche)* Évolution de la sensibilité du démonstrateur en fonction de la contamination ^{208}Tl pour les approches univarié (en bleu) et multivariée (en rouge). *(droite)* Amélioration sur la sensibilité apportée par l'utilisation d'une analyse multivariée en fonction de la contamination ^{208}Tl.

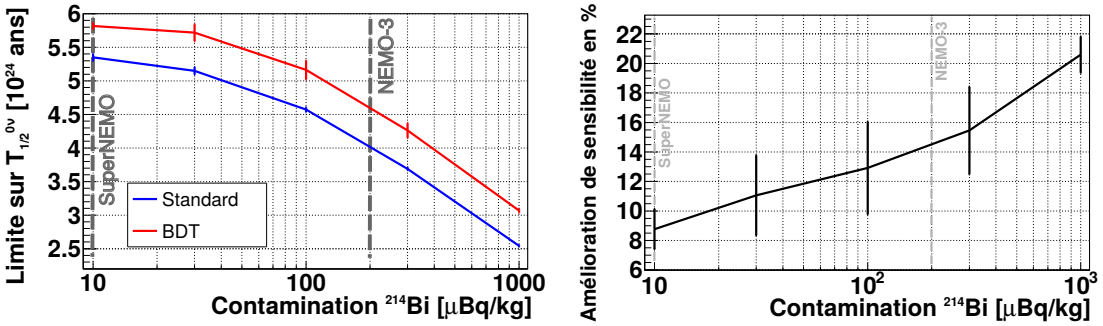

Figure 8.24 – *(gauche)* Évolution de la sensibilité du démonstrateur en fonction de la contamination ^{214}Bi pour les approches univarié (en bleu) et multivariée (en rouge). *(droite)* Amélioration sur la sensibilité apportée par l'utilisation d'une analyse multivariée en fonction de la contamination ^{214}Bi.

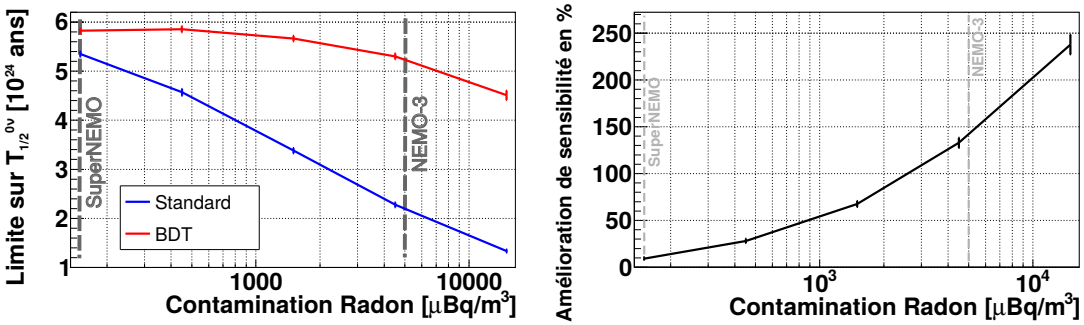

Figure 8.25 – *(gauche)* Évolution de la sensibilité du démonstrateur en fonction de la contamination Radon pour les approches univarié (en bleu) et multivariée (en rouge). *(droite)* Amélioration sur la sensibilité apportée par l'utilisation d'une analyse multivariée en fonction de la contamination Radon.

Enfin, à titre d'exemple, en supposant les niveaux de bruit de fond de NEMO-3 dans le démonstrateur SuperNEMO, l'analyse multivariée permettrait d'augmenter la sensibilité de 90 %.

Bibliography

[1] J. Chadwick, Intensitätsverteilung im magnetischen Spektrum der β-Strahlen von Radium B+C, Phys. Ges. vol. 16, (1914) 383-91.

[2] W. Pauli, Letter to the physical society of Tübingen, Physics Today 9,1930.

[3] E. Fermi, Versuch einer Theorie der β-Strahlen. I, Zeitschrift für Physik vol. 88, no. 3, (1934) 161–177

[4] C. L. Cowan, F. Reines et al., Detection of the Free Neutrino: a Confirmation, Science vol. 124, no. 3212, (1956) 103–104.

[5] G. Danby, J.-M. Gaillard, K. Goulianos, L. M. Lederman, N. Mistry, M. Schwartz, and J. Steinberger, Observation of high-energy neutrino reactions and the existence of two kinds of neutrinos, Phys. Rev. Lett. vol. 9, (1962) 36–44

[6] The ALEPH Collaboration, the DELPHI Collaboration, the L3 Collaboration, the OPAL Collaboration, the SLD Collaboration, the LEP Electroweak Working Group, the SLD Electroweak and Heavy Flavour Groups. Precision electroweak measurements on the Z resonance. Physics Reports , 427 (2006) 257–454

[7] K. Kodama et al., Observation of tau neutrino interactions, Phys. Lett. B 504, (2001) 218–224,

[8] B. Pontecorvo, Mesonium and anti-mesonium, Sov. Phys. JETP 6 (1957) 429.

[9] B. Pontecorvo, Inverse beta processes and nonconservation of lepton charge, Sov. Phys. JETP 7 (1958) 172–173.

[10] L. Wolfenstein, Neutrino oscillations in matter, Phys. Rev. D vol. 17 (May 1978) 2369–2374.

[11] S.P. Mikheyev et A. Yu. Smirnov, Neutrino oscillations in matter, Phys. Rev. D vol. 17 (May 1978) 2369–2374.

[12] G. Jonkmans, The Sudbury Neutrino Observatory, Nuclear Physics B - Proceedings Supplements, 70 (1999) 329–331.

[13] S. Fukuda et al. The Super-Kamiokande detector. Nuclear Instruments and Methods in Physics Research Section A : Accelerators, Spectrometers, Detectors and Associated Equipment 501, (2003) 418-462

[14] Z. Maki, M. Nakagawa, S. Sakata, Remarks on the Unified Model of Elementary Particles, Progress of Theoretical Physics. 28, (1962) 870

[15] F.Capozzi et al., Neutrino masses and mixings: Status of known and unknown 3ν parameters, arXiv:1601.07777

[16] E. Majorana. Teoria Symmetrica dell'Elettrone e del Positrone. Nuobo Cimento 14, 1937.

[17] A. Osipowicz et al., KATRIN: A next generation tritium beta decay experiment with sub-eV sensitivity for the electron neutrino mass arXiv:hep-ex/0109033

[18] AA. Esfahani et al., Determining the neutrino mass with Cyclotron Radiation Emission Spectroscopy – Project 8, arXiv:1703.02037

[19] A. Nucciotti, Neutrino mass calorimetric searches in the MARE experiment, arXiv:1012.2290

[20] Ch. Yeche et al., Constraints on neutrino masses from Lyman-alpha forest power spectrum with BOSS and XQ-100, arXiv:1702.03314

[21] Adapted from Katrin spectrum, Wikimedia Commons

[22] M. Goeppert-Mayer. Double Beta-Disintegration. Phys. Rev. 48, 1935.

[23] Search for the proton decay via $p \to e^+ \pi^0$ and $p \to e^+ \pi^0$ in 0.31 megaton.years exposure of the SuperKamiokande water Cherenkov detector.

[24] M. Mirea et al., Phase Space Factors for Double Beta Decay: an up-date, arXiv:1411.5506

[25] W. H. Furry, On Transition Probabilities in Double Beta-Disintegration , Phys. Rev. 56 , 1184-1193, 1939.

[26] J. Schechter and J. W. F. Valle. Neutrinoless Double-β Decay in SU(2)×U(1) Theories. Phys. Rev. D25, 1982.

[27] S. Dell'Oro, S. Marcocci, M. Viel and F. Vissani, Neutrinoless double beta decay: 2015 review, Advances in High Energy Physics, Volume 2016 (2016), arXiv:1601.07512

[28] R. A. Sen'kov and M. Horoi, Accurate shell-model nuclear matrix elements for neutrinoless double-beta decay, Phys. Rev. C 90, 051301(R) (2014) arXiv:1411.1667

[29] J. Terasaki, Many-body correlations of quasiparticle random-phase approximation in nuclear matrix element of neutrinoless double-beta decay, Phys. Rev. C 91, 034318 (2015) arXiv:1408.1545

[30] J. Barea, J. Kotila and F. Iachello, Nuclear matrix elements for double-β decay, Phys. Rev. C 87, 014315 (2013) arXiv:1301.4203

[31] P. K. Rath et al, Neutrinoless $\beta\beta$ decay transition matrix elements within mechanisms involving light Majorana neutrinos, classical Majorons and sterile neutrinos, Phys. Rev. C 88, 064322 (2013) arXiv:1308.0460

[32] Tomás R. Rodríguez and G. Martinez-Pinedo, Energy density functional study of nuclear matrix elements for neutrinoless $\beta\beta$ decay, Phys.Rev.Lett. 105:252503 (2010) arXiv:1008.5260

[33] J.F. Berger, M. Girod and D. Gogny, Nucl. Phys. A, 428 (1984)

[34] J. M. Yao et al., Systematic study of nuclear matrix elements in neutrinoless double-β decay with a beyond-mean-field covariant density functional theory, Phys. Rev. C 91, 024316 (2015) arXiv:1410.6326

[35] F. Iachello, J. Barea and J. Kotila, Quenching of g_A and its impact in double beta decay, PoS(NEUTEL2015)047

[36] Mark G. Inghram and John H. Reynolds, Double Beta-Decay of ^{130}Te Phys. Rev. 78, 822 – Published 15 June 1950

[37] M. Agostini et al., Background free search for neutrinoless double beta decay with Gerda Phase II, Nature, Volume 544, Number 7648, pp5-132 (2017), arXiv:1703.00570

[38] H. Klapdor-Kleingrothaus et al., Latest results from the Heidelberg-Moscow Double Beta Decay Experiment, Eur.Phys.J. A12 (2001) 147–154, arXiv:hep-ph/0103062

[39] H.V. Klapdor-Kleingrothaus, First Evidence for Neutrinoless Double Beta Decay - and World Status of Double Beta Experiments, arXiv:hep-ph/0512263

[40] C. Aalseth et al., The IGEX Ge-76 neutrinoless double beta decay experiment: Prospects for next generation experiments, Phys.Rev.D65 (2002) 092007, arXiv:hep-ex/0202026

[41] S.R. Elliott et al., Initial Results from the MAJORANA DEMONSTRATOR, arXiv:1610.01210

[42] E. Andreotti et al., ^{130}Te Neutrinoless Double-Beta Decay with CUORICINO, arXiv:1012.3266

[43] K. Alfonso et al., Search for Neutrinoless Double-Beta Decay of ^{130}Te with CUORE-0, Phys. Rev. Lett. 115, 102502 (2015), arXiv:1504.02454

[44] C. Alduino et al., The projected background for the CUORE experiment, arXiv:1704.08970

[45] E. Armengaud et al., Development of ^{100}Mo-containing scintillating bolometers for a high-sensitivity neutrinoless double-beta decay search, arXiv:1704.01758

[46] J.B. Albert et al., Searches for Double Beta Decay of ^{134}Xe with EXO-200, arXiv:1704.05042

[47] Thomas Brunner, Lindley Winslow, Searching for $0\nu\beta\beta$ decay in ^{136}Xe – towards the tonne-scale and beyond, arXiv:1704.01528.

[48] V. Álvarez et al., Ionization and scintillation response of high-pressure xenon gas to alpha particles, arXiv:1211.4508

[49] KamLAND-Zen collaboration, Search for Majorana Neutrinos near the Inverted Mass Hierarchy Region with KamLAND-Zen, Phys. Rev. Lett. 117, 082503 (2016), arXiv:1605.02889

[50] H.M. O'Keeffe, E. O'Sullivan, M.C. Chen, Scintillation decay time and pulse shape discrimination in oxygenated and deoxygenated solutions of linear alkylbenzene for the SNO+ experiment,Nucl.Instrum.Meth.A640:119-122,2011, arXiv:1102.0797

[51] Photo of the SNO experiment

[52] R. Arnold et al., Result of the search for neutrinoless double-β decay in ^{100}Mo with the NEMO-3 experiment, Physical Review D 92 (2015) 072011 arXiv:1506.05825

[53] A.S. Barabash et al., Calorimeter development for the SuperNEMO double beta decay experiment, Nuclear Instruments and Methods in Physics Research Section A, July 2017.

[54] http://geant4.cern.ch

[55] Stycast Technical Data Sheet http://resintek.co.uk/datasheets/2651MM.pdf

[56] C. Vilela, PhD thesis: Search for $\beta\beta$-decay of ^{48}Ca in NEMO-3 and commissioning of the tracker for the SuperNEMO experiment (2014).

[57] H. de Préaumont, SuperNEMO coil, Internal presentation DocDB:3072-v1

[58] S. Blondel, PhD thesis: Optimisation du blindage contre les neutrons pour le démonstrateur de SuperNEMO et analyse de la double désintégration β du néodyme-150 vers les états excités du samarium-150 avec le détecteur NEMO 3 (2013).

[59] C. Macolino, Energy calibration of the SuperNEMO demonstrator calorimeter, Internal note DocDB:4038 (2016).

[60] T. Le Noblet, Status design of the Light Injection System, Internal presentation, DocDB:3874 (2015).

[61] A.S. Barabash et al., The BiPo-3 detector for the measurement of ultra low natural radioactivities of thin materials, JINST 12 (2017) P06002

[62] https://github.com/SuperNEMO-DBD/homebrew-cadfael

[63] https://github.com/BxCppDev/Bayeux

[64] https://github.com/SuperNEMO-DBD/Falaise

[65] http://linuxbrew.sh/

[66] https://www.gnu.org/software/gsl/

[67] http://www.boost.org

[68] R. Brun and F. Rademakers, ROOT: An object oriented data analysis framework, Nucl. Inst. Meth. in Phys. Res A 389 (1997) 81–86. https://root.cern.ch/

[69] https://github.com/tegesoft/camp

[70] https://billyquith.github.io/ponder

[71] http://proj-clhep.web.cern.ch/proj-clhep

[72] http://xerces.apache.org/xerces-c

[73] http://geant4.cern.ch

[74] http://www.stack.nl/~dimitri/doxygen/

[75] http://doc.qt.io/qt-5/

[76] O. Ponkratenko, V. Tretyak, and Y. Zdesenko, The Event generator DECAY4 for simulation of double beta processes and decay of radioactive nuclei, Phys.Atom.Nucl. 63 1282–1287.

[77] J. Argyriades et al., Spectral modelling of scintillator for the NEMO-3 and SuperNEMO detectors, Nucl. Inst. and Meth. Section A, Vol. 625 (2011)

[78] X. Garrido, Tracker clustering & tracker fitting within snanalysis, Internal presentation, DocDB:2279-v4

[79] R. Arnold et al., Measurement of the $2\nu\beta\beta$ decay half-life of ^{150}Nd and a search for $0\nu\beta\beta$ decay processes with the full exposure from the NEMO-3 detector, Phys. Rev. D 94, 072003 (2016) arXiv:1606.08494

[80] W. Fischer https://www-d0.fnal.gov/d0dist/dist/packages/collie/devel/doc/CollieDocumentation.pdf

[81] https://twiki.cern.ch/twiki/bin/view/RooStats/WebHome

[82] https://root.cern.ch/roofit

[83] Allen Caldwell, Kevin Kröninger, Signal discovery in sparse spectra: a Bayesian analysis, Phys.Rev.D74:092003,2006, arXiv:physics/0608249

[84] G. J. Feldman and R. D. Cousins. A Unified Approach to the Classical Statistical Analysis of Small Signals, Phys. Rev. D57 (1998)

[85] http://tmva.sourceforge.net/

[86] V. Tretyak, ^{100}Mo neutron background for 0ν e+e- channel, Internal presentation, DocDB:3115-v1

[87] M. Bongrand et al., Magnetic shields summary, Internal presentation DocDB:3280-v1

[88] M. Bongrand, Summary of the magnetic design of the SuperNEMO demonstrator, Internal note DocDB:3633-v1

[89] M. Bongrand and X. Garrido, Hamamatsu 8" PMT Test in Magnetic Shield, Internal presentation, DocDB:2996-v2

[90] S. Snow, Estimate of the influence of the magnetic shields on the field in the tracker, Internal note DocDB:3582-v1

[91] S. Snow, A magnetic field map for the tracker, Internal note DocDB:3784-v1

[92] X. Garrido, Calorimeter Magnetic Shielding : Influence on Magnetic Field, Internal presentation, February 2015

[93] C. Hugon, Analyse des données de l'expérience NEMO-3 pour la recherche de la désintégration double bêta sans émission de neutrinos. Étude des biais systématiques du calorimètre et développements d'outils d'analyse, Ph.D. Thesis, 2012

[94] K. Errahmane, Étude du détecteur de traces de l'expérience NEMO-3. Simulation de la mesure de l'ultra-faible radioactivité en ^{208}Tl des sources de l'expérience NEMO-3 candidates à la double désintegration beta sans émission de neutrino, Ph.D. Thesis, 2001

[95] J.Argyriades et al., Measurement of the background in the NEMO 3 double beta decay experiment, Nucl. Instrum. Meth. A606:449-465 (2009), arXiv:0903.2277v1.

[96] J. Mott, Measurement of the $2\nu\beta\beta$ half-life and a search for $0\nu\beta\beta$ of ^{82}Se with the NEMO-3 experiment, Internal position paper, DocDB:3887-v7

[97] V. Vasiliev, Physics case of SuperNEMO with ^{82}Se source, Internal note DocDB:358-v2

[98] S. Calvez, Updates on the demonstrator sensitivity and Radon study, Internal presentation DocDB:3476-v1

[99] National Nuclear Data Center Database

[100] R. Arnold et al., First results of the search of neutrinoless double beta decay with the NEMO 3 detector, Phys. Rev. Lett. 95 182302 (2005) arXiv:hep-ex/0507083

université PARIS-SACLAY | ÉCOLE DOCTORALE PHENIICS

Titre : Développement d'outils de reconstruction et sensibilité du démonstrateur SuperNEMO

Mots-clés : Neutrino, Double désintégration bêta, SuperNEMO, Simulation Monte-Carlo, Reconstruction d'évènements, Analyse bas bruit de fond

Résumé : L'expérience SuperNEMO cherche à observer la double désintégration beta sans émission de neutrinos, uniquement possible si le neutrino est une particule de Majorana. Le premier module, aussi appelé démonstrateur, est en cours de construction au Laboratoire Souterrain de Modane. Sa capacité à détecter les particules individuelles en plus d'en mesurer l'énergie en fait un détecteur unique. Le démonstrateur peut contenir 7 kg de ^{82}Se sous forme de fines feuilles source. Ces feuilles source sont entourées par une chambre à fils, permettant ainsi la reconstruction en 3 dimensions des traces de particules chargées. Un calorimètre segmenté, composé de scintillateurs plastiques couplés à des photomultiplicateurs, assure quant à lui la mesure de l'énergie de chaque particule. De plus, la chambre à fils peut être soumise à un champ magnétique afin d'identifier la charge des particules. SuperNEMO est donc capable d'effectuer la reconstruction complète de la cinématique d'un évènement ainsi que d'identifier la nature des particules impliquées dans ce dernier: électrons, positrons, particules α ou encore particules γ.

En pratique, la reconstruction des particules repose sur divers algorithmes implémentés dans un logiciel de simulation et de reconstruction développé par et pour la collaboration SuperNEMO. La reconstruction des particules γ est particulièrement délicate puisque ces particules ne laissent pas de traces dans la chambre à fils et sont seulement détectées par le calorimètre, parfois même plusieurs fois. Différentes approches ont été explorées durant cette thèse. Ce travail a abouti à la création d'un nouvel algorithme permettant à la fois d'optimiser l'efficacité de reconstruction des particules γ mais aussi d'améliorer la reconstruction de leurs énergies. D'autres programmes assurant l'identification des particules et l'opération des mesures topologiques pertinentes à chaque évènement ont aussi été développés.

La valeur du champ magnétique a été optimisée pour la recherche de la désintégration $0\nu\beta\beta$ à l'aide de simulations Monte-Carlo. Les performances des blindages magnétique ainsi que leur influence sur le champ magnétique ont été évaluées via des mesures effectuées grâce à des bobines magnétiques à échelle réduite.

Le démonstrateur SuperNEMO est capable de mesurer ses propres contaminations en bruits de fond grâce à des canaux d'analyse dédiés. À l'issue d'une première prise de données de 2,5 ans, les activités visées pour les principaux bruits de fond devraient être connues précisément. En outre, la demi-vie du processus $2\nu\beta\beta$ pour le ^{82}Se devrait être mesurée avec une incertitude totale de 0,3 %.

À la différence d'autres expériences double beta se basant uniquement sur la somme en énergie des deux électrons, SuperNEMO a accès à la totalité de la cinématique d'un évènement et donc à de plus nombreuses informations topologiques. Une analyse multivariée reposant sur des arbres de décision boostés permet ainsi une amélioration d'au moins 10 % de la sensibilité pour la recherche de la désintégration $0\nu\beta\beta$. Après 2,5 ans, et si aucun excès d'évènements $0\nu\beta\beta$ n'est observé, le démonstrateur pourra établir une limite inférieure sur la demi-vie du processus $0\nu\beta\beta$: $T^{0\nu}_{1/2} > 5.85\ 10^{24}$ ans, équivalant à une limite supérieure sur la masse effective du neutrino $\langle m_{\beta\beta}\rangle < 0.2 - 0.55$ eV. En extrapolant ce résultat à une exposition de 500 kg.an, ces mêmes limites deviendraient $T^{0\nu}_{1/2} > 10^{26}$ ans et $\langle m_{\beta\beta}\rangle < 40 - 110$ meV.

Université Paris-Saclay
Espace Technologique / Immeuble Discovery
Route de l'Orme aux Merisiers RD 128 / 91190 Saint-Aubin, France

université PARIS-SACLAY | ÉCOLE DOCTORALE PHENIICS

Title : Development of reconstruction tools and sensitivity of the SuperNEMO demonstrator

Keywords : Neutrino, Double beta decay, SuperNEMO, Monte-Carlo simulation, Event reconstruction, Low background analysis

Abstract : SuperNEMO is an experiment looking for the neutrinoless double beta decay in an effort to unveil the Majorana nature of the neutrino. The first module, called the demonstrator, is under construction and commissioning in the Laboratoire Souterrain de Modane. Its unique design combines tracking and calorimetry techniques. The demonstrator can study 7 kg of ^{82}Se, shaped in thin source foils. These source foils are surrounded by a wire chamber, thus allowing a 3-dimensional reconstruction of the charged particles tracks. The individual particles energies are then measured by a segmented calorimeter, composed of plastic scintillators coupled with photomultipliers. A magnetic field can be applied to the tracking volume in order to identify the charge of the particles. SuperNEMO is thus able to perform a full reconstruction of the events kinematics and to identify the nature of the particles involved: electron, positron, α particle or γ particle.

In practice, the particle and event reconstruction relies on a variety of algorithms, implemented in the dedicated SuperNEMO simulation and reconstruction software. The γ reconstruction is particularly challenging since γ particles do not leave tracks in the wire chamber and are only detected by the calorimeter, sometimes multiple times. Several γ reconstruction approaches were explored during this thesis. This work lead to the creation of a new algorithm optimizing the γ reconstruction efficiency and improving the γ energy reconstruction. Other programs allowing the particle identification and performing the topological measurements relevant to an event were also developed.

The value of the magnetic field was optimized for the $0\nu\beta\beta$ decay search, based on Monte-Carlo simulations. The magnetic shieldings performances and their impact on the shape of the magnetic field were estimated with measurements performed on small scale magnetic coils.

The SuperNEMO demonstrator is able to measure its own background contamination thanks to dedicated analysis channels. At the end of the first 2.5 years data taking phase, the main backgrounds target activities should be measured accurately. The ^{82}Se $2\nu\beta\beta$ half-life should be known with a 0.3 % total uncertainty.

Unlike other double beta decay experiments relying solely on the two electrons energy sum, SuperNEMO has access to the full events kinematics and thus to more topological information. A multivariate analysis based on Boosted Decision Trees was shown to guarantee at least a 10 % increase of the sensitivity of the $0\nu\beta\beta$ decay search. After 2.5 years, and if no excess of $0\nu\beta\beta$ events is observed, the SuperNEMO demonstrator should be able to set a limit on the $0\nu\beta\beta$ half-life of $T^{0\nu}_{1/2} > 5.85\ 10^{24}$ y, translating into a limit on the effective Majorana neutrino mass $\langle m_{\beta\beta}\rangle < 0.2 - 0.55$ eV. Extrapolating this result to the full-scale SuperNEMO experiment, *i.e.* 500 kg.y, the sensitivity would be raised to $T^{0\nu}_{1/2} > 10^{26}$ y or $\langle m_{\beta\beta}\rangle < 40 - 110$ meV.

Université Paris-Saclay
Espace Technologique / Immeuble Discovery
Route de l'Orme aux Merisiers RD 128 / 91190 Saint-Aubin, France